Electrochemical Oxygen Reduction and Oxygen Evolution from DMSO Based Electrolytes

Dissertation

Zur

Erlangung des Doktorgrades (Dr. rer. nat.)

Der

Mathematisch-Naturwissenschaftlichen Fakultät

der

Rheinischen Friedrich-Wilhelm-Universität Bonn

vorgelegt von

Christoph Johannes Bondü

aus Köln

Bonn September, 2016

Angefertigt Mit Genehmigung Der Mathematisch-

Naturwissenschaftlichen Fakultät der Rheinischen Friedrich-Wilhelm-

Universität Bonn

1. Gutachter: Prof. Dr. Helmut Baltruschat

2. Gutachter: Prof. Dr. Thomas Bredow

Tag der Promotion: 11.07.2017

Erscheinungsjahr: 2017

Abstract

In the present work the oxygen reduction reaction in organic electrolytes was investigated. Quantitative DEMS-studies (differential electrochemical mass spectroscopy) revealed that oxygen is reduced electrochemically to superoxide in $TBAClO_4$ (tetrabutyl ammonium perchlorate) containing, DMSO- (dimethyl sulfoxide) based electrolytes. This was derived from the fact that 1 electron is transferred in order to reduce one molecule of oxygen. 2 e^-/O_2 are transferred in the presence of Li^+, hence, resulting in the formation of Li_2O_2. This is also true for NMP- (*N*-methyl-2-pyrolidone) based electrolytes.

At smooth gold electrodes and at low overpotentials the z-value (number of electrons per reduced oxygen) is close to 1 e^-/O_2 even in lithium containing electrolytes. Under these conditions electrochemical oxygen reduction results in the formation of superoxide, which undergoes a chemical disproportionation to peroxide in the aftermath. This indirect pathway of peroxide formation shifts to a direct pathway of peroxide formation at higher overpotentials: Oxygen is reduced electrochemically to peroxide when the potential becomes more negative than -1.2 V (vs. Ag/Ag^+) which is indicated by a z-value close to 2 e^-/O_2. This mechanism was also ascertained by RRDE (Rotating Ring Disc Electrode) measurements. These measurements show that during oxygen reduction at the disk electrode species are formed that are oxidised at the ring electrode (*i.e*. detection electrode). It is generally assumed that the species that reacts at the ring electrode under these conditions is superoxide. As the overpotential increases and the potential range of the indirect pathway of peroxide formation is entered, less current is observed at the ring electrode.

It is a reasonable assumption that it is superoxide reacts at the ring electrode. However, it cannot be taken for granted. Therefore, a novel cell for RRDE like applications in combination with DEMS was designed. It allows proper identification of the species reacting at the detection electrode by means of mass spectroscopy. Employing the so-called 6-electrode cell showed that it is, indeed, superoxide that is detected at the ring electrode.

Further support for the proposed mechanism of oxygen reduction at gold stem from eQCMB (electrochemical Quartz Crystal Microbalance) measurements: Only at potentials lower than -1.2 V the formation of a deposit takes place. This corresponds well to the formation of soluble superoxide at low overpotentials, whereas solid Li_2O_2 forms at high overpotentials.

No such transition takes place when porous gold electrodes are employed. At these electrodes the z-value is always above 1.5 e^-/O_2. This difference has been ascribed to the structure of the porous gold electrode: Gold at open circuit catalyses a reaction that results in the oxidation of superoxide. Due to this reaction that takes place at electrical isolated gold particles in the porous gold electrode it is not possible to distinguish between the indirect and the direct pathway of peroxide formation.

There are also other parameters that influence the pathway by which electrochemical oxygen reduction takes place: The electrode material, the presence of water and the cation of the electrolyte. At rhodium oxygen reduction proceeds *via* the direct pathway of peroxide formation irrespective of the applied overpotential. At ruthenium and glassy carbon a z-value of approximately 1.5 e^-/O_2 indicates that both the direct and the indirect pathway of peroxide formation take place in parallel. Much alike to rhodium, also platinum appears to favour the direct pathway of peroxide formation even at low overpotentials. However, the deposition of Li_2O_2 inhibits the ability of platinum to reduce oxygen to peroxide. Therefore, in the course of oxygen reduction the mechanism shifts from the direct to the indirect pathway of peroxide formation. At BDD- (Boron Doped Diamond) electrodes no oxygen reduction takes place. The impact of the electrode material on the oxygen reduction reaction reveals an electrocatalytic effect on both, the oxygen reduction to superoxide and to peroxide. This indicates that both oxygen and superoxide need to undergo specific interaction with the electrode material prior to any charge transfer.

At gold electrodes the potential at which the transition from the indirect to the direct pathway takes place depends on the charge density of the cation in the electrolyte. As the charge density increases the transition takes place at lower overpotentials. No effect of the cation was found on the onset potential of oxygen reduction. Hence, the first charge transfer takes place without the involvement of the cation, whereas the second charge transfer is likely to take place after the cation has coordinated to superoxide.

With increasing water contents the potential at which the transition from the indirect to the direct pathway takes place shifts to higher overpotentials. However, this was only observed at gold, the only electrode material at which a sharp transition from the indirect to the direct pathway of peroxide formation takes place. The origin of the water-effect is still elusive.

During oxygen reduction, reduced oxygen species are deposited on the electrode. These are oxidised in the following anodic sweep. Oxygen evolution comes along with a z-value of 2 e^-/O_2 indicative for the oxidation of Li_2O_2 formed during oxygen reduction. There is no dependence of the onset potential of oxygen evolution on the used electrode material. However, the kinetics of this reaction is more sluggish at gold then at other electrode materials, which indicates also an electrocatalytic effect on the oxygen evolution reaction.

At potentials more positive then 0.3 V evolution CO_2-evolution takes place which indicates electrolyte decomposition. The amounts of evolved CO_2 linearly depend on the amounts of reduced oxygen during the previous cathodic sweep. This indicates that electrolyte decomposition takes place during oxygen reduction and that CO_2 evolution is due to the oxidation of decomposition products. The deposition of decomposition products during oxygen reduction shows up in higher then expected m.p.e-values (mass per electron)

observed *via* eQCMB measurements. The parallel deposition of Li_2O_2 and decomposition products leads to an inhomogeneous film on the electrode. This film-structure is responsible for the missing mass changes during oxygen evolution: When Li_2O_2 is oxidised the remaining decomposition products form cavities, which are filed up with electrolyte. The additional mass of the electrolyte offsets at least partially the mass losses due to Li_2O_2 oxidation.

Erklärung gemäß §6, Absatz 2 der Promotionsordnung der mathematisch naturwissenschaftlichen Fakultät

Die vorgelegte Arbeit wurde von mir persönlich, selbstständig und ohne Benutzung anderer als der angegebenen Hilfsmittel angefertigt. Alle direkt oder indirekt übernommenen Daten oder Konzepte wurden durch entsprechende Quellenangaben kenntlich gemacht. Ich versichere, dass diese Arbeit weder vollständig noch in Teilen als Dissertation zu irgendeinem Zeitpunkt eingereicht wurde. Ich habe weder vor noch während meiner Promotion oder bei der Anfertigung dieser Dissertation entgeltliche oder nicht-entgeltliche Beratungs- oder Vermittlungsdienstleistungen in Anspruch genommen.

Ich versichere damit, dass diese Dissertation im Einklang der in §6, Absatz 2 der Promotionsordnung der mathematisch naturwissenschaftlichen Fakultät der Universität Bonn vom 3. Juni 2011 geforderten Bedingungen steht.

_____

(C. Bondü)

Danksagung

Ich finde es seltsame eine Erklärung abzugeben, dass ich diese Arbeit selbstständig und ohne fremde Hilfsmittel als die angegebenen angefertigt habe. Seltsam deshalb, weil eine wissenschaftliche Arbeit letztlich immer ein gemeinsames Projekt ist aus dem einzelne Teile herausgelöst und in eine isolierte Promotion gesteckt werden. Wo aber beginnt der Beitrag des einen und wo endet der eines anderen? Die Grenzen verwischen – auch deshalb habe ich die Form der kumulativen Dissertation gewählt bei der die Beiträge anderer über die Autorenschaft der einzelnen Artikel ersichtlich sind. Nichts desto trotz gebietet mir das Einreichen dieser Arbeit einigen Menschen im speziellen zu danken.

Zu aller erst möchte ich Herrn Baltruschat danken, der mich als Doktorand und diese Arbeit betreut hat. Das Maß an Zeit, dass Herr Baltruschat in die Betreuung seiner Doktoranden investiert ist nicht selbstverständlich. Herr Baltruschat erklärt seine Gedankengänge und ist bereit diese mit offenem Ausgang zu diskutieren. Daher ist es möglich seine Gedanken wirklich nach zu vollziehen, anstatt sie einfach abzuknicken, oder sie in selteneren Fällen zu korrigieren. Ich denke, dass dieses Vorgehen eher die Ausnahme als die Regel ist und ich glaube daher, dass es nicht viele Gruppen gibt, in denen ich fachlich so hätte wachsen können, wie es in der Grupp von Herrn Baltruschat der Fall war. Zudem hatte ich ein hohes Maß an Freiheit auch eigene Fragestellungen zu verfolgen. Gleichzeitig konnte ich auf die notwendige Führung vertrauen. Auch das sind Dinge die nicht immer selbstverständlich sind.

Zudem möchte ich Jan Kaul und Abd El Aziz Abd El Latif danken, die vom Anfang bis zum Ende meiner Promotion meine Kollegen waren. Wir haben uns gegenseitig geholfen und lange Zeit viele Lasten geteilt. Wir haben Rücksicht auf einander genommen und lustige Unterhaltungen geführt.

Eine Promotion ist ein ganzer Lebensabschnitt, der vermutlich immer von Unsicherheit, Zweifeln und Rückschlägen geprägt ist. Ich muss allen Menschen Danken, die diese Zeit mit mir verbracht haben. Ganz besonders muss ich meiner Familie danken, die immer für mich da war. Wie oft haben meine Eltern und meine Schwester geholfen, wenn mir Alles über den Kopf gewachsen ist? Viel wichtiger ist aber das Gefühl gewesen, dass Sie einfach da waren und zu wissen, dass ich mich auf sie verlassen konnte. In den Zeiten in denen ich glaubte, dass ich niemals fertig werde, wusste ich, dass ich trotzdem keine Enttäuschung für meine Familie wäre, wenn ich aufgegeben hätte. Ich weiß um die Sorgen, die ich meiner Familie bereitet habe wenn ich drüber geklagt habe was alles nicht funktionierte. Vermutlich hat meine Familie darunter mehr gelitten als ich. Meinen Eltern möchte ich zudem noch dafür danken, dass Sie mich durch mein Studium getragen haben und mir dadurch überhaupt ermöglicht haben die vorliegende Arbeit zu beginnen.

Zuletzt möchte ich meinen Freunden danke vor allem jenen, die seit Beginn meines Studiums dazu gehören und mein Leben in Bonn so sehr bereichert haben: Lisa und Christian Landvogt, Christian Kube, Tobias Damen, Yvonne Lorenz, Maria und Thomas Linden.

Contents

1. Introduction

Each paper that is part of this work features an introduction and a discussion section that puts the results reported in the respective paper in context with the literature. In order to avoid redundancies no exhaustive literature survey will be given at this point. However, it seems to be beneficial to put the current work briefly into an historic context as far as the research on lithium-air batteries is concerned.

1. 1. Motivation

It is common knowledge that present motorised private transport depends largely on the combustion of fossil fuels which releases CO_2 into the atmosphere. For different reasons the emission of CO_2 has become politically unwanted in the German society and beyond [1, 2]. The German federal government aims to reduce greenhouse gas emissions drastically. By 2050 CO_2-emissions are to drop to 20% to 5% of the level it had in 1990 [2]. It is clear that such ambitious aims are only attainable if it becomes possible to shift transportation of individuals and goods to CO_2-neutral forms. One approach, among others, is to make use of secondary batteries in order to electrify automotive transportation [2, 3]. By doing so CO_2-neutrality would be achieved if the electricity that is used to charge batteries is generated by zero-emission technologies.

However, battery technologies that are commercially available already lack specific energy densities that match those of petrol [4]. For that reason and because of the huge economic potential of secondary batteries with specific energy densities that reach close to those of petrol a political momentum has developed that aims at the advancement of new battery concepts [3].

One of these new battery concepts are lithium-air-batteries which, other then lithium ion batteries, do not require the intercalation of lithium ions in heavy metal oxides. Upon discharge of a lithium air battery the lithium anode is oxidised and provides electrons *via* an external circuit to the air electrode, where they are used to reduce oxygen from air. Given the low weight of the active components (lithium and oxygen) and the large differences of their standard potentials, lithium air batteries have a theoretical specific energy density of 11.14 kWh/kg (40.1 kJ/g) [5]. This very large value is obtained when the weight of oxygen is excluded (since it is supplied by air) and when it is assumed that Li_2O is formed as the final discharge product. However, if the weight of oxygen is included and if it is assumed that Li_2O_2 forms as the dominant discharge product then the theoretical energy density is reduced to 13.8 kJ/g with a theoretical efficiency of 90.2%. These values were calculated from the relevant thermodynamic data [6, 7]. The theoretical efficiency diverts from 100% because of the heat flow due to the entropy.

There are two construction concepts for lithium air batteries. In the first concept the air electrode is in contact with an aqueous electrolyte. This requires either an ion conducting membrane or a ceramic that protects the anode from humidity. In the second concept both the cathode as well as the anode are immersed into the same non-aqueous, aprotic electrolyte. The latter concept was introduced by Abraham in 1996 [5]. The crucial processes during discharge and charge of lithium-air batteries are the electrochemical reduction and evolution of oxygen from organic electrolytes. Therefore, the present work aimed at gaining a genuine understanding of these processes.

1. 2. Situation Prior to the Dissertation

In the past a lot of research connected to lithium-air batteries involved predominantly the construction of model batteries (this approach has not been abandoned, but arguably in current research efforts it is less prominent). The concept of a non-aqueous lithium air battery was developed by Abraham in 1996 [5]. Abraham, allegedly, demonstrated the working principle with a model battery that employed a polymer electrolyte containing ethylene carbonate (indeed, it needs emphasising that in retrospective this model battery did everything but follow the principle of a lithium-air battery). The choice of the electrolyte, in particular the ethylene carbonate component, was probably inspired by its widespread use in lithium ion batteries. Carbonate based electrolytes are frequently used there because they form a "solid electrolyte interphase" (SEI; indeed, inter*phase* as the SEI is an extended phase, rather than a two dimensional interface) in front of the lithium anode [8]. The SEI acts as an ion conducting membrane that separates the anode from the electrolyte and, hence, protects both anode and electrolyte from further decomposition.

One decade later the concept of lithium-air battery was embraced by the Bruce-group [9]. In 2006 Ogasawara *et al*. reported a model lithium-air battery that had an initial capacity of approximately 1000 mAh/g at a discharge plateau of 2.5 V (*i.e*. 9 kJ/g) and that retained 60% of its capacity after 50 charge-discharge cycles. Similar to the battery reported by Abraham [5] this battery employed a carbonate based electrolyte. To the scientist at that time a battery with capacities and cycling performances as those reported by Ogasawara *et al*. must have appeared as a benchmark system. In addition Ogasawara *et al*. showed by means of differential electrochemical mass spectroscopy (DEMS) that during the first charge of this battery predominantly oxygen was evolved.

Simply passing charge into the battery and recording the voltage respond does not give any information on the reactions that consume and deliver charge. Therefore, the DEMS measurements done by Ogasawara *et al*. were perceived to be of great value, because they supposedly showed that oxygen reduction and oxygen evolution were the reactions that provided current during discharge and charge. However, the reported DEMS results of

Ogasawara *et al*. only refer to an electrode to which Li_2O_2 was added, rather than to an experiment where oxygen was reduced from the gas phase during discharge prior to the DEMS measurement [9]. Hence, the report of Ogasawara *et al*. only shows that it is possible to evolve oxygen by oxidation of Li_2O_2 in the described setup. It neither shows that Li_2O_2 actually forms during discharge *via* oxygen reduction nor that electrochemically formed Li_2O_2 is oxidised during charge. (Electrochemically formed Li_2O_2 does not necessarily deposit in the oxygen electrode. If Li_2O_2 precipitates at locations in the battery without electric contact to the oxygen electrode complete charge is not possible.) Therefore, it would have been interesting if Ogasawara *et al*. had provided DEMS-results for the second discharge-charge cycle. However, the report of Ogasawara *et al*. strongly suggests that lithium-air batteries employing carbonate based electrolytes are properly working and only require optimisation [9].

In the years that followed the report of Ogasawara *et al*. no less than 11 reports on lithium air batteries - all of which featuring a carbonate based electrolyte - were published by various groups [10-20]. In *post mortem* analysis some authors supposedly verified by means of XRD [10, 17], FTIR [10] and/or Raman spectroscopy [11] that Li_2O_2 formed during oxygen reduction (*e.g*. discharge) while the presence of (major amounts of) Li_2CO_3 was ruled out.

In 2011 then numerous papers were published that showed that superoxide formed during oxygen reduction initiates the decomposition of carbonate based electrolytes [21-28]. The techniques used in these studies included theoretical calculations [23, 24], NMR [22] [26], SERS (surface enhanced Raman spectroscopy) [22], XPS (X-ray photoelectron spectroscopy) [25], DEMS [22] [21, 27, 28], Raman spectroscopy [25], FTIR spectroscopy [22, 25-27] and XRD [26-28]. Scheme 1 shows the decomposition mechanism of propylen carbonate as proposed by Freundberger *et al*. [22].

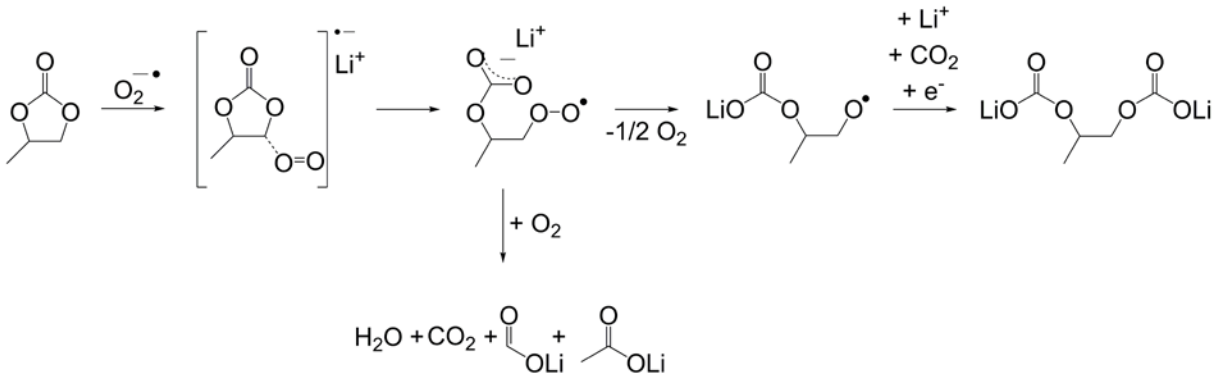

Scheme 1: Decomposition of propylene carbonate during oxygen reduction reaction as proposed by Freudenberger *et al*. [22].

Discharge (oxygen reduction) in lithium air batteries operating with carbonate based electrolytes results in the formation Li_2CO_3, $C_3H_6(OCO_2Li)_2$, CH_3CO_2Li, HCO_2Li, CO_2 and H_2O [22]. In the subsequent charging these compounds are oxidised, hence, evolving predominantly CO_2. Note that among others Raman-spectroscopy, FTIR-spectroscopy,

DEMS and XRD were used to show that carbonates decompose in the presence of reduced oxygen species. The very same techniques were used in previous studies to show that Li_2O_2 (rather than Li_2CO_3) is formed during discharge (*i.e*. oxygen reduction) of lithium air batteries that employ carbonate based electrolytes [5, 9-11]. Today, it is accepted that oxygen reduction in carbonate based electrolytes results in formation of decomposition products. But it remains hard to understand why there was a need to rectify the literature in the first place. This history also emphasises the need to flank battery research by more fundamental approaches to the underling processes than it is possible in model battery studies.

After 2011 the quest for new and stable solvents began. Post 2011 electrolytes were based on ethers [22, 29-32], ionic liquids [30], NMP (*N*-methyl-2-pyrrolidone) [33] and DMSO (dimethyl sulfoxide) [34]. With the exception of ionic liquids (which were not tested) the stability of all of these solvents was questioned by the DEMS-results published by McCloskey *et al*. in 2012 [35]. McCloskey *et al*. observed that lithium-air batteries employing electrolytes based on either NMP, DMSO or DME (dimethoxyethane) consumed more oxygen during discharge (oxygen reduction) than they evolved during charge. In addition McCloscey *et al*. observed the evolution of CO_2 which they deemed the product of electrolyte decomposition. However, decomposition of these electrolyte systems seems to be less severe than in carbonate based systems.

At least in the case of DMSO the results presented by McCloskey *et al*. [35] are at odds with those presented by Peng *et al*. [34]. The latter presented a model battery that employed a DMSO based electrolyte with rather good cycling performance. By means of DEMS Peng *et al*. showed that no CO_2 evolution takes place during charge when the employed oxygen electrode consisted of porous gold. On the other hand CO_2 evolution was observed when the oxygen electrode was made from carbon [34]. Although not stated explicitly, the paper of Peng *et al*. strongly implies that CO_2 evolution to carbon corrosion. McCloskey *et al*. did not provide any DEMS experiments at gold but only at carbon based electrode [35]. It is conceivable that different results presented by Peng *et al*. [34] and McCloskey *et al*. [35] are, indeed, due to different electrode material. However, until then there was barely any knowledge available on how the electrode material might influence the oxygen reduction reaction or the oxidation of Li_2O_2. Only Lu *et al*. found that the current density during oxygen reduction depends on the electrode material in a DME based electrolyte [36]. But whether and how the electrode material might influence the cycling behaviour of lithium air batteries was still unknown.

Although much work in literature concerns construction of model lithium-air batteries, there are also more fundamental studies available. Already in 1965 Peover and White mentioned in a brief communication that oxygen is reduced to superoxide at a mercury

electrode in a variety of solvents, when *tert*-butylammonium perchlorate ($TBAClO_4$) was present [37]. This conclusion was based mainly on the evaluation of CV data, but also on EPR-results. In 1966 Swayer and Roberts found that oxygen was reduced to peroxide in an electrolyte of 0.05 M NH_4ClO_4 in DMSO at mercury or gold electrodes [38]. However, superoxide was formed in the same electrolyte at platinum electrodes or in an electrolyte of 0.05 M NEt_4ClO_4 in DMSO irrespective of the electrode material. Swayer and Roberts employed for their study cyclovoltammetry and chronoamperometry, but no spectroscopy techniques were used. Although Swayer and Roberts were the first to show that the cation exerts an influence on the product of oxygen reduction in organic electrolytes, Laoire *et al*. are more often cited in this context. From CV data and kinetic considerations Laoire *et al*. proposed that oxygen reduction in TBA^+ containing electrolytes results in the formation of superoxide, whereas in the presence of smaller and more polarising cations such as Li^+ and Na^+ peroxide was formed [39, 40].

It should not come as a surprise that oxygen reduction in Li^+-containing electrolytes leads to the formation of Li_2O_2 (rather than to other conceivable lithium oxide species such as Li_2O or LiO_2). In aqueous electrolytes oxygen is reduced to water (*i.e*. the proton analogue of Li_2O) only at electrode materials at which strong oxygen adsorption is observed [41]. The presence of adsorbates on the surface hampers oxygen adsorption and favours the formation of H_2O_2 [42]. It appears logic that large molecules of organic solvents adsorbed at the electrode disfavours the formation of Li_2O (although work on that issue is still required). LiO_2 on the other hand is known to exist only in the argon matrix and disproportionates to O_2 and Li_2O_2 under ambient conditions [43, 44].

Although it is clear that oxygen reduction in organic lithium-containing electrolytes eventually leads to the formation of Li_2O_2 the path to Li_2O_2 remains largely elusive. For the oxygen reduction in DMSO based and lithium containing electrolytes Laoire *et al*. proposed that oxygen is reduced to superoxide at low overpotentials. In that case Li_2O_2 is formed by lithium induced disproportionation. Furthermore, Laoire *et al*. proposed that at high overpotentials electrochemical peroxide formation dominates. Laoire *et al*. based this mechanism on a potential opening experiment and kinetic considerations [40].

It can be said in summary that at the beginning of the project little was known about the oxygen reduction reaction in organic media. Laoire *et al*. had already proposed important fundamental concepts on the effect of the solvent and the cation on the mechanism of oxygen reduction reaction [39, 40] but these concepts where not yet put to a test by other groups. Nothing was known about the effect of water or the electrode material. Electrolyte systems which were not based on carbonates were proposed, but experimental work on these electrolytes was still rare. Our aim was, therefore, to gain a fundamental insight into

the oxygen reduction reaction, which we deem necessary to succeed in the strive for a properly working lithium-air battery.

2. Experimental Techniques

In each of the Papers that are part of this work a detailed experimental section describes how the experiments were conducted and the reader is referred to the respective papers for practical details. This section describes the employed techniques for the reader who is less familiar with standard techniques of electrochemistry.

2. 1. Rotating Ring Disc Electrode

The rotating (ring) disc electrode is a powerful tool that allows the experimentalist to separate limitations due to diffusion from limitations due to kinetics. By doing so it is possible to determine the rate constant of an electrochemical reaction [45] or even the rate constant of a chemical decay that follow the electrochemical generation of a substance [45]. In addition the maximum achievable current depends on the diffusion coefficient and the concentration of the reactant, on the viscosity of the electrolyte and the number of electrons transferred per reacting molecule. If only one of these quantities is unknown it can be determined by an RRDE measurement [45]. However in the present study the potential of the RRDE technique was harnessed only to a limited degree, as the technique is hampered by the formation of solid Li_2O_2. Therefore only a very brief overview over the principle that underlies the technique is given.

Principle of the Rotating Ring Disc Electrode

The centrepiece of the technique are two independent electrodes embedded in a tip of polymeres (in the present study a tip of Teflon was used). The first electrode is a disc electrode situated in the centre of the tip. The second electrode is a ring that encircles the disc electrode with a constant distance. Ideally the surface of the ring, the disc and the tip form a plane [45].

During an RRDE experiment the tip is immersed into the electrolyte and rotated along the surface normal of the disc electrode. The rotation accelerates the electrolyte in contact with the tip in radial direction (r-direction in Figure 1). This in turn causes bulk electrolyte to approach the tip in the direction of the surface normal of the disc electrode (y-direction in Figure 1) [45].

The forced convection has two consequences. The *Nernstian Diffusion Layer* in front of the electrode has a defined thickness, which can be adjusted by choosing an appropriate rotation speed. Molecules can reach the electrode only after diffusing through the *Nernstian Diffusion Layer*. It is possible to calculate the maximal flux of reactants to the electrode, if the thickness of the diffusion layer and the diffusion coefficient of the reactant are known [45].

The second consequence of forced convection is that intermediates or soluble products formed at the disk electrode are transported to the ring electrode. It is possible to choose the potential at the ring electrode independently from the potential at the disc electrode. Usually a fixed potential is applied to the ring electrode while the potential at the disc electrode is swept between certain limits. If the intermediates that were formed at the disc electrode undergo an electrochemical reaction at the potential applied to the ring electrode, a current at the ring electrode is observed. Hence, the RRDE technique can be employed to test whether soluble products or intermediates are formed during electrochemical experiments [45]. Mainly because of this application the RRDE technique was employed in the presented study.

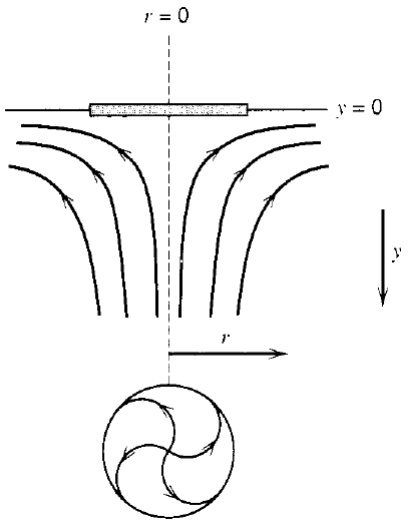

Figure 1: Convection behaviour of the electrolyte during an (R)RDE experiment. Picture source: [45]

2. 2. Differential Electrochemical Mass Spectroscopy (DEMS)

The DEMS technique has been reviewed by Baltruschat [46]. The following section will largely summarize his article, as far as its content is of importance for the current study.

Introduction

Based on current voltage curves (*e.g*. cyclo voltamogramms) it is hardly possible to determine reactants and products of electrochemical reactions. Application of purely electrochemical techniques to unknown reactions is, therefore, of very limited value to chemists if not combined with other techniques that give at least qualitative information on the product distribution. Electrochemists are limited in their choice of electrode dimension and electrode geometry, because they have to maintain potential control and they have to avert inhomogeneous IR-drop across the electrolyte. Therefore, product formation rates are

too low to employ insensitive techniques such as NMR, popular in synthetic chemistry. In addition electrochemists seek to study dynamic processes. Such studies demand a small retention time of the technique that is employed parallel to the electrochemical method.

In 1971, therefore, Bruckenstein and Gadde came up with a cell design that allowed them to combine electrochemistry with mass spectroscopy [47]. Using a porous Teflon membrane this set up allowed the Bruckenstein group the qualitative and quantitative analysis of volatile products of electrochemical reactions [48, 49] [50, 51]. However, there is a general consensus in literature that the technique employed by Bruckenstein can be referred to as electrochemical mass spectroscopy (EMS) [46, 52, 53]. In EMS a mass spectroscopic response is observed only after rise times of 20 seconds [52] and the term electrochemical mass spectroscopy is, therefore, used to discriminate the technique from differential electrochemical mass spectroscopy (DEMS) with faster response times. A rise time of 20 seconds is much too long to register changes in the formation rate of volatile reaction products. This is why EMS is not suited to study dynamic processes. This issue was addressed by Wolter and Heitbaum who introduced DEMS in 1984 [52]. The latter technique allows the experimentalist to correlate the ionic current to the faradic current, whereas EMS only allowed the correlation of the ionic charge to the faradic charge. Hence, Wolter and Heitbaum achieved a much faster response time.

Interface Between Vacuum and Electrolyte

It is crucial for the combination of electrochemistry and mass spectroscopy to allow volatile reaction products to pass into the vacuum, while keeping the liquid phase out. In traditional DEMS this is achieved by employing a non-wettable membrane on which the electrolyte rests [46, 47, 52, 53]. When Wolter and Heitbaum introduced DEMS they also defined the prerequisite of the membrane: It must be hydrophobic to hold back the liquid and at the same time it must be porous so that molecules can diffuse through the membrane into the vacuum chamber. This is generally achieved by employing a porous Teflon membrane. In order to maintain a high permeability of the membrane for volatile compounds the pores must not be flooded with electrolyte. Otherwise diffusion in the liquid phase would be required which would prohibit a rapid transfer of volatile reaction products to the mass spectrometer. From the relationship in Equation 1 Wolter and Heitbaum determined that the pore radius must be smaller than 0.8 µm when aqueous electrolytes are employed to keep the liquid phase from penetrating the vacuum.

$$r < -\frac{2\sigma\cos(\theta)}{p_{atm}} \qquad \text{Eq. 1}$$

In Equation 1 σ is the surface tension of the electrolyte, θ is the contact angle between electrolyte and Teflon, p_{atm} is the atmospheric pressure and r is the radius of the pore [52]. Indeed, the pressure difference across the pore rather than p_{atm} should enter the denominator of the relation in Equation 1. However, in the cell setup described by Wolter and Heitbaum the pressure difference is dominated by atmospheric pressure. Because the manufacturer of the Teflon membrane provides only average pore radii and because pore flooding must be avoided it is advisable to use membranes with a pore sizes well below 0.8 µm. In practice and in the current study membranes that feature pore sizes of 0.02 µm are used [46, 52, 53].

Although the Teflon membrane prevents liquid electrolyte to enter the vacuum system, the solvent can still evaporate. This causes a constant flux of vapour into the vacuum and thus increases the pressure in the ionization chamber. Assuming molecular flow in the pores the flow rate of any gaseous species per unit area into the vacuum was calculated by Wolter and Heitbaum according to Equation 2,

$$\dot{n} = \frac{8}{3}\sqrt{\frac{RT}{2\pi M}} \cdot \frac{r}{l}\left(p_1 - p_2\right) \qquad \text{Eq. 2}$$

where R is the gas constant, T is the temperature, r is the radius of the pore, l is the pore length, p_1 is the partial pressure of the solvent and p_2 is the pressure in the ionization chamber [52] (considering a vapour pressure of 23.4 hPa and assuming an unreasonable large cross section of 1 nm^2 the mean free pathway of water is estimated to be larger then 1.7 µm. This value is much larger then the dimensions of the pore, hence, the assumption of molecular flow is valid). The total influx $\dot{n}$ is then given by the flow per unit area times the surface area (A_{tot}) times the porosity (γ). Using a membrane with a porosity of 50%, a total surface area of 0.28 cm^2, a pore length of 50 µm and a pore radius of 0.02 µm Kohdayari has recently found experimentally that 0.05 µl/s of liquid water evaporate into the mass spectrometer. This fits well to the theoretical value of 0.04 µl/s of liquid water that is calculated from Equation 2 and the ideal gas law.

In order to avoid a pressure higher then 10^{-3} hPa the dimensions of the membrane have to be chosen accordingly. In order to achieve this the effective pumping speed (S) at 10^{-3} hPa must at least equal the influx (eq. 3).

$$\dot{n} \cdot A_{tot} \cdot \gamma = 10^{-3} hPa \cdot S \qquad \text{Eq. 3}$$

Wolter and Heitbaum found that the maximal acceptable surface area of a membrane with a porosity of 50%, a thickness of 150 µm and a pore size of 0.02 µm is 1 cm^2, when the effective pumping speed is 200 l/s [52]. For the current work a membrane with a porosity of 50%, a thickness of 75 µm and a pore size of 0.02 µm was used and a surface area of 0.3 cm^2 was exposed to the vacuum.

The Vacuum System

Figure 2 shows the set up of the vacuum system introduced by Wolter and Heitbaum.

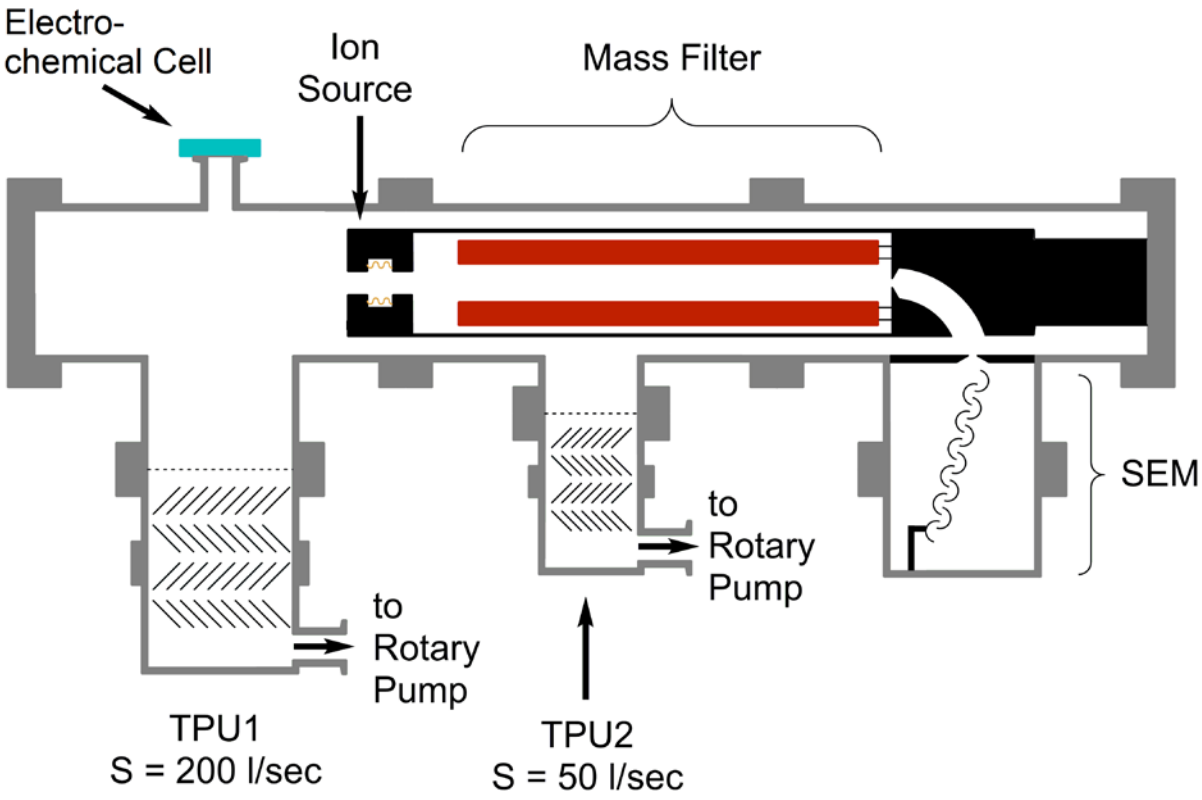

Figure 2: Schematic drawing of the DEMS-setup presented by Wolter and Heitbaum [52] which was also used in the present study.

In principal the quadrupol mass spectrometer separates the vacuum system in two compartments: The ionization section containing the ionisation chamber and the analyzer section, where the ions are separated by their mass to charge ratio and are then detected. Both sections are differentially pumped (ionization section: 200 l/s; analyzer section: 50 l/sec). The electrochemical cell is placed on top of the ionization section and volatile species can pass over into the gas phase through a porous Teflon membrane (*vide supra*) [52].

Although the design of the electrochemical cell placed on the DEMS-system has been subject to many improvements, no advancements of the actual DEMS set up were achieved (of course with the exception of a general improvement in pumping techniques and in partial

pressure measurement). Hence, in the current work essentially the same set up was used as that shown in Figure 2

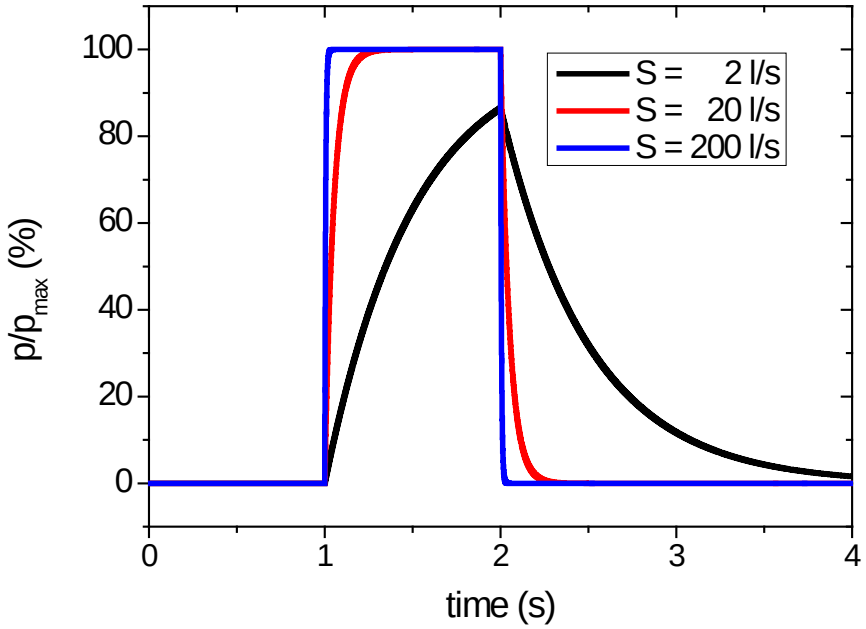

Figure 3: Percentage of the maximal attainable pressure in a volume of 1 l, which is pumped with the indicated effective pumping speed, when at second 1 an influx of 0.001 mbar·l/s was allowed and at second 2 the influx was stopped. The curves were calculated by Equations 4A and 4B.

The relatively large effective pumping speed of 200 l/s is not only necessary to maintain a low pressure in the ionization section while allowing for a relatively large surface area of the membrane, but also to keep the time constant of the mass spectrometer low. That is, rapid changes in the influx of gaseous species should be paralleled by rapid changes in the ionic current for that species. In order to fulfil this requirement the partial pressure of the species in question must enter its equilibrium value on a time scale of milliseconds. After a sudden increase of the influx $\dot{n}$ of a gaseous species its partial pressure p will change according to Equation 4A and after a sudden decrease according to Equation 4B

$$p = \left(\frac{\dot{n}}{S}\right) \cdot \left(1 - \exp\left(-t/\tau\right)\right) \qquad \text{Eq. 4A}$$

$$p = p_0 \cdot \exp\left(-t/\tau\right) \qquad \text{Eq. 4B}$$

where t is the time and τ is the time constant which is given by $\tau = V/S$ with V as the volume of the ionization chamber [46, 52]. p_0 in Equation 4B is the partial pressure of the gaseous species before the influx decreases. Figure 3 shows the evolution of the partial pressure for various pumping speeds after an influx of 0.001 mbar·l/s is allowed after one second and stopped after two seconds. The curves in Figure 3 were simulated according to

Equations 4A and 4B. The assumed influx is in the order of magnitude that was observed experimentally for the evaporation of ethanol and methanol from aqueous solution [54]. Figure 3 visualises that an effective pumping speed lower than 20 l/s comes at the cost of an unacceptable response time. In that case the time constant of the mass spectrometer is 50 ms, when the ionization section has a volume of 1 l and is pumped with an effective pumping speed of 20 l/s [46]. It is pointless to reduce the time constant much further, since the time constant of the electrochemical cell is larger (*i.e*. the time constant of the transfer of volatile species from the electrolyte into the gas phase) [46]. However, a sufficient pumping speed is necessary to maintain an acceptable pressure of max. 10^{-3} mbar in the ionization chamber.

The second turbo molecular pump is necessary to reduce the pressure in the analyser section to below 10^{-5} hPa. A sufficiently low pressure in the analyser section is required to reduce sensitivity limitations due to collisions with residual gas.

Cell Design

A large number of various cell designs are described in literature and a detailed review of various cell designs has been provided by Baltruschat [46]. In the following section some types of DEMS cells are briefly discussed:

Traditional Cells: In here all cell designs where the working electrode forms the interface between vacuum and electrolyte are considered "traditional cells". In these cells the working electrode is deposited directly on the Teflon membrane. This is done by either painting a conducting lacquer of metal particles or by sputter deposition of the metal directly on the membrane. The close proximity between electrode and vacuum ensures that reaction products can rapidly pass into the gas phase.

Because a thin porous Teflon membrane has not the mechanical stability to withstand the pressure difference between atmosphere and high vacuum it is supported by some kind of frit. In the very first setup described by Wolter and Heitbaum this was a glass frit, which was connected to the vacuum system *via* a ground glass joint. Later, steel frits were used in order to support the Teflon membrane [46, 53, 55]. In all cases the membrane is pressed onto the frit by a cell made from glass or Teflon. A hole in the cell allows contact between the electrolyte and the working electrode. The reference and counter electrode are kept in the same compartment, as the working electrode.

One disadvantage of traditional cells is that no defined convection is applicable. Although the electrolyte is stirred while purging with gas, no defined conditions are achieved as with the rotating disc electrode. In order to address this problem Tegtmeyer combined the rotating disc electrode technique with DEMS [56]. However, in this arrangement the

experimentalist is still bound to metal sputtered electrodes, which prohibits the use of electrode materials that cannot be sputtered or the use of single crystals.

Dual Thin Layer Cell: In the dual thin layer cell defined convection can be applied. The setup of this cell as described by Jusys *et al*. is shown in Figure 4 [57]. In this cell the electrolyte enters the upper compartment through the inlet which then flows along the working electrode through six capillaries into the lower compartment. Reaction products formed at the working electrode are transported along with the electrolyte into the lower compartment, where they can evaporate into the vacuum of the mass spectrometer. The electrolyte leaves the lower compartment *via* the outlet placed at the centre of the cell.

This cell geometry is reminiscent of a wall jet arrangement were a jet of electrolyte is directed parallel to the surface normal of the electrode. In such an arrangement the diffusion limited current I_{Diff} is proportional to $u^{3/4}$ [58, 59], where u is the flow rate of the electrolyte. However, it was found experimentally that I_{Diff} is proportional to $u^{1/3}$ [46, 60] which is more typical for the laminar channel flow behaviour. Indeed, it has been shown recently that the diffusion limited current follows the relationship in Equation 5

$$I_{Diff} = g \cdot z \cdot F \cdot c \cdot D^{2/3} \cdot u^{x} \qquad \text{Eq. 5}$$

In Equation 5 g is a geometry factor that varies in each cell setup, D is the diffusion coefficient of the reactant, c is the concentration of the reactant and x is either 1 (at low flow rates) or 1/3 (at large flow rates) [60].

The dual thin layer cell is an improvement of the thin layer cell where the working electrode is placed in a distance to the membrane of less then 100 µm[46]. It is possible to work with single crystal in this cell and it has a high collection efficiency. However, working under flow reduces the collection efficiency significantly and convection is inefficient to increase mass transport in this cell setup.

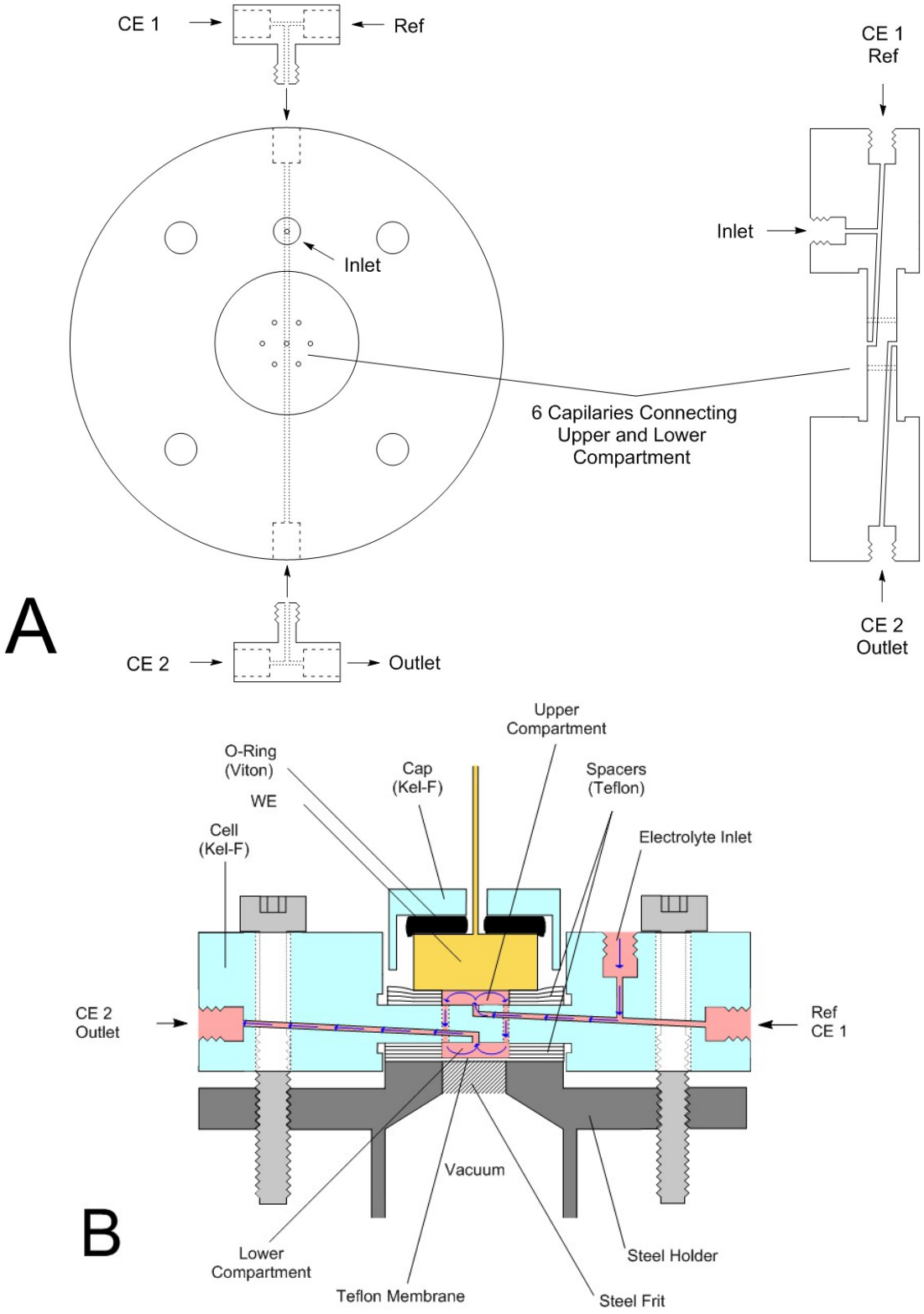

Figure 4: Drawing of the dual thin layer cell. A: Cross section of the cell. B: Cross section of the cell during operation.

Head space cells: The requirements for DEMS established by Wolter and Heitbaum [52] are often not fulfilled when organic electrolytes are used. Due to a lower surface tension the pores of the Teflon membrane are often flooded by organic electrolytes. In addition the sometimes very high vapour pressure of organic solvents means that the influx of gaseous species into the ionization chamber is too high to maintain a total pressure of lower than 10^{-3} hPa. Hence, if the electrolyte has a low surface tension and/or a high vapour pressure the cell types discussed so far are not applicable.

Both the Bruce [34] and the McClokey groups [35] therefore used headspace cells in studies related to lithium-air batteries. In these cells the membrane does not separate the electrolyte from the vacuum directly, but from a space in the cell that is at ambient pressure. In the relationship of Equation 1 p_{atm} must be replaced by the much smaller pressure difference between gas phase and electrolyte. In this case a much lower surface tension of the electrolyte and a much lower contact angle between electrolyte and membrane is affordable. This also means that membrane materials other than Teflon can be used, which offers the opportunity to use gas diffusion electrodes that would be employed in actual batteries. McCloskey for instance used a gas diffusion electrode based on carbon black instead of a membrane [35].

Still volatile reaction products can diffuse through the membrane from the electrolyte into the space above the cell. This space is continuously purged with a carrier gas. Through a capillary a portion of the carrier gas along with volatile reaction products is sampled and introduced to the mass spectrometer. It is also possible to supply the reactant from the gas phase if volatile enough and to observe its consume *via* mass spectroscopy.

Unfortunately head space cells employed in Li-air battery studies were never characterised in terms of time constants. Given that the CV presented by Peng *et al*. were recorded with a sweep rate of 0.1 mV/sec it is unlikely that the temporal resolution is high. Indeed, Johnson *et al*. of the Bruce group, doubted that it is possible to distinguish *via* DEMS between the indirect and the direct pathway of peroxide formation [61].

Calibration

DEMS is a quantitative [52, 53] or at least a semi quantitative method [46]. However, before it is possible to correlate the ion current I_i (e.g. the mass spectroscopic signal) for a given mass number to the actual influx $\dot{n}$ of gaseous species according to Equation 6 it is necessary to determinate the proportionality constant K° [46].

$$I_i = K^\circ \cdot \dot{n} \qquad \text{Eq. 6}$$

The calibration constant K° is easily determined by leakage calibration which is described in Paper 1 and elsewhere [56]. During leakage calibration a known amount of gas is introduced to the ionization section of the DEMS setup and the ion current is measured. The calibration constant determined from the ratio of influx and ionic current contains all influences on the detection sensitivity which are due to the state and the settings of the mass spectrometer [46]. Because of non-linearities in partial pressure measurements it is necessary to calibrate the mass spectrometer under similar conditions under which the actual measurement is done. That is, during calibration the electrochemical cell should be attached to the DEMS system (to ensure that the same amount of electrolyte evaporates as during the measurement). Furthermore, the influx of gaseous species through the calibration leak should be chosen such that it is in the range of the influx expected during the experiment.

It needs to be borne in mind that $\dot{n}$ is only the influx of gaseous species into the mass spectrometer and does not necessarily equal the formation rate of volatile reaction products. However, according to Equation 7A the influx of gaseous species is proportional to their formation rate

$$\dot{n} = N \cdot \frac{I_F}{z \cdot F} \qquad \text{Eq. 7A}$$

where I_F is the current passed during the electrochemical experiment, z is the number of electrons transferred per molecule of reaction product, F is Faraday's constant and N is the transfer efficiency, that is the portion of the electrochemically generated volatile reaction product that actually enters the mass spectrometer [46]. When less than 100% of the current is used to form the volatile species in question Equation 7A becomes Equation 7B

$$\dot{n} = N \cdot \frac{a_{eff} \cdot I_F}{z \cdot F} \qquad \text{Eq. 7B}$$

in which a_{eff} is the current efficiency.

It is not self-evident that N is 100% as volatile reaction products can diffuse away from the interface between vacuum and electrolyte into the bulk of solution [46]. At working electrodes used in traditional cell designes two diffusion layers form. One diffusion layer extends in the direction of the bulk of solution and the other in the direction of the vacuum. Provided convection is low and the reaction products are volatile the thickness of the diffusion layer in the direction of the vacuum is much smaller than in the direction of bulk solution [46]. This is only the case when the electrode consists of a very thin, sputter

deposited metal film of only 50 nm thickness. At such an electrode Tegtmayer *et al*. found a transfer efficiency of 0.95 for the electrochemical oxidation of CO to CO_2 in the absence of convection [56]. Hence, when a metal sputtered Teflon membrane is employed as working electrode the deviation of N from 100% can be neglected and calibration of the mass spectrometer is sufficiently accurate.

The thickness of the diffusion layer in the direction of the bulk of solution decreases when strong convection is applied. Under strong convection, therefore, an appreciable amount of reaction products do not diffuse into the vacuum but into the bulk of solution [56]. This is also true when the reaction products are not volatile enough. In that case the transfer of the reaction product into the vacuum is not diffusion limited but by sluggish evaporation. Although the thickness of the diffusion layer is not affected by hampered evaporation the concentration gradient is reduced. Therefore, a larger share of reaction products diffuses into the bulk of solution. In either case, strong convection or low volatility, N is smaller 100%.

However, the situation is more complex when a cell setup is used where electrochemistry takes place at another location than the transition of volatile products into the vacuum. This is the case in the dual thin layer cell where convection is employed to transport reaction products from the upper compartment to the detection compartment. Since new electrolyte enters continuously the electrochemical compartment, the electrolyte of a given volume increment will only reside in the electrochemical compartment for a limited amount of time. This time span is usually not sufficient for products that were formed at the electrode to diffuse across the thickness of the electrolyte layer and to equalise the concentration over the whole volume increment. Therefore, a concentration gradient develops in the electrochemical compartment that is maintained when the electrolyte is transported to the detection compartment [46]. This incomplete mixing largely effects the transfer efficiency N, which has severe consequences for calibration: It is not possible to prepare the electrolyte with different concentrations of the species for which calibration should be done and measure the ionic current as a function of that concentration. Such an experiment would only give the collection efficiency f [46], but not N because in such an experiment the concentration gradient cannot be emulated, that arises during electrochemical formation of the products. The situation is further complicated by the fact that N is both a function of the flow rate and the cell geometry (the latter changes in each experiment, because the employed spacers are soft and due to different forces applied during cell setup are compressed differently) [46]. Hence, calibration must be repeated for each flow rate and for each experiment. Therefore, calibration is only achieved, when an electrochemical reaction with known stoichiometry is performed and the response in the ionic current is observed. From the current then the exact amount of formed species is calculated.

Correlation to the ionic current delivers according to Equation 8 the calibration constant K^* with $K^* = K^\circ N / F$ [46].

Eq. 8

$$I_i = (K^* / z) I_F$$

From K^* and the ionic current it is not possible to determine the actual influx of gaseous species into the ionization chamber, but it is possible to correlate the ionic current to the faradic current quantitatively.

2. 3. The (Electrochemical) Quartz Crystal Micro Balance

The basic principles that underlie any application of the quartz crystal micro balance (QCMB) technique have nearly exhaustively been reviewed by Buttry and Ward [62]. The following section, therefore, will largely reproduce and summarize their discussion. However, it also aims at a better visualisation of effects that are of importance to the present study, and it provides insights to certain aspects that have not been discussed in detail so far.

Theoretical Considerations

The QCMB technique relies fundamentally on the piezoelectric effect, which is only observed with materials that are missing an inversion centre, that is, materials that crystallize in a noncentrosymmetric space [62]. The centres of positive and negative charge are deflected from each other resulting in a voltage across the crystal if these materials are compressed along the surface normal of certain crystallographic planes. The reverse effect is also possible: The crystal experiences a mechanical strain that displaces the ions from their crystallographic position in such a way that the resulting internal electric field levels off the external field if a voltage is applied to certain surfaces [62].

During a QCMB-measurement an AC-voltage is applied to a specially prepared wafer of α-quartz which conversely undergoes an oscillation motion. The AC-voltage is applied to the crystal by two metal electrodes which are sputter deposited on both surfaces of the quartz wafer. The oscillation motion can be understood as a standing acoustic wave that propagates through the crystal [62, 63]. The *eigen*frequency f_E of the oscillation motion and the acoustic wave, respectively, are given by Equation 9

Eq. 9

$$f_E = \frac{v_{tr}}{2d}$$

in which v_{tr} is the velocity with which the acoustic wave propagates through the crystal and d is the thickness of the quartz wafer [62, 63]. The factor 2 in the denominator of Equation 9 results from the fact that the surfaces of the wafer are the antinodes of the acoustic wave.

Therefore, the thickness of the crystal corresponds only to half a wavelength. This also means that the acoustic wave will propagate through matter that is in contact with the crystal surface. [62, 63]. According to Equation 10 v_{tr} can be expressed as a function of the density ρ_Q and the shear modulus μ_Q of the quartz crystal [62]

$$v_{tr} = \sqrt{\frac{\mu_Q}{\rho_Q}} \qquad \text{Eq. 10}$$

When the thickness of the quartz is increased by Δd then the *eigen*frequency will shift by Δf according to Equation 11 [62, 63]

$$\frac{\Delta f_E}{f_E} = -\frac{\Delta d}{d} = -\frac{2 \cdot f_E \cdot \Delta d}{d \cdot v_{tr}} \qquad \text{Eq. 11}$$

The above equations were converted by Sauerbrey to Equation 12

$$\Delta f_E = -2 \cdot f_E^2 \frac{\Delta m}{A\sqrt{\mu_Q \cdot \rho_Q}} \qquad \text{Eq. 12}$$

which is, therefore, widely referred to as the Sauerbrey Equation [62, 63]. According to Equation 12 it is possible to determine the mass change Δm during an experiment if the frequency change Δf_E is observed. The constants in Equation 12 can be summarised to a single constant C_f, which is determined for each crystal in a calibration experiment [62, 63].

However, it was pointed out by Buttry and Ward that Δd in Equation 11 is converted to a mass change Δm in Equation 12 by assuming that any deposit has the same density as the alpha quartz [62]. Furthermore, Equation 12 implicitly assumes that the acoustic wave propagates through the surrounding material with the same velocity as through the quartz crystal [62]. Notwithstanding this, Equation 12 remains valid, when Δm and Δf_E, correspondingly, remain small [62].

Experimentally the problem arises on how to determine the frequency change Δf_E. Luckily the quartz crystal in the field of an AC-voltage can be described by the equivalent circuit in Figure 5 [62, 63].

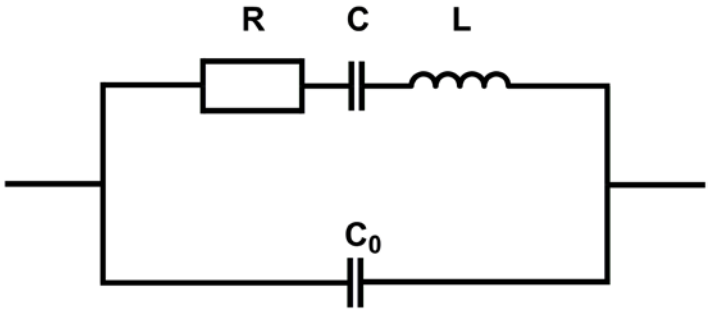

Figure 5: Circuit that is used to describe a quartz crystal in the field of an AC-voltage [62].

The series of resistor, capacitor and inductor is a damped LC-circuit that describes the motion of the quartz crystal and is, therefore, referred to as the motional branch. Naturally an electrode on either side of the crystal is necessary to apply an AC-voltage. Usually these electrodes are thin metal films that were sputter-deposited on the crystal. This introduces another element into the circuit of Figure 5 that is not related to the actual motion of the crystal. The capacitor C_0 describes the fact that the quartz (dielectric) confined between two electrodes behaves as a genuine capacitor.

The capacitor of the motional branch describes the potential energy that can be stored in the distortion of the quartz crystal and, hence, C is linked to the shear modulus μ_Q (which, for small shear angles, is proportional to the elastic constant c, *c.f.* Equation 14)[62]. The inductor describes the kinetic energy during the motion of the crystal and its inductivity L is, therefore, linked to the mass of the crystal. The resistor represents any dissipation of energy due to friction.

The Equations 14 to 17 give a relationship on how the properties of the elements in the circuit of Figure 5 relate to the properties of alpha quartz [62]. For a quartz crystal with an *eigen*frequency of 5 MHz one finds the following values for the elements in the equivalent circuit of Figure 5 [62].

$$C = \frac{8 \cdot A \cdot \varepsilon^2}{\pi^2 \cdot c} \approx 10 \text{ aF} \qquad \text{Eq. 14}$$

$$L = \frac{d^3 \cdot \rho_Q}{8 \cdot A \cdot \varepsilon^2} \approx 75 \text{ mH} \qquad \text{Eq. 15}$$

$$R = \frac{d^3 \cdot r}{8 \cdot A \cdot \varepsilon^2} \approx 100\ \Omega \qquad \text{Eq. 16}$$

$$C_0 = \frac{D_Q \cdot \varepsilon_0 \cdot A}{d} \approx 10 \text{ pF} \qquad \text{Eq. 17}$$

In the above equations A is the surface area of the quartz crystal, ε is the piezoelectric stress constant of alpha quartz, c is the elasticity constant of alpha quartz, ε_0 is the permittivity in vacuum and D_Q is the dielectric constant of alpha quartz.

Sometimes a third capacitor C_1 parallel to C_0 is introduced to the equivalent circuit of Figure 5. This capacitor accounts for parasitic capacities that arise when the quartz is mounted in a crystal holder. The capacity of C_1 depends on the specifics of each experiment, therefore, no tangible value for C_1 can be given here. However, in the following C_1 will be

chosen arbitrarily 40 pF. Given that capacities of parallel capacitors simply add up, C_0 will be considered 50 pF from now on, and no further reference to C_1 will be given.

Only the series of resistor R, capacitor C and inductor L describes the motion of the crystal and, hence, only the resonance frequency of the pure motional branch (*i.e.* C_0 = 0 F) equals the *eigen*frequncy f_E of the quartz crystal. Therefore, the introduction of the capacitor C_0 to the equivalent circuit of Figure 5 has consequences: The electronic resonance frequencies of the circuit do not coincide with the acoustic *eigen*frequency of the quartz crystal. The effect of the capacitor C_0 is visualised by plotting the susceptance B (*i.e.* the imaginary part of the admittance Y, *c.f.* Equation 23) versus the conductance G (*i.e.* the real part of the admittance Y, *c.f.* Equation 23) of the circuit in Figure 5. This plot is shown Figure 6.

The susceptance B_Q of the quartz is given by the sum of the susceptance of the motional branch B_M and the susceptance of the parallel capacitor B_P. B_P is given by Equation 18

$$B_P = \frac{1}{X_P} = \varpi \cdot C_0 \qquad \text{Eq. 18}$$

where X_P is the reactance (*i.e.* the imaginary part of the impedance Z) of the capacitor parallel to the motional branch with the capacity C_0 and ϖ is the angular frequency of the AC-voltage. The susceptance of the motional branch is given by Equation 19

$$B_M = \pm \frac{X_M}{X_M^2 + R^2} \qquad \text{Eq. 19}$$

where X_M is the total reactance of the motional branch and R is the resistance of the resistor. The former is given by Equation 20

$$X_M = X_L + X_C = \varpi \cdot L - \frac{1}{\varpi \cdot C} \qquad \text{Eq. 20}$$

where X_L is the reactance of the inductor with the inductivity L, X_C is the reactance of the capacitor with the capacity C. Combining Equation 18, 19 and 20 yields Equation 21 which gives the suscepance of the quartz.

$$B_Q = \frac{-\varpi L + \frac{1}{\varpi C}}{\left(\varpi L - \frac{1}{\varpi C}\right)^2 + R^2} + \varpi C_0 \qquad \text{Eq. 21}$$

The conductance G_M of the motional branch is given by Equation 22.

$$G_M = \frac{R}{R^2 + X_M^2} = \frac{R}{\left(\varpi L - \frac{1}{\varpi C}\right)^2 + R^2}$$ Eq. 22

Assuming that the resistance of the lead to the parallel capacitor is negligible the overall conductance of the quartz G_Q can be approximated to be equal to G_M .

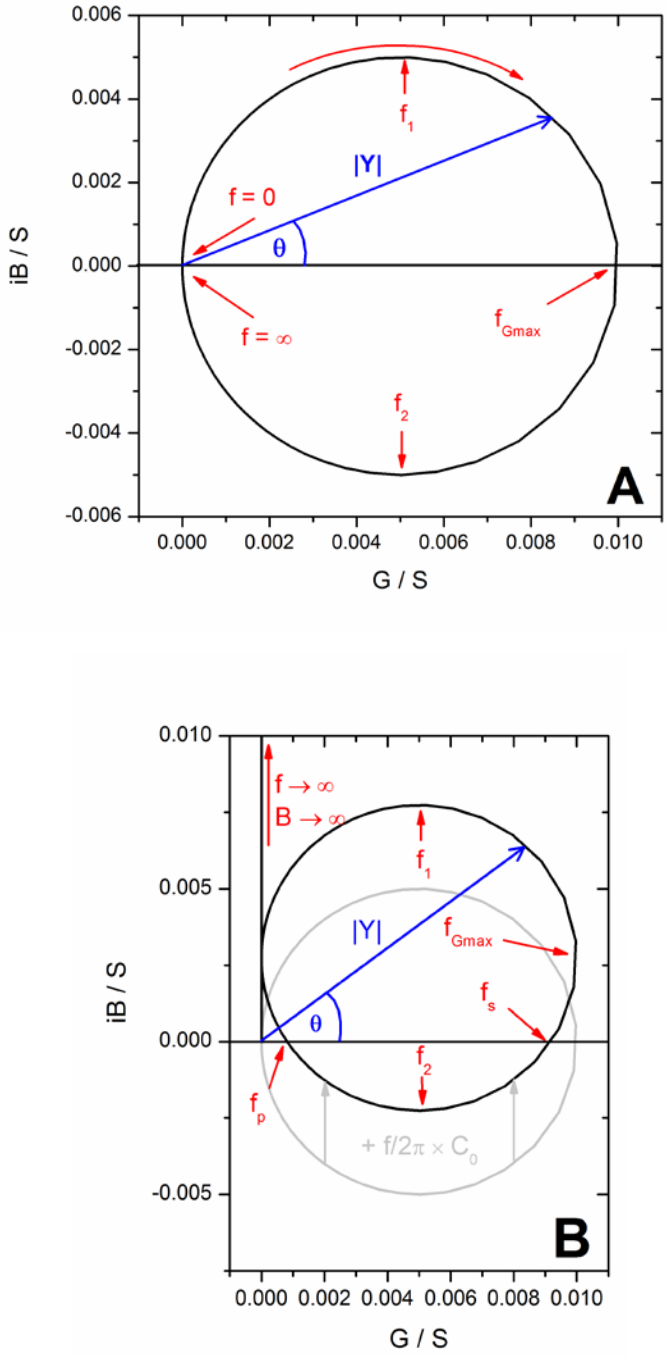

Figure 6: Plot of the susceptance versus the conductance of the circuit in Figure 5 with R = 100 Ω, C = 10 aF, L = 75 mH. A: C_0 = 0 pF; B: C_0 = 50 pF.

Figure 6A shows the susceptence as a function of the conductance when the capacity of the capacitor C_0 equals zero. Both the susceptance and the conductance approach zero, when the (angular) frequency approaches zero or infinity. The frequencies f_1 and f_2 in Figure 6A are those frequencies at which the susceptance becomes maximal and minimal, respectively. The frequency at which the conductance becomes maximal is $f_{G,\max}$. Figure 6A also features the phasor $|Y|$ which is the absolute value of the admittance. The admittance is given by Equation 23 and its absolute value is given by Equation 24.

$$Y = G + iB \qquad \text{Eq. 23}$$

$$|Y| = \sqrt{G^2 + B^2} \qquad \text{Eq. 24}$$

In Figure 6 the x-axis and the phasor $|Y|$ confine the phase angle θ. In order to achieve resonance conditions θ must become zero (otherwise interference would prohibit the existence of a stationary wave). θ is given by Equation 25.

$$\theta = \tan^{-1}\left(\frac{B}{G}\right) \qquad \text{Eq. 25}$$

It is apparent from Figure 6A that the phase angle is zero in $f_{G,\max}$, hence, $f_{G,\max}$ is the resonance frequency of the motional branch and the *eigen*frequency f_E of the acoustic motion of the quartz crystal. Both zeroing the differentiation of Equation 22 and zeroing Equation 25 (if only the susceptance of the motional branch is considered) yields Equation 26.

$$f_{G,\max} = f_E = \frac{1}{\sqrt{C \cdot L}} \qquad \text{Eq. 26}$$

Figure 6B shows how the situation changes when the capacity C_0 is introduced. Because the susceptance is shifted by $\varpi \cdot C_0$ to more positive values $f_{G,\max}$ is not at resonance conditions any more. Still $f_{G,\max}$ is given by Equation 26, because C_0 does not enter Equation 22, but zeroing Equation 25 now yields the resonance frequencies f_s and f_p expressed by Equations 27 and 28, respectively.

$$2 \cdot \pi \cdot f_s = \sqrt{-\frac{C_0 \cdot R^2 \cdot C - L \cdot C - 2 \cdot C_0 \cdot L}{2 \cdot C_0 \cdot L^2 \cdot C} - \sqrt{\frac{C_0 \cdot R^2 \cdot C - L \cdot C - 2 \cdot C_0 \cdot L}{2 \cdot C_0 \cdot L^2 \cdot C} - \frac{1}{C_0 \cdot L^2 \cdot C} - \frac{1}{L^2 \cdot C^2}}} \qquad \text{Eq. 27}$$

$$2 \cdot \pi \cdot f_P = \sqrt{-\frac{C_0 \cdot R^2 \cdot C - L \cdot C - 2 \cdot C_0 \cdot L}{2 \cdot C_0 \cdot L^2 \cdot C} + \sqrt{\frac{C_0 \cdot R^2 \cdot C - L \cdot C - 2 \cdot C_0 \cdot L}{2 \cdot C_0 \cdot L^2 \cdot C} - \frac{1}{C_0 \cdot L^2 \cdot C} - \frac{1}{L^2 \cdot C^2}}} \qquad \text{Eq. 28}$$

At those frequencies the plot in Figure 6B intercepts the x-axis. Although the frequency domain is not shown in Figure 6, it is easy to imagine that f_s approaches $f_{G,\max}$ as C_0 decreases and that f_s and $f_{G,\max}$ coincide, when C_0 becomes zero. When L or C in Figure 5 increase then f_E and f_s shift by Δf_E and Δf_s, respectively, to lower frequencies. Although f_E and f_s do not coincide, they are effected similarly by changes in L or C. Hence, Δf_s can be used to approximate Δf_E. However, f_s and f_p are not easily accessible in practical measurements, because measuring θ requires elaborate impedance analysis [62]. In practice instruments usually measure only the absolute value of the impedance |Z| and approximate f_s and f_p, as those frequencies where |Z| has a minimum ($f_{s,\min}$, maximum in $|Y|$) and a maximum ($f_{p,\max}$, minimum in $|Y|$), respectively. The absolute value of the impedance can be calculated according to Equation 29

$$|Z| = \frac{1}{|Y|} = \frac{1}{\sqrt{G^2 + B^2}} \qquad \text{Eq. 29}$$

Figure 7A shows a plot of the absolute value of the impedance of the circuit in Figure 5, and Figure 7B shows a plot of the phase angle. It should become clear from Figure 7 that there is a difference between f_s, f_p, $f_{s,\min}$ and $f_{p,\max}$ of several Hz. But when doing a QCMB experiment the experimentalist is usually interested in detecting mass changes and, therefore, in detecting frequency changes. As long as the deposited mass is rigid in nature (*e.g.* sputtered deposited metals) also $\Delta f_{s,\min}$ instead of Δf_s can be used to approximate Δf_E and the difference between f_s and $f_{s,\min}$ is of no practical importance.

Figure 7C and D show the absolute value of the impedance and the phase angel in the relevant frequency region for an equivalent circuit of the quartz that is missing a parallel capacity. Different from the plot in Figure 7B the phase angel passes through zero only once in Figure 7D. This is consistent with Figure 6A where the susceptence never becomes positive again after passing the into the negative domain. Hence, f_p (and $f_{p,\max}$) do not exist. This is also evident from the plot of the absolute value of the impedance in Figure 7C. The resonance frequency f_s and the frequency $f_{s,\min}$ at which the absolute value of the impedance becomes minimal coincide in the resonance frequency of the quartz crystal f_E.

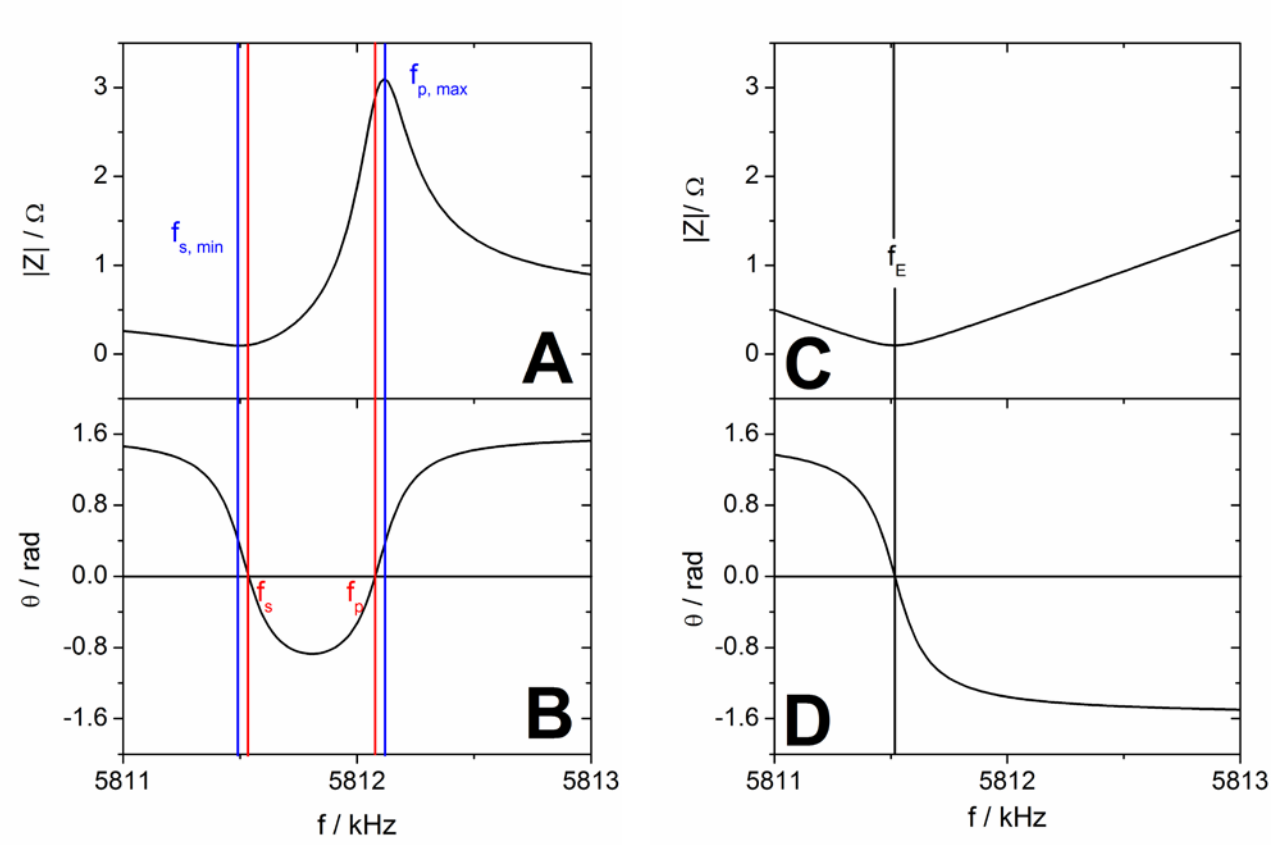

Figure 7: Absolute value of the impedance (A and C) and phase angle (B and D) of the circuit in Figure 5, with R = 100 Ω, C = 10 aF, L = 75 mH. A and B: C_0 = 50 pF; C and D: C_0 = 0 pF.

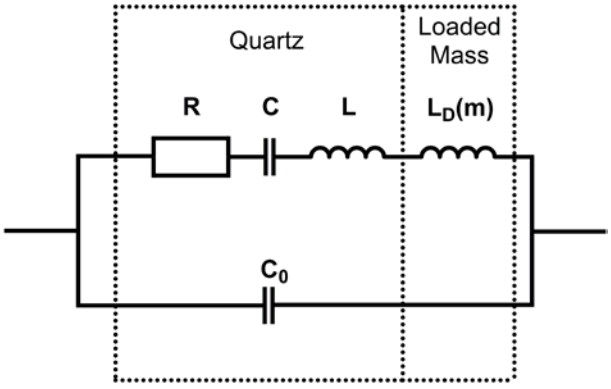

Figure 8: Extension of the equivalent circuit in Figure 5. The additional inductor in the motional branch describes any mass that is deposited on the quartz crystal and, hence, its inductivity is a function of the deposited mass.

As already pointed out the inductivity L of the inductor in Figure 5 accounts for the inertia of the mass of the quartz crystal. In order to account for the additional mass that is loaded onto the crystal the circuit in Figure 5 can be altered: Another inductor is introduced into the motional branch (Figure 8). This inductor has an inductivity $L_D(m)$ that is a function of the loaded mass [62].

Equation 30a gives the relationship between $L_D(m)$ and the loaded mass Δm (derived from the equation given in Ref. [64], after substitution of a more complicated constant by μ_Q).

$$L_D(m) = \frac{4 \cdot f_s \cdot L}{\sqrt{\mu_Q \cdot \rho_Q}} \cdot \frac{\Delta m}{A} \qquad \text{Eq. 30a}$$

A similar expression as that given by Martin *et al*. can be derived from Equation 15.

$$\begin{aligned} L_D(m) = L_1 - L_2 \quad &= \frac{{d_1}^3 \cdot \rho_Q}{8 \cdot A \cdot \varepsilon^2} - \frac{{d_2}^3 \cdot \rho_Q}{8 \cdot A \cdot \varepsilon^2} \qquad \text{with: } d = \frac{m}{A \cdot \rho_Q} \\ &= \frac{{m_1}^3}{8 \cdot A \cdot {\rho_Q}^2 \cdot \varepsilon^2} - \frac{{m_2}^3}{8 \cdot A \cdot \rho_Q \cdot \varepsilon^2} \\ &= \frac{1}{8 \cdot A \cdot {\rho_Q}^2 \cdot \varepsilon^2} \left({m_1}^3 - (m_1 + \Delta m)^3 \right) \\ &= \frac{1}{8 \cdot A \cdot {\rho_Q}^2 \cdot \varepsilon^2} \left(3 \cdot \Delta m \cdot {m_1}^2 + 3 \cdot \Delta m^2 \cdot m_1 + \Delta m^3 \right) \end{aligned}$$

For small mass changes Δm and large masses m_1, terms of higher order in Δm can be neglected which yields:

$$\begin{aligned} L_D(m) = L_1 - L_2 \quad &= \frac{3 \cdot \Delta m \cdot {m_1}^2}{8 \cdot A \cdot {\rho_Q}^2 \cdot \varepsilon^2} \\ &= \frac{3 \cdot d^2}{8 \cdot A \cdot \varepsilon^2} \cdot \frac{\Delta m}{A} \end{aligned}$$

Inserting Equations 9, 10 and 15 and assuming $f_E \approx f_s$, yields:

$$L_D(m) = L_1 - L_2 \quad = \frac{3 \cdot f_s \cdot \sqrt{\rho_Q} \cdot d^3}{16 \cdot \sqrt{\mu_Q} \cdot A \cdot \varepsilon^2} \cdot \frac{\Delta m}{A}$$

Finally inserting Equation 15 yields Equation 30b which differs from Equation 30a only by a factor 8/3. Possibly this difference results from the approximations made during derivation of Equation 30b.

$$L_D(m) = \frac{3 \cdot f_s \cdot L}{2 \cdot \sqrt{\rho_Q \cdot \mu_Q}} \cdot \frac{\Delta m}{A} \qquad \text{Eq. 30b}$$

Derivation of Equation 30b shows that a linear relationship between $L_D(m)$ and Δm can only be assumed for the limiting case of small mass changes. The reader should also note that another assumption enters Equation 30b that also led to Equation 12: That any deposit

has the same density as alpha quartz. Rearranging either Equation 30a or Equation 30b, substitution of Δm in Equation 12 appears to yield a linear relationship between $L_D(m)$ and Δf_E. However, it has to be born in mind that the resulting equation is actually the homogeneous Differential Equation 31

$$\frac{1}{f_s} df_s = -\frac{4}{3}\frac{L_D(m)}{L} \cdot dL \qquad \text{Eq. 31}$$

This notwithstanding, Δf_s is approximately proportional to $L_D(m)$ as long as the *e*-function can be approximated by $(1+x)$. That is the case when $L_D(m)$ is small compared to L, which is the very same limiting case for which Equation 30b is valid: Δm is small compared to m_1.

Figure 9 visualises that f_s (calculated from Equation 27) indeed changes linearly with $L_D(m)$, as long as the latter remains small. The inset in Figure 9 shows that this is not true when large changes in $L_D(m)$ occur.

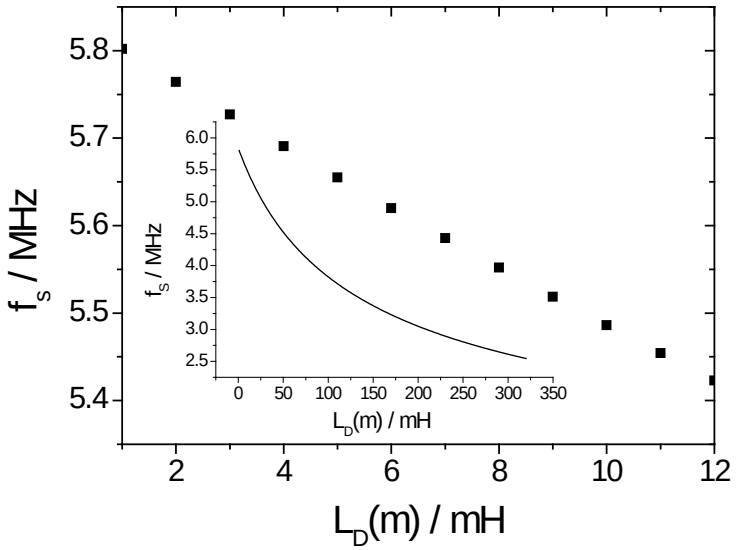

Figure 9: Plot f_s versus $L_D(m)$. f_s was calculated from Equation 27 for the circuit in Figure 8, assuming the following characteristics for the remaining components: R = 100 Ω, C = 10 aF, L = 75 mH. A: C_0 = 0 F; B: C_0 = 50 pF. Inset: f_s over a larger region of $L_D(m)$.

When the deposited mass is rigid in nature then the extension of the equivalent circuit in Figure 8 is sufficient. However, when the QCMB is used in electrochemical experiments this is not the case anymore. Electrochemical QCMB measurements are possible when one of the electrodes, which are used to apply the AC-voltage to the quartz, is exposed to an electrolyte and is employed in addition as an electrode for electrochemical experiments. The electrolyte at the phase boundary will follow the shear motion of the quartz with the same

velocity of the surface of quartz (no-slip-plane conditions). This velocity, however, will decline rapidly as the distance to the quartz increases in the direction of the surface normal. The mass of the liquid that couples to the motion of the quartz causes an additional mass load and the rapid dampening of the motion in the liquid phase (due to different layers of liquid that move relative to each other) adds friction [62, 65-67]. This is accounted for by extending the equivalent circuit in Figure 8 by an additional resistor and inductor with the resistance R_L and the inductance L_L (*c. f.* Figure 10), which are given by Equation 27 and 28, respectively (these were derived from the equations given in Ref. [64], after substitution of a more complicated constant by μ_Q).

$$R_L = 2 \cdot f_s \cdot L \sqrt{\frac{f \cdot \rho_L \cdot \eta_L}{\pi \cdot \mu_Q \cdot \rho_Q}} \qquad \text{Eq. 32}$$

$$L_L = 2 \cdot f_s \cdot L \sqrt{\frac{\pi \cdot \rho_L \cdot \eta_L}{f \cdot \mu_Q \cdot \rho_Q}} \qquad \text{Eq. 33}$$

ρ_L and η_L in Equation 32 and 33 are the density and viscosity of the electrolyte and f is the frequency of the AC-voltage. With decreasing velocity of the surface of the quartz crystal the velocity profile of the electrolyte in the direction of the surface normal drops to zero more rapidly. Hence, less mass couples to the crystal and less friction arises. That is why f_s enters Equation 32 and 33. When large masses are deposited this has to be taken into account, as the load due to the liquid decreases. However, as long as only small mass changes occur L_L and R_L should be constant. This statement is only true as long as the interaction between liquid and surface remains unaltered. Surface phenomena or phenomena in the double layer that occur during an electrochemical experiment might affect the interaction between electrolyte and the surface. For instance when due to a weaker interaction between electrolyte and surface the liquid at the phase boundary follows the motion of the crystal only with a smaller velocity (slip-plane condition) L_L and R_L decrease, causing an increase in f_s. Electrochemical reactions that affect L_L and R_L can, therefore, simulate large mass changes [62].

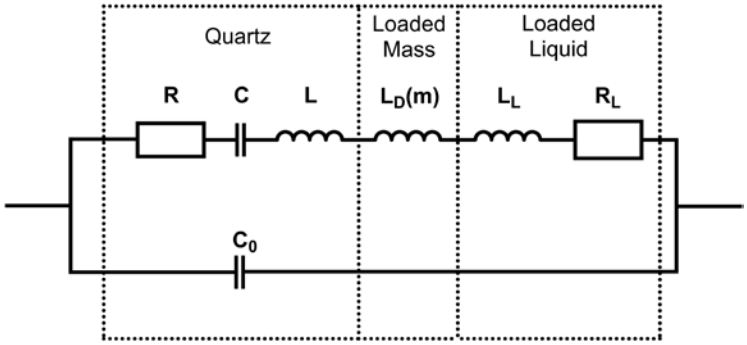

Figure 10: Equivalent circuit for a QCMB immersed in a liquid. L_L accounts for the mass of the liquid that couples to the motion of the crystal and R_L accounts for the additional friction when different layers of liquid move relative to each other.

The equivalent circuit in Figure 10 only holds when the deposited mass is rigid. This is the case when for instance metals are deposited electrochemically. However, other deposits such as polymers can be viscous, elastic or both. In the case of a viscous deposit the same considerations apply as for the contact with a viscous liquid such as the electrolyte. Therefore, a resistor with resistance $R_D(\eta)$ and an inductor with the inductance $L_D(\eta)$ enter the motional branch of the equivalent circuit [62], whereas both $R_D(\eta)$ and $L_D(\eta)$ are functions of the viscosity and the density of the film.

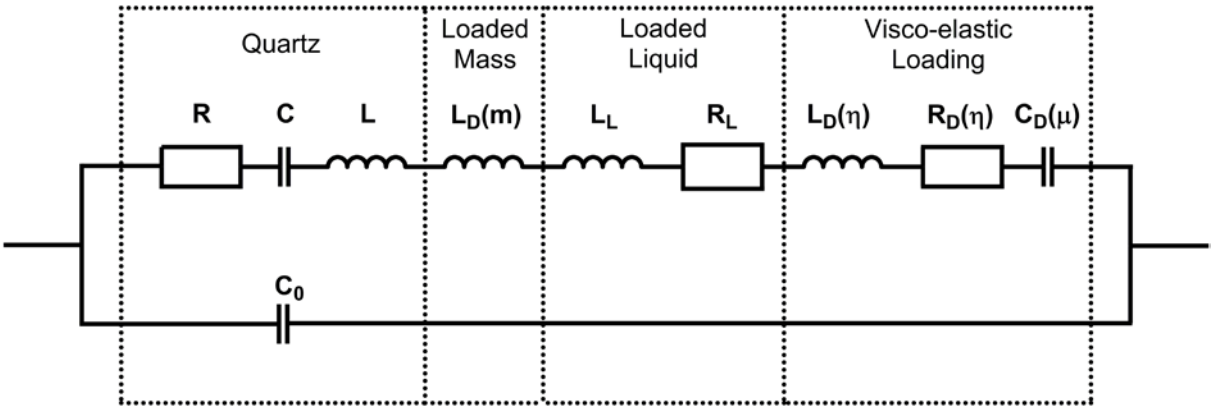

Figure 11: Equivalent circuit for a QCMB immersed in a liquid and loaded with a visco-elastic film. $L_D(\eta)$ accounts for the mass of the film that couples to the motion of the crystal and accounts $R_D(\eta)$ for the additional friction when different layers of the film move relative to each other. $C_D(\mu)$ accounts for the elasticity of the film.

In the circuit of Figure 11 also a capacitor $C_D(\mu)$ enters. This capacitor accounts for the elasticity of a film. An elastic film coupling to the motion of the quartz, deforms and exerts a restoring force in the direction opposed to the shear motion. The capacity C describes this behaviour for the quartz crystal itself, but not for a film on top of it. $C_D(\mu)$ is a function of the elasticity coefficient of the film. Figure 11 shows the equivalent circuit that accounts for a

quartz crystal loaded both with a rigid and a visco-elastic mass immersed into an electrolyte [62].

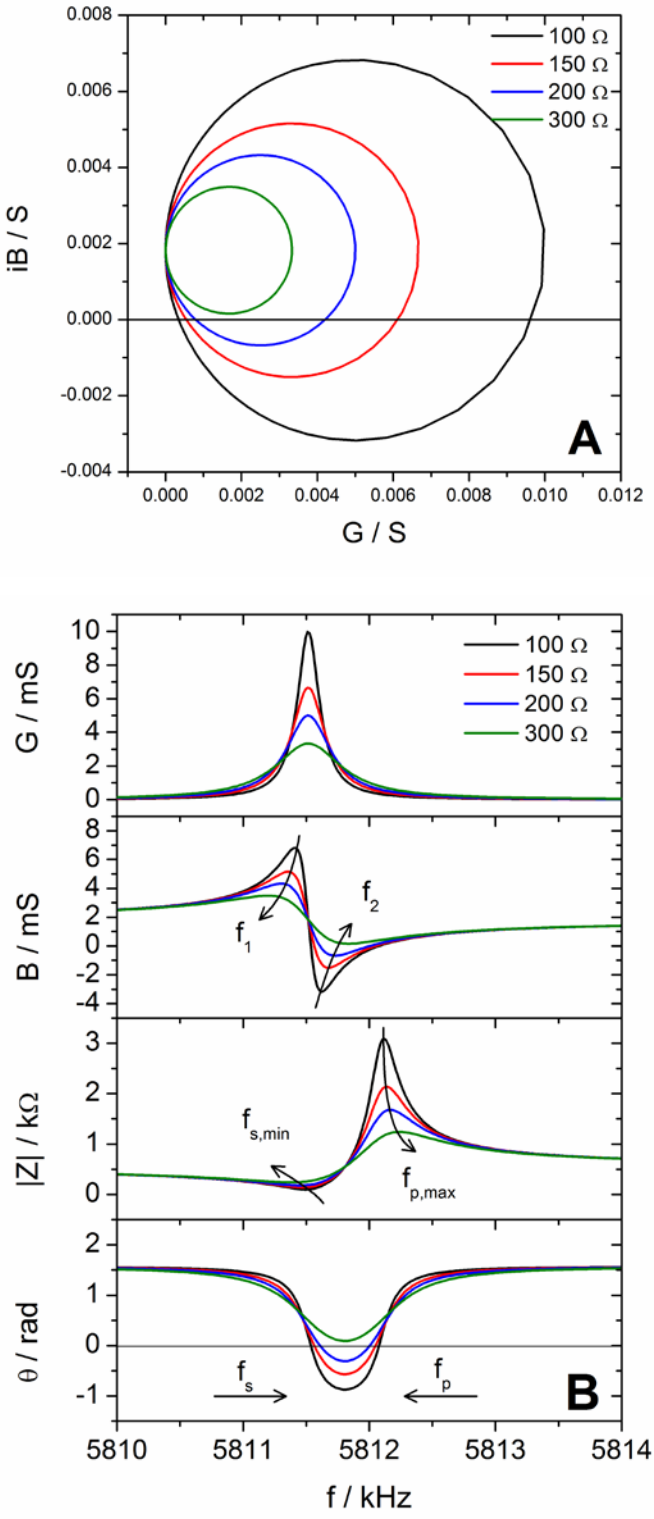

Figure 12: Plot of the susceptance versus the conductance (A), and plot of the conductance, the susceptance, the absolute value of the impedance and the phase angle versus frequency (B) for a circuit with C = 10 aF, L = 75 mH, C_0 = 50 pF and different values for R.

When the film is subject to an electrochemical reaction, $R_D(\eta)$, $L_D(\eta)$ and $C_D(\mu)$ change if during the reaction either the viscosity or the elasticity coefficient changes [62]. Changes in the viscosity or the elasticity coefficient, therefore, can simulate mass changes.

When using the QCMB-technique the experimentalist is usually interested in measuring mass change, hence, the term *balance*. According to Equations 30a and 30b there is a linear relationship between $L_D(m)$ and Δm, and according to Equation 12 there a linear relationship between Δf_E and Δm. It was pointed out before that the change of *eigen*frequency of the acoustic motion of the quartz crystal can be approximated by changes of the electronic resonance frequency Δf_s (*i.e.* the frequency at which θ is zero) of the quartz crystal in an AC-field and that this frequency change in turn is usually approximated by $\Delta f_{s,\min}$ (the frequency at which the absolute value of the impedance is minimal and which is instrumentally more easily accessible). However, given that a number of elements enter the motional branch that describes the acoustic motion of the crystal when electrochemical experiments are performed it will be elaborated in the following how the relevant frequencies are affected by the properties of the elements in the circuit of Figure 11.

Figure 12A shows the plot of the susceptance versus the conductance for different overall resistances. The resistance of several resistors in series simply adds up. That is why only a cumulated resistance in the legend of Figure 12 is given and no difference between R, R_L and $R_D(\eta)$ is made. The green curve in Figure 12A shows that the susceptance never becomes negative, when the resistance is high enough. Hence, resonance condition can never be achieved and there are no frequencies f_s and f_p. Figure 12B shows the conductance, the susceptance, the absolute value of the impedance and the phase angle as a function of the frequency. Figure 12B shows that $f_{G,\max}$ is not affected by the resistance, which is not surprising, given that R does not enter Equation 26. It is also clear that neither f_s nor $f_{s,\min}$ differ much from $f_{G,\max}$. However, while there is no f_s or f_p for a resistance of 300 Ω a device that only measures the absolute value of the impedance and not the phase delivers the frequencies $f_{s,\min}$ and $f_{p,\max}$ nonetheless. Furthermore, Figure 12B shows that a change in the resistance affects both f_s and $f_{s,\min}$. In either case that means that during an eQCMB experiment a change in friction will show up as a change in the frequency and is, therefore, easily misinterpreted as a mass change.

In order to check whether the frequency change is really due to mass deposition or due to changing properties at the phase boundary between electrode and electrolyte it is advisable to check whether changes in the quality factor occur. The proper quality factor, that

is, the resonance frequency divided by the full width at half maximum is given Equation 34 [62].

$$Q = \frac{f_s}{f_2 - f_1} \qquad \text{Eq. 34}$$

Practically f_1 and f_2 are only accessible when the instrument performs an impedance analysis which is usually not the case. However, also changes in the reduced quality factor given by Equation 35a [68] or Equation 35b (provided by Gamry Instruments) can be used to estimate whether interactions at the phase boundary change.

$$Q_R = \frac{f_s + f_p}{2\left(f_p - f_s\right)} \qquad \text{Eq. 35a}$$

$$Q_R = \frac{f_s}{\left(f_p - f_s\right)} \qquad \text{Eq. 35b}$$

In Figure 12 f_1 and f_2 as well as $f_{s,\min}$ and $f_{p,\max}$ diverge, whereas f_s and f_p converge when R increases. Hence, Q and $Q_{R,\max}$ (the reduced quality factor calculated from $f_{s,\min}$ and $f_{p,\max}$) decrease, whereas Q_R decreases when R increases. This is also shown in Figure 13, where the Q_R (Figure 13A) as well as Q and $Q_{R,\max}$ (Figure 13B) are plotted as a function of R. Figure 13B shows that in the case of changing friction at the phase bopundary the difference between f_s and $f_{s,\min}$ matters and the experimentalist must be aware which kind of frequency is detected by the instrument.

It is relatively easy to simulate the dependence of Q_R on R (or of L and C) because the Equations 27 and 28 give an expression for f_s and f_p, respectively. But it is much more challenging (if possible at all) to derive an analytical expression for f_1, f_2, $f_{s,\min}$ and $f_{p,\max}$. In order to calculate Q and $Q_{R,\max}$ the susceptance and the absolute value of the impedance of the equivalent circuit in Figure 11 were simulated for several values of R. The frequencies f_1, f_2, $f_{s,\min}$ and $f_{p,\max}$ were then determined graphically from the corresponding plot. All values for Q and $Q_{R,\max}$ given in Figure 13B and later in this section were determined in this way.

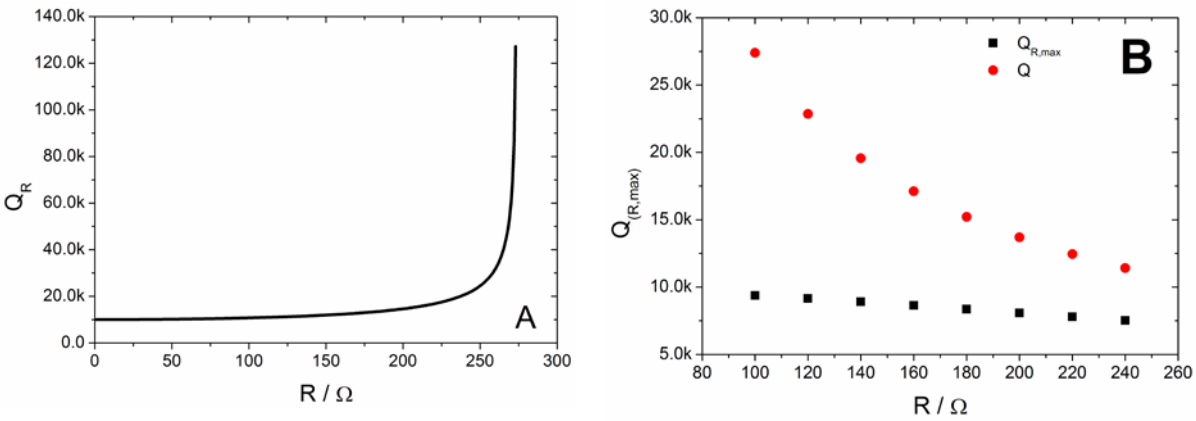

Figure 13: Plot of Q_R (A) Q and $Q_{R,\max}$ (B) as a function of the resistance. The characteristics of remaining components of the circuit in Figure 11 were chosen as follows: C = 10 aF, L = 75 mH and C_0 = 50 pF.

It is necessary to show how the inductivity and the capacity affect the quality factor if it is to be consulted to determine whether changes in the frequency are really due to the deposition of mass or due to changes of the friction. However, it is difficult to show a plot as in Figure 12 for various capacities, because according to Equation 26 the *eigen*frequncy f_E and, therefore, f_s will shift to larger values as the capacity C decreases. The plot in Figure 14 exemplifies this. In order to compare at least relative changes of the relevant frequencies when the capacity changes, the data in Figure 15 were plotted versus ($f - f_{G,\max}$).

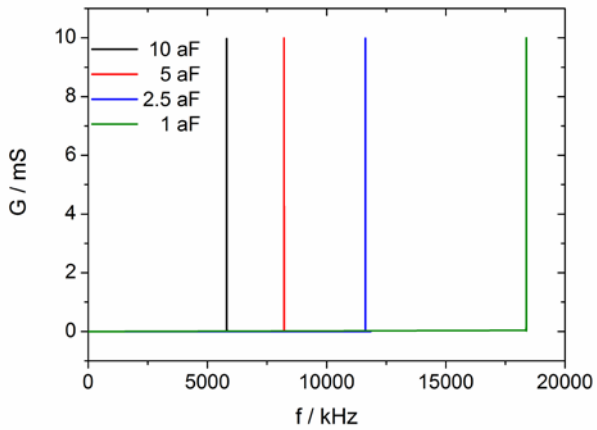

Figure 14: Plot of the conductance as a function of frequency for different capacities. The characteristics of remaining components of the circuit in Figure 11 were chosen as follows: R = 100 Ω, L = 75 mH and C_0 = 50 pF.

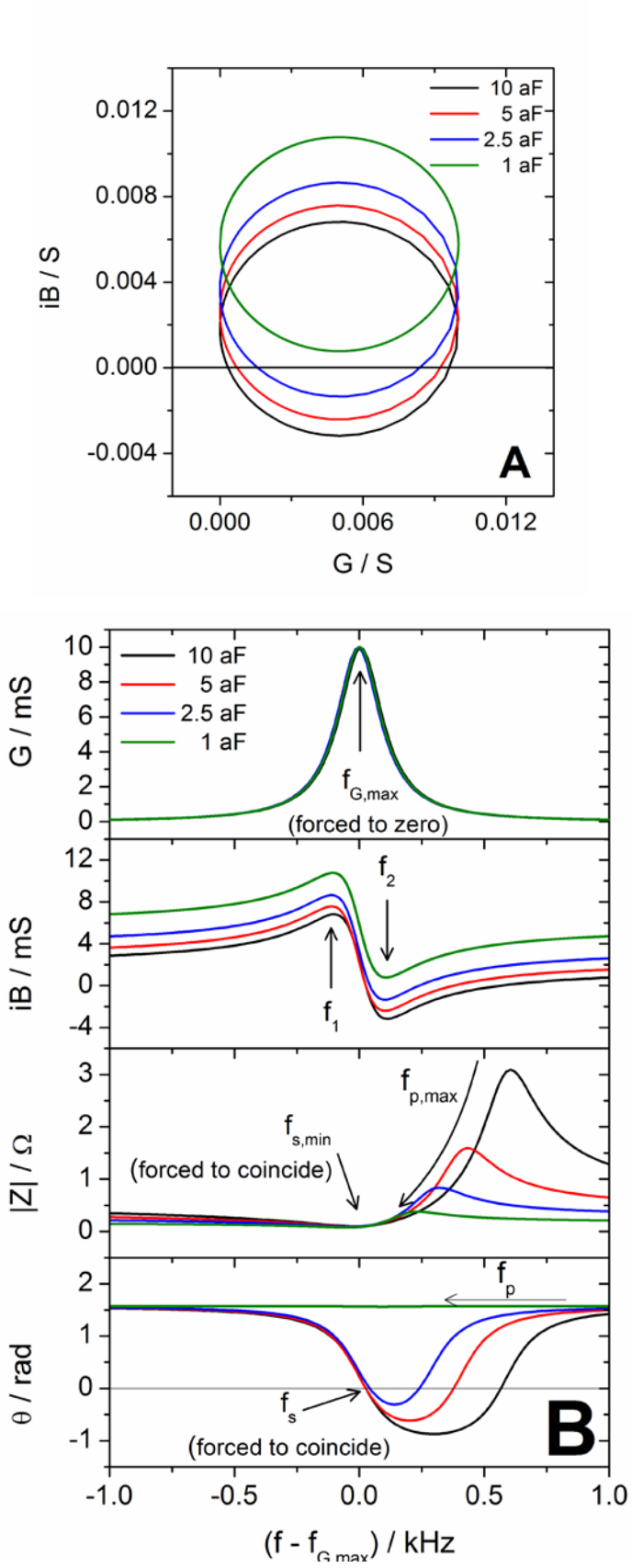

Figure 15: Plot of the susceptance versus the conductance (A), and plot of the conductance, the susceptance, the absolute value of the impedance and the phase angle versus $f - f_{G,\max}$ (B) for a circuit with R = 100 Ω, L = 75 mH, C_0 = 50 pF and different values for C. Because f_s and $f_{s,\min}$ do not coincide with $f_{G,\max}$. For various values of C, therefore, the respective values of f_s (and $f_{s,\min}$) do not coincide in the above plot as well. However, "forced to coincide" is meant to emphasis that the relative changes in f_p (and $f_{p,\min}$) are actually due to relative changes in both, f_s and f_p.

The crucial point of Figure 15B is to show how the relevant frequencies behave relative to each other. The difference between f_1 and f_2 is not affected by a decrease of the overall capacity, whereas $f_{s,\min}$ and $f_{p,\max}$, as well as f_s and f_p converge. Since all frequencies f_1, f_2, $f_{s,\min}$, $f_{p,\max}$, f_s and f_p increase along with $f_{G,\max}$ also Q, Q_R and $Q_{R,\max}$ increase with decreasing overall capacity. This is also shown in Figure 16, where the different quality factors are plotted as a function of the overall capacity (Figure 16A and 16B) and as a function of $C_D(\mu)$ (Figure 16C and 16D).

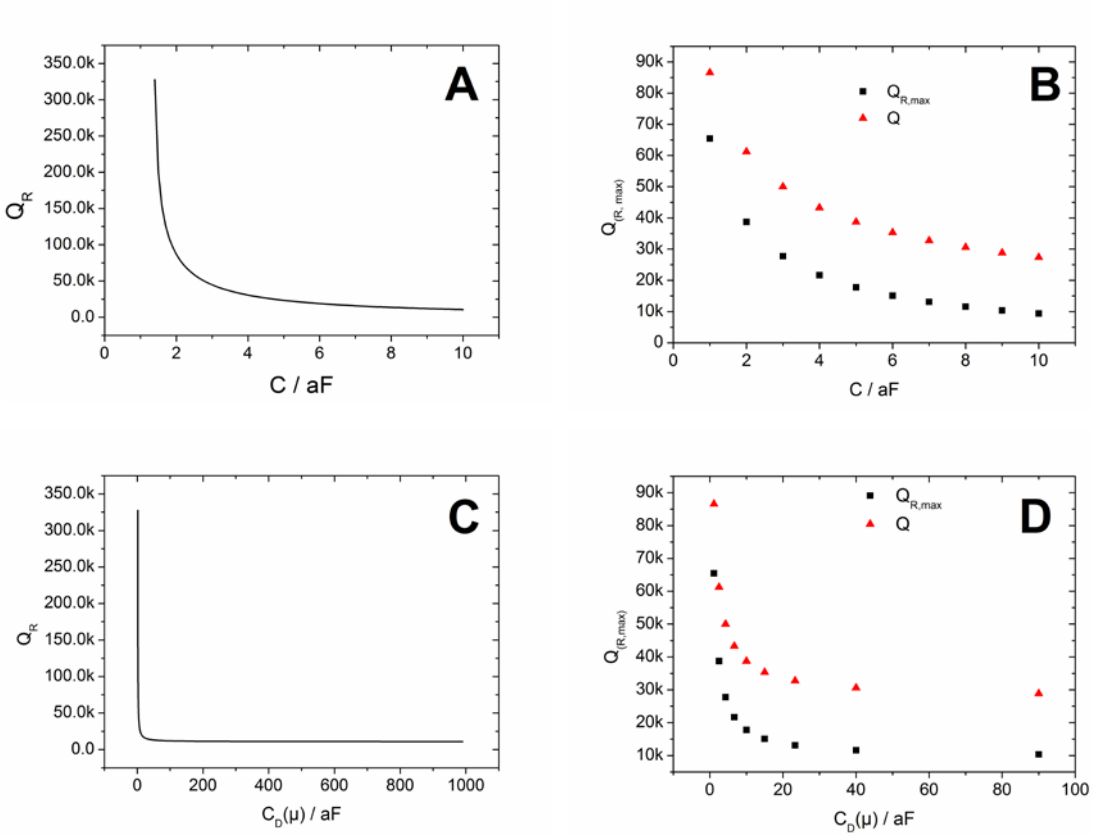

Figure 16: Plot of Q_R (A) Q and $Q_{R,\max}$ (B) as a function of the overall capacity of the circuit in Figure 11. Q_R (C) Q and $Q_{R,\max}$ (D) are also shown as a function of $C_D(\mu)$ while C is kept constant. The characteristics of remaining components of the circuit in Figure 11 were chosen as follows: R = 100 Ω, C = 10 aF, L = 75 mH and C_0 = 50 pF.

Figure 16 reveals changes in $C_D(\mu)$ cause significant changes of the quality factor. It might appear strange to the reader that very small values of $C_D(\mu)$ cause major changes in the quality factor. The series of capacitors in Figure 11 are the electronic analogue of a classical picture, where two parallel springs are attached to a weight [62]. The capacity of each capacitor is inversely proportional to Hook's constant of one of the springs. It is

noteworthy in this context, that the elasticity constant enters Equation 14 as a denominator, whereas Hook's constant is proportional to the elasticity constant. Hence, a capacitor with a very small capacity $C_D(\mu)$ represents a highly elastic film which exerts a large restoring force. In Figure 17 the quality factor is plotted versus the inverse of $C_D(\mu)$ which should be proportional to the elasticity constant of the film on the quartz. It is evident that the quality factor changes nearly linearly with changes in the elasticity constant.

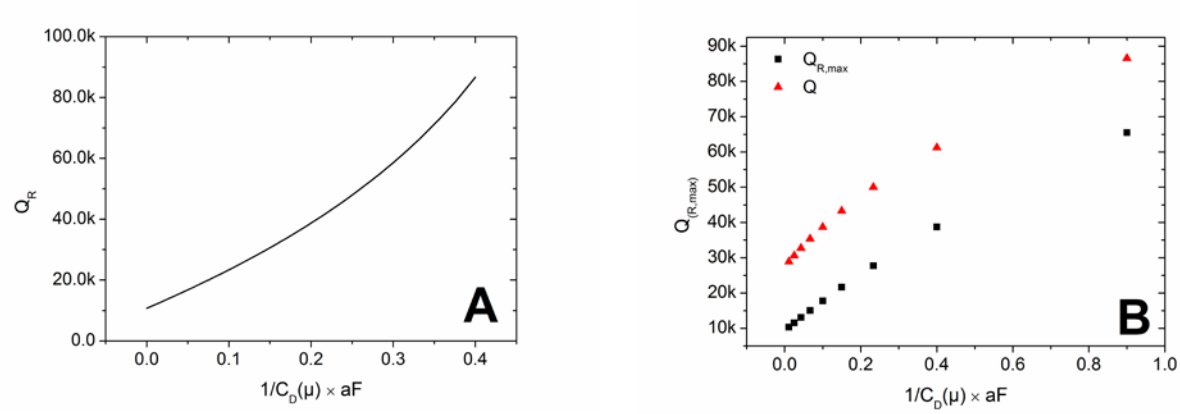

Figure 17: Plot of Q_R (A) Q and $Q_{R,\max}$ (B) as a function of the inverse of $C_D(\mu)$ while C is kept constant. The characteristics of remaining components of the circuit in Figure 11 were chosen as follows: R = 100 Ω, C = 10 aF, L = 75 mH and C_0 = 50 pF.

It is apparent from Figure 16 and Figure 17 that changes in the quality factor are not only restricted to changes in resistance but also occur when the overall capacity changes. Hence, it is not straight forward to assume based on changes in the quality factor, that the friction at the interface between electrode and electrolyte changes. However, before it can be elaborated how changes in the quality factor can be used to estimate whether changes in R or C appear, the effect of the inductivity must be discussed first.

As in the case of the capacity C also L has a large impact on $f_{G,\max}$. In order to compare at least relative changes of the relevant frequencies when the inductivity changes, B, G, $|Z|$ and θ are plotted versus ($f - f_{G,\max}$) for various values of L in Figure 18. As with a series of resistors also the inductivity of several inductors in series add up. Therefore no difference between L, L_L and $L_D(\eta)$ is made in Figure 18.

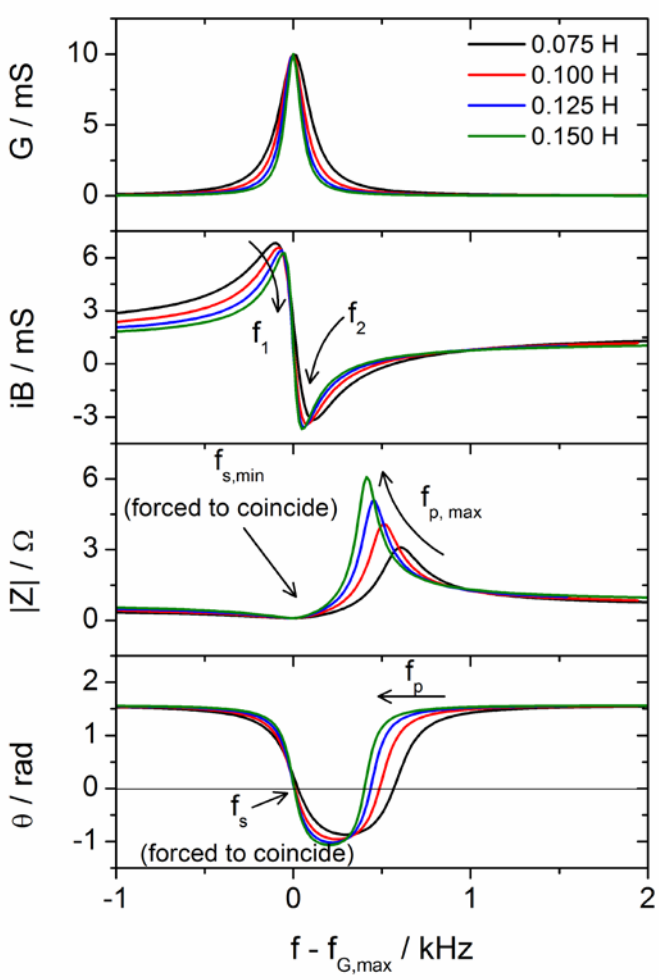

Figure 18: Plot of the conductance, the susceptance, the absolute value of the impedance and phase angle versus $f - f_{G,\max}$ for a circuit with R = 100 Ω, C = 10 aF, C_0 = 50 pF and different values for L. Because f_s and $f_{s,\min}$ do not coincide with $f_{G,\max}$. For various values of L, therefore, the respective values of f_s (and $f_{s,\min}$) do not coincide in the above plot as well. However, "forced to coincide" is meant to emphasis that the relative changes in f_p (and $f_{p,\min}$) are actually due to relative changes in both, f_s and f_p.

Figure 18 shows that f_1 and f_2, $f_{s,\min}$ and $f_{p,\max}$ as well as f_s and f_p converge as the inductivity increases. This means that the denominator in Equations 34, 35a and 35b decreases as L increases. But also the numerator in these equations (*c.f.* Figure 9) decreases, therefore, it is not straightforward to derive from Figure 18 whether the quality factor will change at all when L changes. Indeed, Figure 19 shows that Q_R decreases, whereas Q and $Q_{R,\max}$ increase as L increases.

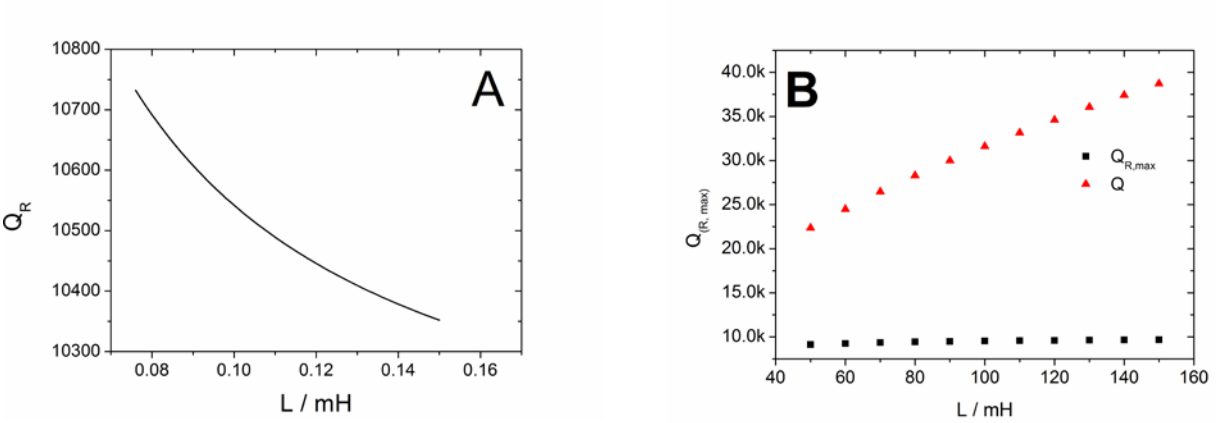

Figure 19: Plot of Q_R (A) Q and $Q_{R,\max}$ (B) as a function of the inductivity. The characteristics of remaining components of the circuit in Figure 11 were chosen as follows: R = 100 Ω, C = 10 aF, and C_0 = 50 pF.

In order to estimate whether changes in the quality factor are due to changes in L, R or $C_D(\mu)$ it is necessary to look at f_s in addition. It was mentioned before that changes in each L, R and $C_D(\mu)$ effect the resonance frequency f_s. But for each element the impact on the quality factor and on f_s is different. Figure 20 shows how $Q_{R,\max}$ relates to the frequency $f_{s,\min}$ of the circuit in Figure 11 when the overall resistance (Figure 20A), the capacity $C_D(\mu)$ (Figure 20B) or the overall inductivity (Figure 20C) changes independent from the properties of the remaining elements. It is quite clear that $f_{s,\min}$ and $Q_{R,\max}$ are very differently affected by changes in R, L or $C_D(\mu)$: Large changes in $Q_{R,\max}$ due to R come along with very small changes in $f_{s,\min}$, whereas $C_D(\mu)$ influences both $f_{s,\min}$ and $Q_{R,\max}$. Hence, the experimentalist should be able to estimate from the ratio of $Q_{R,\max}$ to $f_{s,\min}$ (considering Equation 345b this ratio equals $\left(f_{s,\min} - f_{p,\max}\right)^{-1}$) whether a change in the quality factor indicates changes in R (*i.e.* friction) or C (*i.e.* changes in elasticity). During an eQCMB experiment frequency changes due to mass deposition (*i.e.* an increase in $L_D(m)$) on the scale required to observe changes in $Q_{R,\max}$ should be avoided anyway. Therefore, the impact of L on the quality factor can be neglected.

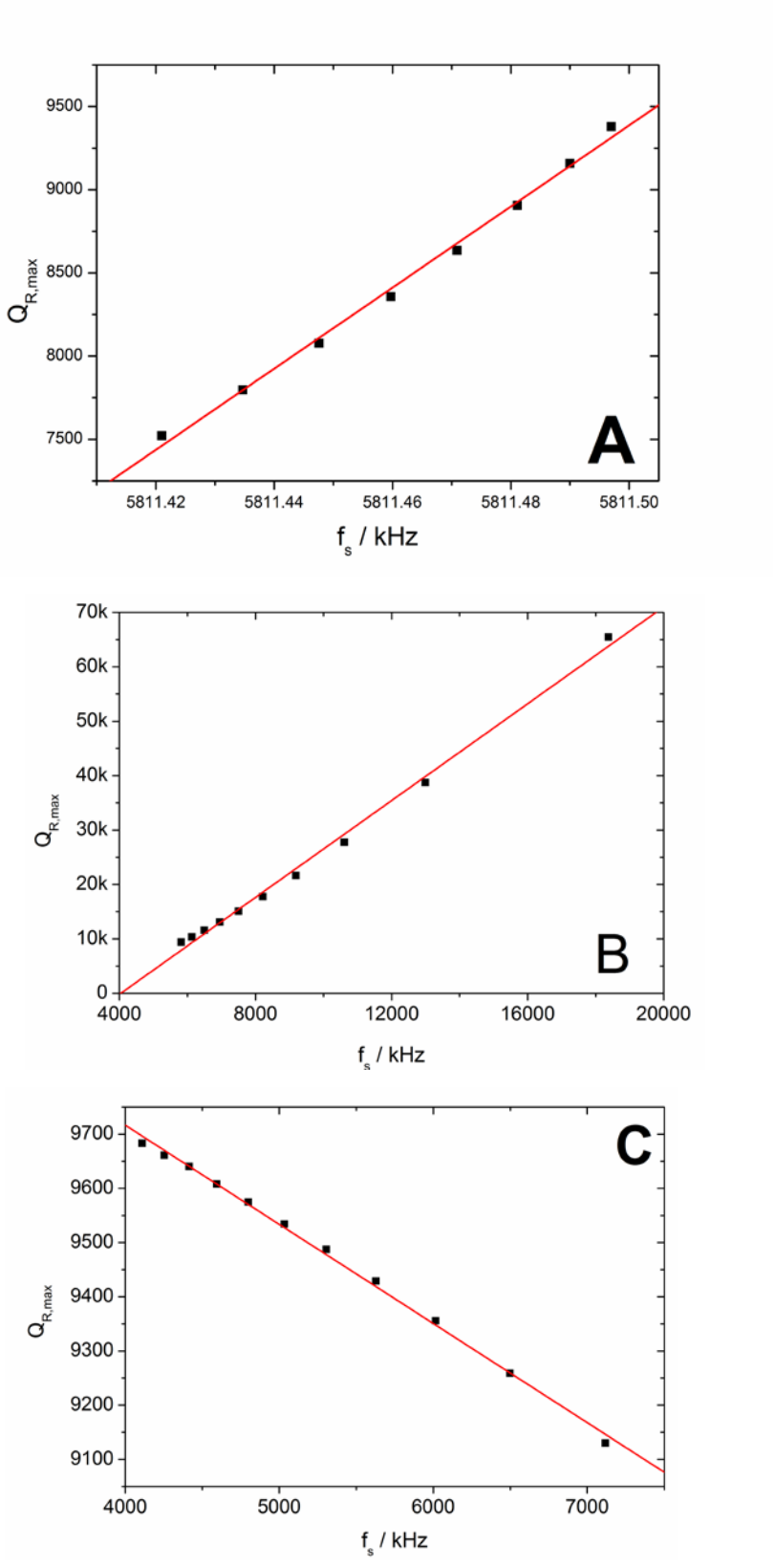

Figure 20: Plot of $Q_{R,\max}$ versus frequency, when the overall resistance (A, 100 Ω - 240 Ω), $C_D(\mu)$ (B, 1.11 aF - 90 aF) or the overall inductivity (C, 50 mH to 150 mH) of the circuit in Figure 11 changes. The characteristics of the remaining components were chosen as follows: L = 75 mH, R = 100 Ω, C = 10 aF, and C_0 = 50 pF.

Figures 20A-B can only give a qualitative relation between $f_{s,\min}$ and $Q_{\max}$ but not a quantitative relation. The actual value of $Q_{\max}$ and its sensitivity towards changes in R, L and C depends also on the actual value of C_0. As mentioned above C_0 also contains parasitic capacities which arise due to the mounting of the quartz crystal (other authors prefer to introduce a third capacitor parallel to C_0). Therefore, C_0 is different in each experimental setup and neither absolute values nor relative changes of $Q_{\max}$, obtained in different experiments, are comparable.

T / °C	ρ_{H2O} / g·mol^{-1}	η_{H2O} / mPa·s
10	1.00150	1.3403
15	1.00900	1.1361
20	0.99744	1.0000
25	0.99884	0.8876
30	0.99744	0.7945
35	0.99582	0.7171
40	0.99400	0.6510
45	0.99199	0.5943
50	0.98982	0.5456
55	0.98747	0.5033
60	0.98498	0.4664
65	0.98233	0.4336
70	0,.97954	0.4045

Table 1: Density and Viscosity of water as a function of temperature. The values were taken from Ref. [69].

Notwithstanding this, it is hard to construct a case where isolated changes in R take place. When the interaction between electrode and electrolyte changes in such a way that the no-slip-plane turns into a slip-plane R_L becomes smaller because friction between different layers of electrolyte moving relative to each other is reduced. However, under these conditions also L_L changes to lower values, because the liquid loading, the mass of liquid that moves along with the crystal, is reduced. Changes in the viscosity is another example for parallel changes in R_L and L_L. According to Equation 32 and 33 the viscosity enters both, R_L and L_L. Changes in the viscosity of the electrolyte can arise when the temperature

changes. As an example Table 1 gives the density and the viscosity of water for various temperatures [69].

One might think that parallel changes of R_L and L_L cause both, large changes of $Q_{R,\max}$ and $f_{s,\min}$. This would mean that changes in the overall resistance of the circuit in Figure 11 cannot be distinguished from changes in the in the capacity of $C_D(\mu)$. However, absolute changes of L_L due to changes in viscosity and density are smaller than changes of R_L, because $\sqrt{f}$ enters the denominator of Equation 33 but enters the numerator of Equation 32. Therefore, still large changes in the quality factor come along with small changes of the resonance frequency. This is shown in Figure 21, where the simulated quality factor of a quartz crystal immersed in water is plotted versus the temperature (Figure 21A) and versus the resonance frequency (Figure 21B). R_L and L_L that are necessary to determine $f_{s,\min}$ and $f_{p,\max}$ were calculated from the data in Table 1 according to Equations 32 and 33. The slope of $Q_{R,\max}$ in Figure 21B is smaller than in Figure 20A, but still larger then in Figure 20B and is sufficient to give the experimentalist a reasonable estimate whether changes in the overall resistance or in the capacity of $C_D(\mu)$ cause changes in the quality factor.

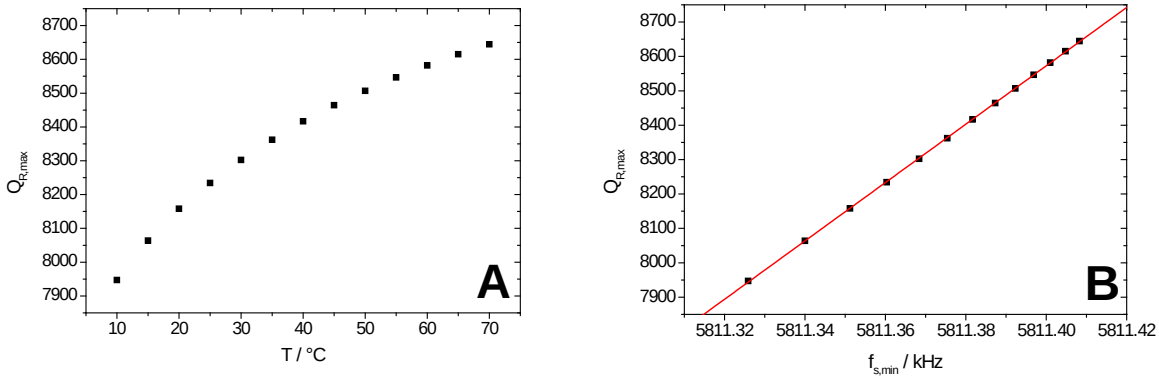

Figure 21: $Q_{R,\max}$ of a quartz crystal described by the circuit in Figure 11, plotted versus temperature (A) and $f_{s,\min}$ (B). $Q_{R,\max}$ was simulated for a quartz crystal immersed in water, R_L and L_L were calculate form Equations 32 and 33 taking the values given in Table 1 into account. $f_{s,\min}$ and $f_{p,\max}$ were determined graphically after simulation of the absolute value of the impedance. The characteristics of the remaining components of the circuit in Figure 11 chosen as follows: L = 75 mH, R = 100 Ω, C = 10 aF, and C_0 = 50 pF.

3. Paper 1 - Quantitative Study for Oxygen Reduction and Evolution in Aprotic Organic Electrolytes at Gas Diffusion Electrodes by DEMS

3. 1. Introduction to Paper 1

Paper 1 is the outcome of an electrolyte screening at the beginning of the project. DEMS results concerning oxygen reduction in DMSO and NMP based electrolytes are presented. The screening also involved other electrolyte systems which were based on sulfolane (tetrahydrothiophene 1,1-dioxide; *c.f.* Appendix A1), benzonitrile (*c.f.* Appendix A2) tetraglyme (2,5,8,11,14-pentaoxapentadecane; *c.f.* Appendix A3) or nitrobenzene. However, efforts to use these solvents were quickly abandoned: In lithium containing electrolytes that were based on sulfolane, benzonitrile and tetraglyme oxygen reduction turned out to be rather irreversible. (Here "irreversible" is not used in a kinetic sense but to express the fact that the ratio of reduced to evolved oxygen is much smaller then one. In the following paper we coin the term "true coulombic efficiency" to describe this ratio and irreversibility in the above sense is used from now on as "a true columbic efficiency much lower than one"). Nitrobenzene on the other hand was considered an unfeasible solvent because it undergoes electrochemical reduction to the nitrobenzene anion radical at a potential higher than that of oxygen reduction. The amount of experimental data obtained in tetraglyme, sulfolane, benzonitrile and nitrobenzene is limited and was, therefore, considered unfit for publication.

Although there were already DEMS results available on various electrolyte systems including those based on DMSO and NMP [35] we felt compelled to do a screening of our own. Given the history of carbonate based electrolytes in the lithium-air battery research we were weary to trust literature results. Furthermore, the DEMS setup in the present study is very different from the DEMS setup used in other studies related to lithium-air battery research: Both the McCloskey-group and the Bruce-group [35] [34] employ some sort of head space cell. In this setups, as pointed out in Section 2.2. the membrane separates the electrolyte from a space at ambient pressure. In our setup, however, the "traditional" or "conventional" cell was used, where the membrane constitutes the interface between electrolyte and vacuum. As properties like the surface tension σ and the contact angle θ are scarcely available for the solvents and certainly not for the final electrolyte we had to test *via* trial and error whether Equation 1 in Section 2.2. holds for the respective electrolytes.

In Paper 1 we also show that the metal sputtered Teflon membrane can be used as a gas diffusion electrode during oxygen reduction. We have done several experiments, where we used a metal sputtered Teflon membrane as a gas diffusion electrode, which have not been subject of any publication yet. In Appendix A5 one rather interesting aspect concerning this kind of experiments is briefly presented.

3. 2. Quantitative Study for Oxygen Reduction and Evolution in Aprotic Organic Electrolytes at Gas Diffusion Electrodes by DEMS (as published in JECS)

The version of record of Paper 1 as published in the Journal of the Electrochemical Society is shown in the following. The article was published under the Creative Commons Licence (CC-BY-NC-ND; "Open Access"). Therefore, no special permission of the publisher is required to display the version of record. Any use of the material of the article shown below is permissible only after proper citation:

C. J. Bondue, A. A. Abd-El-Latif, P. Hegemann and H. Baltruschat, *J. Electrochem. Soc.*, **162**, A479 (2015).

Quantitative Study for Oxygen Reduction and Evolution in Aprotic Organic Electrolytes at Gas Diffusion Electrodes by DEMS

C. J. Bondue,[a] A. A. Abd-El-Latif,[a,b] P. Hegemann,[a] and H. Baltruschat[a,*,z]

[a]*Institut für Physikalische und Theoretische Chemie, Universität Bonn, D-53117 Bonn, Germany*
[b]*National Research Centre, Physical Chemistry Department, 12311 Cairo, Egypt*

Cyclic voltammetry and differential electrochemical mass spectrometry (DEMS) have been combined to study the cycling performance of the oxygen reduction reaction (ORR) and the oxygen evolution reaction (OER) at a gold electrode in non-aqueous dimethyl sulfoxide (DMSO) and *N*-methyl-2-pyrrolidone (NMP) based $LiClO_4$ and $N(Bu)_4ClO_4$ containing electrolytes. An Au-sputtered Teflon membrane (with a thickness of Au of only 50 nm resulting in an extremely short pore length on the electrolyte side) has been used as a model for a gas diffusion electrode (GDE) in this study: The oxygen molecules diffuse through a membrane from the gas side and are reduced at Au on the electrolyte side. The redox couple $O_2^{-\bullet}/O_2$ is the predominant reaction during ORR in $N(Bu)_4ClO_4$ based electrolytes whereas the calculated number of electron transferred is one. In presence of Li-ions, the average number of electrons transferred is 2 during oxygen reduction, which indicates the formation and oxidation of peroxide during ORR and OER respectively. The mass spectrometric cyclic voltammograms (MSCVs) data show that the maximum true coulombic efficiency of OER/ORR in DMSO and NMP is about 60% and 25%, respectively, with the evolution of CO_2 in NMP at 0.1 V (vs. Ag^+/Ag) due to the decomposition of the electrolyte.
 [DOI: 10.1149/2.0871503jes]

Manuscript submitted September 18, 2014; revised manuscript received December 30, 2014. Published January 9, 2015.

One of today's challenges is the development of an energy storage system that can provide both high capacity and good cycling performance. Secondary lithium-air batteries are promising candidates as they provide a high theoretical capacity. However in practice, cycling performance is bad. The key step in discharging these batteries is the reduction of oxygen present in air. So far the oxygen reduction reaction has been investigated thoroughly in aqueous media, but only little fundamental research has been done in non-aqueous solvents.

The first non-aqueous lithium-air battery was introduced in 1996 by Abraham and Jiang[1] as an alternative energy storage system for future applications. The specific energy of a Li-air battery amounts to 5.21 kWh/kg (including the weight of O_2), based on the assumption that Li fully reacts with O_2 to form Li_2O.[1] However, in practice the route to Li_2O has proven irreversible. Hence, a more reasonable specific energy of 3.5 kWh/kg is obtained assuming lithium peroxide (Li_2O_2)[2] as the sole discharge product. In practice Li-air batteries suffer from rapid capacity fading due to several obstacles such as poisoning the lithium electrode with CO_2,[3] moisture and the instability of organic electrolyte used today against superoxide ion radical ($O_2^{-\bullet}$).[4] One main challenge to overcome in the attempt to develop a reversible Li-O_2 batteries with high capacity is the selection of an appropriate non-aqueous electrolyte which is characterized by high stability in the presence of lithium oxide species and a wide potential window. There are further requirements for the electrolyte in battery applications, such as low flammability, low vapor pressure and a large temperature range in which it is present in liquid form.

Li-air batteries based on the non-aqueous organic carbonate electrolyte showed poor cycling efficiency due to the decomposition of the electrolyte to lithium carbonate ($LiCO_3$) and lithium alkylcarbonate (RO-(C=O)-OLi)[5,6] that accumulated on the cathode. In addition dendrite formation was observed.[7]

Read[8] reported an excellent rate capability and good stability of ether-based electrolyte in Li/O_2 cell. Recently, Scrosati[9] showed by XRD that tetraglyme-$LiCF_3SO_3$ is a convenient electrolyte for Li-air batteries whereas Bruce[10] using XRD, FTIR- and NMR techniques demonstrated that tetraglyme-$LiPF_6$ is not a suitable electrolyte as it decomposes in the first few cycles to form a mixture of Li_2CO_3, HCO_2Li, CH_3CO_2Li, polyethers/esters, CO_2, and H_2O.[10] Also Laoire et al. attributed the low rechargeability of the uncatalyzed Li-O_2 battery using tetraglyme-$LiPF_6$ based electrolyte to the poor cycling efficiency of the Li anode and to the high impedance associated with the deposition of Li_2O_2 on the cathode.[11]

Recently, dimethyl sulfoxide (DMSO)[12,13] and *N*-methyl-2-pyrrodione (NMP)[14,15] have been suggested as candidates for a rechargeable non-aqueous Li-air battery because they show high stability versus the superoxide ion and the main discharge product is Li_2O_2.

In general it seems to be established in literature that the oxygen reduction in organic electrolytes containing lithium ions results in the formation of lithium peroxide.[12,16–18] For that a number of techniques have been employed ranging from purely kinetic considerations after recording a CV to more meaningful techniques such as XRD-profiling,[16] SEM-imaging[18] and FTIR-,[12] Raman-[12] and XP-spectroscopy[17] of the discharge electrode.

Employing cyclic voltammetry (CV) and rotating disk electrode (RDE) techniques, Abraham group[13,16] concluded that DMSO is a practical electrolyte for Li-O_2 batteries since it facilitates the reversibility of oxygen reduction/oxidation reaction. On the other hand, Li_2O_2 has been reported as the major discharge product at a nanoporous gold electrode[12] or at a TiC-based cathode[19] using 0.1 M $LiClO_4$ in DMSO as the electrolyte in Swagelok design cell for DEMS; the number of electrons per O_2 molecule during discharging or charging is 2.

NMP is one of the most stable organic solvents versus the superoxide anion radical. It has a higher theoretical energy barrier (>40 kcal/mol) than that of organic carbonates (≈20 kcal/mol) for the nucleophilic attack at any ring carbon atom during oxygen reduction reaction.[15]

Differential electrochemical mass spectrometry (DEMS) has become a versatile tool for the on-line detection of volatile products and intermediates which are formed during the electrochemical reaction either in aqueous or non-aqueous electrolytes.[20] So far, for instance, reductive and oxidative decomposition products of organic carbonate electrolyte solutions used in Li-ion batteries were detected by DEMS using a porous working electrode[21–23] or headspace cell.[24–27] Using a headspace cell for DEMS, oxygen evolution from a Li-O_2 battery featuring a $LiPF_6$/PC electrolyte was detected.[28]

In the papers mentioned thus far only the apparent coulombic efficiency of ORR and OER was determined by comparing the faradaic

*Electrochemical Society Active Member.
[z]E-mail: baltruschat@uni-bonn.de

charge transferred during discharge (Q_c) with that transferred upon charging (Q_a). Based on the faradaic charges, Laoire et al.[11] for instance found that the Q_a/Q_c is 95% in TEGDME-$LiPF_6$ based electrolyte whereas Wang et al.[14] reported the high ratio (97%) in NMP-$LiClO_4$ based electrolyte. Since the apparent coulombic efficiency is not a sufficient criterion for the real cycleability of Li-O_2 batteries, McCloskey et al.[29] determined the true coulombic efficiency (the ratio of evolved and reduced amounts of oxygen) of Li-O_2 battery for a variety of organic solvents in a head space cell combined with DEMS. With this setup the true coulombic efficiency of a Li-O_2 battery with a DMSO-TFSI and NMP-TFSI based electrolyte was found to be 50 and 60%, respectively.[29] The term "coulombic efficiency," typically used in batteries research for the ratio of charge during charging and discharging has to be well distinguished from the current efficiency, relating the true amount of formed or consumed species to the amounts as calculated from Faraday's law. A quantitative study, done by McCloskey et al.[30] (again using a head space DEMS cell), demonstrated that the charging and discharging peaks in a DME-LiTFSI based electrolyte are due to oxygen reduction and oxidation reactions with $2e^-/O_2$ without any evidence for LiO_2 or Li_2O formation at any potential. However only 60% of oxygen reduced are re-evolved in this experiment. Using the same cell set-up, Barile and Gewirth[31] reported that the presence of Au nanoparticles as a cathode improve the cycleability of the cell and increase the amount of evolved oxygen gas during the charge process. On the other hand, the presence of Pt, Pd or Cu(II)O reduces the cell performance.

DEMS combined with a sealed battery designed cell was applied for quantitative gas evolution analysis during charging of Li-O_2 battery in propylene carbonate (PC) and diglyme-LiTFSI based electrolytes.[32] The dominant product is O_2 in case of diglyme electrolyte whereas PC is not stable at high potential producing CO_2 gas.

In some of the experiments described here, we mimic the applied air breathing battery by supplying oxygen from atmosphere at a gas diffusion electrode. In this study a porous working electrode (50 nm Au sputtered onto a teflon membrane) serves as a model for gas diffusion electrodes. The apparent coulombic efficiency was calculated from the faradaic charge obtained from cyclic voltammetry. However the true coulombic efficiency of oxygen evolution/consumption in NMP-$LiClO_4$ and DMSO-$LiClO_4$ based electrolytes were determined from the corresponding ionic charge obtained by means of DEMS using a conventional DEMS cell. In the later case oxygen was supplied to the electrode from solution. The main difference (and advantage for fundamental research) is that the electrode is relatively smooth (as compared to battery electrodes which have been used in the past for similar measurements) with a roughness factor of about 10 and a pore length on the electrolyte site of only about 50 nm. Therefore there are no diffusion effects in the pores and no complications, i.e. due to pore clogging (a severe problem observed in model batteries), are to be expected. This enables us to investigate the underlying electrochemistry and its limitations to the concept of lithium-air batteries.

Experimental

Mass spectrometry combined with the conventional DEMS cell was used in this study to detect in situ the volatile products and intermediates which are produced during electrochemical reactions.[20,33]

The DEMS cell setup is schematically shown in Figure 1. The working electrode and a 6 mm i.d-Teflon spacer are clamped between the glass body and the steel holder whereas the porous steel frit works as a mechanical support for the Au-sputtered Teflon membrane working electrode.

This cell is directly connected to the vacuum system through an angle valve and a T-piece. This cell also has the advantage of the small electrolyte volume needed ($\leq$ 1.5 ml) for an experiment.

The gold-sputtered (50 nm Au) Teflon membrane serves both as a working electrode and as the electrolyte-vacuum interface. Due to the high surface tension of the electrolyte used here, they do not penetrate the capillaries of the membrane. An Au wire was used as a counter electrode. As a reference electrode a silver wire immersed in a solution of 0.1 M $AgNO_3$ in the solvent used to prepare the working electrolyte was employed. Electrically the reference electrode was connected to the working electrode compartment by a salt bridge made from a Teflon tube filled with the $AgNO_3$ solution. In order to protect the working electrolyte from contamination with silver ions the Teflon tube was closed with a rough glass bead. Ion migration along the glass surface maintains sufficient conductivity. A drawing of the reference electrode is shown in Figure 2.

The standard electrode potentials of the Ag^+/Ag and the Li^+/Li couple were determined versus the standard hydrogen electrode (SHE) in several non-aqueous solvents by Gritzner.[34] Taking these values into account the reference electrode's potential is calculated to be +0.43 V in DMSO and +0.54 V in NMP versus SHE. Versus the Li^+/Li couple the respective potentials are −3.89 V and −3.80 V.

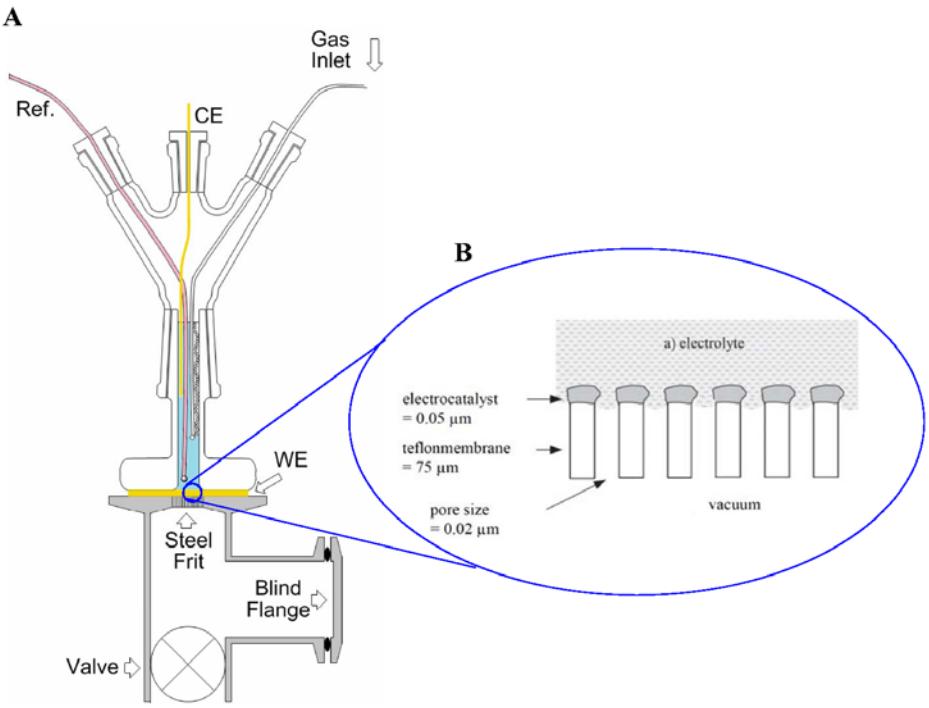

Figure 1. Conventional DEMS setup used in gas diffusion electrode experiments (A). A model of the gas diffusion working electrode (sputtered Teflon membrane) (B).

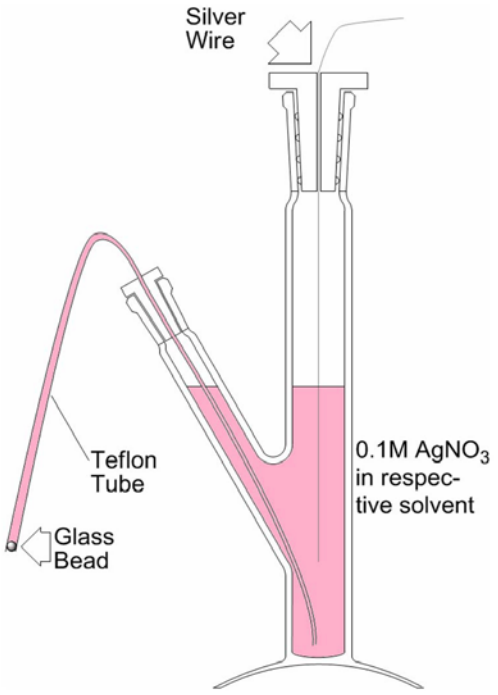

Figure 2. Design of the used Ag^+/Ag reference electrode: A silver wire is immersed in 0.1 M $AgNO_3$ solution. The solvent is either DMSO or NMP. A Teflon tube filled with silver solution and closed with a glass bead (with a roughened surface) ensures ionic contact to the electrolyte in the cell.

Highly pure lithium perchlorate ($LiClO_4$) (Sigma-Aldrich, $\geq 98\%$) used for preparing the electrolyte was dried under reduced pressure at 180°C until the weight was constant. $AgNO_3$ (AppliChem, *p. a grade*.) was used as received. *N*-methyl-2-pyrrolidone (NMP) (Sigma-Aldrich, anhydrous 99.5%) was used as received and extra dry dimethyl sulfoxide (DMSO) (Acros Organics, 99.7%) was dried in addition over activated molecular sieves. The water contents of the dried electolytes were checked using the Karl-Fischer titration method. Highly pure Ar (Air Liquid, 99.999%) was used for purging the electrolyte and highly pure oxygen (Air Liquid, 99.9995%) as a source for oxygen.

The Au-sputtered electrode was used as a gas diffusion electrode in some experiments. In contrast to the normal cell setup in which the electrolyte was saturated with oxygen, in these air was introduced from the gas side (the volume underneath the working electrode). Therefore, during the first cathodic going sweep, the valve (c.f. Figure 1) which directly connects the electrochemical cell to the vacuum system was closed and ion currents cannot be recorded. By removing the blind flange, atmospheric oxygen diffuses through the steel frit to the membrane where it is reduced at the electrode surface.

As soon as a potential of −1.25 V was reached, the potential sweep was stopped and the blind flange was mounted again. The volume underneath the electrode was then evacuated. By opening the valve, the electrochemical cell was directly connected to the mass spectrometer. In the first anodic sweep, the reduced oxygen species present at the electrode surface were oxidized and the ionic current of oxygen for mass 32 was recorded.

The calibration constant of DEMS (K°) is defined as the proportionality constant between the rate of species entering the mass spectrometer (dn_i/dt) and the corresponding ionic current I_i (eq 1):

$$I_i = K^o \left(\frac{dn_i}{dt}\right) = K^o \cdot \dot{n} \qquad [1]$$

The calibration leak experiment was performed under the same condition as the experiments.

The calibration leak was connected through a gas dosing valve to the T-piece which was directly connected with the cell and the vacuum system. The calibration volume of 54 mL was repeatedly evacuated with a Dual-stage rotary vane pump (DUO 2.5, Pfeiffer Vacuum) to ca. 0.02 mbar and purged with oxygen. A certain amount of calibrating gas (oxygen) was introduced into the volume to about 8 mbar. Once the dosing valve was opened to introduce the calibrating gas to the mass spectrometer with a defined flow rate, the reduction in the pressure was recorded via the attached gauge and the ionic current for mass 32 was recorded simultaneously.

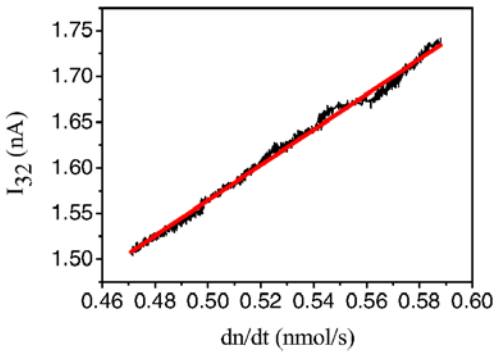

Figure 3. The linear relationship between the ionic current for mass 32 and the rate of oxygen molecules entering the mass spectrometer from calibration leak volume.

The linear relationship between the ionic current (I_i) vs. dn_i/dt gives a slope equal to the value of K° for a given gas as shown in Fig. 3.

Since the collection efficiency of the DEMS cell in use, the measured ion current and the calibration constant are all linked to some uncertainties.[35] It is therefore common practice to assume an error of ±10 to ±20% on DEMS results.[36–40] While we have found a high accuracy for the collection efficiency (ratio of formed species to those entering the vacuum system) of our cell in the past (close to 100% for this kind of cell), the calibration process comes along with uncertainties especially due to the pressure measurements - a well known problem in vacuum technology.

Results and Discussion

To demonstrate the suitability of the membrane we first performed typical DEMS experiments with the volume underneath the gas diffusion electrode being evacuated and connected to the MS in an electrolyte of 0.1 M Bu_4NClO_4 in NMP (Fig. 4A) and DMSO (Fig. 4B). The resulting curves are shown in Figure 4 and match well those curves shown in literature. Since the electrolyte is constantly purged with oxygen, there is a steady flow of molecules into the vacuum resulting in a relatively high baseline for mass 32, which was subtracted from the MSCV data shown in Fig. 4.

The potential was cathodically swept starting at –0.5 V. Oxygen was reduced at a potential of –1.22 V in NMP and of –1.05 V in DMSO and is re-evolved in the following anodic sweep at a potential of –1.38 V in NMP and at –1.15 V in DMSO, as seen in both the faradaic and ionic current. Obviously ORR and OER are the dominant reactions in DMSO. DEMS also allows for a quantitative correlation. This is not only true for O_2 evolution; at this type of electrode, the gas evolved is nearly quantitatively diffusing through the membrane into the vacuum of the MS. It is also true for oxygen reduction, where O_2 is consumed: the flow of oxygen into the vacuum is diffusion limited and according to Fick's law determined by the concentration gradient over the Nernstian diffusion layer. As the dimensions of the diffusion layer as well as the concentration gradient are fixed for a given experimental setup (i.e. a given convection as determined by the oxygen flow through the tubing), the overall flow of oxygen to the electrode and membrane $\frac{\partial n(O_2)}{\partial t} = \dot{n}_{tot}$ also is constant. As soon as the electrode approaches the potential of oxygen reduction a portion $\dot{n}_{el}$ of the influx is consumed electrochemically. Hence the flux of oxygen

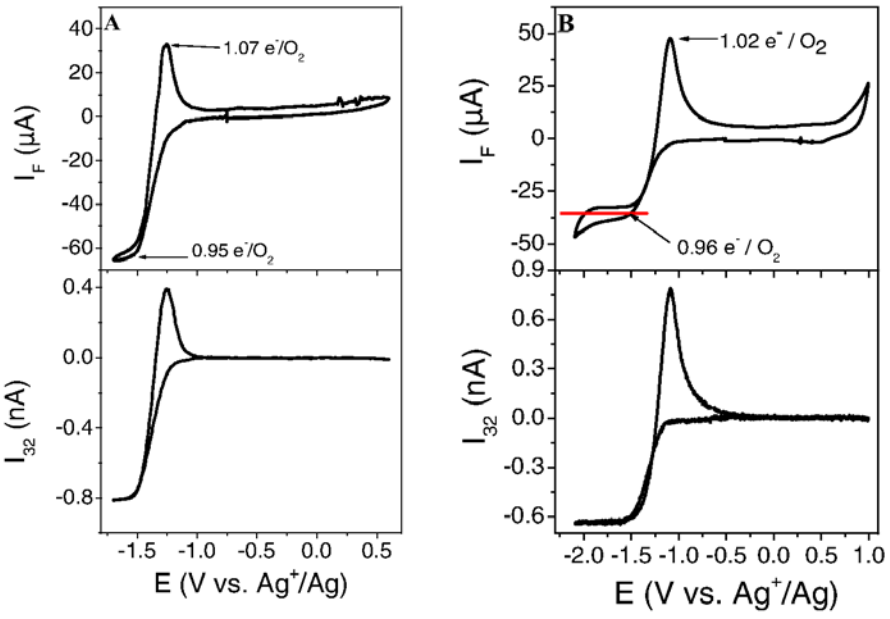

Figure 4. Simultaneously recorded CVs and MSCVs for mass 32 for oxygen reduction and evolution reactions at Au sputtered Teflon membrane in O_2-saturated electrolyte. 0.1 M $TBAClO_4$-NMP (A) and (B) 0.1 M $TBAClO_4$-DMSO based electrolytes. Scan rate: 10 mV/s.

entering the mass spectrometer $\dot{n}_{MS}$ is

$$\dot{n}_{MS} = \dot{n}_{tot} - \dot{n}_{el} \quad [2]$$

and thus

$$-I_I = K^0 \cdot \dot{n}_{el} + const \quad [3]$$

(In reality some O_2 originating from leaks and residual gas in the vacuum adds to this, resulting in a slowly changing baseline. Therefore, in the following, the baseline of ionic current is corrected.)

Since both, faradaic and ionic currents, are proportional to the amount of oxygen consumed and re-evolved, respectively, we can calculate from equation 4 the number of electrons transferred per molecule of oxygen (z in e^-/O_2) both upon reduction and evolution.

$$z = \frac{I_F \cdot K^\circ}{I_I \cdot F} \quad [4]$$

whereas I_F is the faradaic current with $I_F = zF\dot{n}_{el}$ assuming a current efficiency of 100%, I_I the ionic current, F the Faraday constant and K° a calibration constant determined in a calibration leak experiment as presented in details in the experimental section.

For DMSO we find 1.02 electrons upon oxygen reduction and 0.96 upon oxygen evolution. A value of z = 1 during oxygen reduction is indicative for the formation of superoxide. Therefore the formation of other reduced oxygen species such as peroxides is ruled out. Since the z-values observed during oxygen reduction and oxygen evolution match each other, side reactions are unlikely to occur. Side reactions are improbable to alter z-values for oxygen reduction and oxygen evolution in the same way. Therefore we can show here that oxygen is reduced to superoxide in an electrolyte of 0.1 M Bu_4NClO_4 in DMSO, thus supporting Loire et al. who came to this conclusion by purely kinetic considerations.[16]

The diffusion limited reduction current observed in Figure 4 was caused by the continuous bubbling with oxygen. Since the corresponding convection is not very strong, one might expect the typical diffusion limited peak as in cyclic voltammetry similar to the re-oxidation peak. Such a peak is not observed here because the transport of oxygen to the electrode is always diffusion limited: If oxygen is not consumed electrochemically it evaporates in to the vacuum. Since the product of reduction ($O_2^{-\bullet}$) is largely transported into the bulk of the electrolyte, only a small portion re-oxidized is to O_2.

In the case of NMP 0.95 e^-/O_2 are transferred during oxygen reduction and 1.07 e^-/O_2 are transferred during oxygen evolution. As in the case of DMSO superoxide is formed during oxygen reduction in a NMP-$TBAClO_4$ based electrolyte.

It is important to show that oxygen reduction both in DMSO and NMP based electrolytes results in superoxide formation when only TBA cations are present. This reaction can be used in future experiments to calibrate other DEMS cells such as flow trough cells and dual-thin-layer cells, where calibration through a leak is not an option.[41]

The results of a measurement performed in an electrolyte of 0.1 M $LiClO_4$ in DMSO are shown in Figure 5. The onset of oxygen reduction at −1.05 V is at the same potential as in the electrolyte containing 0.1 M Bu_4NClO_4. Oxygen evolution is shifted by 0.4 V to more positive potentials with respect to 0.1 M Bu_4NClO_4 containing electrolyte. Oxygen evolution in Figure 5 has an onset of −0.73 V and a peak potential of about –0.5 V. It is noteworthy that the electrode is completely deactivated at –1.75 V. During a full cathodic sweep 19.1 nmol of oxygen are reduced. If this oxygen is transformed into lithium

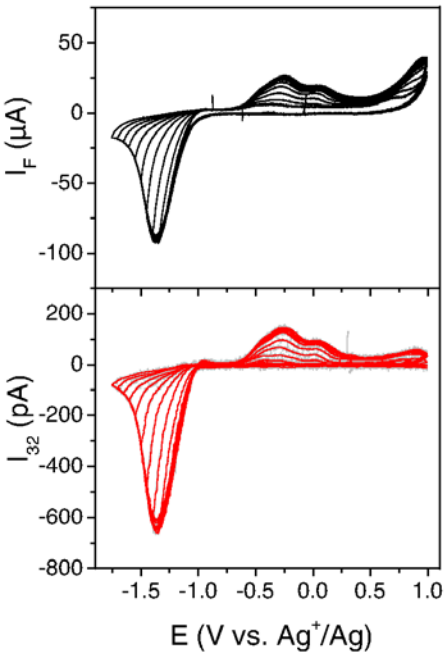

Figure 5. Simultaneously recorded CV (A) and MSCV for mass 32 (B) for oxygen reduction and evolution reactions at Au sputtered Teflon membrane in 0.1 M $LiClO_4$-DMSO based electrolyte. Scan rate: 20 mV/s.

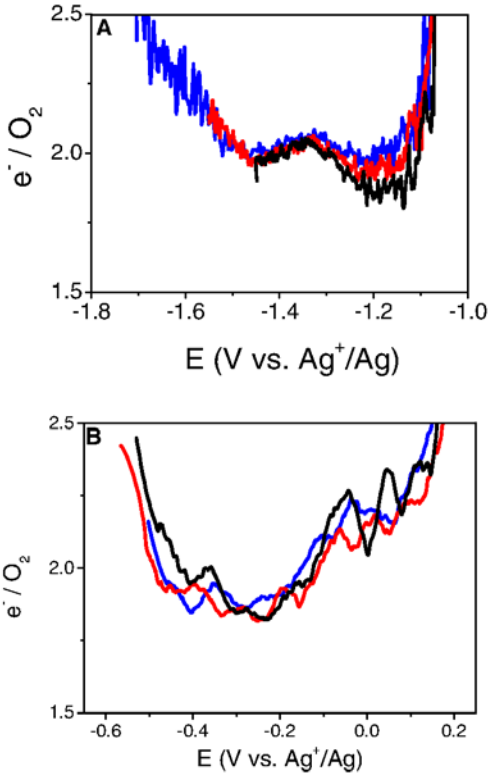

Figure 6. The calculated number of electrons transferred per oxygen molecule during the oxygen reduction (A) and (B) evolution reactions at Au sputtered Teflon membrane electrode in 0.1 M $LiClO_4$ in DMSO (A: cathodic sweep only). Scan rate: 20 mV/s. Lower potential limits are: Black: −1.45 V; Red: −1,55 V; Blue 1.70 V.

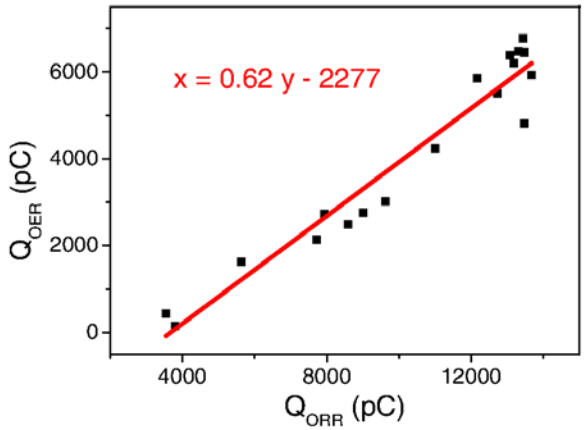

Figure 7. Ionic charge of oxygen evolution versus the ionic charge of oxygen reduction. The values are derived from each cycle shown in Figure 5.

peroxide this would correspond to the formation of just 3 monolayer (we define a monolayer as the ratio of Li_2O_2 units per surface atom of gold) of lithium peroxide - a very small amount to deactivate the electrode considering that Li_2O_2 is expected to form crystallites rather than a film.

Form equation 4, z was calculated for some cathodic sweeps shown in Figure 5. Calculations were done after correction for double layer capacity and the results are plotted in Figure 6, showing that roughly two electrons are transferred per molecule of oxygen. The increase in the number of electrons transferred as a potential of −1.6 V is passed is due to a side reaction that also occurs in Argon saturated electrolyte. In a potential range from −1.1 V to −1.6 V z roughly equals 2.

For the corresponding anodic sweeps of Figure 5, z-values have been calculated and are displayed in Figure 6B. The z-value at −0.25 V (where a peak is present in Figure 5) for oxygen evolution is about 1.9. This value fits well to the oxidation of peroxide. As the potential is increased further the z-value increases slightly to 2.2. This increase corresponds to the shoulder observed in Figure 5. At this point we have no explanation why oxygen evolution in the potential range from −0.67 V to 0.32 V proceeds in two distinct processes associated with a slight change in the electron number. But we note that the CVs in DMSO-based electrolyte at a gold electrode shown by Sharon et. al.,[42] by Laoire et al.,[16] by Peng et al.[12] and by us, differ from each other in the exact shape in the region of oxygen evolution. However the general features are the same in all cases. A peak during oxygen reduction is observed and oxygen evolution has an onset potential 300 mV more positive than the onset potential of oxygen reduction. In anodic direction there is a continuous current up to at least 0.1 V (4.0 V vs. Li^+/Li).

Literature findings that lithium peroxide is formed in organic electrolytes if Li^+ is present are based in their vast majority on *post mortem* analysis of discharged electrodes. However, this does not demonstrate that the amount of formed peroxide matches the charge transferred; the fact that lithium peroxide is the only product found does not mean that lithium peroxide is the sole reduction product, since discharge products might either not be accessible by the techniques employed or might remain in the electrolyte. McCloskey et al.[43] have already shown by means of DEMS that oxygen reduction in DMSO proceeds via the consumption of 2 electrons per molecule of oxygen. However this z-value was determined in a galvanostatic experiment, where the potential was around 2.7 V vs. Li^+/Li (−1.14 V vs. Ag^+/Ag) with a highly porous electrode. Peng et al. on the other hand reported a z-value ranging from 1.99 to 2.03 in a potentiostatic experiment but did not give any potential at which they determined those values. In fact a graphic evaluation of their curves results in an appreciable decrease of the z-value from roughly 2 to roughly 1 as the potential is decreased. The finding that oxygen reduction proceeds by the transfer of 2 electrons per molecule of oxygen in a potential window ranging from −1.1 V to −1.6 V at a rough electrode is of importance because it shows that no Li_2O is formed at potentials 400 mV lower than those used by McCloskey et al. at a rough gold electrode. Furthermore we are going to show in a subsequent paper that the z vs. E-plot differs from that shown in Figure 6 if a smooth gold electrode is used. (We would like to point out that a z-value of 2 for oxygen reduction would also be obtained, if the peroxide reacts with the solvent molecules in a subsequent reaction.)

The fact that oxygen reduction sets in at the same potential as in the electrolyte containing 0.1 M Bu_4NClO_4, despite the observation of lithium peroxide formation, might be taken as an indication that the first electron transfer is the rate determining step.

The true coulombic efficiency of the oxygen reduction/evolution is evaluated from the integrated ion currents during reduction and oxidation. In Fig. 5 the amount of reduced oxygen is altered by successively decreasing the lower potential limit. In Figure 7 the ionic charge of oxygen evolution of each cycle is plotted against the ionic charge of oxygen reduction of the respective cycle. The slope of the linear fit represents the true coulombic efficiency of the OER/ORR which is found here to be about 60%. It is interesting to note that the linear fit has a negative intercept with the y-axis. While a slope smaller than 1 means that in each cathodic sweep a certain percentage of the reduced oxygen is not re-oxidized in the following anodic sweep; a negative intercept means that a certain amount of the reduced oxygen is lost in each cycle. We are going to address this observation in a subsequent paper.

It is obvious, that this is not sufficient for a properly working lithium-air battery. On the other hand, Peng et al., have recently constructed a lithium-air battery and claim that it works on the basis of highly reversible formation and decomposition of lithium peroxide.[12] Peng et al. undertook much effort to show that the sole reaction product upon discharge is lithium peroxide using various spectroscopic methods. They show DEMS results (obtained with a swagelock type

Table I. Amounts of oxygen consumed and evolved from a lithium-air battery derived from the curves published by Peng et al.[12] From those values the true coulombic efficiency of OER/ORR was calculated.

Cycle number	$n(O_2)_{ORR}$ (mmol)	$n(O_2)_{OER}$ (mmol)	True coulombic efficiency (%)
1	0.39	0.18	46.11
5	0.30	0.13	43.69
10	0.33	0.15	45.67
100	0.26	0.19	72.90

cell) to confirm that only oxygen, but no CO_2, SO_2 or SO_3, is evolved during the anodic scan and that 2 electrons are transferred indeed both in the anodic and cathodic scan (*vide supra*).

However, they did not compare the amount of O_2 consumed with that evolved in the subsequent anodic cycle. We therefore calculated the true coulombic efficiency by integrating their curves, thus obtaining the amounts of reduced and evolved oxygen. The results are listed in Table I, with typical values below 50%. Therefore our results at model electrodes are in agreement with those of Peng et al. (but not with their interpretation) and confirm the results of McCloskey et al.,[4] which have found so far, undeservedly, little attention in literature among experimenters. With such a poor true coulombic efficiency the high cycling performance claimed by Peng et al. is bound to be due to some kind of side reaction. However, Peng et al. rule out the major formation of side products, based on several techniques (FTIR-, SERS-, ^{1}H–NMR and ^{13}C–NMR-spectroscopy). But the low sensitivity of NMR-spectroscopy is well known. In fact the ^{13}C-NMR-spectrum shown by Peng et al. features no signal from the carbon atoms of the conducting salt LiTFSI, which have fair intensity at a chemical shift of 120 ppm,[44,45] rendering the shown spectra meaningless. Furthermore different by-products other than the observed small amounts of HCO_2Li and Li_2CO_3 might form, undetectable by FTIR and SERS-spectroscopy. Therefore the high apparent cycleability of the lithium-air battery published by Peng et al. probably stems from the involvement of side reactions and the consumption of the electrolyte.

For instance, Sharon et al. have proposed a decomposition mechanism of DMSO resulting either in the formation of sulfate or of dimethylsolfone initiated by the deprotonation of one methyl group by either lithium hydroxide or superoxide and a subsequent nucleophilic attack at sulfur.[42] Such a mechanism might serve as an explanation for the reduced reversibility of oxygen reduction/evolution reactions. However other explanations are possible for the reduced reversibility of oxygen reduction/evolution reactions. For instance some of the formed peroxide might precipitate somewhere without electrical contact to the electrode or some larger particles might loss contact to the electrode in the course of oxygen evolution.

As mentioned above the gold sputtered Teflon membrane can also serve as a gas diffusion electrode. An experiment in which the electrode was used in such a way is shown in Figure 8. During the first cathodic sweep in 0.1M $LiClO_4$-DMSO based electrolyte, the electrode was exposed to laboratory air by closing the valve and opening the blind flange, thus filling the volume underneath the electrode with air which has been evacuated previously. During the first cathodic sweep there was no oxygen reduction until the current begins to decrease at a potential of −0.72 V. As soon as a potential of −1.25 V is reached the potential was stopped and the blind flange was mounted again. The volume underneath the electrode then was evacuated by opening the valve, thus connecting the electrochemical cell to the mass spectrometer. As the supply of oxygen from underneath the electrode is cut-off the current drops to zero.

Since there was no connection to the mass spectrometer no ionic current was recorded during the first cathodic sweep; nevertheless in the following anodic sweep the oxidation of those oxygen species

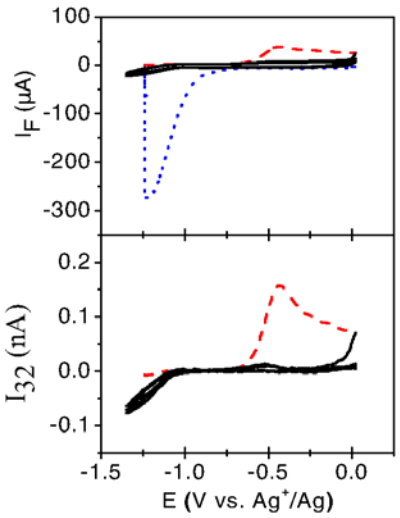

Figure 8. Simultaneously recorded CV (a) and MSCV for mass 32 (b) during oxygen reduction and evolution reactions at gas diffusion electrode (Au sputtered Teflon membrane) in 0.1 M $LiClO_4$-DMSO based electrolyte. Oxygen source is atmospheric air in the first cathodic going sweep, electrolyte purged with oxygen. Blue: first cathodic going sweep; red: first anodic going sweep; Black: ensuing cycles with oxygen supplied from solution. Sweep rate 10 mV/s.

formed in the first cathodic sweep were observed by mass spectroscopy.

In the subsequent cycles, the dissolved oxygen in the electrolyte was reduced. It is obvious that much larger current are obtained when the electrode is employed as a gas diffusion electrode, since oxygen transport is much more efficient from gas phase then by diffusion through a liquid.

It is important to show that also under these ambient conditions oxygen reduction and evolution takes place as well. This can be seen from the ionic current in the first anodic sweep. But a major drawback is the lower true coulombic efficiency of OER/ORR under these conditions, amounting only to 16% (derived from faradaic current). The reason for that may be humidity and also CO_2. In the presence of CO_2, carbonate is formed as has been shown previously by both theoretical calculations and post mortem analysis.[46]

Similar to the gas diffusion experiment shown in Figure 8, the CVs and in situ MSCVs for ORR and OER in 0.1 M $LiClO_4$-NMP based electrolyte containing 60 and 380 ppm of water were recorded starting at −0.2 V vs. $Ag^+/Ag_{(NMP)}$ as shown in Figure 9A and 9B respectively. That figure shows the sweep starting at −0.2 V in the negative going scan where the GDE was exposed to the atmospheric air from the gas side. In the beginning of the cathodic sweep, the current is close to zero because no oxygen reduction reaction takes place. The onset potential for ORR is −0.86 V whereas the faradaic current starts to decrease followed by the reduction peak of oxygen at −1.35 V with a current density of 500 μA/cm^2 (based on geometric surface area). The sweep was held once the potential reached −1.35 V. The electrochemical cell was then directly connected to the mass spectrometer by opening the valve (Figure 1) after evacuating the volume underneath the electrode.

In the following anodic going sweep the evolution of oxygen was observed in the MSCV. Oxygen evolution has an onset potential of −0.69 V and continues to proceed until the upper potential limit is reached with peaks at −0.46 V and 0.52 V respectively. Major amounts of oxygen are evolved at potentials more positive than 0.23 V paralleled by the evolution of a signal for mass 44 after the electrode was employed as a GDE electrode. In the following cycles in which oxygen is reduced from solution, most of the oxygen is evolved in a potential range from −0.7 to 0.0 V, while the signal intensity for mass 44 is reduced. Although NMP causes a high baseline for mass 44 due to a fragment formed during the ionization process, there is no reason why this baseline should be dependent on the potential applied to the

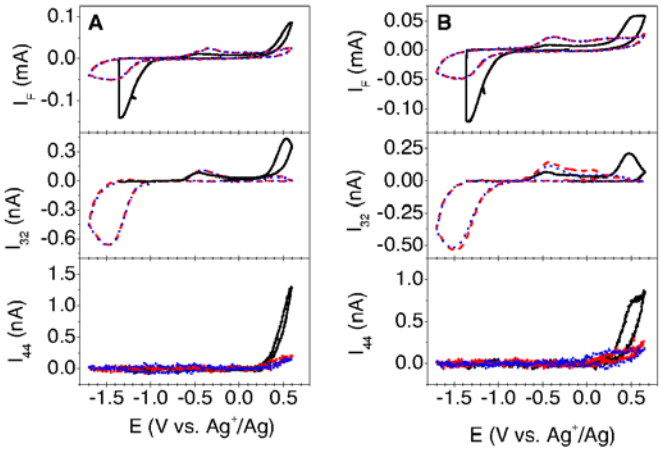

Figure 9. Simultaneously recorded CV and MSCVs for mass 32 and mass 44 during oxygen reduction and evolution at gas diffusion electrode (Au sputtered Teflon membrane) in 0.1 M $LiClO_4$-NMP based electrolyte containing (A) 60 and (B) 380 ppm of water. Oxygen source is atmospheric air in the first cathodic going sweep, electrolyte purged with oxygen. Sweep rate 10 mV/s. Black: 1st cycle, electrode was used as a GDE; Red and blue: 2nd and 3rd cycle, oxygen was supplied from solution.

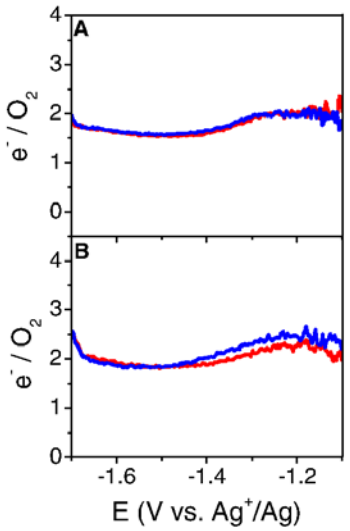

Figure 11. z-value of ORR as a function of potential in a NMP-$LiClO_4$ based electrolyte. The z-value has been calculated for the curves shown in Figure 9. A: Water content: 60 ppm, B: water content: 380 ppm. Colors are as indicated in Figure 9.

electrode. Hence the evolution of a signal for mass 44 is probably due to the formation of CO_2. But the only source of carbon in the system under investigation is NMP. Hence the evolution of CO_2 indicates the decomposition of the electrolyte.

Since there is no CO_2 evolution observable in the same potential range when the electrode is cycled in Ar-saturated electrolyte (c.f. Figure 10) and as with decreasing amounts of reduced oxygen in the previous cathodic sweeps there are also decreasing amounts of CO_2 evolved, there is clearly a connection between oxygen reduction and CO_2 evolution. As with DMSO, oxygen reduction proceeds via the transfer of 2 electrons per molecule of oxygen (c.f. Figure 11). Hence also here oxygen is reduced to peroxide. But as pointed out in the case of DMSO the formation of peroxide does not mean that it precipitates as lithium peroxide. In the case of NMP at least parts of the formed peroxide react with the electrolyte to form some compound that ultimately reacts to form CO_2 in the next anodic cycle at potentials above 0.1 V.

The black curves in Figure 12 show that the z-value in this potential region is 2 when the electrode was used as a gas diffusion electrode in the previous cathodic sweep. However in the same potential range 3 to 7 e^-/O_2 were transferred when oxygen was supplied to the electrode from solution. While a z-value of 2 fits nicely with the oxidation of peroxide a value of 3 or even 7 is much to large to assume oxygen evolution as the only source of faradaic current.

In Figure 12C the anodic sweeps of the CV already displayed in Figure 9A are shown in more detail. In the black curve the peak potential is at −0.46 V. But at this potential only a faint shoulder appears in the red and blue curves while the peak potential shifts by 120 mV to a less negative potential of –0.34 V. The corresponding

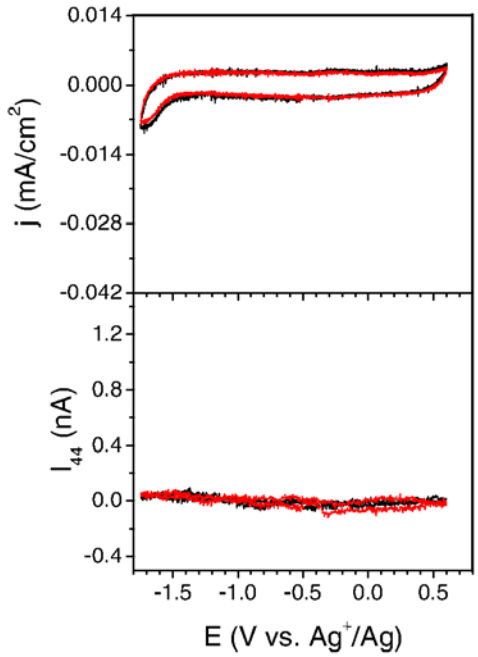

Figure 10. Simultaneously recorded CV and MSCV for mass 44 in Ar-saturated 0.1 M $LiClO_4$-NMP based electrolyte.

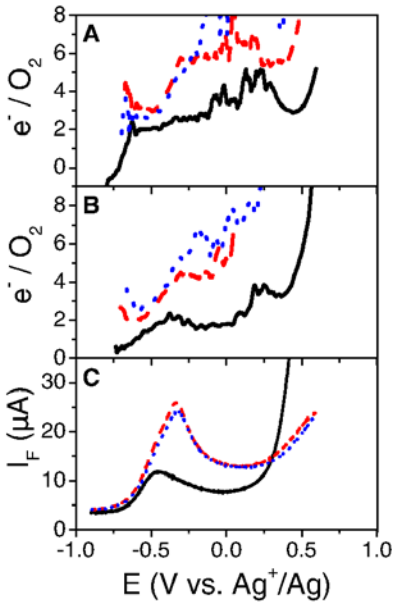

Figure 12. z-value of OER as a function of potential in a NMP-$LiClO_4$ based electrolyte. The z-value has been calculated for the curves shown in Figure 9. A: Water content: 60 ppm, B: water content: 380 ppm. C: expended faradaic current of Figure 9. Colors are as indicated in Figure 9.

shift of the peak potential in the MSCV for mass 32 is only 30 mV. Hence some other reaction appears in the anodic sweep unrelated to the OER when oxygen was reduced from solution in the previous cathodic sweep. This reaction is superimposed to peroxide oxidation and increases therefore the observed z-value significantly.

As pointed out already in the introduction there should not be any effect like pore clogging or diffusion effects in pores with the electrode employed in this experiment. Therefore whether the electrode is supplied with oxygen from solution or from the gas phase should not have any effect on the shape of the CV other than the observed current densities. However in those experiments where oxygen is reduced from the solution side, smaller quantities of peroxide are formed. If a stepwise degradation process of NMP is assumed then a lower concentration of peroxide might lead to the formation of other decomposition products than would be observed with larger peroxide concentrations. Large peroxide concentrations in NMP would then lead to decomposition products that are oxidized at potentials higher than 0.1 V to form CO_2, while lower peroxide concentrations lead to decomposition products that are electrooxidized at –0.34 V close to the potential of peroxide oxidation.

The evolution of oxygen in the second peak might be due to the oxidation of organic peroxides, but might also stem from lithium peroxide embedded and insulated from the electrode by a matrix of decomposition products. As this matrix is oxidized and removed from the electrode, the lithium peroxide regains electrical contact to the electrode and is oxidized as well. Despite the presence of lithium peroxide in the later case, electrocatalysis of electrolyte oxidation is improbable as CO_2-evolution causes lithium peroxide to regain contact with the electrode, rather than lithium peroxide in contact with the electrode causes CO_2-evolution.

Decomposition of NMP upon oxygen reduction has previously been found by Wang et al.[14] The mechanism the authors give is based on the abstraction of protons by superoxide and a subsequent oxidation both electrochemically and chemically by oxygen. However as we find no evidence for electrolyte decomposition upon oxygen reduction in NMP-$TBAClO_4$ based electrolyte this mechanism probably is not correct.

McCloskey et al. who have observed CO_2 evolution in NMP based electrolyte also used an electrode made of carbon for their experiments.[29] Therefore their assignment of CO_2-evolution to electrolyte oxidation is not beyond doubt, as the carbon-electrode is another probable source of CO_2 evolution. Furthermore McCloskey at el. suggested the electrooxidation of the electrolyte to be due to the defect states in the semiconductor Li_2O_2 resulting in an electrocatalytic effect. But in Figure 9A oxygen evolution from Li_2O_2 in contact with Au terminates before a potential of 0.1 V is reached. Hence no lithium peroxide with electronic contact to the electrode is left and no electrocatalytic effect due to defective states in Li_2O_2 is possible.

Figures 9A and 9B do not differ from each other significantly in shape. However the ratio of evolved to reduced oxygen is seemingly more favorable in the case of the electrolyte containing 380 ppm water. In those cycles of Figure 9B where oxygen is reduced from solution the ratio was on average 29% while in the electrolyte with a water content of only 60 ppm the ratio was on average 18.5%. On the other hand, when the electrode is used as a GDE then nearly the same faradaic charge is transferred but in the electrolyte with water content of 380 ppm only half the amount of oxygen is evolved than in the experiment with a water content of 60 ppm. We cannot give any explanation for this contradicting behavior, but we note that the presence of water seems to have some influence on oxygen reduction in NMP. To some extend this is not surprising as 60 ppm and 380 ppm of water content correspond to a water concentration of 3.4 and 21.7 mmol/l respectively. Both values are relatively high as compared to the solubility of oxygen in NMP, which is 3.2 mmol/l.[47] But on the other hand with a pk_a value of 31.2 of water on the Brodwell scale[48] and a virtually non-existing proton concentration the source of any effect of water is hard to imagine. A possible effect might result from the participation of water in the solvation sphere of the Li-ions.

Conclusions

The experiments show that under ambient conditions with humidity and in presence of CO_2, oxygen can be reduced from atmospheric air at a gold sputtered membrane used as a gas diffusion electrode. In this way we achieve very high current densities upon discharge of up to 0.53 mA/cm^2 in case of NMP and 0.97 mA/cm^2 in case of DMSO. However, the true coulombic efficiency of OER/ORR (as obtained from mass spectrometric ion currents) differs clearly from 100% and side reactions take place in both NMP and DMSO based electrolytes. Therefore, a cycleable and highly reversible secondary lithium-air battery with a DMSO based electrolyte is unlikely to work purely on the principle of reversible formation of lithium peroxide.

By employing in situ techniques we were able to confirm that in presence of Li^+-ions oxygen reduction results in the formation of peroxide in both DMSO and NMP. For DMSO it has been shown that 2 electrons per molecule of oxygen are transferred ranging from –1.1 to –1.6 V. No indications for the formation of Li_2O have been found.

We have found that superoxide is formed upon oxygen reduction in TBA containing electrolyte. This claim has previously been based only on kinetic considerations. The importance of this finding is that this reaction can be used in future studies to calibrate DEMS cells, where leakage calibration is not an option and a known reproducible electrochemical reaction is required.

It has been shown that NMP decomposes during the reduction of oxygen in the presence of Li^+. The decomposition is probably induced by peroxide and results in different decomposition products depending on the concentration of formed peroxide.

Acknowledgment

The authors acknowledge the Federal Ministry of Education and Research for funding this work. This work is part of the "LuLi – Strom aus Luft und Li" project (FKZ:03X4624A).

References

1. K. M. Abraham and Z. Jiang, *Journal of the Electrochemical Society*, **143**, 1 (1996).
2. P. G. Bruce, S. A. Freunberger, L. J. Hardwick, and J.-M. Tarascon, *Nature Materials*, **11**, 19 (2012).
3. S. R. Gowda, A. Brunet, G. M. Wallraff, and B. D. McCloskey, *The Journal of Physical Chemistry Letters*, **4**, 276 (2013).
4. B. D. McCloskey, D. S. Bethune, R. M. Shelby, G. Girishkumar, and A. C. Luntz, *The Journal of Physical Chemistry Letters*, **2**, 1161 (2011).
5. F. Mizuno, S. Nakanishi, Y. Kotani, S. Yokoishi, and H. Iba, *Electrochemistry*, **78**, 403 (2010).
6. K. Xu, *Chemical Reviews*, **104**, 4303 (2004).
7. H. Kim, G. Jeong, Y.-U. Kim, J.-H. Kim, C.-M. Park, and H.-J. Sohn, *Chemical Society Reviews*, **42**, 9011 (2013).
8. J. Read, *Journal of the Electrochemical Society*, **153**, A96 (2006).
9. H.-G. Jung, J. Hassoun, J.-B. Park, Y.-K. Sun, and B. Scrosati, *Nature Chemistry*, **4**, 579 (2012).
10. S. A. Freunberger, Y. Chen, N. E. Drewett, L. J. Hardwick, F. Barde, and P. G. Bruce, *Angewandte Chemie-International Edition*, **50**, 8609 (2011).
11. C. O. Laoire, S. Mukerjee, E. J. Plichta, M. A. Hendrickson, and K. M. Abraham, *Journal of the Electrochemical Society*, **158**, A302 (2011).
12. Z. Peng, S. A. Freunberger, Y. Chen, and P. G. Bruce, *Science*, **337**, 563 (2012).
13. M. J. Trahan, S. Mukerjee, E. J. Plichta, M. A. Hendrickson, and K. M. Abraham, *Journal of the Electrochemical Society*, **160**, A259 (2013).
14. H. Wang, K. Xie, L. Wang, and Y. Han, *Journal of Power Sources*, **219**, 263 (2012).
15. V. S. Bryantsev, V. Giordani, W. Walker, M. Blanco, S. Zecevic, K. Sasaki, J. Uddin, D. Addison, and G. V. Chase, *Journal of Physical Chemistry A*, **115**, 12399 (2011).
16. C. O. Laoire, S. Mukerjee, K. M. Abraham, E. J. Plichta, and M. A. Hendrickson, *Journal of Physical Chemistry C*, **114**, 9178 (2010).
17. W. Xu, J. Hu, M. H. Engelhard, S. A. Towne, J. S. Hardy, J. Xiao, J. Feng, M. Y. Hu, J. Zhang, F. Ding, M. E. Gross, and J.-G. Zhang, *Journal of Power Sources*, **215**, 240 (2012).
18. D. Xu, Z.-l. Wang, J.-j. Xu, L.-l. Zhang, L.-m. Wang, and X.-b. Zhang, *Chemical Communications*, **48**, 11674 (2012).
19. M. M. Ottakam Thotiyl, S. A. Freunberger, Z. Peng, Y. Chen, Z. Liu, and P. G. Bruce, *Nature Materials*, **12**, 1050 (2013).
20. A. A. Abd-El-Latif and H. Baltruschat, in *Encyclopedia of Applied Electrochemistry*, G. Kreysa, K.-i. Ota and R. Savinell Editors, p. 507 Springer New York Dordrecht Heidelberg London (2014).
21. G. Eggert and J. Heitbaum, *Electrochimica Acta*, **31**, 1443 (1986).

22. R. Imhof and P. Novak, *Journal of the Electrochemical Society*, **145**, 1081 (1998).
23. R. Imhof and P. Novak, *Journal of the Electrochemical Society*, **146**, 1702 (1999).
24. P. Novak, J. C. Panitz, F. Joho, M. Lanz, R. Imhof, and M. Coluccia, *Journal of Power Sources*, **90**, 52 (2000).
25. M. Hahn, A. Wursig, R. Gallay, P. Novak, and R. Kotz, *Electrochem. Commun.*, **7**, 925 (2005).
26. P. Novak, D. Goers, L. Hardwick, M. Holzapfel, W. Scheifele, J. Ufhiel, and A. Wursig, *Journal of Power Sources*, **146**, 15 (2005).
27. J. Ufheil, A. Wursig, O. D. Schneider, and P. Novak, *Electrochemistry Communications*, **7**, 1380 (2005).
28. T. Ogasawara, A. Débart, M. Holzapfel, P. Novák, and P. G. Bruce, *Journal of the American Chemical Society*, **128**, 1390 (2006).
29. B. D. McCloskey, D. S. Bethune, R. M. Shelby, T. Mori, R. Scheffler, A. Speidel, M. Sherwood, and A. C. Luntz, *The Journal of Physical Chemistry Letters*, **3**, 3043 (2012).
30. B. D. McCloskey, R. Scheffler, A. Speidel, G. Girishkumar, and A. C. Luntz, *Journal of Physical Chemistry C*, **116**, 23897 (2012).
31. C. J. Barile and A. A. Gewirth, *Journal of The Electrochemical Society*, **160**, A549 (2013).
32. N. Tsiouvaras, S. Meini, I. Buchberger, and H. A. Gasteiger, *Journal of the Electrochemical Society*, **160**, A471 (2013).
33. H. Baltruschat, in *Interfacial Electrochemistry*, A. Wieckowski Editor, p. 577 Marcel Dekker, Inc., New York, Basel (1999).
34. G. Gritzner, *Journal of Molecular Liquids*, **156**, 103.
35. S. J. Aston, Design, Construction and Research Application of a Differential Electrochemical Mass Spectrometer (DEMS), in *Department of Chemistry*, p. 224, University of Copenhagen, Copenhagen (2012).
36. R. Stadler, Z. Jusys, and H. Baltruschat, *Electrochimica Acta*, **47**, 4485 (2002).
37. T. Löffler, R. Bussar, E. Drbalkova, P. Janderka, and H. Baltruschat, *Electrochimica Acta*, **48**, 3829 (2003).
38. N. Fietkau, R. Bussar, and H. Baltruschat, *Electrochimica Acta*, **51**, 5626 (2006).
39. U. Müller and H. Baltruschat, *The Journal of Physical Chemistry B*, **104**, 5762 (2000).
40. T. Löffler, R. Bussar, X. Xiao, S. Ernst, and H. Baltruschat, *Journal of Electroanalytical Chemistry*, **629**, 1 (2009).
41. H. Baltruschat, *J. Am. Soc. Mass Spectrom.*, **15**, 1693 (2004).
42. D. Sharon, M. Afri, M. Noked, A. Garsuch, A. A. Frimer, and D. Aurbach, *The Journal of Physical Chemistry Letters*, **4**, 3115 (2013).
43. B. D. McCloskey, D. S. Bethune, R. M. Shelby, T. Mori, R. Scheffler, A. Speidel, M. Sherwood, and A. C. Luntz, *The Journal of Physical Chemistry Letters*, **3**, 3043.
44. I. Nicotera, C. Oliviero, W. A. Henderson, G. B. Appetecchi, and S. Passerini, *The Journal of Physical Chemistry B*, **109**, 22814 (2005).
45. R. Arvai, F. Toulgoat, B. R. Langlois, J.-Y. Sanchez, and M. Médebielle, *Tetrahedron*, **65**, 5361 (2009).
46. H.-K. Lim, H.-D. Lim, K.-Y. Park, D.-H. Seo, H. Gwon, J. Hong, W. A. Goddard, H. Kim, and K. Kang, *Journal of the American Chemical Society*, **135**, 9733 (2013).
47. J. Read, K. Mutolo, M. Ervin, W. Behl, J. Wolfenstine, A. Driedger, and D. Foster, *Journal of the Electrochemical Society*, **150**, A1351 (2003).
48. F. G. Bordwell, *Accounts of Chemical Research*, **21**, 456 (1988).

3. 3. Summary of Paper 1

In Paper 1 we have investigated the oxygen reduction in electrolytes that were based on NMP and DMSO and which contained either TBA or lithium cations. In both solvents oxygen reduction is highly reversible in the absence of lithium. Quantitative analysis showed that oxygen is converted to superoxide in the presence of TBA, which affirms previous studies [39, 40].

In the presence of lithium cations the reaction becomes irreversible, which has been assigned to the formation of Li_2O_2 in previous studies [39, 40]. Quantitative analysis shows that during oxygen reduction in lithium containing electrolytes 2 electrons per oxygen are transferred which affirms that Li_2O_2 is formed during oxygen reduction. However, in the present study we failed to observe the transition from an indirect to a direct mechanism of peroxide formation as proposed by Laoire *et al*. for lithium containing DMSO based electrolytes [40].

In both, DMSO and NMP based electrolytes, the true coulombic efficiency deviates from one. Based on this observation we challenged the results of Peng *et al*. [34] and pointed out inconsistencies in their report. This affirms the results presented by McCloskey *et al*. [35]. In the case of NMP sever electrolyte decomposition was observed. Because of this and NMPs damaging effect on polymers we did not intensified our studies on oxygen reduction in this solvent.

The most important aspect of the results presented in this study is the fact that our DEMS setup is easily employable to investigate oxygen reduction and oxygen evolution from organic electrolytes. That is, when the surface tension σ and the contact angle θ of the used electrolyte are large and the vapour pressure of the solvent small enough. In Paper 1 we show that it is possible with our DEMS setup to give the number of transferred electrons as a function of the applied potential. This has not been done in previous studies. Some minor problems occur because the continues influx of vapour of the organic electrolyte into the mass spectrometer causes a relatively rapid contamination of the ion source of the quadruple mass spectrometer with graphite, but the aging effect on the filament and the resulting effort in maintenance is justifiable. However, a more severe problem arises when two different electrolytes were used at the same DEMS-system. Due to some undefined cross contamination the CVs that were obtained in DMSO based electrolytes are different, when NMP was used within a time span of two weeks (*c.f*. Appendix A5). We do not understand the origin of this problem, but we believe that this is due to the adsorption of organic compounds in the vacuum system during one experiment, which then desorb in the next experiment. In any case, it is not possible to work with different electrolytes at the same time at one DEMS-system.

4. Paper 2 - Oxygen reduction and oxygen evolution in DMSO based electrolytes: the role of the electrolcatalyst

4. 1. Introduction to Paper 2

In the previous report (Paper 1) we employed the DEMS technique in combination with the traditional or conventional cell to investigate the oxygen reduction reaction in DMSO and NMP based electrolytes at gold sputtered Teflon membranes. In Paper 2 we employed the dual thin layer cell which allowed us to test the effect of the electrode material more effectively and which enabled us to apply defined convection conditions. As pointed out in Section 2.2. calibration is needed to correlate the ionic current to the faradic current. In the case of the dual thin layer cell this is difficult and impossible if there is no reaction with a known stoichiometry available. Therefore, the results presented in Paper 1 are crucial for the current study: Only the knowledge that oxygen is converted quantitatively to superoxide during oxygen reduction in TBA containing DMSO based electrolytes allowed us to calibrate the dual thin layer cell. Although it has been proposed previously that superoxide was formed under these conditions [39, 40], it was never shown that this reaction is quantitative. Hence, previously a_{eff} in Equation 7B was unknown (note that a_{eff} enters Equation 8 indirectly *via* Equation 6) which prohibited the use of this reaction for calibration of the dual thin layer cell.

4. 2. Oxygen reduction and oxygen evolution in DMSO based electrolytes: the role of the electrolcatalyst (as published in PCCP)

The version of record of Paper 2 as published Physical Chemistry Chemical Physics (PCCP) is shown in the following. It is the policy of PCCP that versions of record of articles can be used in Theses. Therefore, no special permission of the publisher is required to display the version of record in here. Any use of the material or content of the article shown below is permissible only after proper citation:

C. Bondue, P. Reinsberg, A.-E.-A. A. Abd-El-Latif and H. Baltruschat, *Physical Chemistry Chemical Physics*, 2015, 25593 - 25606.

PCCP

PAPER

View Article Online
View Journal | View Issue

Cite this: *Phys. Chem. Chem. Phys.*, 2015, 17, 25593

Oxygen reduction and oxygen evolution in DMSO based electrolytes: the role of the electrocatalyst†

C. J. Bondue,[a] P. Reinsberg,[a] A. A. Abd-El-Latif[ab] and H. Baltruschat*[a]

Received 24th July 2015,
Accepted 4th September 2015

DOI: 10.1039/c5cp04356e

www.rsc.org/pccp

In the present paper the role of the electrode material in oxygen reduction in DMSO based electrolytes is elucidated using DEMS. We have found, employing platinum, gold, ruthenium rhodium, selenium decorated rhodium and boron doped diamond (BDD) as electrode materials, that the actual mechanism of oxygen reduction largely depends on the electrode material. At platinum, rhodium and selenium decorated rhodium the final reduction product, peroxide, is formed electrochemically. At gold and at low overpotentials oxygen is reduced to superoxide and peroxide is only formed by disproportionation of the latter. No oxygen reduction takes place at the diamond surface of the BDD-electrode, hence, showing unambiguously that oxygen reduction is an inner sphere reaction. Also, the rate of oxygen evolution varies with the electrode material, although the onset potential of oxygen evolution is not influenced. The amount of peroxide formed is limited to 1–2 monolayers. Contrary to intuition oxygen reduction and oxygen evolution from peroxide, therefore, are heterogeneous, electrocatalytic reactions. The finding of such an electrocatalytic effect is of great importance for the development and optimization of lithium–air batteries. Aside from the electrode material there are also effects of water as well as of the cation used in the electrolyte. This suggests an influence of the double layer at the interface between the electrode and the electrolyte on oxygen reduction in addition to the well-known higher stability of Na_2O_2 and K_2O_2. Electrospray ionization (ESI) results show that any effect of water in the Li^+ containing electrolyte is not due to an altered solvation of the cation.

Introduction

In 1996 Abraham introduced the concept of lithium–air batteries with a theoretical specific energy density of 18.7 kJ g^{-1} based on the discharged battery and assuming Li_2O as the final discharge product.[1] Since then a lot of effort was put into research related to lithium–air batteries, mainly because the construction of a secondary battery with such capacities would certainly pose a large leap forward in electrifying automotive traffic.[2–5] It is established now that oxygen reduction in various organic electrolytes is not reduced to Li_2O but forms Li_2O_2 instead.[6–10] Discharge to Li_2O_2 reduces the theoretical capacity of the battery to 13.8 kJ g^{-1}. This was calculated from thermodynamic data.[11,12] Only 90.2% of that energy can be harnessed, while the remaining 10% are lost to entropic heat flow. Even though discharge to Li_2O_2 (instead of Li_2O) reduces the theoretical energy density of lithium–air batteries, they continue to attract attention.

In lithium–air batteries employing ether based electrolytes some authors described the formation of toroid shaped Li_2O_2 particles upon discharge at low current density, whereas no such particles were found when large current densities were applied.[13–15] However, under similar experimental conditions other authors did not observe the formation of toroid shaped particles.[15,16] Although it was recently suggested that the difference observed in the literature might be due to different water contents of the electrolyte, with water favouring the formation of toroid shaped particles, the growth mechanism of Li_2O_2 remains poorly understood.[17,18] A proposed mechanism involves the LiO_2 mediated dissolution and re-deposition of Li_2O_2 with water facilitating the formation of soluble LiO_2.[17] Others proposed the formation of LiO_2 as an intermediate of oxygen reduction that adsorbs with higher probability at certain sites where it is reduced.[19]

All model batteries reported in the literature so far suffer from large charging overpotentials. Because of that some authors employed precious metals[20–22] or transition metal oxides[23–25] in the oxygen electrode in order to reduce the charging potential. Given that the batteries in these studies employed carbonate based electrolytes the claimed catalytic effect is most probably due to the enhanced kinetics of oxidation of decomposition products rather than the enhanced kinetics of Li_2O_2 oxidation.[23,24]

[a] *Institut für Physikalische und Theoretische Chemie, Universität Bonn, Römerstraße 164, D-53117 Bonn, Germany. E-mail: baltruschat@uni-bonn.de*
[b] *National Research Centre, Physical Chemistry Department, El-Bohouth St. Dokki, 12311 Cairo, Egypt*

† Electronic supplementary information (ESI) available. See DOI: 10.1039/c5cp04356e

Nevertheless, the choice of electrode material for the gas diffusion electrode seems to have an effect on the cycleability of a lithium–oxygen battery. Marinaro *et al.* found that batteries employing an oxygen electrode made from gold sputtered Super-P could be cycled 5 times more often than a battery that featured an oxygen electrode without any gold coating. In addition Marinaro *et al.* found that the Au/Super-P electrode could sustain larger current densities upon discharge.[26] A similar superior performance of an Au/Super-P electrode over a Super-P electrode was found by the same group in a battery featuring a tetraglyme based electrolyte.[27]

Beside the construction of model batteries fundamental research on oxygen reduction has also been carried out.[7,10,17,22,28–36] It was found that the current density for oxygen reduction in ether based electrolytes depends on the electrode material. Lu *et al.* found a volcano like behaviour when the potential at which a given current density was observed is plotted against the binding energy of oxygen at the given electrode material.[22]

Laoire *et al.* reported on both the effect of cations and the effect of the solvent on oxygen reduction:[7,28] oxygen reduction leads to the formation of peroxide in the presence of hard and small cations like Li^+, while in electrolytes containing soft and large cations, such as TBA^+, oxygen is reduced to superoxide.[28] Lithium superoxide is known only in the argon matrix[37] and disproportionates to lithium peroxide and oxygen under ambient conditions. Therefore, it is not surprising that oxygen reduction in lithium containing electrolytes leads to the formation of Li_2O_2. The situation in the case of the somewhat larger Na^+ cation is less clear. Both NaO_2 and Na_2O_2 are metastable and known to exist. Laoire *et al.* proposed the formation of Na_2O_2 in an acetonitrile based and sodium containing electrolyte during oxygen reduction.[28] Also in some sodium oxygen batteries Na_2O_2 was found as the final discharge product,[38–40] while others convincingly showed the formation of NaO_2 under similar experimental conditions in their batteries.[41,42] So far it is entirely unknown under which conditions NaO_2 is formed and under which Na_2O_2.[42]

To understand when and why oxygen reduction results in Na_2O_2 it seems helpful to turn to Li_2O_2 where much knowledge is available on its formation process. There are two conceivable pathways to Li_2O_2: *via* an indirect pathway superoxide is formed electrochemically and then undergoes Li^+-induced disproportionation in the aftermath. *Via* a direct pathway oxygen accepts two electrons from the electrode and forms peroxide electrochemically. Indeed Laoire *et al.* found superoxide as an intermediate in a lithium containing DMSO based electrolyte[7] during oxygen reduction. However, no indication for superoxide was found in acetonitrile based electrolytes. Laoire *et al.* ascribed this difference to the higher donor number of DMSO of 125 kJ mol^{-1} [43] as compared to that of acetonitrile with 58.9 kJ mol^{-1} [43] allowing for a better solvation of Li^+ in DMSO and therefore for a longer lifetime of superoxide.[7] Also, others observed the formation of superoxide in DMSO based electrolytes: Cao *et al.* employing spin traps showed the presence of superoxide by means of EPR.[44] During RRDE experiments in Li^+-containing, DMSO based electrolytes positive currents were observed at the ring electrode that were ascribed to the oxidation of superoxide.[29,31] Based on the evaluation of CV data by the Nicholson and Shain relationship Laoire *et al.* proposed that at higher overpotentials peroxide is formed electrochemically while at lower overpotentials peroxide is formed indirectly by the disproportionation of superoxide.[7]

Experimental

Chemicals

All electrolytes were prepared in an MBraun glove box. During electrolyte preparation the humidity in the glove box atmosphere never exceeded 0.6 ppm. After preparation the electrolyte was kept in a sealed vessel and stored inside the glove box. The electrolyte was used within a time span of one week. The water content of the as-prepared electrolyte did not exceed 13 ppm (with the exception of the Mg^{2+} containing electrolyte, which had a water content of $\sim$50 ppm). During transfer the electrolyte gathered water in the single digit ppm-range.

Extra dry DMSO (99.7%, over molecular sieve, Acros Organics), $LiClO_4$ (battery grade, Sigma-Aldrich), highly pure lithium trifluoromethanesulfonate (LiTfO) (Sigma-Aldrich, $\geq$99.995%) acetic acid (KMF, 96%) and methanol (Fluka, 99.9%) were used as received. Sodium perchlorate (p.a., Fluka) and potassium perchlorate (99%, Sigma Aldrich) were dried at 180 °C under reduced pressure, while magnesium perchlorate (p.a. Sigma-Aldrich) was dried at 245 °C. Highly pure Ar (air liquid, 99.999%) was used for purging the electrolyte and highly pure nitrogen (air liquid, 99.9995%) was used as the auxiliary and sheath gas in ESI experiments to facilitie the evaporation of solvents. A custom made mixture of argon and oxygen ($Ar : O_2 = 80 : 20$) was obtained from air liquid.

A coulometric KF titrator (C20, Metler Toledo) with a diaphragm electrode was used to determine the water content. The sample was taken at the outlet of the dual thin layer cell, hence, giving the water content after the measurement was completed. According to the manufacturer of the used electrolyte, the accumulation of DMSO affects the chemistry involved in the detection process of water. The error was estimated by adding a water standard. The water contents given in this article already account for an error of up to 30%.

BDD-electrodes were purchased from Adamant La-Chaux-de-Fonds, Switzerland. The electrode consisted of a layer of 1 μm diamond doped with 6000 ppm boron on a 1 mm thick silicon wafer.

Dual thin layer cell

In the dual thin layer cell the electrolyte flows into the first compartment where the working electrode is placed. Reaction products are flushed along with the electrolyte into the second compartment where a porous Teflon membrane is pressed on a steel frit. Volatile reaction products evaporate through the Teflon membrane into the vacuum of the mass spectrometer. The electrolyte is then flushed to the outlet. The flow of the electrolyte from the upper to the lower compartment causes a

delay between the faradaic current and the response in the ionic current. In all calculations where the ionic current was correlated with processes appearing at the working electrode this delay time was accounted for.

The reference electrode is placed at the inlet. The main counter electrode is placed at the outlet. In order to reduce electronic oscillations, a second counter electrode is placed at the inlet. The main counter electrode is connected *via* a resistance of 1 Ω, the second *via* a 1 MΩ resistance to ascertain an optimal distribution of the current.

A more detailed description of the dual thin layer cell along with its versatile applications for DEMS can be found elsewhere.[45–49]

Calibration for O_2

In order to correlate the ionic current observed by mass spectroscopy with the faradaic current calibration is required. To account for the collection efficiency of the dual thin layer cell electrochemical calibration with a reaction of known stoichiometry is required.

Calibration was done on the same day as the experiment by reducing oxygen from an electrolyte of 0.5 M $KClO_4$ in DMSO where at low overpotentials superoxide is formed. This potential region was identified by comparing the results to oxygen reduction in an electrolyte of 0.5 M $TBAClO_4$ in DMSO, where oxygen reduction is known to proceed *via* the formation of superoxide.[7,28,50] We avoided calibration with $TBAClO_4$ in order to reduce costs and errors. The latter arise when the used $TBAClO_4$ contains impurities, noticeable by electrochemical side reactions at potentials close to the onset potential of oxygen reduction. The extent of impurities seems to depend on the manufacturer and the charge.

Reference electrode

The reference electrode used in this study was a silver wire immersed in a solution of 0.1 M $AgNO_3$ in DMSO. Electrolyte contact to the working electrode was achieved by filling a Teflon tube with the silver containing solution and sealing it with a rough glass bead. The end with the glass bead was immersed into the working electrolyte, while the other open end was immersed into the silver containing solution. A drawing of the reference can be found elsewhere.[50]

According to the values given by Gritzner *et al.*[51] the reference electrode described above has a potential of +3.89 V with respect to the Li^+/Li couple.

Determination of the roughness factor and electrode preparation

Prior to the experiment in the organic electrolyte all electrodes were cycled in deaerated 0.5 M sulphuric acid until no changes in the CV were observed. From these CVs the roughness factor (RF) of the gold electrodes was determined by integrating the region of oxide formation in the potential range from 1.36 to 1.78 V (*vs.* RHE) following the method described by Trasatti and Petrii.[52] The roughness factor of the platinum electrodes was determined by integrating the current due to H-upd in the potential region from 0.07 to 0.35 V (*vs.* RHE), in which 77% of a monolayer are formed.[52] Also for rhodium the true surface area was determined from the charge due to H-upd (0.25 V to 0.0 V).[53] The true surface area of the ruthenium electrode was determined following the method described by Nagel *et al.* from the charge due to the dissolution of a monolayer of copper.[54] Given that there is no easy approach to determine the true surface area of the other electrode materials (glassy carbon, boron-doped diamond (BDD)) all current densities are given with respect to the exposed geometric surface area of 0.283 cm^2.

The Au(111)-electrode was prepared by the method described by Clavilier *et al.*[55] for platinum single crystals. The Au(111) single crystal was flame annealed and was allowed to cool down to room temperature in an argon atmosphere. The crystallinity of the surface was checked by recording a CV in 0.5 M sulphuric acid. Before transferring the gold crystal to the dual thin layer cell the electrode was rinsed with water. Droplets of water attached to the crystal were carefully removed by a lint-free laboratory wipe.

Prior to selenium deposition the rhodium electrode was flame annealed and was allowed to cool down in an atmosphere of argon and hydrogen (approximately 20% H_2) in order to remove any surface oxide. This electrode then was transferred with a droplet of H_2-saturated water attached to its surface to a cell, where selenium was deposited by a potential sweep to 0.6 V (*vs.* RHE) in an electrolyte of 0.1 M $HClO_4$ containing 10^{-3} M SeO_2.[56] From the charge passed during Se-deposition, and assuming that per Se 4 electrons are passed, the surface coverage of selenium was determined to be 0.72 ML (1 ML (=mono layer) is defined here as one Se-atom per Rh-surface atom).

Some reactions were shown to be sensitive to the surface termination of the BDD-electrode.[57] Therefore, in the present study experiments at the BDD-electrode were performed both with oxygen and hydrogen terminated surfaces. In order to prepare an oxygen terminated BDD-surface (BDD_{ox}) the electrode was swept to 2.5 V *versus* RHE in 0.5 M H_2SO_4 and was kept there for at least 10 minutes. The hydrogen terminated surface (BDD_{red}) was prepared by the polarisation of the electrode to −1 V *versus* RHE in 0.5 M H_2SO_4 for at least 10 minutes.

ESI measurements

ESI-MS measurements were performed in the positive electrospray ionization mode on a Finnigan MAT SSQ7000 instrument at 4.5 kV and a capillary temperature of 250 °C. The sample solution in the gas-tight syringe (Hamilton) was introduced into the ESI system *via* a 125 μm inner diameter PEEK tube at a flow rate 20 μL min^{-1} using a syringe pump (Syringe Infusion Pump 22, Harvard Apparatus, Inc., Cambridge, MA).

Results and discussion

Oxygen evolution

We have investigated the electrochemistry of oxygen reduction and oxygen evolution in an electrolyte of 0.5 M $LiClO_4$ in DMSO

at a variety of electrode materials. Prior to the evolution of any oxygen in the anodic sweep, Li_2O_2 must be deposited on the electrode in a preceding cathodic sweep. However, for a better flow of reading we choose to discuss the oxygen evolution first. Fig. 1 shows the CV and MSCV for masses 32 and 44 at those materials with the most striking differences in the potential region of oxygen evolution: gold and platinum. From the experiment shown in Fig. 1 and all other DEMS experiments discussed in this report several cycles were recorded. More than one cycle is only observed when differences appeared. In the measurements of Fig. 1 this was not the case. In order to achieve a large response, especially in the MSCV for mass 32 during oxygen evolution, electrodes with a relatively high roughness factor were used (Pt: RF = 5.5; Au: RF ~ 3). Fig. 2 shows the CV and MSCV for masses 32 and 44 obtained under the same experimental conditions as those in Fig. 1 at rhodium, ruthenium and glassy carbon.

It is clear, both from the CV and the MSCV for mass 32, that oxygen evolution takes place in two distinguishable waves at the gold electrode. This is different at the platinum electrode where oxygen evolution proceeds in a single peak. Indeed among the

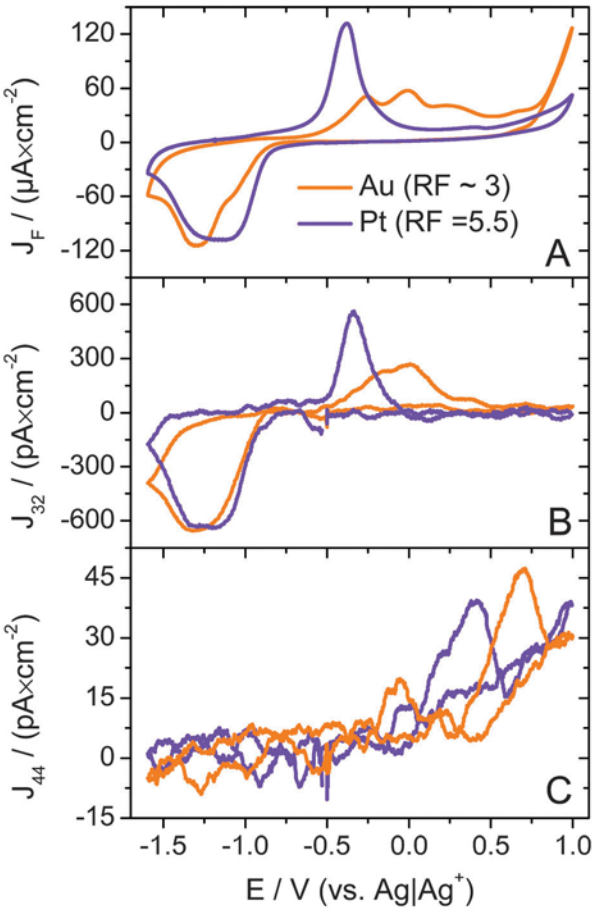

Fig. 1 1st CV (A) and 1st MSCV for mass 32 (B) and mass 44 (C) in an electrolyte of 0.5 M $LiClO_4$ in DMSO purged with a mixture of argon and oxygen (Ar : O_2 = 80 : 20); sweep rate: 10 mV s^{-1}; flow rate: 5 μL s^{-1}; orange: at a gold electrode (RF ~ 3); purple: at a platinum electrode (RF = 5.5). Current densities are given with respect to the geometric surface area.

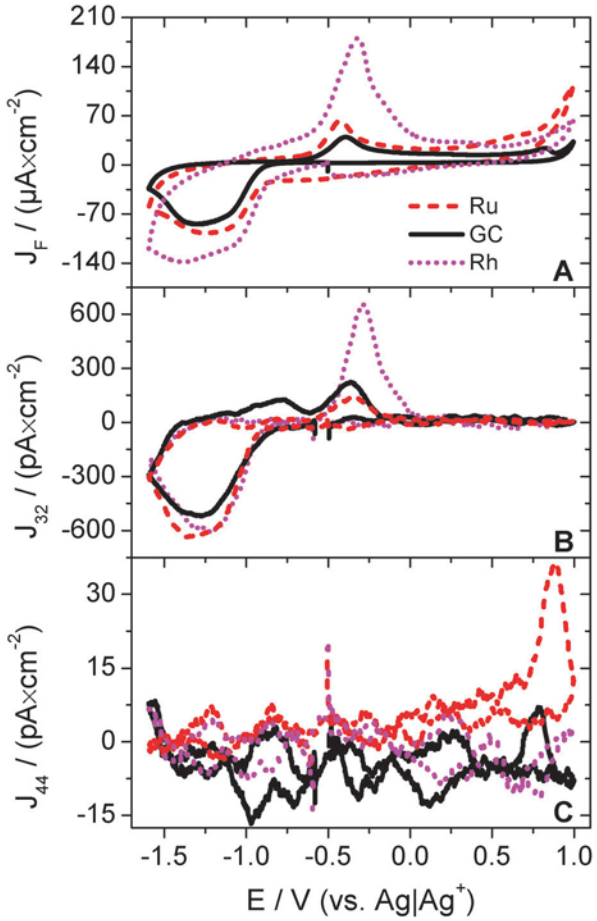

Fig. 2 1st CV (A) and 1st MSCV for mass 32 (B) and mass 44 (C) in an electrolyte of 0.5 M $LiClO_4$ in DMSO purged with a mixture of argon and oxygen (Ar : O_2 = 80 : 20); sweep rate: 10 mV s^{-1}; flow rate: 5 μL s^{-1}; red/dashed: at a ruthenium electrode; magenta/dotted: at a rhodium electrode; black/solid: at a glassy carbon electrode. Current densities are given with respect to the geometric surface area.

electrode materials under investigation the gold electrode is unique in this regard as Fig. 2 shows. The current density, based on the real surface area, at the peak potential of −0.4 V is 24 μA cm^{-2} at the platinum electrode. At the gold electrode the largest current density of 17 μA cm^{-2} is observed at −0.25 V. Not only is the current density at platinum higher than that at the gold electrode, but it is also achieved at a lower overpotential. There are 2.2 nmol cm^{-2} platinum atoms and 2.5 nmol cm^{-2} gold atoms in the surface of the respective electrodes. From that we calculate a Li_2O_2 coverage of 1 ML at the platinum electrode and of 2 ML on the gold electrode. (In a previous report we have determined 3 monolayers of Li_2O_2 from the amount of reduced oxygen, however, from the amount of evolved oxygen, a coverage of only 1.7 monolayer is calculated (*cf.* Table 1).[50]) The appearance of two distinguishable peaks in the potential region of oxygen evolution at gold suggests that the first monolayer of Li_2O_2 is thermodynamically more stable than the second. Different from what was proposed by Albertus *et al.*,[58] the charge transfer is not limited by the resistance of Li_2O_2 since oxygen evolution is the reaction of a mono- or biatomic surface

Table 1 Amounts of reduced and evolved oxygen at various electrode materials, calculated from the ionic charge for mass 32 (Q_{32}). All values are given with respect to the true surface area. From these values the true coulombic efficiency was calculated. From the amount of evolved oxygen the surface coverage of Li_2O_2 in terms of monolayers (MLs) deposited on the electrode was determined

	$n(O_2)_{ORR}$/(nmol cm^{-2}) (Q_{32}/pC cm^{-2})	$n(O_2)_{OER}$/(nmol cm^{-2}) (Q_{32}/pC cm^{-2})	$n(O_2)_{OER}/n(O_2)_{ORR}$	RF	$\theta(Li_2O_2)$/(ML)
Gold (ref. 50)	6.8[a] (3738)[a]	4.2[a] (2311)[a]	0.62	10	1.7
Gold (RF ~ 3)	12.2 (11 728)	4.9 (4750)	0.41	3	2.0
Gold (RF ~ 1)	21.6 (20 830)	4.4 (4286)	0.21	1	1.8
Gold (Au(111))	18.2 (17 561)	7.2 (6978)	0.40	1	2.9
Platinum (RF = 5.5)	5.6 (5430)	2.3 (2183)	0.40	5.5	1.0
Platinum (RF = 1.7)	10.3 (9929)	2.8 (2708)	0.27	1.7	1.3
Rhodium	2.8 (2680)	1.5 (1465)	0.55	10.8	0.6
Rh/Se	2.9 (2764)	1.0 (993)	0.36	10.8 (θ_{Se} = 0.72)	0.4
Ruthenium	25.2 (24 310)	4.2 (4089)	0.17	1.15	2.0
Glassy carbon	32.7[b] (31 501[b])	4.4[b] (4226[b])	0.13		

[a] Values determined from the curves shown in ref. 50. [b] With respect to the geometric surface area of 0.283 cm^2.

layer of Li_2O_2. The different kinetics at the different electrodes clearly indicates a catalytic effect on the charge transfer. However, none of the electrode materials under review have an effect on the onset potential of oxygen evolution which is at −0.67 V.

In order to gain a better understanding on why oxygen evolution at a gold electrode is different from that on other electrode materials we repeated the experiment with an Au(111) single crystal. The resulting CVs and MSCVs are shown in Fig. 3. Qualitatively the region of oxygen reduction is not different from that obtained at a polycrystalline electrode. The roughness factor of a single crystal is one. Hence, less Li_2O_2 is deposited on the electrode and the electrode is deactivated at lower overpotentials than at the rough electrode. However, the region of oxygen evolution is different from that in Fig. 1. In the first anodic sweep at the single crystal two peaks are present. Because of the bad signal to noise level in the MSCV for mass 32 it is not clear whether both peaks are connected to oxygen evolution. After the electrode was polarised to a potential, where roughening occurs, changes appeared in the CV. In the region of oxygen evolution three peaks appear with the third peak at 0.15 V. Except for the third peak which is much more pronounced, the CV for the second sweep at the single crystal resembles that of the rough electrode. The changes observed in the CV in the potential region of oxygen evolution when the surface of the electrode is roughened suggest a strong interaction between the gold surface and the deposited Li_2O_2. This would explain why a portion of Li_2O_2 appears to be thermodynamically more stable which was already pointed out for the polycrystalline gold electrode. However, much work on that issue is required to ensure the interpretation presented herein.

We consider glassy carbon as a model material for carbon black, which is used to manufacture gas diffusion electrodes in model lithium–air batteries. Even though oxygen evolution at glassy carbon proceeds with a low current density (note that only 4.38 nmol cm^{-2} of oxygen are evolved from that electrode) the overpotential is low. Thus, glassy carbon has reasonable activity for oxygen evolution. The difference between the onset potential for oxygen reduction and for oxygen evolution amounts only to 0.4 V (Fig. 2). Therefore, it seems unlikely that the lack of activity for Li_2O_2 oxidation of the carbon black substrate causes the high charging overpotentials observed in the literature.[15]

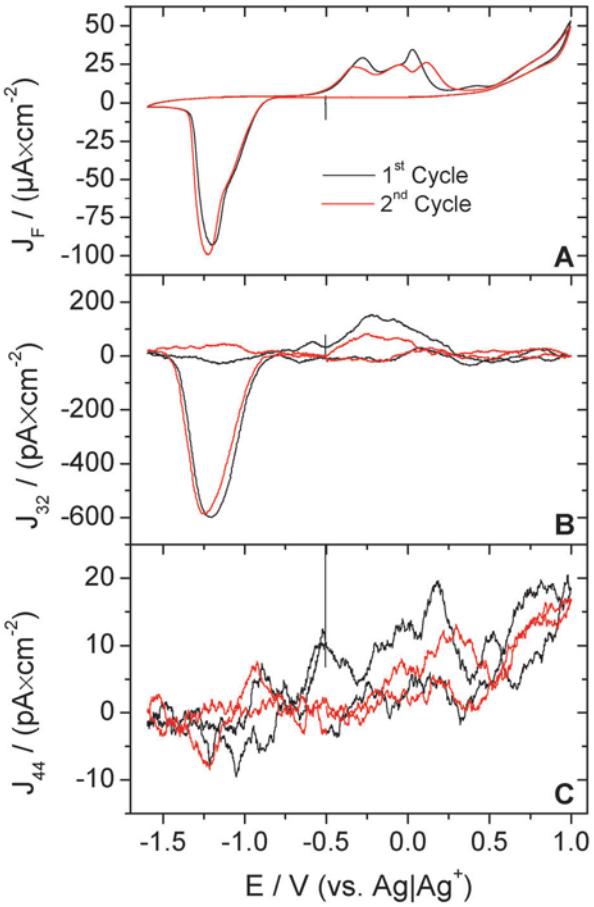

Fig. 3 CV (A) and MSCV for mass 32 (B) and mass 44 (C) in an electrolyte of 0.5 M $LiClO_4$ in DMSO purged with a mixture of argon and oxygen (Ar : O_2 = 80 : 20); sweep rate: 10 mV s^{-1}; flow rate: 5 μL s^{-1}; electrode: Au(111) single crystal. Current densities are given with respect to the geometric surface area.

It has been shown several times before that the true coulombic efficiency of oxygen reduction (*e.g.* the ratio of reduced to evolved oxygen) significantly deviates from 100%.[10,35,50]

Table 1 lists the amounts of reduced and evolved oxygen and the corresponding true coulombic efficiency (defined as the ratio of the amount of evolved to reduced oxygen) at various electrode materials with various roughness factors. At no electrode material the true coulombic efficiency is even close to 100%. In the present study this is to some degree due to convection that removes superoxide (*vide infra*) from the electrode. Therefore, the corresponding amount of oxygen is not available for oxygen evolution in the anodic sweep. But even with the rhodium electrode where oxygen reduction nearly entirely precedes *via* the direct electrochemical formation of peroxide the true electrochemical reversibility remains below 60% (*vide infra*). In addition Table 1 lists the surface coverage of lithium peroxide which was calculated from the amount of evolved oxygen. These values show that only very limited amounts of oxygen are deposited on the electrode and that the maximum surface coverage of Li_2O_2 depends on the electrode material. However, we cannot give any explanation at this point why gold and ruthenium allow the formation of 2 ML of Li_2O_2, whereas at platinum only one and at rhodium a submonolayer is deposited.

At all electrode materials under consideration there is a signal in the MSCV for mass 44. This signal is most probably due to CO_2 evolution. With the exception of the experiments done with the glassy carbon electrode there is no other source of carbon except for DMSO. Hence, the evolution of CO_2 is indicative for electrolyte decomposition. McCloskey *et al.* have proposed for DMSO and other solvents that CO_2 evolution is due to a parasitic reaction of Li_2O_2 with the solvent.[10] Although the signal intensity of the ionic current for mass 44 varies with the electrode material – there is hardly any CO_2 evolution at ruthenium and rhodium but a clear signal at the remaining electrode materials – CO_2 is probably not the result of mere electrooxidation of the electrolyte.

The decomposition of the electrolyte consumes a portion of the reduced oxygen. Hence, there is a deviation of the true coulombic efficiency from 100%. Therefore, we consider it important, to look for new electrolytes that are stable against the exposure to peroxide.

Influence of the electrode material on oxygen reduction

Since the ionic current for mass 32 is proportional to the amount of consumed and evolved oxygen per time and the faradic current is proportional to the conversion rate of oxygen times the number of transferred electrons (z) it is possible to calculate z from the ratio of I_F and I_{32} according to eqn (1).

$$z = \frac{I_F}{I_{32}} \cdot K^* \qquad (1)$$

where K^* is a calibration constant obtained in a separate experiment. In order to calculate accurate z-values I_F was corrected for the double layer charging by subtracting a straight line. Both, double layer charging and side reactions, would alter the calculated z-value.

Fig. 4 shows the number of electrons that is transferred per molecule of oxygen during oxygen reduction at various

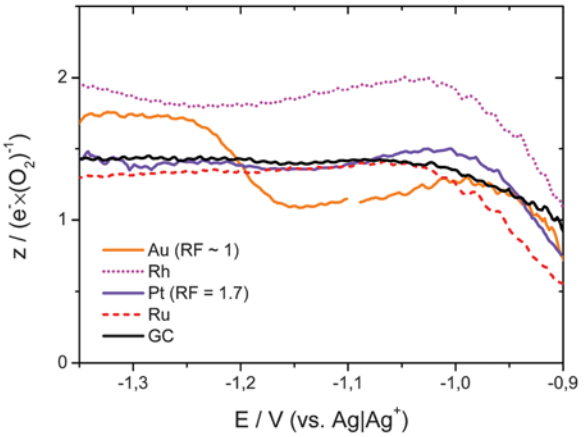

Fig. 4 Number of electrons (z) that is transferred per molecule of oxygen in the potential region of oxygen reduction at various electrode materials. Electrolyte: 0.5 M $LiClO_4$ in DMSO; sweep rate: 10 mV s^{-1}; flow rate: 5 µL s^{-1}.

electrode materials. At a gold electrode z initially has a value of approximately $1e^-$ per O_2. From that we conclude that at low overpotetentials superoxide is formed upon oxygen reduction. Although superoxide is unstable in the presence of Li^+ and disproportionates to peroxide and oxygen, this reaction is relatively slow, as no appreciable amount of superoxide has disproportionated in the time it takes (approximately 2 seconds) to transport it from the upper compartment of the dual thin layer cell to the lower compartment. (O_2 thus formed leads to a diminution of the amount of consumed O_2 and thus to an increase of z). The long lifetime of superoxide in DMSO was assigned to the high donor number of 125 kJ mol^{-1},[43] enabling the solvent to stabilise Li^+.[7] At −1.2 V the mechanism of oxygen reduction changes from an indirect pathway to a direct pathway of peroxide formation. This is indicated by the change in the z-value from approximately $1e^-$ per O_2 to approximately $2e^-$ per O_2. Qualitatively, this is also visible from the shoulder in the CV for the Au-surfaces in Fig. 1 and 3, which does not appear in the MSCVs.

Comparison of the z-values observed at the gold electrode to the z-values observed at other electrode materials under review reveals that such a change from the indirect to the direct pathway of peroxide formation proceeds only at gold. The difference to the rhodium electrode is most striking. At this electrode oxygen reduction proceeds *via* the transfer of $2e^-$ per O_2 throughout the whole potential region of oxygen reduction, whereas the indirect pathway *via* superoxide formation is of little significance.

At platinum, ruthenium and glassy carbon electrodes the transfer of about $1.5e^-$ per O_2 is observed during oxygen reduction. It seems that at these electrodes both pathways of peroxide formation, the direct and the indirect, are in place at all potentials, so that roughly half the oxygen is reduced to superoxide and the other half forms peroxide.

Eqn (1) from which the z-values in Fig. 4 were calculated only holds when there is no electrochemical side reaction in the potential region of oxygen reduction. In order to rule out any such side reaction CVs were recorded in an argon saturated

electrolyte of 0.5 M $LiClO_4$ in DMSO at all electrode materials under review. No such side reaction was observed. However, especially at rhodium electrodes a surface oxide might form in an oxygen containing electrolyte, whereas this reaction does not necessarily occur in an argon saturated electrolyte. Pseudocapacitances due to the reduction of such a surface oxide would significantly alter the observed *z*-values. For that reason oxygen reduction was also examined at a selenium decorated polycrystalline rhodium electrode. The corresponding CVs and MSCVs are shown in Fig. S1 (ESI†). It was shown previously that transition metal surfaces modified with chalcogenides have enhanced stability and are less likely to form a surface oxide.[59–61] Therefore, in the potential region of oxygen reduction no contribution to the current due to pseudocapacities is expected, when a selenium modified rhodium is used as a working electrode.

Fig. 5 displays the *z*-values obtained at a Se-modified rhodium electrode as a function of potential. There are little differences before (2nd and 4th cycles) and after (5th cycle) Se stripping. In Fig. 5 oxygen reduction proceeds *via* the transfer of $2e^-$ per O_2 as already observed at the unmodified rhodium electrode. Since pseudocapacities due to the reduction of a surface oxide are unlikely to contribute to the current observed in the potential region of oxygen reduction at a selenium modified electrode, it is also unlikely that the observed *z*-values are distorted by any side reaction.

In aqueous electrolytes platinum is the most active material for the oxygen reduction reaction among all metals. In addition oxygen reduction at Pt electrodes results nearly exclusively in the formation of water, when the reaction is conducted in acid electrolytes.[62,63] For that reason it seems strange that oxygen reduction in DMSO based electrolytes does not proceed exclusively *via* the direct pathway of peroxide formation, as observed at the rhodium electrode.

Fig. 6 compares the *z*-values observed at a Pt-electrode with a roughness factor of 1.7 (already included in Fig. 4) with those

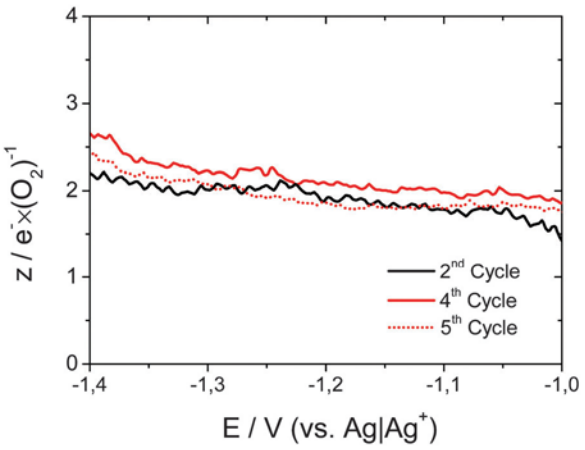

Fig. 5 *z*-values during oxygen reduction obtained at a rhodium electrode modified with approximately 0.72 ML of Se. The values were calculated according to eqn (1) from the curves shown in Fig. S1 (ESI†). Black: before Se stripping; red: after Se-stripping.

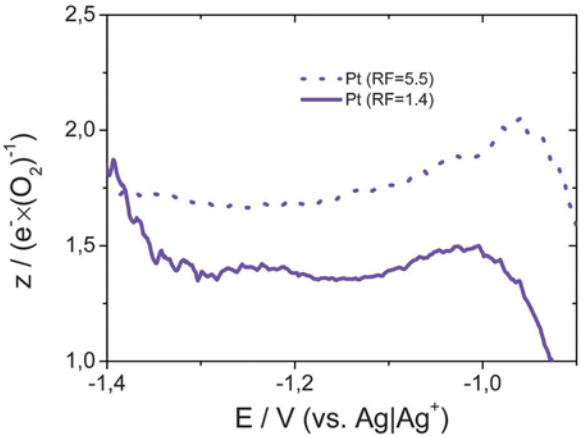

Fig. 6 Number of electrons (*z*) that is transferred per molecule of oxygen in the potential region of oxygen reduction at a platinum electrode. Dotted: with a roughness factor of 5.5; solid: with a roughness factor of 1.7; electrolyte: 0.5 M $LiClO_4$ in DMSO; sweep rate: 10 mV s^{-1}; flow rate: 5 µL s^{-1}.

observed at a Pt-electrode with a roughness factor of 5.5. From Fig. 6 it becomes clear that the roughness factor has an influence on the observed *z*-values. At the rough Pt-electrode more electrons are transferred per oxygen than at the smooth electrode throughout the entire potential region of oxygen reduction. The difference is most pronounced in the potential range between −0.9 V and −1.0 V, where at both electrodes a peak appears. The increased portion of oxygen that is reduced to peroxide at the rough electrode as compared to the smooth electrode is in accordance with the increased coloumbic efficiency (*cf.* Table 1).

This peak is not very distinct at the smooth electrode but at the rough electrode *z* increases to $2e^-$ per O_2 in a small potential range. During oxygen reduction Li_2O_2 is deposited on the surface of the electrode. Increasing the roughness changes the ratio of the portion of the surface that is not covered with Li_2O_2 to the portion of the surface that is blocked already. Therefore, a larger portion of the surface of the rough electrode is still not covered by Li_2O_2 than that of the smooth electrode at any given potential.

The fact that more electrons per oxygen are transferred when the electrode is relatively free of any deposit (low overpotentials and high roughness) than when it is covered to a large degree by Li_2O_2 (large overpotentials low roughness) points to the poisoning of the electrode as Li_2O_2 precipitates. The impact of a deposit on the *z*-value is not simply due to a blocking of the electrode (although blocking of the electrode also occurs). In this case less oxygen would be reduced and the reduction current would drop correspondingly, hence, leaving the observed *z*-value unaffected. However, the deposition of Li_2O_2 on a Pt-electrode reduces the ability of the latter to reduce oxygen *via* the direct pathway of peroxide formation, while the ability to form superoxide is maintained.

As shown above, the deposition of 1 ML Li_2O_2 (here a ML is defined as a unit of Li_2O_2 per surface atom) blocks the Pt-electrode entirely. Hence, there is no oxygen reduction taking place at those parts of the surface that are covered by Li_2O_2.

Consequently the increasing degree of superoxide formation with an increasing degree of surface coverage is not due to the change of the reaction site.

The catalytic performance of an electrode may be altered by an adlayer in three different ways: by a bifunctional mechanism, by a ligand-effect or by a geometric effect.[64] It is rather unlikely that an insulator exerts a ligand-effect. A bifunctional mechanism is expected when two intermediates adsorbed at the surface of the electrode react. Such a mechanism is hard to imagine as intermediates other than reduced oxygen species are not expected to be of any importance for the oxygen reduction reaction in organic electrolytes. However, Li_2O_2 might exert a geometric effect, when more than one surface atom of the Pt-electrode is required in order to form peroxide *via* the direct pathway.

Working in aqueous electrolytes, Adžić and Wang showed that oxygen reduction at Pt(111) electrodes is inhibited by Ag-adatoms.[65] From that they concluded that oxygen adsorption at bridge sites precedes oxygen reduction. Furthermore they concluded that prior to the $4e^-$-reduction the oxygen–oxygen bond is disrupted. Similarly in organic electrolytes the $2e^-$-reduction at polycrystalline platinum electrodes could require the weakening of the oxygen–oxygen bond by adsorption in a bridge position.

From a fundamental point of view it is interesting to note that oxygen reduction does not proceed *via* a $4e^-$-process at platinum electrodes in DMSO based electrolytes: There is abundant experimental proof that oxygen is reduced to water when aqueous electrolytes are employed.[62,63] Indeed, for aqueous systems the cleavage of the O–O bond is expected at surfaces that strongly bind oxygen, such as platinum, while a $2e^-$-process is observed at weakly oxygen-binding surfaces such as Au(111)[66] and on partially blocked Pt-surfaces.[65] Also, McCloskey *et al.* observed that increasing amounts of CO_2 were evolved when recharging a Li–O_2 battery that employed a DME based electrolyte, when instead of a gold or carbon electrode a platinum containing electrode was used.[67] The formation of CO_2 involves at some point the cleavage of the O–O-bond. However, it is not clear whether cleavage of the bond occurs during discharge or charge (*e.g.* the cleavage could occur during oxidation of an organic peroxide that favourably forms at platinum electrodes during oxygen reduction).

Notwithstanding this, we do not observe the cleavage of the O–O-bond (except for the evolution of minor quantities of CO_2) regardless of the electrode material. However, oxygen reduction in DMSO based electrolytes shows some parallels to oxygen reduction in aqueous solution if the direct pathway of peroxide formation is considered the organic analogue of the $4e^-$-process. Platinum catalyses in aqueous electrolytes predominantly the formation of water,[62,63] but shows sensitivity towards adlayers and impurities, which tilt product distribution towards hydrogen peroxide formation.[65,68–70] Similarly oxygen reduction in DMSO based electrolytes at platinum proceeds initially by the direct pathway of peroxide formation. However, as the electrode is increasingly covered with Li_2O_2 the indirect pathway of peroxide formation gains importance. At gold electrodes in aqueous solution hydrogen peroxide is the dominant product of oxygen reduction,[71,72] whereas only superoxide is formed at low overpotentials in DMSO based electrolytes. Therefore, we wonder whether the same mechanisms and parameters that sustain the $4e^-$-process in aqueous electrolytes are also at work in order to foster the direct pathway of peroxide formation.

Irrespective of the detailed mechanism of oxygen reduction at platinum, it is clear that the nature of the surface plays a crucial role in oxygen reduction. This is not only clear from what we believe to be a geometric effect of the Li_2O_2 deposit on the platinum electrode that tilts the mechanism of oxygen reduction away from the direct to the indirect pathway. Fig. 4 shows that there is a more general influence of the electrode material: while at gold and at low overpotentials oxygen is reduced to superoxide, peroxide is formed at rhodium.

It is rather unexpected to observe an electrocatalytic effect of the electrode material on the oxygen reduction reaction in organic electrolytes. The oxygen reduction reaction in DMSO proceeds without the disruption of the oxygen–oxygen bond and very close to the thermodynamic potential of Li_2O_2-formation (onset of oxygen reduction: −0.88 V; thermodynamic potential of peroxide formation *versus* Ag/Ag^+: −0.79 V[7,51]). Therefore, we expected the oxygen reduction reaction to be an outer sphere reaction. At least for the direct pathway of peroxide formation this is clearly not the case, where the influence of the electrode material suggests an inner sphere reaction.

Our finding of an electrocatalytic effect of the electrode material is supported by the findings of Lu *et al.*[22] These authors found a volcano like behaviour, when they plotted the potential, at which a certain current density was observed, against the adsorption enthalpy of oxygen at the used electrode material.

Fig. 7 shows the CV and MSCVs for mass 32 in an electrolyte of 0.5 M $LiClO_4$ in DMSO at hydrogen terminated BDD-electrodes. The current density at BDD_{red} reduces from cycle to cycle while the CV at BDD_{ox} (Fig. S2, ESI†) remains relatively constant and resembles that obtained in the third cycle at BDD_{red}. This observation might be due to the oxidation of the BDD_{red}-electrode at high potentials. Both at BDD_{red} and BDD_{ox} oxygen reduction takes place at −0.9 V at the same potential as with the other electrode materials. However, the observed current densities at both electrodes are much lower than those at all the other electrode materials under review.

It was shown for acidic solutions that, contrary to oxygen evolution and other oxidation reactions which proceed *via* OH radicals,[73,74] oxygen reduction proceeds at functional groups such as quinones, formed from sp^2-carbon impurities in the surface of the BDD-electrode upon oxidation, at potentials significantly larger than at the diamond surface.[75] The nature of these functional groups and their capacity to catalyse electrochemical reactions depends on the way the electrode is terminated.[75,76] Both, the overall low current density observed at the BDD-electrodes as compared to other electrode materials as well as their sensitivity to the termination mode of the electrode (terminated by hydrogen or oxygen *cf.* Fig. S2, ESI†), suggest that the oxygen reduction observed in Fig. 7 does not proceed at the diamond surface itself but at functional groups

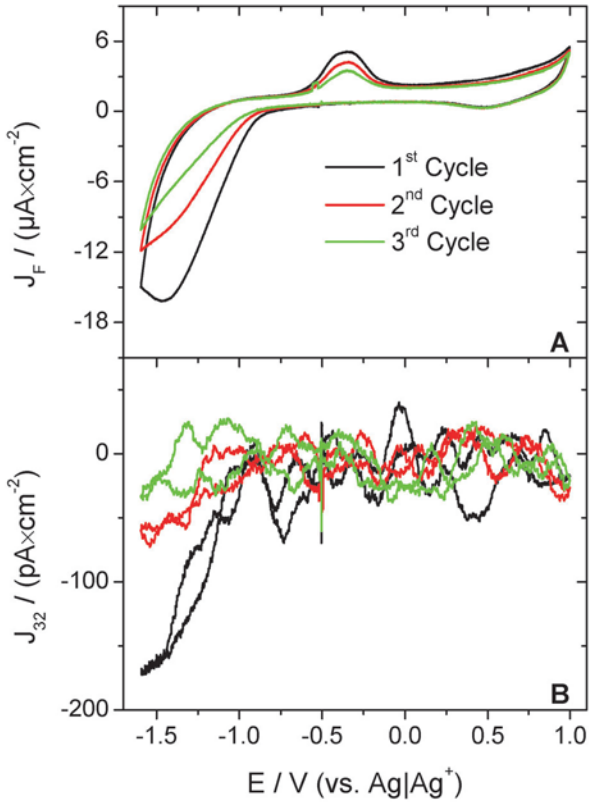

Fig. 7 CV (A) and MSCV for mass 32 (B) in an electrolyte of 0.5 M $LiClO_4$ in DMSO purged with a mixture of argon and oxygen (Ar : O_2 = 80 : 20) at the BDD electrode with the H-terminated surface (BDD_{red}); sweep rate: 10 mV s^{-1}; flow rate: 5 μL s^{-1}. Current densities are given with respect to the geometric surface area.

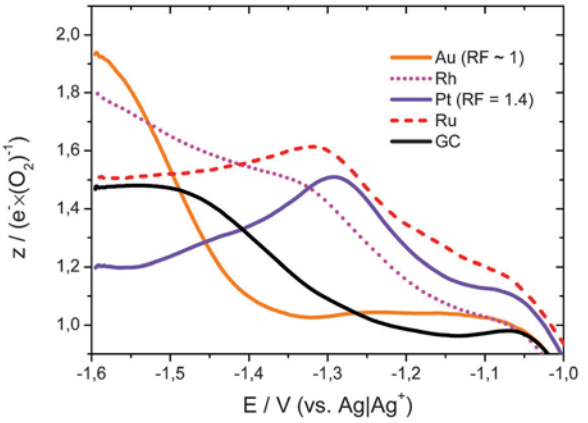

Fig. 8 Number of electrons (z) that is transferred per molecule of oxygen in the potential region of oxygen reduction. Black/solid: at glassy carbon; red/dashed: at ruthenium; purple/solid: at platinum; magneta/dotted: at rhodium; orange/solid: at gold. Electrolyte: 0.5 M $NaClO_4$ in DMSO; sweep rate: 10 mV s^{-1}; flow rate: 5 μL s^{-1}.

on the BDD surface, as was previously observed in aqueous solutions.

Reactions that involve the formation of adsorbed intermediates at other electrode materials proceed at BDD electrodes only at rather large overpotentials. Outer sphere reactions on the other hand are highly reversible at BDD electrodes. The absence of oxygen reduction at the BDD-electrode suggests that also superoxide formation is an inner sphere reaction that requires the specific adsorption of O_2 at the surface of the electrode. In this context it is noteworthy that 1 ML of Li_2O_2 on platinum and 2 ML on gold are sufficient to deactivate the electrode entirely. If oxygen reduction were an outer sphere reaction, tunnelling of electrons through the Li_2O_2-layer would allow the continuous formation of superoxide.

Influence of cations on oxygen reduction

An inner sphere reaction suggests that the structure of the electrochemical double layer at the interface between the electrode and the electrolyte exerts an effect on the mechanism of oxygen reduction. Different conducting salts or additives should alter the structure of the double layer and consequently could influence the mechanism of oxygen reduction.

Fig. 8 shows the *z*-values for the oxygen reduction reaction as a function of potential observed in an electrolyte of 0.5 M $NaClO_4$ in DMSO. The values in Fig. 8 were obtained in the same way as those displayed in Fig. 4. As an example Fig. 9 shows the corresponding CVs and MSCVs obtained at platinum and gold. The CV- and MSCV-data at rhodium, ruthenium and glassy carbon are available in the ESI† (Fig. S3–S5, ESI†).

In Fig. 8 the most pronounced difference to Fig. 4 occurs at the gold electrode. In both, lithium and sodium containing electrolytes, the *z*-value increases from $1e^-$ per O_2 to $2e^-$ per O_2 as the potential decreases. However, this increase is delayed by 200 mV from −1.2 V in the lithium-containing electrolyte to −1.4 V in the sodium-containing electrolyte. Furthermore the *z*-value observed at all electrode materials starts out close to $1e^-$ per O_2 and then increases as the overpotential increases. In Fig. 4 only gold shows this behaviour. At ruthenium and more pronounced at platinum the *z*-value passes through a maximum. This is probably due to the same effect as observed in Fig. 6. Deposits on the electrode surface inhibit the ability of the electrode to sustain the direct pathway of peroxide formation.

From the comparison of the *z*-values in Fig. 8 to those in Fig. 4 it becomes clear that the cation exerts an effect on the oxygen reduction. Since the thermodynamic potential of Na_2O_2-formation is at −0.97 V ($E_0(Li_2O_2)$ = −0.79 V *versus* Ag/Ag$^+$[7,51]) and that of NaO_2-formation is at −1.03 V *versus* Ag/Ag$^+$[42,51] the observed effect is of kinetic nature. Not only sodium but also other cations alter the potential at which the direct pathway of peroxide formation is observed. The charge density of the cation seems to be the crucial parameter. This is shown by Fig. 10, where the half wave potential of peroxide formation at a gold electrode is plotted against the charge density of the cation. We cannot give any explanation for the linear dependency observed in Fig. 10. However, it was shown by Si and Gewirth[77] that the addition of nitric acid changes the structure of DMSO adsorbed at the non-polarised Au(111) surface. An altered structure (due to a change of the conducting salt) at the interface between the electrode and the electrolyte should have an influence on an inner sphere reaction.

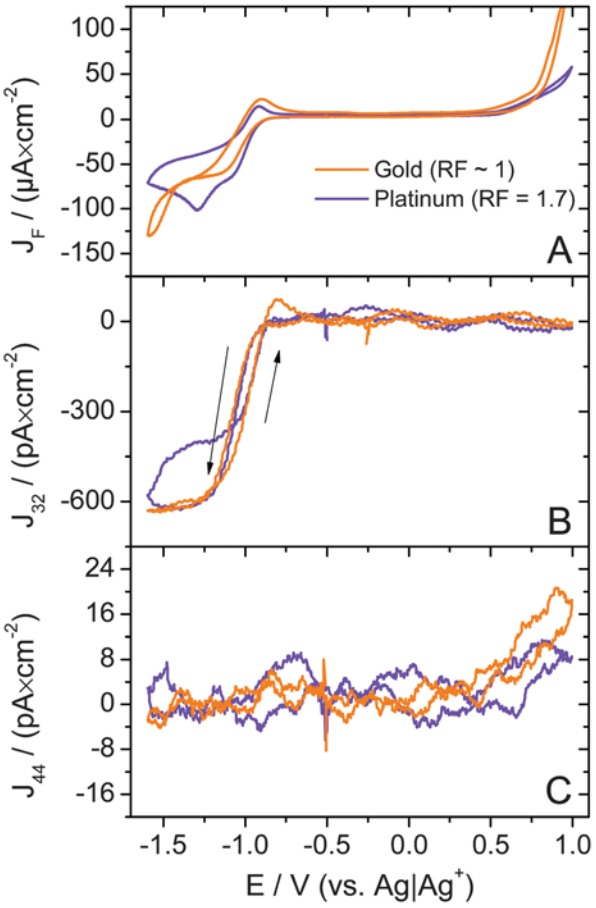

Fig. 9 CV (A) and MSCV for mass 32 (B) and mass 44 (C) in an electrolyte of 0.5 M $NaClO_4$ in DMSO purged with a mixture of argon and oxygen ($Ar:O_2$ = 80 : 20); sweep rate: 10 mV s^{-1}; flow rate: 5 μL s^{-1}; orange: at a gold electrode (RF ~ 3); purple: at a platinum electrode (RF = 5.5). Current densities are given with respect to the geometric surface area.

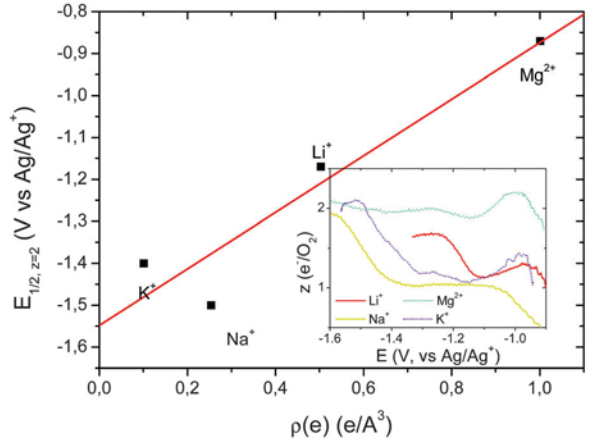

Fig. 10 Plot of the half wave potential at which the transfer of 2 electrons per molecule of oxygen is observed at gold, against the charge density $\rho(e)$ of the cation of the conducting salt. Electrolyte: 0.5 M of the respective perchlorate in DMSO (0.4 M $Mg(ClO_4)_2$ in DMSO); sweep rate: 10 mV s^{-1}; flow rate: 5 μL s^{-1}. The CV and MSCV of the potassium and magnesium containing electrolyte are available in the ESI† (Fig. S14 and S15, ESI†). Inset: Number of electrons as a function of potential transferred at a gold electrode in an DMSO based electrolyte containing various cations.

Alternatively, the relationship between the half wave potential of peroxide formation and the charge density of the cation might originate from the mechanism of oxygen reduction. It is hard to imagine that peroxide formation proceeds *via* two subsequent single electron transfers (SET), thus, creating a highly charged O_2^{2-}. It is more likely that the coordination of the cation to adsorbed superoxide is required in order to facilitate the second SET.

It is clear that the coordination of a cation with larger charge density would polarise adsorbed superoxide more effectively. Hence, a cation with large charge density could facilitate the second SET at lower overpotentials.

The effect of water on oxygen reduction

Metal–air batteries are supposed to work under ambient conditions with oxygen supplied by air. Hence, humidity is always present and might affect the charge and discharge of the battery. Therefore, we investigated the effect of the water content on oxygen reduction reaction. Fig. 11 shows the CV and MSCV for masses 32 and 44 obtained in an electrolyte of 0.5 M $LiClO_4$ in

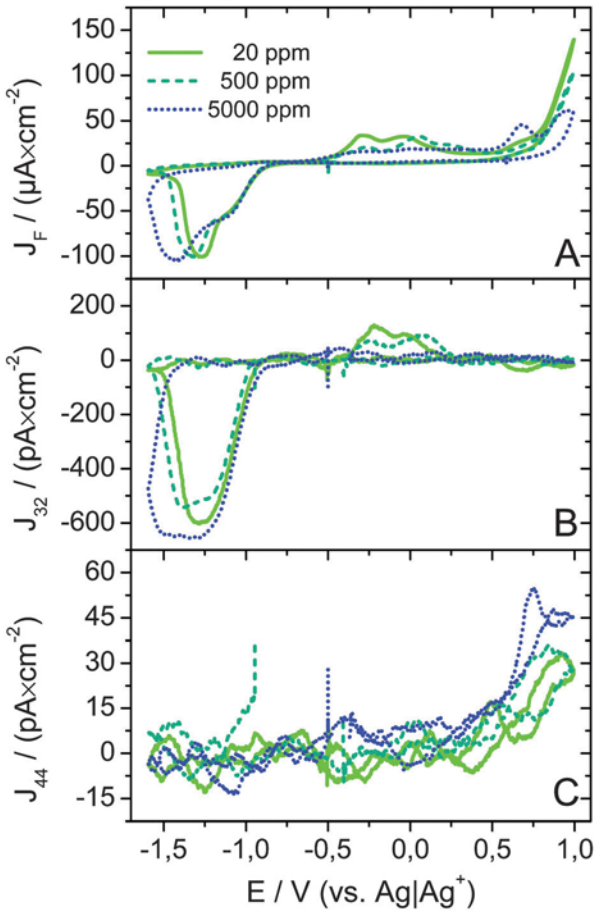

Fig. 11 CV (A) and MSCV for mass 32 (B) and mass 44 (C) in an electrolyte of 0.5 M $LiClO_4$ in DMSO with various water contents and purged with a mixture of argon and oxygen ($Ar:O_2$ = 80 : 20); sweep rate: 10 mV s^{-1}; flow rate: 5 μL s^{-1}; electrode: Au(pc); solid: 20 ppm water (absolute); dashed: 500 ppm water (added); dotted: 5000 ppm water (added). Current densities are given with respect to the geometric surface area.

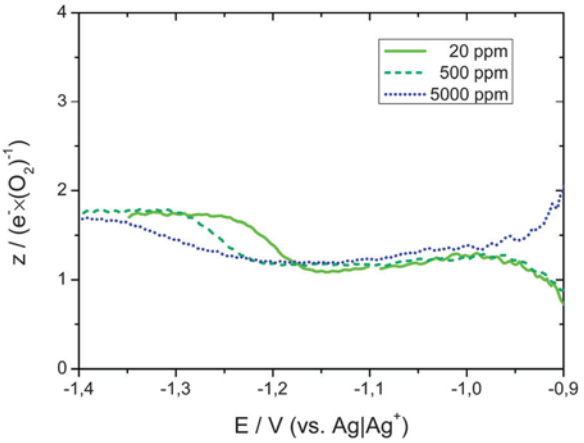

Fig. 12 Number of electrons (z) that is transferred per molecule of oxygen in the potential region of oxygen reduction at a polycrystalline gold electrode in an electrolyte of 0.5 M $LiClO_4$ in DMSO with various water contents. Solid: 20 ppm water (absolute); dashed: 500 ppm water (added); dotted: 5000 ppm water (added); sweep rate: 10 mV s^{-1}; flow rate: 5 µL s^{-1}.

DMSO with various water contents at the gold electrode. In addition, Fig. 12 shows the z-values calculated from the CV and MSCV data shown in Fig. 11. The CVs and MSCVs as well as the calculated z-values that were obtained with various water contents in the electrolyte at the remaining electrodes are available in the ESI† (Fig. S6–S13, ESI†).

From the z-values presented in Fig. 12 it is clear that the presence of water inhibits the ability of the gold electrode to form peroxide. In this respect gold is unique among the electrode materials under review as the water content has no effect on the z-values obtained at the other electrodes. Since only at gold a step in the z-value is observed when a lithium-containing electrolyte is employed, it is not surprising that the water effect is restricted to this electrode material. The direct pathway of peroxide formation is an inner sphere reaction (as derived from the results presented in Fig. 4) suggesting that water also exerts an effect on the double layer structure. However, it is less clear than in the case of the cation that water even participates in the formation of the double layer. From the ESI results presented in Fig. 13 we can at least rule out any effect of water on the solvation sphere of the cation.

In Fig. 13A the ESI spectrum of 1 mM LiTfO in DMSO is shown. A peak appears at mass 163 and another at 241 corresponding to $[Li(DMSO)_2]^+$ and $[Li(DMSO)_3]^+$, respectively. From that we observe that lithium is solvated in DMSO by two to three solvent molecules. When the DMSO based electrolyte is mixed with another electrolyte consisting of a 1 : 1 mixture of methanol and water plus 1% acetic acid the spectrum does not change in Fig. 13B. There is no peak that corresponds to the substitution of DMSO by water or methanol in the solvation sphere of lithium. Hence, the solvation shell of Li^+ remains unaltered when water is added to the electrolyte. The effect of water on the oxygen reduction reaction as described above does not stem from a solvation effect of lithium.

It was recently found that water favours the formation of large NaO_2 crystallites upon discharge of sodium–oxygen batteries.[36]

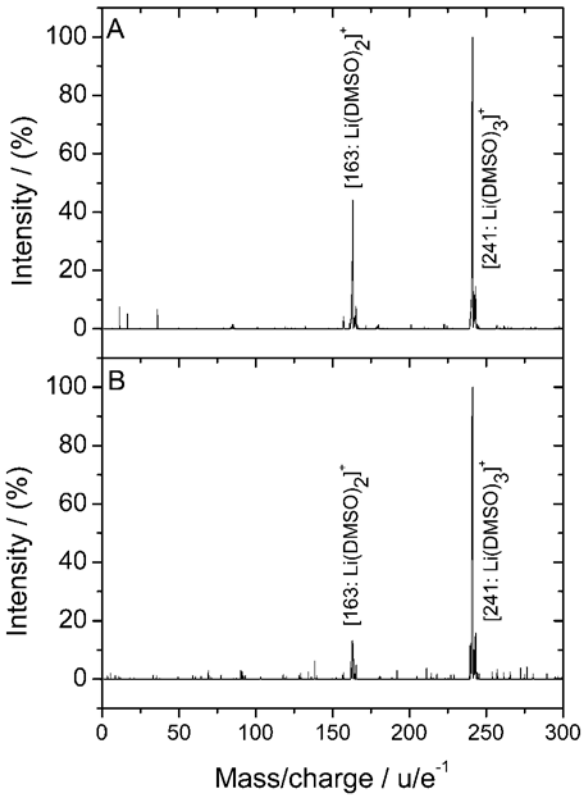

Fig. 13 ESI spectrum of (A) 1 mM LiTfO in DMSO and (B) 50% 1 mM LiTfO in DMSO and 50% of a 1 : 1 mixture of water and methanol containing 1% CH_3COOH.

The authors of that paper considered water as a proton phase transfer catalyst, with water donating a proton to NaO_2 in order to solubilize it as HO_2. In that view HO_2 can diffuse to certain nucleation sites and deposit as NaO_2, thus forming larger particles. Also for the formation of toroid shaped Li_2O_2 particles in lithium–oxygen batteries a similar mechanism was proposed, that is driven by a better solubility of LiO_2 in water containing electrolytes.[17] However, we do not believe that the acidity of water is a viable explanation for the effect observed in Fig. 12. Water has a pK_a value of 31.2 in DMSO, whereas DMSO has a pK_a value of 35.[78] With a water concentration of 500 ppm (approximately 25 mmol L^{-1}), at which a clear effect of water is observed already, and a DMSO concentration of approximately 14 mol L^{-1} the concentration of protons in the electrolyte is increased 10 fold at best. Considering that the coordination of Li^+ to DMSO probably enhances its acidity, the relative increase of the proton concentration due to water is likely to be lower. However, one order of magnitude in the proton concentration might make the difference whether an acid–base reaction occurs or not. But even if the concentration of protons were sufficient to influence the mechanism of oxygen reduction we would rather expect protons, with their high charge density, to favour the direct pathway of peroxide formation (*cf.* Fig. 10).

Others, working in the field of Li–O_2 batteries, have considered the formation of toroid shaped Li_2O_2 particles of a mechanism that is driven by an enhanced solubility of LiO_2, in

the presence of water.[17] Indeed, it has been found that the acceptor number (AN) of solvent will largely affect the solubility of superoxide.[79] Since water has a much larger acceptor number (AN = 229 kJ mol^{-1} [80]) than DMSO (AN = 81 kJ mol^{-1} [80]), the enhanced solubility of water seems to be a viable explanation for the delayed peroxide formation with increasing water content.

In Fig. 11C the amount of evolved CO_2 increases as the water content in the electrolyte is increased. The effect is small, but is present at all electrode materials. It was reported that CO_2 is only formed in this electrolyte after oxygen reduction.[10] Therefore, the evolution of CO_2 in the anodic sweep is the result of oxidation of decomposition products formed during oxygen reduction in the preceding cathodic sweep. However, it is not clear whether enhanced CO_2 evolution is due to the facilitated electrolyte decomposition during oxygen reduction or due to the facilitated oxidation of these decomposition products in the presence of water.

Conclusions

By correlating the consumed amounts of oxygen as obtained by DEMS with the faradaic current, the number of electrons transferred per molecule of oxygen during oxygen reduction was calculated as a function of potential. Distinctively different behaviors were observed at different electrode materials: oxygen reduction in a lithium containing electrolyte at rhodium electrodes proceeds *via* the direct electrochemical formation of peroxide, while at platinum, ruthenium and glassy carbon electrodes both the direct and the indirect formation of peroxide take place in parallel. Only at gold electrodes a transition from the indirect to the direct pathway was observed when the applied overpotential was increased. Such a transition at different overpotentials was observed with all electrode materials when a sodium containing electrolyte was used. This shows that the electrode material exerts a catalytic effect, and that peroxide formation is not an outer sphere reaction. Based on the differences observed in the electron number, when platinum electrodes with different roughness factors were employed, it was proposed that the Li_2O_2-deposit exerts a geometric effect.

The required overpotential to observe the transition from the indirect to the direct pathway of peroxide formation at gold electrodes in lithium containing electrolytes is sensitive to the water content in the electrolyte. With increasing water content the required overpotential also increases. This effect is not due to an altered solvation shell of Li^+ in the presence of water, as it is always coordinated by two or three molecules of DMSO, irrespective of the presence of water. Therefore, it was proposed that the effect is due to an alteration of the structure of the double layer in front of the electrode.

Comparing the current densities due to oxygen evolution at platinum and gold electrodes with similar Li_2O_2 coverage showed enhanced kinetics at the platinum electrode. This also suggests a catalytic effect for oxygen evolution. In the CV at gold single crystals differences to polycrystalline gold were observed in the region of oxygen evolution, suggesting sensitivity to certain surface sites.

Acknowledgements

The authors acknowledge the Federal Ministry of Education and Research for funding this work. This work is part of the "LuLi – Strom aus Luft und Li" project (FKZ:03X4624A).

References

1 K. M. Abraham and Z. Jiang, *J. Electrochem. Soc.*, 1996, **143**, 1–5.
2 A. Kraytsberg and Y. Ein-Eli, *J. Power Sources*, 2011, **196**, 886–893.
3 J. Christensen, P. Albertus, R. S. Sanchez-Carrera, T. Lohmann, B. Kozinsky, R. Liedtke, J. Ahmed and A. Kojic, *J. Electrochem. Soc.*, 2012, **159**, R1–R30.
4 J. Hou, M. Yang, M. W. Ellis, R. B. Moore and B. Yi, *Phys. Chem. Chem. Phys.*, 2012, **14**, 13487–13501.
5 D. Capsoni, M. Bini, S. Ferrari, E. Quartarone and P. Mustarelli, *J. Power Sources*, 2012, **220**, 253–263.
6 Z. Peng, S. A. Freunberger, Y. Chen and P. G. Bruce, *Science*, 2012, **337**, 563–566.
7 C. O. Laoire, S. Mukerjee, K. M. Abraham, E. J. Plichta and M. A. Hendrickson, *J. Phys. Chem. C*, 2010, **114**, 9178–9186.
8 D. Xu, Z.-L. Wang, J.-J. Xu, L.-L. Zhang, L.-M. Wang and X.-B. Zhang, *Chem. Commun.*, 2012, **48**, 11674–11676.
9 W. Xu, J. Hu, M. H. Engelhard, S. A. Towne, J. S. Hardy, J. Xiao, J. Feng, M. Y. Hu, J. Zhang, F. Ding, M. E. Gross and J.-G. Zhang, *J. Power Sources*, 2012, **215**, 240–247.
10 B. D. McCloskey, D. S. Bethune, R. M. Shelby, T. Mori, R. Scheffler, A. Speidel, M. Sherwood and A. C. Luntz, *J. Phys. Chem. Lett.*, 2012, **3**, 3043–3047.
11 M. W. Chase, Jr., *J. Phys. Chem. Ref. Data, Monogr.*, 1998, **9**, 1–1951.
12 J. D. Cox, D. D. Wagman and V. A. Medvedev, *CODATA Key Values for Thermodynamics*, Hemisphere Publishing Corp., New York, 1989.
13 B. D. Adams, C. Radtke, R. Black, M. L. Trudeau, K. Zaghib and L. F. Nazar, *Energy Environ. Sci.*, 2013, **6**, 1772–1778.
14 R. R. Mitchell, B. M. Gallant, Y. Shao-Horn and C. V. Thompson, *J. Phys. Chem. Lett.*, 2013, **4**, 1060–1064.
15 A. C. Luntz and B. D. McCloskey, *Chem. Rev.*, 2014, **114**, 11721–11750.
16 V. Viswanathan, K. S. Thygesen, J. S. Hummelshoj, J. K. Norskov, G. Girishkumar, B. D. McCloskey and A. C. Luntz, *J. Chem. Phys.*, 2011, **135**, 10.
17 N. B. Aetukuri, B. D. McCloskey, J. M. García, L. E. Krupp, V. Viswanathan and A. C. Luntz, *Nat. Chem.*, 2014, **7**, 50–56.
18 K. U. Schwenke, M. Metzger, T. Restle, M. Piana and H. A. Gasteiger, *J. Electrochem. Soc.*, 2015, **162**, A573–A584.
19 M. Safari, B. D. Adams and L. F. Nazar, *J. Phys. Chem. Lett.*, 2014, **5**, 3486–3491.
20 A. K. Thapa and T. Ishihara, *J. Power Sources*, 2011, **196**, 7016–7020.
21 A. K. Thapa, Y. Hidaka, H. Hagiwara, S. Ida and T. Ishihara, *J. Electrochem. Soc.*, 2011, **158**, A1483–A1489.

22 Y.-C. Lu, H. A. Gasteiger and Y. Shao-Horn, *J. Am. Chem. Soc.*, 2011, **133**, 19048–19051.
23 S. A. Freunberger, Y. Chen, N. E. Drewett, L. J. Hardwick, F. Barde and P. G. Bruce, *Angew. Chem., Int. Ed.*, 2011, **50**, 8609–8613.
24 S. A. Freunberger, Y. Chen, Z. Peng, J. M. Griffin, L. J. Hardwick, F. Barde, P. Novak and P. G. Bruce, *J. Am. Chem. Soc.*, 2011, **133**, 8040–8047.
25 X. Ren, S. S. Zhang, D. T. Tran and J. Read, *J. Mater. Chem.*, 2011, **21**, 10118–10125.
26 M. Marinaro, P. Balasubramanian, E. Gucciardi, S. Theil, L. Jörissen and M. Wohlfahrt-Mehrens, *SusChemSus*, 2015, DOI: 10.1002/cssc.201500600.
27 M. Marinaro, U. Riek, S. K. Eswara Moorthy, J. Bernhard, U. Kaiser, M. Wohlfahrt-Mehrens and L. Jörissen, *Electrochem. Commun.*, 2013, **37**, 53–56.
28 C. O. Laoire, S. Mukerjee, K. M. Abraham, E. J. Plichta and M. A. Hendrickson, *J. Phys. Chem. C*, 2009, **113**, 20127–20134.
29 W. Torres, N. Mozhzhukhina, A. Y. Tesio and E. J. Calvo, *J. Electrochem. Soc.*, 2014, **161**, A2204–A2209.
30 W. R. Torres, A. Y. Tesio and E. J. Calvo, *Electrochem. Commun.*, 2014, **49**, 38–41.
31 M. J. Trahan, S. Mukerjee, E. J. Plichta, M. A. Hendrickson and K. M. Abraham, *J. Electrochem. Soc.*, 2013, **160**, A259–A267.
32 D. Sharon, V. Etacheri, A. Garsuch, M. Afri, A. A. Frimer and D. Aurbach, *J. Phys. Chem. Lett.*, 2012, **4**, 127–131.
33 N. Mozhzhukhina, L. P. Méndez De Leo and E. J. Calvo, *J. Phys. Chem. C*, 2013, **117**, 18375–18380.
34 E. J. Calvo and N. Mozhzhukhina, *Electrochem. Commun.*, 2013, **31**, 56–58.
35 B. D. McCloskey, D. S. Bethune, R. M. Shelby, G. Girishkumar and A. C. Luntz, *J. Phys. Chem. Lett.*, 2011, **2**, 1161–1166.
36 C. Xia, R. Black, R. Fernandes, B. Adams and L. F. Nazar, *Nat. Chem.*, 2015, **7**, 496–501.
37 L. Andrews, *J. Chem. Phys.*, 1969, **50**, 4288–4299.
38 W. Liu, Q. Sun, Y. Yang, J.-Y. Xie and Z.-W. Fu, *Chem. Commun.*, 2013, **49**, 1951–1953.
39 Q. Sun, Y. Yang and Z.-W. Fu, *Electrochem. Commun.*, 2012, **16**, 22–25.
40 J. Kim, H.-D. Lim, H. Gwon and K. Kang, *Phys. Chem. Chem. Phys.*, 2013, **15**, 3623–3629.
41 P. Hartmann, C. L. Bender, M. Vračar, A. K. Dürr, A. Garsuch, J. Janek and P. Adelhelm, *Nat. Mater.*, 2013, **12**, 228–232.
42 C. L. Bender, P. Hartmann, M. Vračar, P. Adelhelm and J. Janek, *Adv. Energy Mater.*, 2014, **4**, 1301863.
43 V. Gutmann, *Coord. Chem. Rev.*, 1976, **18**, 225–255.
44 R. Cao, E. D. Walter, W. Xu, E. N. Nasybulin, P. Bhattacharya, M. E. Bowden, M. H. Engelhard and J.-G. Zhang, *ChemSusChem*, 2014, **7**, 2436–2440.
45 A. A. Abd-El-Latif and H. Baltruschat, in *Encyclopedia of Applied Electrochemistry*, ed. G. Kreysa, K. -I. Ota and R. Savinell, Springer, New York Dordrecht Heidelberg London, 2014, pp. 507–516.
46 A. A. Abd-El-Latif, C. J. Bondue, S. Ernst, M. Hegemann, J. K. Kaul, M. Khodayari, E. Mostafa, A. Stefanova and H. Baltruschat, *TrAC, Trends Anal. Chem.*, 2015, **70**, 4–13.
47 H. Baltruschat, in *Interfacial Electrochemistry*, ed. A. Wieckowski, Marcel Dekker, Inc., New York, Basel, 1999, pp. 577–597.
48 H. Baltruschat, *J. Am. Soc. Mass Spectrom.*, 2004, **15**, 1693–1706.
49 H. Baltruschat, R. Bussar, S. Ernst and F. Hernandez-Ramirez, in *In situ* Spectroscopic Studies of Adsorption at the Electrode and Electrocatalysis, ed. S.-G. Sun, P. A. Christensen and A. Wieckowski, Elsevier, Amsterdam, 2007, pp. 471–537.
50 C. J. Bondue, A. A. Abd-El-Latif, P. Hegemann and H. Baltruschat, *J. Electrochem. Soc.*, 2014, **162**, A479–A487.
51 G. Gritzner, *J. Mol. Liq.*, 2010, **156**, 103–108.
52 S. Trasatti and O. A. Petrii, *Pure Appl. Chem.*, 1991, **63**, 711–734.
53 S. Gilman, *J. Phys. Chem.*, 1967, **71**, 4330–4338.
54 T. Nagel, N. Bogolowski and H. Baltruschat, *J. Appl. Electrochem.*, 2006, **36**, 1297–1306.
55 J. Clavilier, D. Armand, S. G. Sun and M. Petit, *J. Electroanal. Chem.*, 1986, **205**, 267–277.
56 S. Iqbal, C. Bondü and H. Baltruschat, *J. Phys. Chem. C*, 2015, **119**, 20515–20523.
57 M. C. Granger, M. Witek, J. Xu, J. Wang, M. Hupert, A. Hanks, M. D. Koppang, J. E. Butler, G. Lucazeau, M. Mermoux, J. W. Strojek and G. M. Swain, *Anal. Chem.*, 2000, **72**, 3793–3804.
58 P. Albertus, G. Girishkumar, B. McCloskey, R. S. Sanchez-Carrera, B. Kozinsky, J. Christensen and A. C. Luntz, *J. Electrochem. Soc.*, 2011, **158**, A343–A351.
59 A. Lewera, J. Inukai, W. P. Zhou, D. Cao, H. T. Duong, N. Alonso-Vante and A. Wieckowski, *Electrochim. Acta*, 2007, **52**, 5759–5765.
60 P. K. Babu, A. Lewera, J. H. Chung, R. Hunger, W. Jaegermann, N. Alonso-Vante, A. Wieckowski and E. Oldfield, *J. Am. Chem. Soc.*, 2007, **129**, 15140–15141.
61 D. X. Cao, A. Wieckowski, J. Inukai and N. Alonso-Vante, *J. Electrochem. Soc.*, 2006, **153**, A869–A874.
62 D. B. Sepa, M. V. Vojnovic and A. Damjanovic, *Electrochim. Acta*, 1981, **26**, 781–793.
63 N. M. Markovic, H. A. Gasteiger and P. N. Ross, *J. Phys. Chem.*, 1995, **99**, 3411–3415.
64 H. Baltruschat, S. Ernst and N. Bogolowski, in *Catalysis in Electrochemistry*, ed. E. Santos and W. Schmickler, Wiley, 2011, pp. 297–337.
65 R. R. Adžić and J. X. Wang, *J. Phys. Chem. B*, 1998, **102**, 8988–8993.
66 V. Viswanathan, H. A. Hansen, J. Rossmeisl and J. K. Nørskov, *J. Phys. Chem. Lett.*, 2012, **3**, 2948–2951.
67 B. D. McCloskey, R. Scheffler, A. Speidel, D. S. Bethune, R. M. Shelby and A. C. Luntz, *J. Am. Chem. Soc.*, 2011, **133**, 18038–18041.
68 J. X. Wang, N. S. Marković and R. R. Adžić, *Colloids Surf., A*, 1998, **134**, 165–171.
69 T. Abe, G. M. Swain, K. Sashikata and K. Itaya, *J. Electroanal. Chem.*, 1995, **382**, 73–83.
70 A. J. Appleby, J. O. M. Bockris, E. B. Budevski, B. E. Coneway, A. R. Despic, R. R. Dogonadze, M. Enyo,

D. Inman, S. U. M. Khan, L. I. Krishtalik, A. M. Kuznetsov, D. G. Lovering, R. Memming, E. J. Judd, A. Sadkowski, M. R. Tarasevich and E. Yeager, *Kinetics and Mechanism of Electrode Processes*, Plenum Press, New York, 1983.

71 R. R. Adžić, N. M. Marković and V. B. Vešović, *J. Electroanal. Chem. Interfacial Electrochem.*, 1984, **165**, 105–120.

72 R. R. Adžić and N. M. Marković, *J. Electroanal. Chem. Interfacial Electrochem.*, 1982, **138**, 443–447.

73 S. Ayata, A. Stefanova, S. Ernst and H. Baltruschat, *J. Electroanal. Chem.*, 2013, **701**, 1–6.

74 A. Stefanova, S. Ayata, A. Erem, S. Ernst and H. Baltruschat, *Electrochim. Acta*, 2013, **110**, 560–569.

75 T. Yano, E. Popa, D. A. Tryk, K. Hashimoto and A. Fujishima, *J. Electrochem. Soc.*, 1999, **146**, 1081–1087.

76 A. Kraft, *Int. J. Electrochem. Sci.*, 2007, **2**, 355–385.

77 S. K. Si and A. A. Gewirth, *J. Phys. Chem. B*, 2000, **104**, 10775–10782.

78 F. G. Bordwell, *Acc. Chem. Res.*, 1988, **21**, 456–463.

79 A. Khetan, A. Luntz and V. Viswanathan, *J. Phys. Chem. Lett.*, 2015, **6**, 1254–1259.

80 Y. Marcus, *Chem. Soc. Rev.*, 1993, **22**, 409–416.

Supporting Information

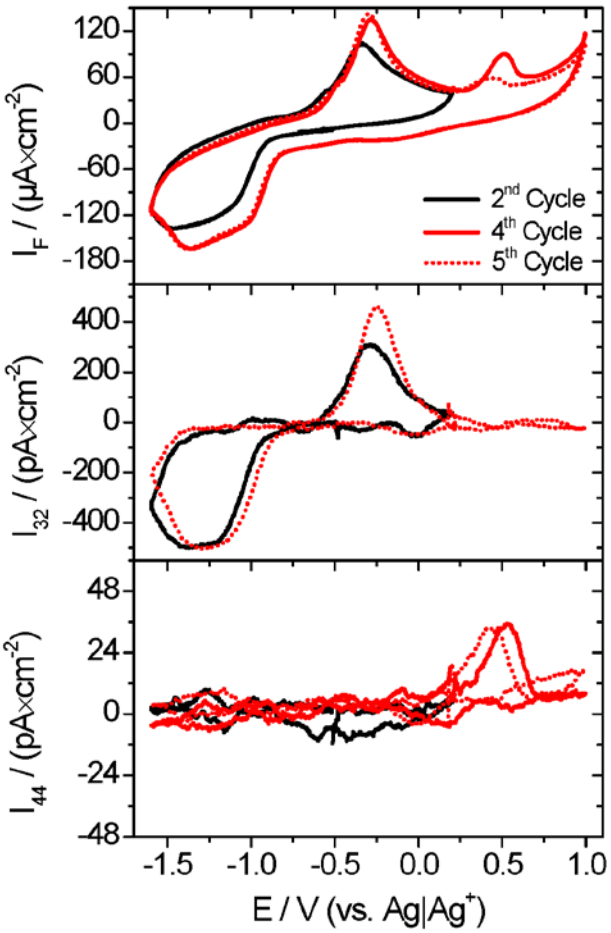

Figure S1: CV (A) and MSCV for mass 32 (B) and mass 44 (C) in an electrolyte of 0.5 M $LiClO_4$ in DMSO purged with a mixture of argon and oxygen (Ar : O_2 = 80 : 20) at a rhodium electrode (RF = 10.8) decorated with approximately 0.72 ML Se (1 ML is defined as one Se-atom per Rh-surface atom); Sweep rate: 10 mV/s; Flow rate: 5µL/s. Current densities are given with respect to the geometric surface area.

In the CV of Figure 5A a peak appears at 0.5 V once the upper potential limit was increased from 0.2 V to 1.0 V. This peak is not present in the CV at an unmodified rhodium electrode and disappears in the subsequent sweeps. Therefore the peak is most probably due to the stripping of Se from the rhodium electrode. It is however unclear why Se stripping comes along with the evolution of CO_2. Stripping of Selenium has little affect on the general appearance of the CV and the MSCV for mass 32 in the region of oxygen reduction and oxygen evolution.

Datei-Pfad: S:\Bondü\three\Supporting Information

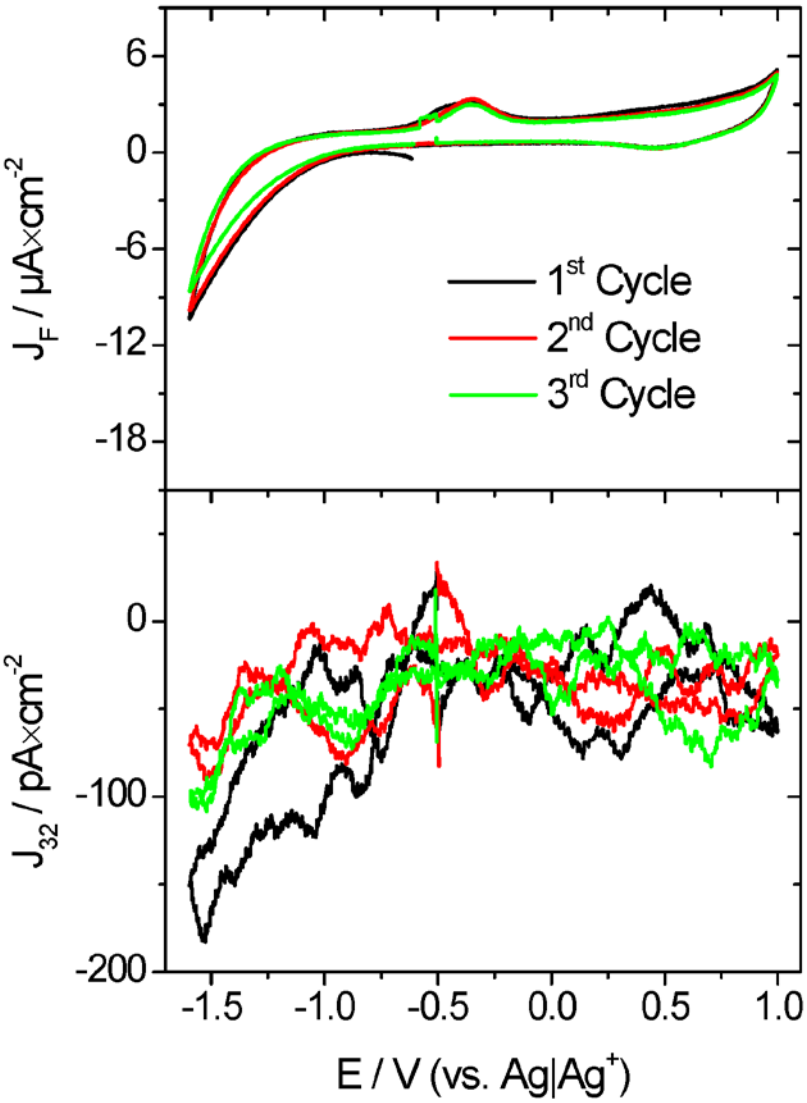

Figure S2: CV and MSCV for mass 32 in an electrolyte of 0.5 M $LiClO_4$ in DMSO purged with a mixture of argon and oxygen (Ar : O_2 = 80 : 20); Sweep rate: 10 mV/s; Flow rate: 5µL/s; Electrode: BDD_{ox}. All current densities are given with respect to the geometric surface area.

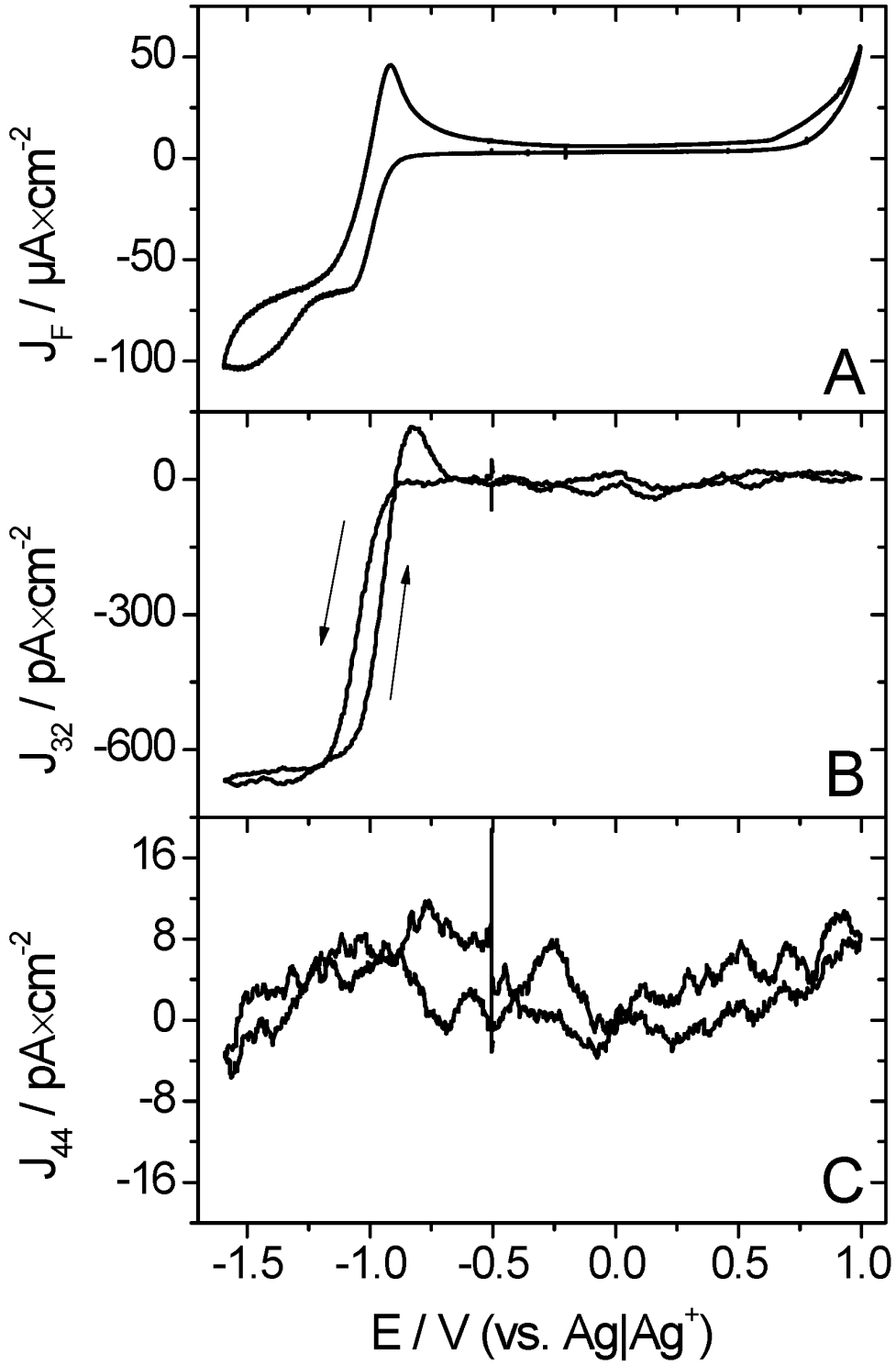

Figure S3: CV (A) and MSCV for mass 32 (B) and mass 44 (C) in an electrolyte of 0.5 M $NaClO_4$ in DMSO purged with a mixture of argon and oxygen (Ar : O_2 = 80 : 20); Sweep rate: 10 mV/s; Flow rate: 5µL/s; Electrode: Glassy carbon. All current densities are given with respect to the geometric surface area.

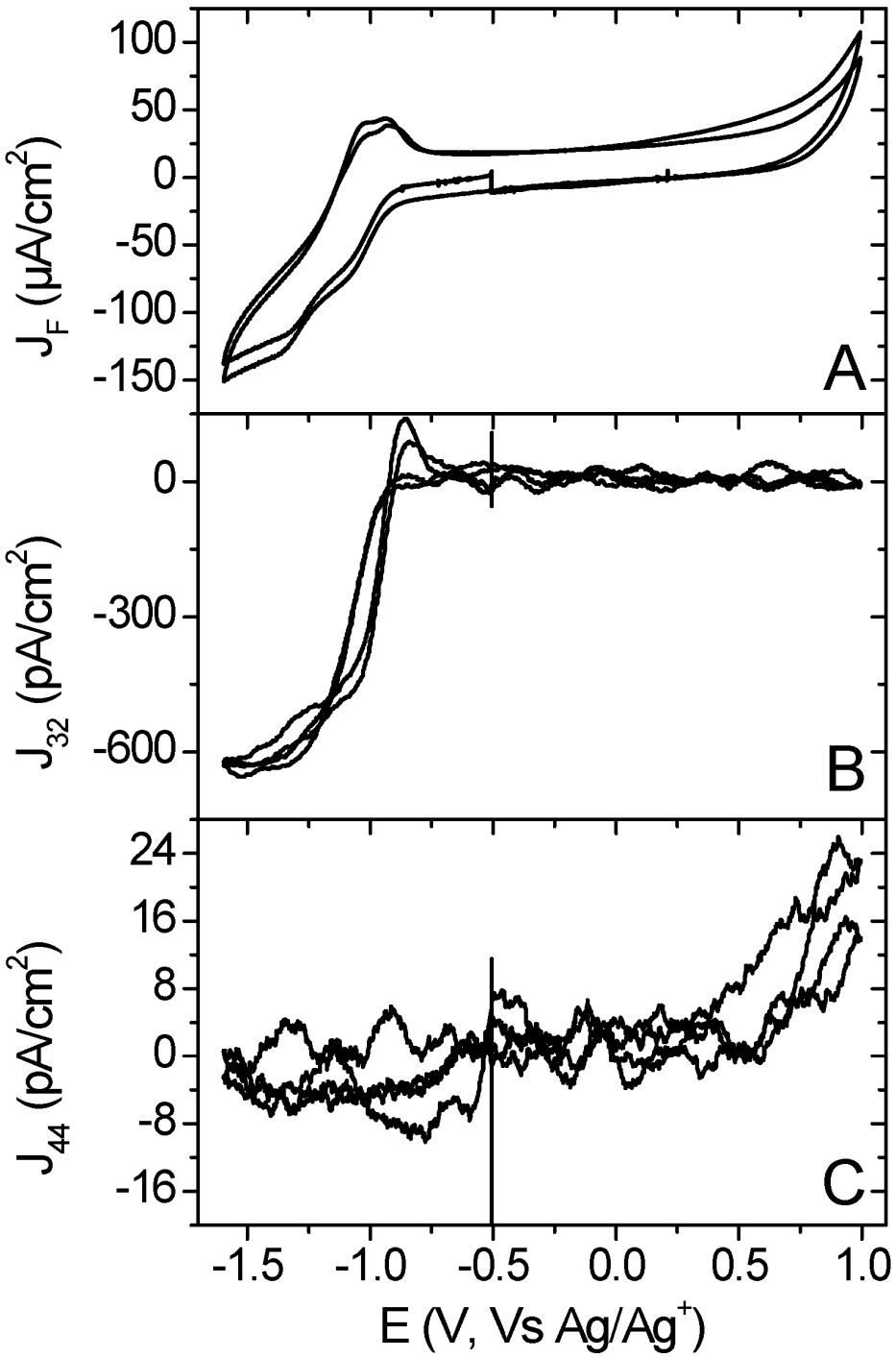

Figure S3: CV (A) and MSCV for mass 32 (B) and mass 44 (C) in an electrolyte of 0.5 M $NaClO_4$ in DMSO purged with a mixture of argon and oxygen (Ar : O_2 = 80 : 20); Sweep rate: 10 mV/s; Flow rate: 5µL/s; Electrode: Rhodium. All current densities are given with respect to the geometric surface area.

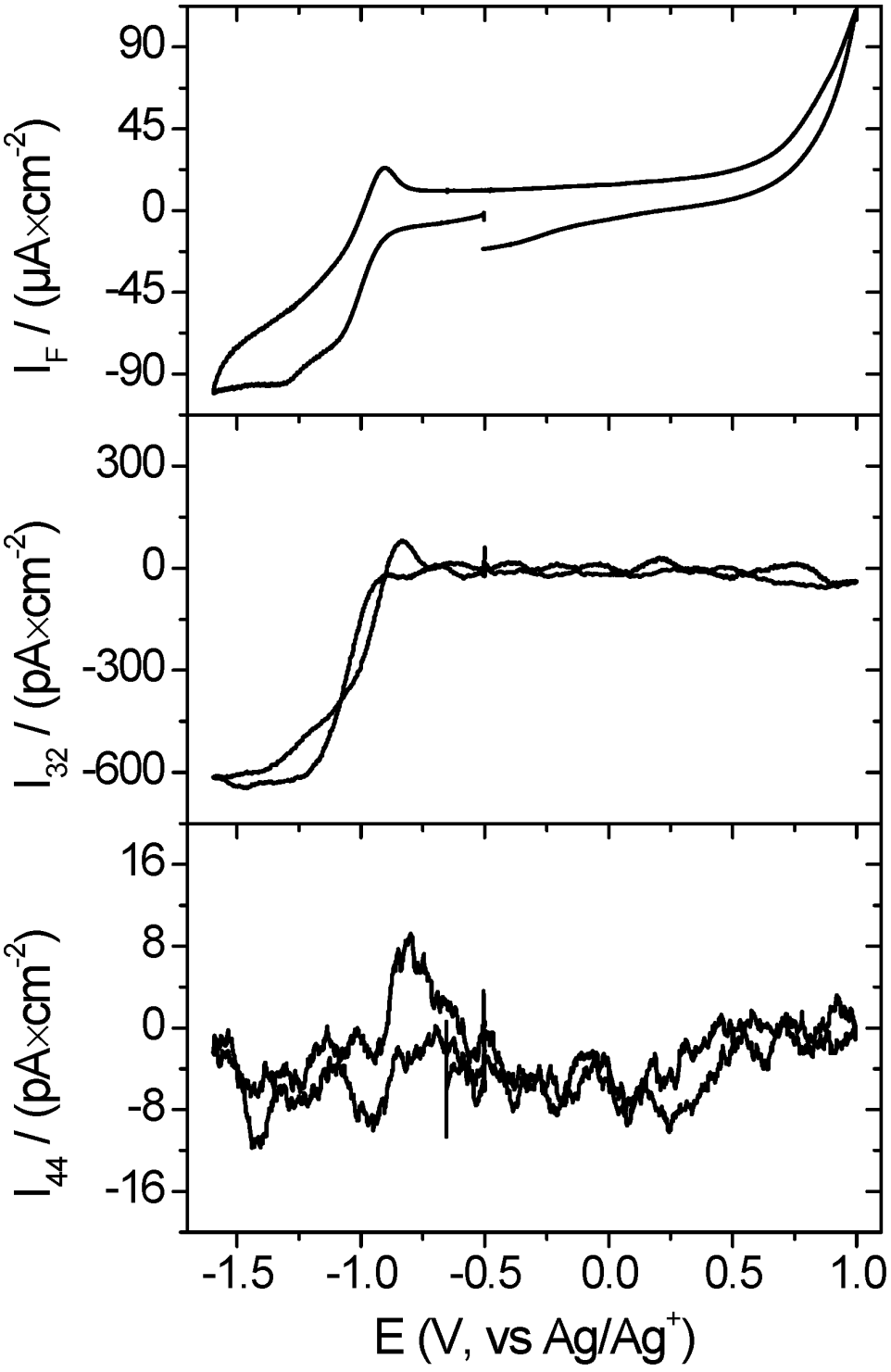

Figure S5: CV (A) and MSCV for mass 32 (B) and mass 44 (C) in an electrolyte of 0.5 M $NaClO_4$ in DMSO purged with a mixture of argon and oxygen (Ar : O_2 = 80 : 20); Sweep rate: 10 mV/s; Flow rate: 5µL/s; Electrode: Ruthenium. All current densities are given with respect to the geometric surface area.

Datei-Pfad: S:\Bondü\three\Supporting Information

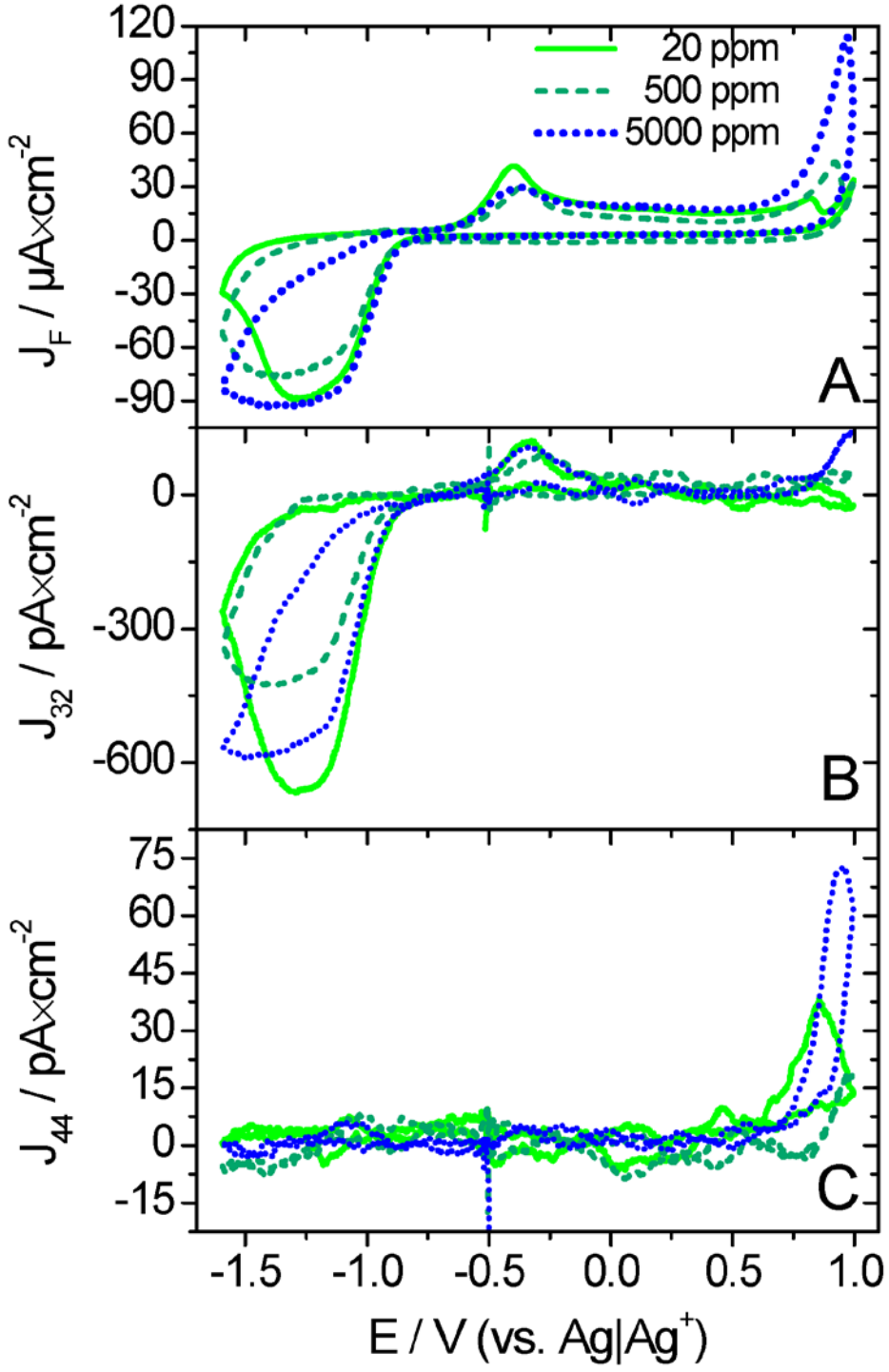

Figure S6: CV (A) and MSCV for mass 32 (B) and mass 44 (C) in an electrolyte of 0.5 M $LiClO_4$ in DMSO with various water contents and purged with a mixture of argon and oxygen (Ar : O_2 = 80 : 20); Sweep rate: 10 mV/s; Flow rate: 5µL/s; Electrode: Glassy carbon; Solid 20 ppm water; dashed: 500 ppm water; dotted: 5000 ppm water. All current densities are given with respect to the geometric surface area.

Datei-Pfad: S:\Bondü\three\Supporting Information

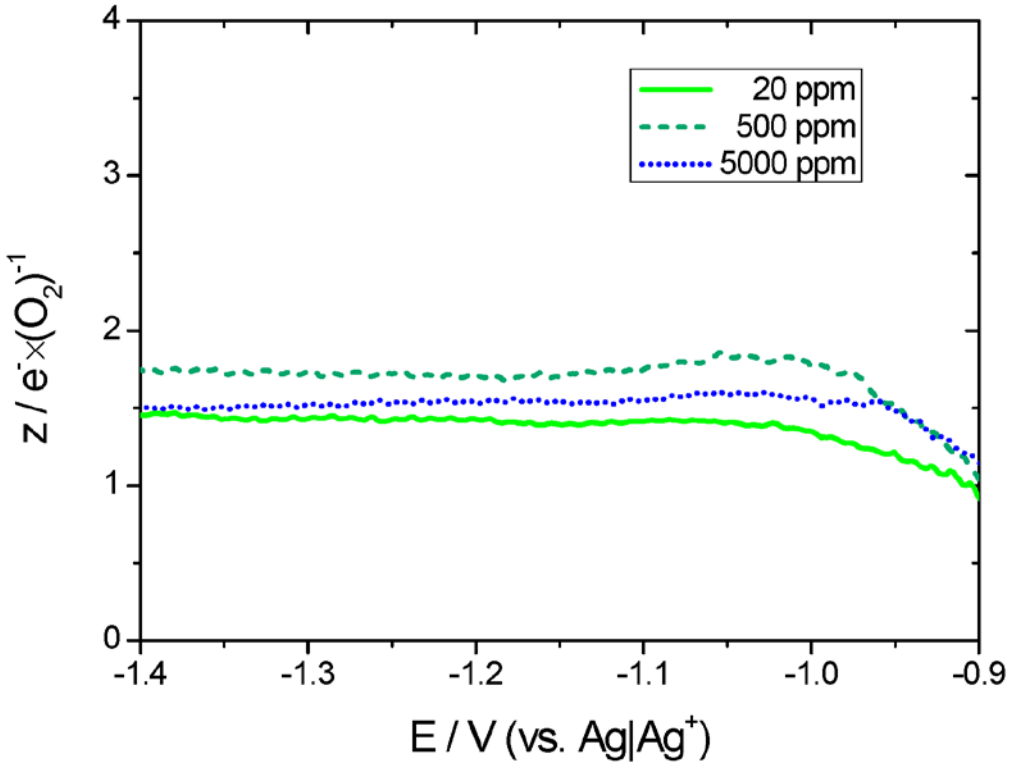

Figure S7: Number of electrons (z) that are transferred per molecule of oxygen in the potential region of oxygen reduction at a glassy carbon electrode in an electrolyte of 0.5 M $LiClO_4$ in DMSO with various water contents. Solid 20 ppm water; dashed: 500 ppm water; dotted: 5000 ppm water; Sweep rate: 10 mV/s; Flow rate: 5µL/s.

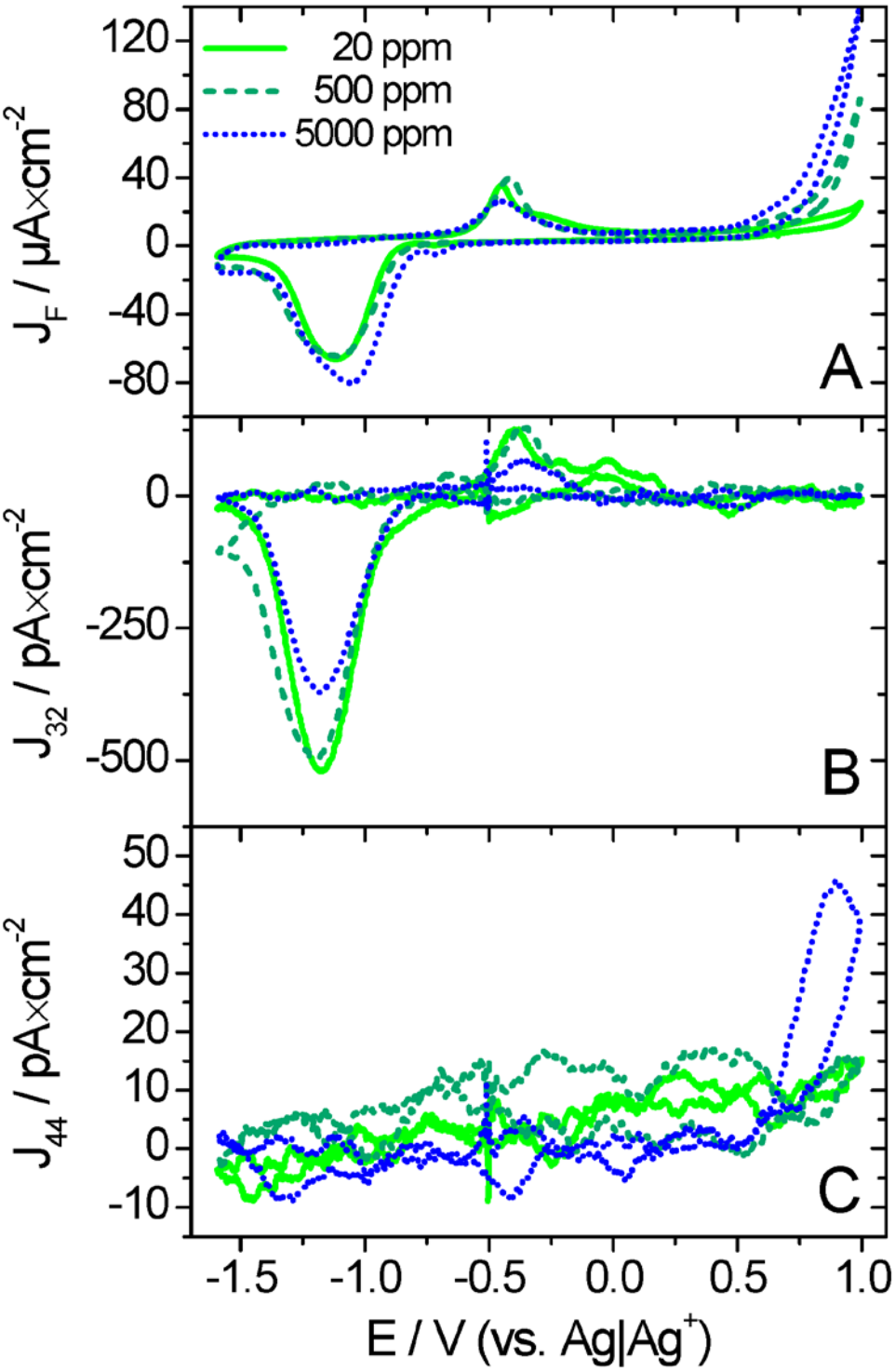

Figure S8: CV (A) and MSCV for mass 32 (B) and mass 44 (C) in an electrolyte of 0.5 M $LiClO_4$ in DMSO with various water contents and purged with a mixture of argon and oxygen (Ar : O_2 = 80 : 20); Sweep rate: 10 mV/s; Flow rate: 5µL/s; Electrode: Pt(pc) (RF = 1.4); Solid 20 ppm water; dashed: 500 ppm water; dotted: 5000 ppm water. All current densities are given with respect to the geometric surface area.

Datei-Pfad: S:\Bondü\three\Supporting Information

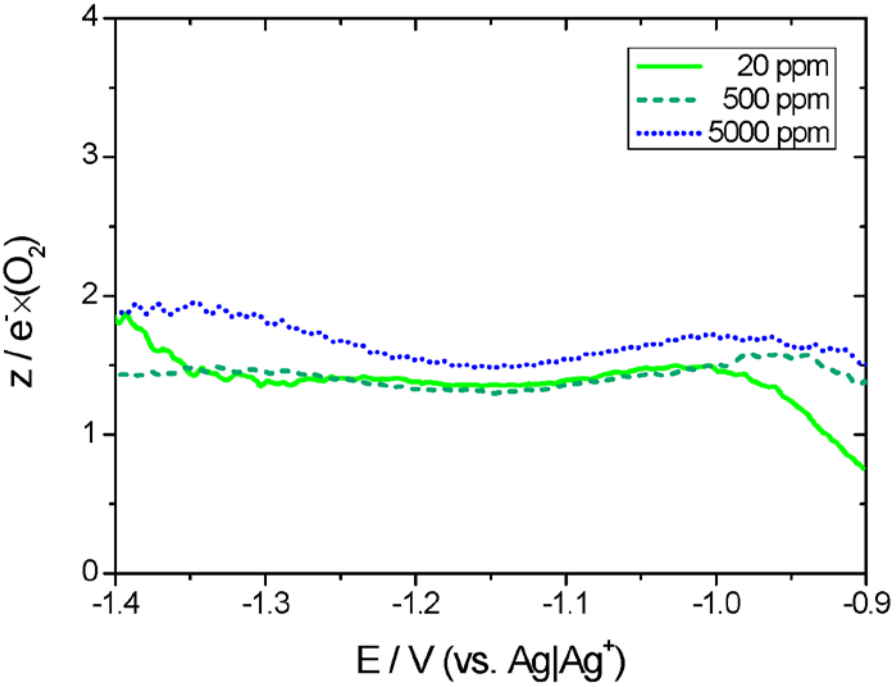

Figure S9: Number of electrons (z) that are transferred per molecule of oxygen in the potential region of oxygen reduction at a polycrystalline platinum electrode in an electrolyte of 0.5 M $LiClO_4$ in DMSO with various water contents. Solid 20 ppm water; dashed: 500 ppm water; dotted: 5000 ppm water; Sweep rate: 10 mV/s; Flow rate: 5µL/s.

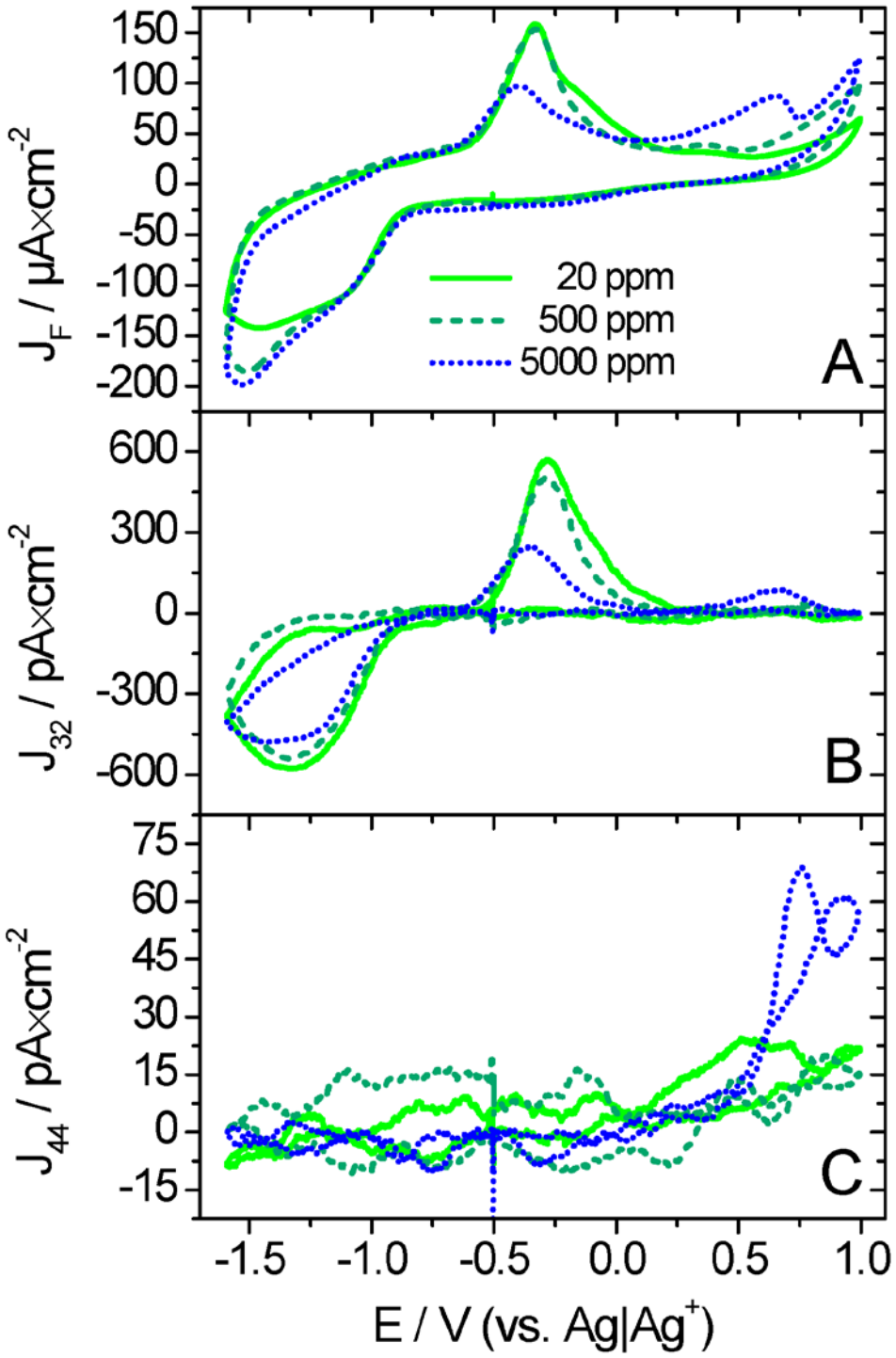

Figure S10: CV (A) and MSCV for mass 32 (B) and mass 44 (C) in an electrolyte of 0.5 M $LiClO_4$ in DMSO with various water contents and purged with a mixture of argon and oxygen (Ar : O_2 = 80 : 20); Sweep rate: 10 mV/s; Flow rate: 5µL/s; Electrode: Rh(pc); Solid 20 ppm water; dashed: 500 ppm water; dotted: 5000 ppm water. All current densities are given with respect to the geometric surface area.

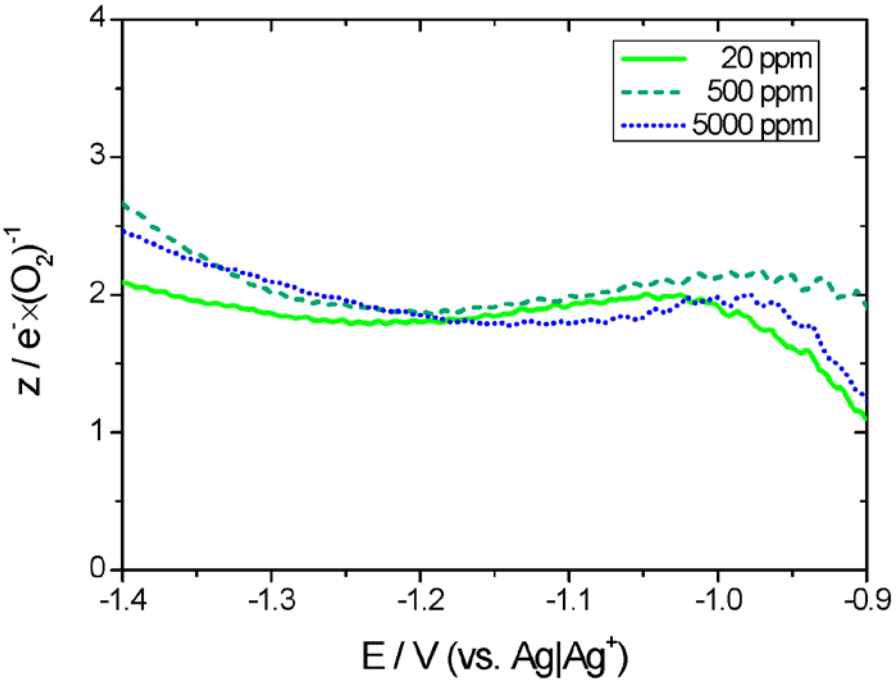

Figure S11: Number of electrons (z) that are transferred per molecule of oxygen in the potential region of oxygen reduction at a polycrystalline rhodium electrode in an electrolyte of 0.5 M $LiClO_4$ in DMSO with various water contents. Solid 20 ppm water; dashed: 500 ppm water; dotted: 5000 ppm water; Sweep rate: 10 mV/s; Flow rate: 5µL/s.

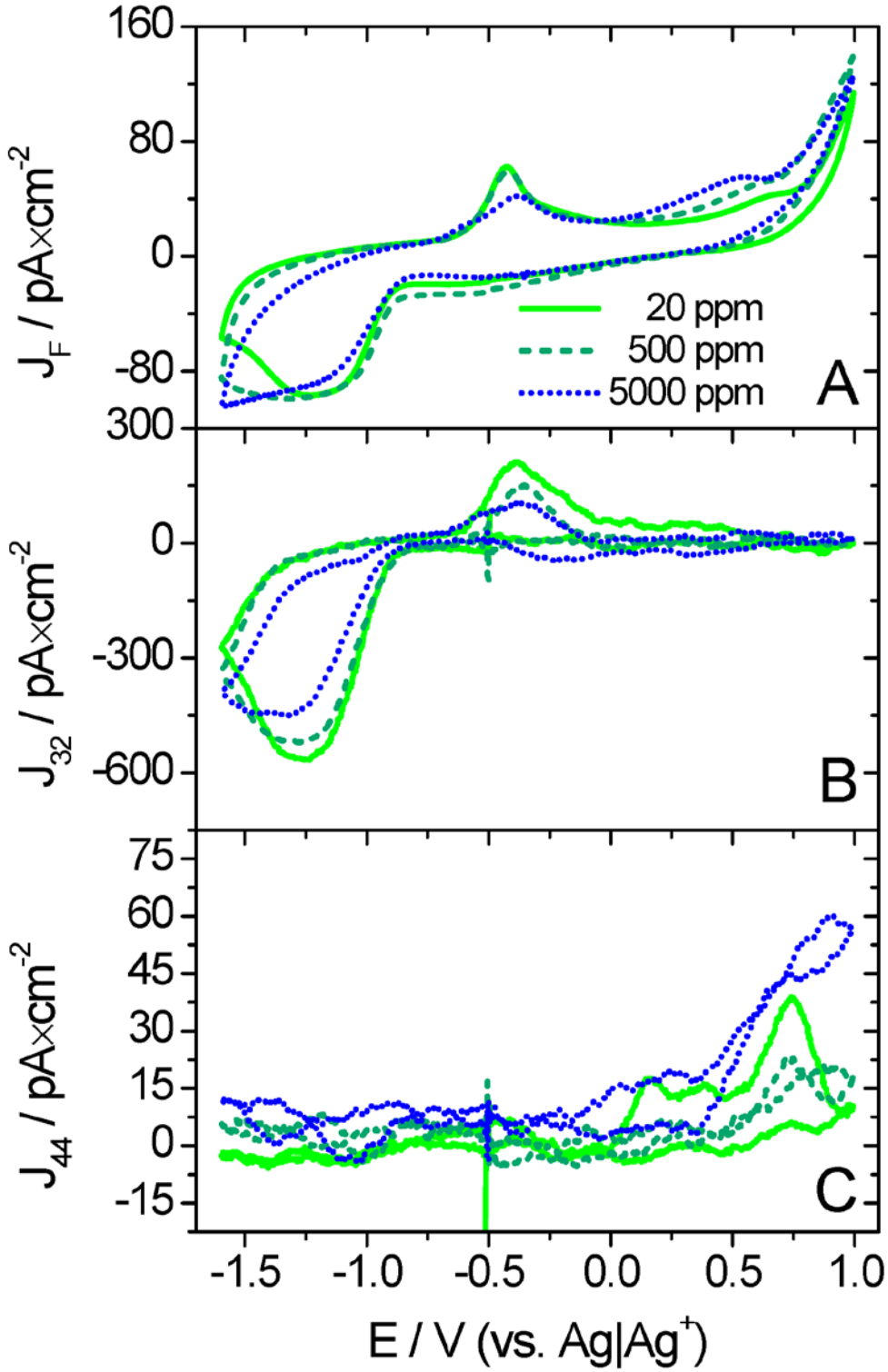

Figure S12: CV (A) and MSCV for mass 32 (B) and mass 44 (C) in an electrolyte of 0.5 M $LiClO_4$ in DMSO with various water contents and purged with a mixture of argon and oxygen (Ar : O_2 = 80 : 20); Sweep rate: 10 mV/s; Flow rate: 5µL/s; Electrode: Ru(pc); Solid 20 ppm water; dashed: 500 ppm water; dotted: 5000 ppm water. All current densities are given with respect to the geometric surface area.

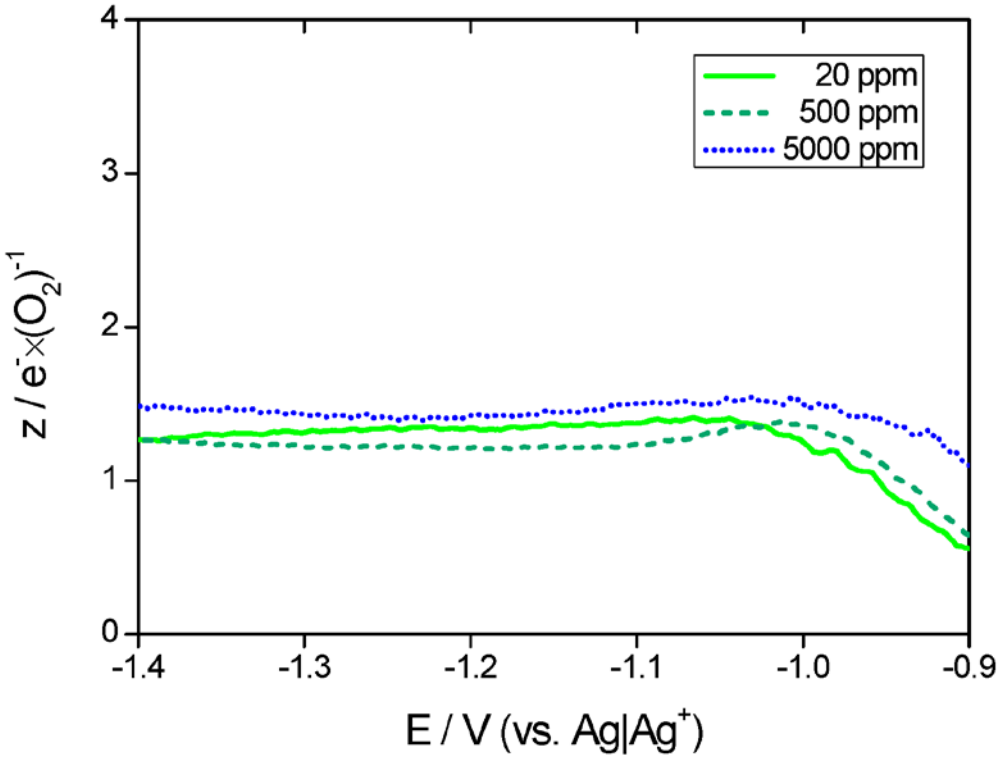

Figure S13: Number of electrons (z) that are transferred per molecule of oxygen in the potential region of oxygen reduction at a polycrystalline ruthenium electrode in an electrolyte of 0.5 M $LiClO_4$ in DMSO with various water contents. Solid 20 ppm water; dashed: 500 ppm water; dotted: 5000 ppm water; Sweep rate: 10 mV/s; Flow rate: 5µL/s.

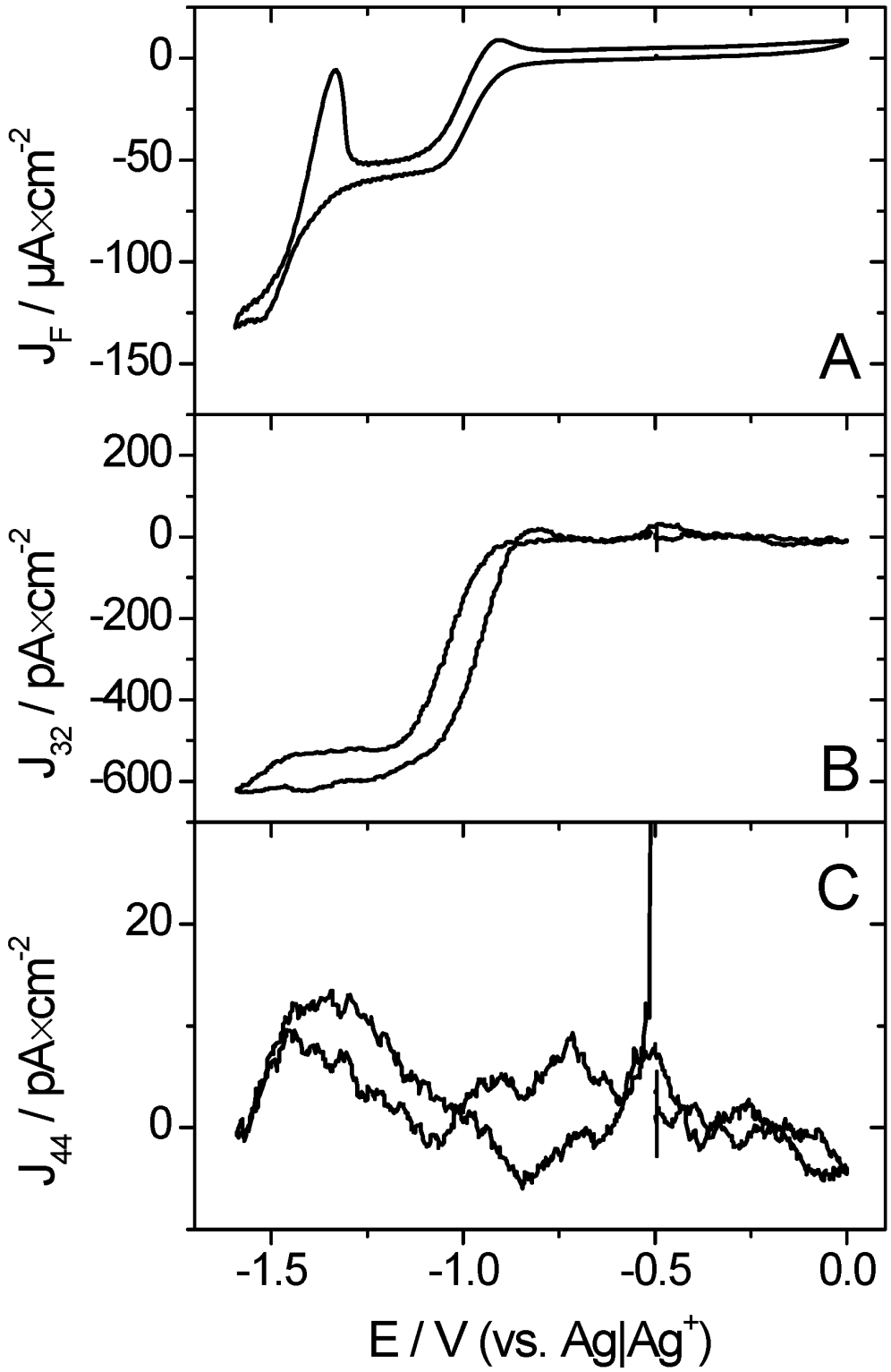

Figure S14: CV (A) and MSCV for mass 32 (B) and mass 44 (C) in an electrolyte of 0.5 M $KClO_4$ in DMSO purged with a mixture of argon and oxygen (Ar : O_2 = 80 : 20); Sweep rate: 10 mV/s; Flow rate: 5µL/s; Electrode: Gold. All current densities are given with respect to the geometric surface area.

Datei-Pfad: S:\Bondü\three\Supporting Information

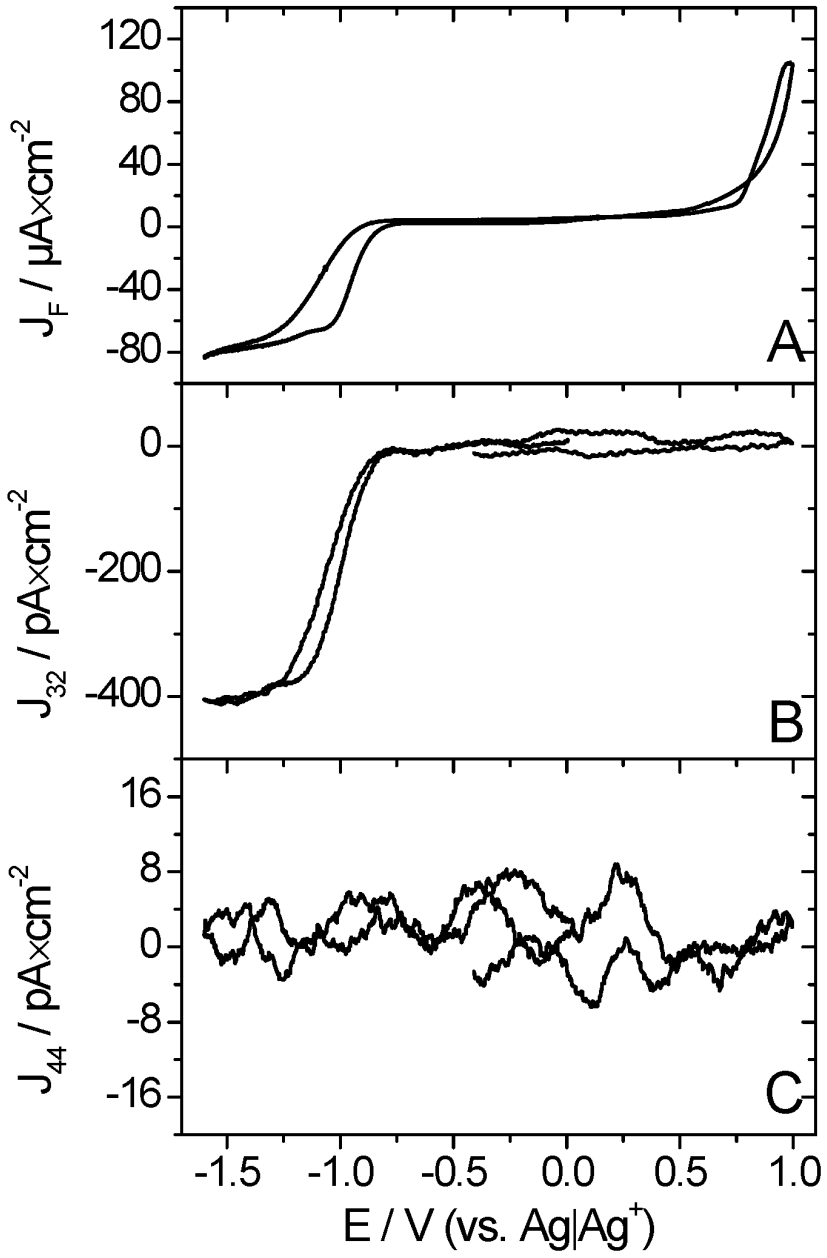

Figure S15: CV (A) and MSCV for mass 32 (B) and mass 44 (C) in an electrolyte of 0.4 M $Mg(ClO_4)_2$ in DMSO purged with a mixture of argon and oxygen (Ar : O_2 = 80 : 20); Sweep rate: 10 mV/s; Flow rate: 5µL/s; Electrode: Gold. All current densities are given with respect to the geometric surface area.

Datei-Pfad: S:\Bondü\three\Supporting Information

4. 3. Summary of Paper 3

In the presented study we investigated the impact of the electrode material on oxygen reduction and oxygen evolution from DMSO based electrolytes.

In the case of oxygen evolution we were able to show that the kinetics of oxygen evolution are affected by the electrode material. A strong interaction between the gold surface and Li_2O_2 was proposed based on results obtained at single crystalline gold surfaces.

In addition, the present study reveals that the impact of the electrode material on the mechanism of oxygen reduction in DMSO based electrolyte is quite severe. No oxygen reduction proceeds at the diamond surface of BDD-electrodes. This shows that oxygen reduction requires an interaction between oxygen and the electrode to allow the first electron transfer. No cleavage of the oxygen-bond takes place when either peroxide or superoxide is formed. It is, therefore, very surprising that oxygen reduction is an inner sphere reaction in organic media.

At other electrode materials such as platinum and rhodium oxygen is reduced *via* the direct pathway of peroxide formation irrespective of the applied potential. On the gold electrode a transition from the indirect to the direct pathway of peroxide formation was observed, which was proposed previously by Laoire *et al*. [40] and others [61, 70-72]. We did not observe such a transition at the gold sputtered Teflon membrane in Paper 1. Furthermore, Paper 2 shows that both water and the cation in the electrolyte affects the potential at which the transition from the indirect to the direct pathway is observed.

5. Paper 3 - A Comprehensive Study on Oxygen Reduction and Evolution from Lithium Containing DMSO Based Electrolytes at Gold Electrodes

5. 1. Introduction to Paper 3

In Paper 2 we observed the transition from the indirect to the direct pathway of peroxide formation at a smooth gold electrode. In this respect gold is unique among all electrode materials we have investigated so far. However, we did not observe such a transition at a gold sputtered Teflon membrane in Paper 1. We felt compelled to resolve this difference and to conduct further research on oxygen reduction at gold electrodes. Therefore, eQCMB and RRDE-measurements were conducted.

In Figure 7 of Paper 1 in which the ionic charge of oxygen evolution was plotted versus the ionic charge of oxygen reduction a linear fit with a negative intercept with the y-axis was obtained. The corresponding experiment was done several times always with a similar outcome. As already mentioned in Paper 1 we deemed this behaviour strange. In Paper 3 we embrace this problem and discuss a mechanism that leads to the described behaviour.

5. 2. A Comprehensive Study on Oxygen Reduction and Evolution from Lithium Containing DMSO Based Electrolytes at Gold Electrodes (as published in JECS)

The version of record of Paper 2 as published in the Journal of the Electrochemical Society is shown in the following. The article was published under the Creative Commons Licence (CC-BY; "Open Access"). Therefore, no special permission of the publisher is required to display the version of record. Any use of the material of the article shown below is permissible only after proper citation:

C. J. Bondue, M. Hegemann, C. Molls, E. Thome and H. Baltruschat, *J. Electrochem. Soc.*, **163**, A1765-A1775 (2016).

A Comprehensive Study on Oxygen Reduction and Evolution from Lithium Containing DMSO Based Electrolytes at Gold Electrodes

C. J. Bondue, M. Hegemann, C. Molls, E. Thome, and H. Baltruschat*,z

Institut für Physikalische und Theoretische Chemie, Universität Bonn, D-53117 Bonn, Germany

In the present study, we investigated the reduction and the evolution of oxygen from lithium containing DMSO based electrolytes at gold. The number of electrons that are transferred per O_2 (z-value) during oxygen reduction depends on the structure of the electrode: Despite the presence of Li^+, O_2 is reduced electrochemically to superoxide at smooth gold electrodes and at low overpotentials. At porous electrodes a z-value close to 2 e^-/O_2 indicates Li_2O_2-formation even at low overpotentials. This is ascribed to a reaction of superoxide, which is catalyzed by gold-particles at open circuit. This behavior is also responsible for the non-proportionality between reduced and evolved amounts of oxygen. Furthermore, we observed a linear relationship between evolved amounts of CO_2 and reduced amounts of oxygen, indicative for electrolyte decomposition during oxygen reduction. Combined electrochemical quartz crystal microbalance (eQCMB) and Differential electrochemical mass spectroscopy (DEMS) measurements reveal that mass changes that occur in the anodic sweep are due to the evolution of CO_2, whereas oxygen evolution takes place without any mass changes. The observed m.p.e-values (mass changes per transferred electron) are affected by convection due to the formation of soluble reduction products which observed in rotating ring disc electrode measurements.

Manuscript submitted March 11, 2016; revised manuscript received May 20, 2016. Published June 17, 2016.

It is common knowledge that, in order to electrify automotive traffic, portable storage systems for electrical energy are required. For the time being lithium-ion-batteries are the most promising candidates for a real life technical application. However, due to the requirement of heavy metal oxides as cathode material their theoretical specific energy density is too low to replace current fuels.[1] Due to the low weight and very negative standard potential of lithium, a lithium-oxygen battery has, in theory, a specific energy density of 13.8 kJ/g (considering the weight of the discharged state and the formation of Li_2O_2 rather than Li_2O) and a theoretical electrochemical efficiency of 90.2% as can easily be calculated from thermodynamics[2,3] (10% of the energy is lost due to the heat flow caused by the entropy).

It is in general accepted that reduction of oxygen in Li^+-containing organic solvents yields Li_2O_2 as a reaction product.[4–6] The process of Li_2O_2 formation in DMSO seems to be unique as it involves the formation of a superoxide intermediate.[7–11] This has not only been shown by CV and rotating ring disc electrode (RRDE) measurements but also by combining electrochemistry with spin-trap experiments and EPR-spectroscopy[12] as well as by DEMS experiments.[7] The remarkable stability of superoxide, despite the presence of Li^+-cations, was ascribed to the large donor number of DMSO[8,13] of nearly 125 kJ/mol[14] as compared to acetonitrile with a donor number of 58.9 kJ/mol.[14] In the latter solvent superoxide intermediates have not been reported so far. However, whether Li_2O_2 forms via lithium induced disproportionation of superoxide or via a direct electrochemical transfer of two electrons depends also on the electrode material: At gold and low overpotentials oxygen is reduced to superoxide, whereas at rhodium direct peroxide formation takes place even at low overpotentials.[7] At glassy carbon both the direct and indirect pathway of peroxide formation take place in parallel irrespective of the applied potential. The formation of superoxide and the formation of peroxide are inner sphere reactions, where the reactants need to adsorb at the electrode surface prior to any charge transfer.[7] The difference in the reaction mechanism of oxygen reduction at gold and glassy carbon might explain why Li-air batteries employing gold sputtered cathodes show superior performance over those electrodes that employ carbon cathodes.[15,16]

Differential electrochemical mass spectroscopy (DEMS) was employed to show that oxygen reduction in DMSO based electrolytes has a true coulombic efficiency (i.e. the ratio of reduced to evolved oxygen) of less than 100%.[17,18] Similar results were also presented by Peng et al.[19] Although the authors of that particular paper did not discuss that their DEMS measurements show that more oxygen is consumed during the cathodic scan than evolved in the subsequent anodic scan the fact remains.

Electrochemical quartz crystal micro balance (eQCMB) measurements produced largely contradicting results. Jie and Uosaki found that per transferred mol of electron 7–37 g/mol of mass were deposited during oxygen reduction.[20] Torres et al. found 60 to 175 g/mol,[21] while Sharon et al. found nearly 23 g/mol.[22] However, in none of the aforementioned studies the potential region of oxygen evolution was discussed. Only very recently Torres et al., employing the more elaborate impedance analysis technique, found a slight decrease of mass in the potential region of oxygen evolution via eQCMB. Yet, this decrease does not account for mass changes observed in the potential region of oxygen reduction.[23]

In the present study we employ RRDE and DEMS in combination with the eQCMB to gain a better understanding of the oxygen reduction and subsequent oxygen evolution from lithium containing DMSO based electrolytes. We try to resolve the different observations by eQCMB in the potential region of oxygen reduction and we discuss the potential region of oxygen evolution in detail. In addition, we will follow up on one of our own papers[18] and will discuss apparently contradicting differences between smooth and porous Au-electrodes in two of our publications. At porous electrodes the number of electrons transferred per oxygen is higher than at smooth electrodes when low overpotentials are applied.[7,18]

Experimental

Chemicals, materials and electrolyte.—Battery grade $LiClO_4$ was purchased from *Sigma Aldrich* and was of 99.99% purity. Tetrabutyl ammonium perchlorate ($TBAClO_4$) was purchased from *Sigma Aldrich* and was of 98% purity. Extra dry DMSO stored over molecular sieves (3 Å) was obtained from *Acros Organics* and was of 99.7% purity. All electrodes in the present study were made from gold.

Argon, oxygen and a 80:20 mixture of argon and oxygen were obtained from *Air Liquide*. All gases were of 99.999% purity. A mixture of 10% oxygen in 90% argon was used in RRDE measurements. This mixture was prepared by adjusting the flow of argon and oxygen correspondingly by the use of two flow metes.

Gold sputtered quartz crystals used for the eQCMB measurements were either obtained from *Indomet GmbH* or from *Quartztechnik Daun GmbH*. Crystals from the first mentioned manufacturer were used in combination with the dual thin layer cell (diameter: 14 mm, 6 MHz). Crystals from the second manufacturer were used in quiescent solution (diameter: 25.4 mm, 5 MHz). The control unit used for the eQCMB measurements was purchased from *Gamry Instruments*. This

*Electrochemical Society Member.
zE-mail: baltruschat@uni-bonn.de

instrument measures, according to the manufacturer two frequencies f_s and f_p which are not the resonance frequencies (with a phase angle 0) but the frequencies at which the impedance goes through a minimum and maximum, respectively.

The electrolyte was prepared under inert gas atmosphere in an *MBraun* glove box. When preparing small amounts of electrolyte (10 ml) and low concentrations (0.1 M) the conducting salt and DMSO where simply mixed.

If larger quantities of electrolyte (200 ml–500 ml) with larger concentrations of $LiClO_4$ (0.5 M) were prepared, it was taken special care that the temperature of the electrolyte did not exceed approximately 50°C. In order to do so the amount of $LiClO_4$ was divided in at least 20 portions and added to the DMSO one at a time under vigorous stirring. After adding 5 portions, the electrolyte was given time to cool down to room temperature again.

A coulometric KF Titrator (C20, *Metler Toledo*) with a diaphragm electrode was used to determine the water content. The freshly prepared electrolyte, had a water content of 6 ppm. However, the water content increases significantly during the experiment, the water content after each measurement is given in the Results section of this paper. In experiments where the dual thin layer cell was used the water content was determined at the outlet. It is likely that the water content in these measurements increases during sampling. Therefore, the water content given for the dual thin layer cell poses a maximum value.

According to the manufacturer of the used electrolyte accumulation of DMSO affects the chemistry involved in the detection process of water. The error was estimated by adding a water standard. The error is in the range of 30%.

Instruments.—All potentiostats and function generators used in this study were homebuilt. RRDE measurements were done with a Ring-Disk Electrode System of *EG&G* (e.g. the motor and control unit) while the tip comprising the disk and ring electrode was obtained from *Pine Instruments*. The mass spectrometer of the DEMS was a QMG 422 from *Pfeiffer Vacuum*.

Reference electrode.—The reference electrode used in this study was a silver wire immersed in a solution of 0.1 M $AgNO_3$ in DMSO. Electrolyte contact to the working electrode was achieved by filling a Teflon tube with the silver containing solution and sealing it with a commercial, rough glass bead. The end with the glass bead was immersed into the working electrolyte, while the other open end was immersed into the silver containing solution. A drawing of the reference can be found elsewhere.[18]

According to the values given by Gritzner et al.[24] the reference electrode described above has a potential of +3.89 V with respect to the Li^+/Li couple.

Dual thin layer cell.—A drawing of this particular cell type (as well as of the conventional cell) can be found in Ref. 25 In short: The dual thin layer cell comprises two compartments that are constantly flushed with electrolyte. The electrolyte enters the first compartment where the working electrode is placed and electrochemistry takes place (upper compartment). Reaction products are flushed along with the electrolyte into the second compartment (lower compartment). A porous Teflon membrane pressed on a steel frit forms a barrier between electrolyte and vacuum. Volatile reaction products evaporate through the Teflon membrane into the vacuum of the mass spectrometer and are detected according to their masses. The electrolyte then is flushed to the outlet. The flow of the electrolyte going from the first to the second compartment causes a delay between the faradaic current and the response in the ionic current. In all calculations where the ionic current was correlated to processes appearing at the working electrode this delay time was accounted for.

The reference electrode is placed at the inlet. The main counter electrode (gold) is placed at the outlet. In order to reduce electronic oscillations, a second counter electrode is placed at the inlet. The main counter electrode is connected via a resistance of 1 Ω, the second via a 1 MΩ resistance to ascertain an optimal distribution of the current.

A more detailed description of the dual thin layer cell along with its versatile applications for DEMS can be found elsewhere.[25–29]

Conventional DEMS cell.—The conventional cell is a cylindrical glass body with a surface grinding at its lower part. The surface grinding is pressed on a gold sputtered porous Teflon membrane, which rests on a steel holder and acts as the working electrode. The steel holder features a steel frit through which volatile reaction products flow into the vacuum. The reference electrode, the counter electrode and a Teflon tube through which gas is bubbled are immersed into the electrolyte if not stated otherwise. A drawing of the cell can be found elsewhere.[18,25,29]

In the classical cell the partial pressure of oxygen at the electrode is very low because oxygen evaporates immediately at the interface between vacuum and electrolyte. The exact value of the partial pressure cannot be determined.

RRDE measurements.—In the RRDE measurements we employed a tip with exchangeable disc electrodes and a ring electrode made from glassy carbon. The tip was purchased from *Pine Instruments*. To ensure that the electrochemical reaction at the ring electrode and at the applied potential takes place under diffusion limitation we reduced oxygen under the same conditions from an electrolyte of 0.5 M $TBAClO_4$ in DMSO. In this electrolyte oxygen is reduced quantitatively to superoxide. We checked for various potentials at the ring electrode whether the observed collection efficiency matches the theoretical collection efficiency. For a rotation speed of 2940 rpm the observed collection efficiency matches the theoretical value at a potential of −0.6 V.

Calibration for O_2.—In order to correlate the measured ionic current for mass 32 to the amount of oxygen that actually enters the mass spectrometer, calibration is required.

In order to account for the collection efficiency of the used cells, the state of the filament and other setting of the mass spectrometer, oxygen was reduced in an electrolyte of 0.5 M $TBAClO_4$. It is known that oxygen in this electrolyte is reduced to superoxide.[6,18] Therefore, the ratio of the measured ionic current for mass 32 and the faradaic current divided by Faraday's constant gives the calibration constant K^*. K^* does not only account for the probabilities of ionization, fragmentation and detection but also for the probability of a compound to enter the mass spectrometer (collection efficiency). The collection efficiency of the dual thin layer cell depends on the flow rate, but also on the exact geometry of the cell that changes in each experiment, due to different forces applied to the cell. Therefore, calibration was done after each experiment (K^* of the dual thin layer cell changes by roughly ±10%).

In both cells, a baseline was subtracted from the ionic currents. Therefore, the ionic current for O_2 (mass 32) appears as a negative current during oxygen reduction.

Calibration of the eQCMB.—The quartz crystal microbalance was calibrated by electrodeposition of copper from a solution of 0.1 M $CuSO_4$ in 0.1 M H_2SO_4. The calibration constant for the quartz crystal in the dual thin layer cell was 313 Hz/μg and for the crystal used in stationary solution was 17.49 Hz/μg

Results

Figure 1 shows a number of CV's and MSCV's (i.e. mass spectroscopic cyclic voltammogram) for mass 32 and 44 that are obtained when a gold sputtered Teflon membrane is used as a working electrode in the conventional cell. In this experiment an electrolyte of 0.1 M $LiClO_4$ in DMSO was employed. As the potential approaches −1 V, oxygen reduction is observed. This is clear from the reduction current in Figure 1A and the negative ionic current for mass 32 in Figure 1B. In the potential region of oxygen reduction both the ionic current for mass 32 and the faradaic current go through a minimum. The peak is not due to diffusion limitation: In the conventional cell the working electrode is situated at the interface between vacuum and electrolyte.

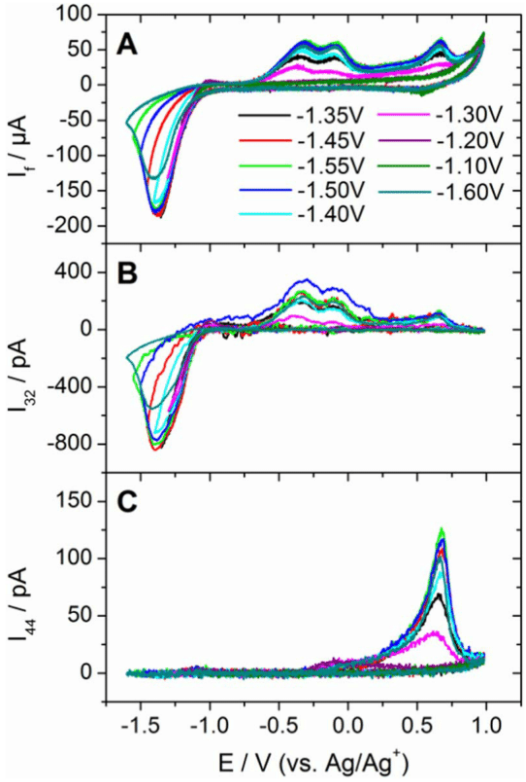

Figure 1. CV (A) and MSCV for mass 32 (B) and 44 (C) obtained at a gold sputtered Teflon membrane in the conventional cell (porous electrode; convection only due to purging with pure oxygen). Electrolyte: 0.1 M $LiClO_4$ in DMSO; water content: 89 ppm; sweep rate: 20 mV/sec. The sequence in the legend follows the sequence of the experiment. Lower potential limit as indicated, upper potential limit: 1.0 V. All curves were obtained in the same experimental set up.

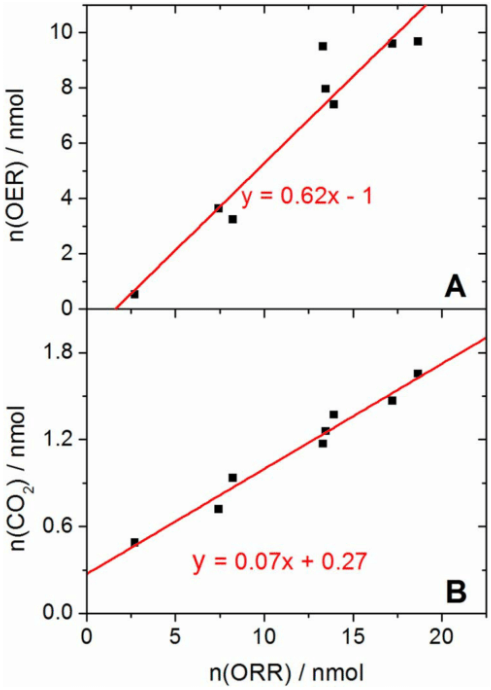

Figure 2. Amounts of evolved oxygen (A) and Amounts of evolved CO_2 (B) plotted against the amount of oxygen reduced in the previous cathodic sweep. Data were obtained from the curves in Figure 1 (porous electrode; convection only due to purging with pure oxygen).

Hence, oxygen that reaches to the electrode passes into the vacuum immediately if it is not reduced electrochemically first. Therefore, in the conventional cell the flux of oxygen to the working electrode is diffusion limited all the time. The peak in Figure 1A appears because reduction products are deposited on the surface and block the electrode. When electrochemical reduction of oxygen stops, every oxygen molecule that reaches the electrode evaporates. Therefore, the ionic current for mass 32 returns to its baseline value and we observe a peak in the ionic current for mass 32 (Figure 1B) as well. This also demonstrates that the pores of the membrane are not blocked.

In the anodic sweep three peaks appear at −0.3 V, at −0.1 V and at 0.7 V in the faradaic current. The peaks at −0.3 V and at −0.1 V are paralleled by oxygen evolution. Minor quantities of oxygen are also evolved during the third peak. However, in Figure 1C a more intense signal parallel to the third peak appears in the ionic current for mass 44, which is indicative for the evolution of CO_2.

In Figure 1 the lower potential window was successively decreased, and by doing so the amount of oxygen, reduced in each cycle, was increased. When the amount of oxygen, evolved in the following anodic sweep of each cycle, is plotted against the amount of reduced oxygen a straight line is obtained which has a slope smaller than one and a positive intercept with the x-axis (c.f. Figure 2A). We have shown similar results in a previous publication, where the intercept with the x-axis is even more positive.[18] In the present paper we will give an explanation for the smaller slope and the positive intercept with the x-axis (see below). The curves shown in Figure 1 were reproduced for the present paper in order to be able to show the MSCV for mass 44 and to be able to give a water content in the electrolyte. (This information was not given in Ref. 18.)

In Figure 1C a peak appears at 0.7 V in anodic direction, which is only present when oxygen was reduced in the previous cathodic sweep. This peak does neither appear in Ar saturated solution (when cycling in the same potential range as in Figure 1) nor in O_2-saturated solution when the potential range of O_2 reduction was excluded. This is shown in Figure S1 and Figure S2 of the supporting information. A fragment with mass 44 is indicative for the evolution of CO_2. Since DMSO is the only carbon source in the system under investigation the evolution of CO_2 must ultimately result from electrolyte decomposition.

In Figure 2B the amount of evolved CO_2 is plotted against the amount of reduced oxygen during the previous cathodic sweep. From the resulting linear relationship it is obvious that electrolyte decomposition relates to oxygen reduction. It is evident from Figure 2 that the sum of the evolved amounts of oxygen and the evolved amounts of CO_2 do not account for the amounts of reduced oxygen. A more detail discussion on the true columbic efficiency (e.g. the ratio of reduced to evolved amounts of oxygen is given in the Discussion section of this paper)

According to Equation 1 it is possible to calculate the number of electrons that are transferred per reduced molecule of oxygen.

$$z = i_f \cdot K^*/i_{32} \qquad [1]$$

In Equation 1, z is the number of transferred electrons in e^-/O_2, i_f is the faradaic current, i_{32} is the ionic current for mass 32 and K^* is a calibration constant.

The z-value was calculated from the data shown in Figure 1 and the result is plotted as a function of the potential in Figure 3. In Figure 3 the z-value starts from 1.5 e^-/O_2 and increases to 2 e^-/O_2 as the potential decreases beyond −1.2 V. The z-value shown here resemble those already shown in Ref. 18. However, they differ from the z-values obtained at smooth gold electrodes, where the z-value at low overpotentials is close to 1 e^-/O_2 (*vide infra*).

Oxygen reduction in lithium-containing electrolytes leads to the formation of solid Li_2O_2.[30,31] In addition, also decomposition products deposit on the electrode. The formation of decomposition products is indicated by the evolution of CO_2. In order to investigate this deposit of reduced oxygen species and decomposition products we employed the electrochemical quartz crystal microbalance technique (eQCMB).

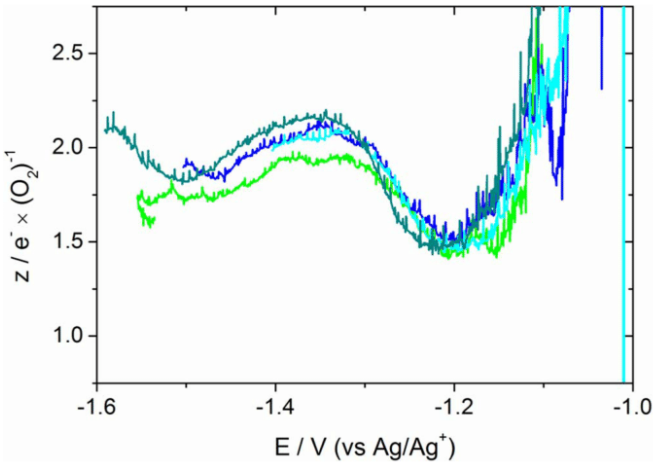

Figure 3. Number of electrons transferred per oxygen as a function of potential. The curves shown were calculated from the data shown in Figure 1 (porous electrode). Color coding as in Figure 1.

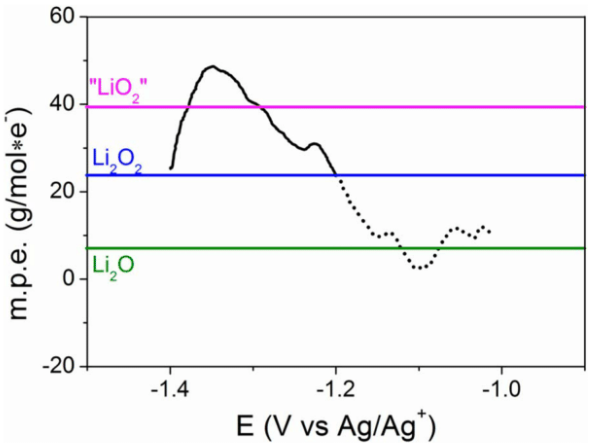

Figure 5. m.p.e.-values during oxygen reduction. The values were calculated from Equation 3 and the averaged curves shown in Figure 4 (smooth gold electrode; stagnant solution).

Figure 4 shows the results that were obtained in a quiescent solution in 0.1 M $LiClO_4$ in DMSO. The curves shown are the average of 12 subsequent cycles in a single set up. In Figure 4A the CV and in Figure 4B the mass change is shown as a function of potential (The derivative of the deposited mass is shown because it allows a better comparison to the current). Note that there is a delay of about 250 mV between the onset of oxygen reduction (CV) and the potential at which mass deposition is observed. In the following anodic sweep a major mass change is only observed at a potential larger than 0.3 V. At this potential the evolution of oxygen has largely ceased and CO_2 evolution starts (c.f. Figure 1). No mass change is observable in the potential region of oxygen evolution (−0.7 V to 0.1 V).

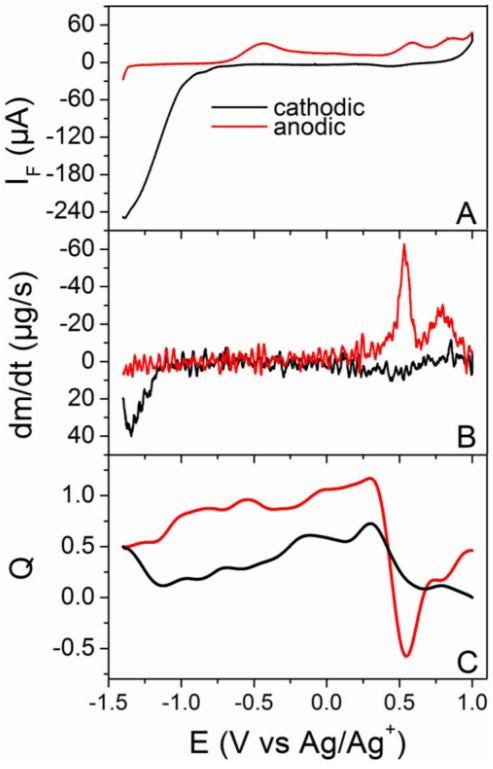

Figure 4. QCM-measurement in a quiescent solution at smooth gold electrodes. 0.1 M $LiClO_4$ in DMSO, saturated with oxygen. Sweep rate 10 mV/s. A: CV; B: First derivative of mass with respect to time as a function of applied potential (inverted y-axis); C: Quality factor as a function of applied potential. The curves shown are the average of 12 cycles obtained in a single setup (In order to average the quality factor the first derivative of Q was formed. dQ/dt was averaged and the result integrated, by doing so constant value was omitted. Because of that Q appears to have unreasonably low values). Red anodic run, black cathodic run.

Figure 4C also features the reduced quality factor Q as a function of the applied potential. Q is calculated according to Equation 2 from the two resonance frequencies f_s and f_p.

$$Q = (f_s + f_p) / (2 \cdot (f_s - f_p)) \quad [2]$$

f_s and f_p in Equation 2 are not the resonance frequencies of the quartz crystal itself (which has only one resonance frequency f_E) but of the BVD-equivalent circuit[32] that describes how the quartz behaves as an electronic element in an AC-field. In practice it is difficult to measure f_E, but f_s and f_p are more easily accessible. Although the exact values of f_E, f_s and f_p differ significantly, it is possible to approximate Δf_E (changes of f_E) by Δf_s or Δf_p (changes of f_s and f_p, respectively). According to the Sauerbrey equation changes in Δf_E arise when the mass of the quartz crystal changes.[33] That is also true for Δf_s or Δf_p, but changes in f_s and f_p can also appear when the friction at the interface between electrode and electrolyte changes. f_E is not affected by the friction and it is, therefore, necessary to check whether changes in f_s and f_p are due to mass changes or due to friction. Changes in friction show up in changes of the reduced quality factor which can be calculated from Equation 2. A decrease in the quality factor Q indicates an increase of friction at the interface between the oscillating electrode and the electrolyte. The latter in turn signifies an altered viscosity of the matter in contact with the electrode.[32]

Given the noise level there are no significant changes in the quality factor in the cathodic sweep. However, considerable changes occur in the anodic sweep. At about 0.3 V Q decreases and reaches a minimum at 0.49 V. The change in Q is mirrored by the first peak in the anodic sweep of the dm/dt vs. E plot. The signal in Q parallel to the second peak in the dm/dt vs. E plot is much less significant.

$$\text{m.p.e} = F \cdot (dm/dt) / i \quad [3]$$

the mass change that is due to the transfer of one mol of electrons (m.p.e. value) was calculated. In Equation 3 i is the current, F is Faraday's constant and dm/dt is the mass change. The m.p.e value is plotted as a function of the applied potential in Figure 5. The m.p.e value steadily increases as the potential becomes more negative than −1.15 V and reaches a value of 48 g/mol · e^- at −1.35 V. There is no plateau at either 23 g/mol · e^- or 39 g/mol · e^- that would be expected for the quantitative deposition of lithium peroxide or lithium superoxide, respectively. The formation of the latter has been suggested previously in literature.[20] Above −1.2 V m.p.e values are not meaningful because the frequency change is negligible.

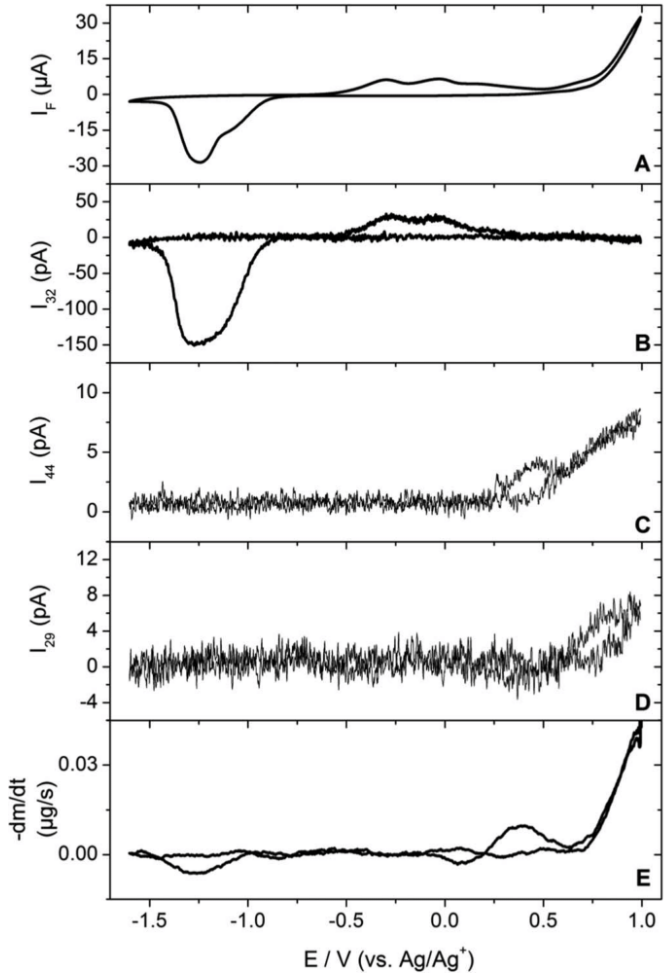

Figure 6. QCM and DEMS measurements combined. This was possible by using a dual thin layer cell. The electrolyte was kept in storage vessel and was bubbled with a mixture of argon and oxygen (Ar : O_2 = 80 : 20) throughout the experiment. The flow rate of the electrolyte was 5 µL/s and the sweep rate was 10 mV/s. Water content max. 105 ppm. A: CV; B: MSCV for mass 32; C: MSCV for mass 44; D: MSCV for mass 29; E: First derivative of mass with respect to time as a function of applied potential (inverted y-axis); The shown curves are the average over 38 cycles. The experiment was conducted at a smooth gold electrode under convective conditions.

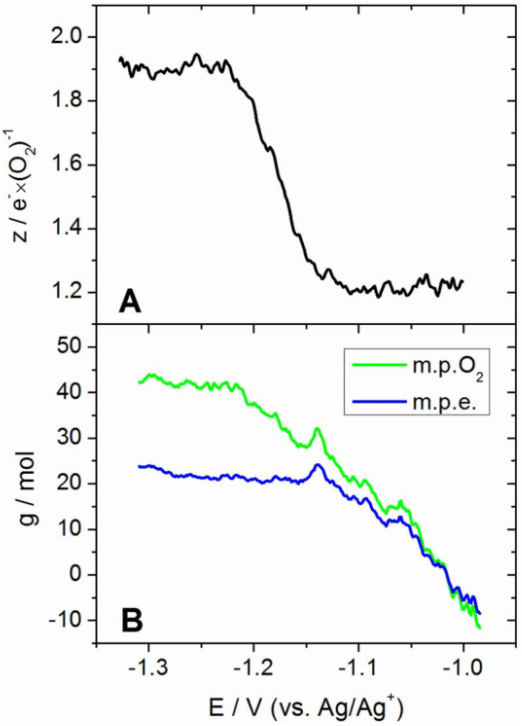

Figure 7. A: z-values for oxygen reduction as a function of potential, calculated via Equation 1 from the data in Figure 6. B: m.p.e.- and m.p.O_2-values for oxygen reduction as a function of potential, calculated via Equation 3 and Equation 4, respectively, from the data in Figure 6 (smooth gold electrode, defined convection).

The missing mass change in the potential region of oxygen evolution is strange because oxygen evolution should result in the removal of solid Li_2O_2 from the electrode. The data presented in Figure 6 show that oxygen is evolved from Li_2O_2, indeed. The curves were obtained when oxygen was reduced under continuous electrolyte flow. The convection conditions in this cell are more defined then in the conventional cell[34,35] and soluble reduced oxygen species are transported away. Hence, they are not available for oxygen evolution. The signal in the ionic current for mass 32 (Figure 6B) must, therefore, be due to the oxidation of species attached to the electrode. Yet, oxygen evolution comes along without mass changes (Figure 6E). A discussion on that will be given in the Discussion section of this paper.

Aside from the CV (A), the MSCV for mass 32 and 44 (B, C) and the dm/dt vs. E plot (E) Figure 6 also features the MSCV for mass 29 (D). The latter was collected to ensure that the evolution of a signal in the MSCV for mass 32 in the anodic sweep can be assigned to oxygen evolution: In principle it is conceivable that other fragments than O_2^+ cause a signal for mass 32. For instance methanol, formed during electrolyte decomposition, could emulate oxygen evolution. However, organic molecules usually form a CHO^+-fragment with mass 29 as well. The absence of a signal in the MSCV for mass 29 in the potential region of oxygen evolution shows unambiguously that the signal in the MSCV for mass 32 is due to oxygen evolution.

As in Figure 4, also in Figure 6 there is a delay between onset of oxygen reduction and mass deposition. This delay correlates to a step in the CV, which is not present in the MSCV for mass 32. As was shown previously,[7] this step corresponds to a change in the mechanism of oxygen reduction from the indirect pathway (where superoxide is formed electrochemically and disproportionates to Li_2O_2 in the aftermath) to the direct pathway (by which peroxide is formed electrochemically). According to Equation 1 the number of electrons transferred per reduced oxygen was calculated from the ratio of the faradaic current and the ionic current for mass 32. The resulting z-values are plotted in Figure 7A as a function of the potential.

The z-values displayed in Figure 7A show again (c.f. Ref. 7) that a transition from the indirect to the direct pathway of peroxide formation takes place. This transition is responsible for the delay between oxygen reduction and mass deposition: Initially soluble superoxide is formed, which is transported away from the electrode. Only when the potential region of peroxide formation is entered the formation of a solid deposit is expected. In previous eQCMB measurements a lower than expected mass change was assigned to the formation of soluble superoxide at low over potentials.[36] Indeed, when the potential of −1.2 V is reached, where Figure 7A indicates that oxygen is reduced nearly entirely to peroxide, both the m.p.e. and the m.p.O_2 values, reach a plateau in Figure 7B. The m.p.e.-values in Figure 7B were calculated according to Equation 2, while the m.p.O_2-values (the mass change that is caused per reduced oxygen) were calculated according to Equation 4 from the data in Figure 6:

$$\text{m.p.}O_2 = (\text{dm}/\text{dt}) \cdot K^*/I_{32} \quad [4]$$

In Equation 4 dm/dt is the mass change, I_{32} is the ionic current for mass 32 and K∗ is the calibration constant for the dual thin layer cell.

Note that the z-plot in Figure 7A differs significantly from the z-plot in Figure 3. That is, at the smooth gold electrode and at low overpotentials the z-value is close to one and experiences a steep

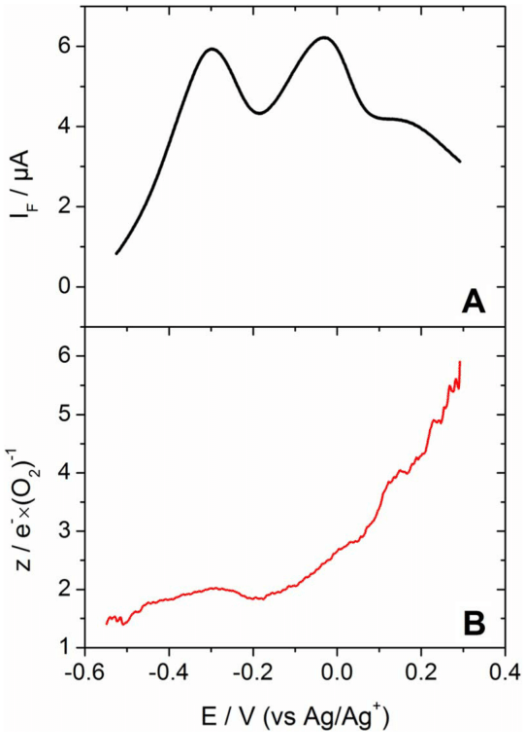

Figure 8. faradaic current (A) and the z-value (B) in the potential range of oxygen evolution. he z-values were calculated from the data shown in Figure 6 (smooth electrode, convection) according to Equation 1.

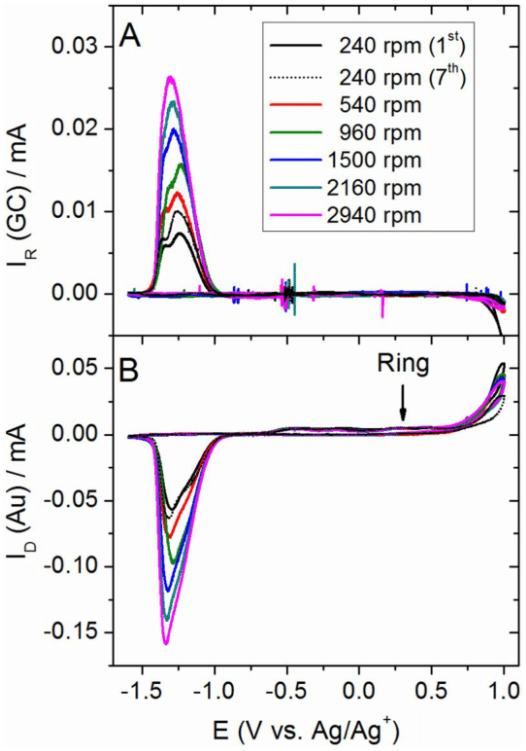

Figure 9. RRDE measurement with various rotation speeds at a gold disc electrode and a GC-ring electrode set to 0.3 V. Electrolyte: 0.1 M $LiClO_4$ in DMSO purged with a mixture of 10% O_2 and 90% Ar. Sweeprate: 10 mV/sec. Water content: 100 ppm. The experiment was conducted at a smooth gold electrode under convective conditions.

increase as the overpotential increases. On the other hand, when gold sputtered electrodes were used the z-value is above 1.5 e^-/O_2 in the whole potential range. These results seem to contradict each other, as in both experiments a Li-containing DMSO based electrolyte and the same electrode material was used. This difference is discussed in detail below.

From the data in Figure 6 we have also calculated the z-values for the oxygen evolution. These data are shown as a function of the applied potential in Figure 8B. To simplify comparison Figure 8A also features the faradaic current in the potential region of oxygen evolution. Oxygen evolution proceeds in two distinct peaks which we have assigned in a previous publication to the oxidation of two different monolayers of Li_2O_2 on the gold surface (refer to Ref. 7 for a detailed discussion of the matter). Oxygen evolution in the first peak at −0.3 V proceeds via the transfer of 2 e^-/O_2 and with 2.4 e^-/O_2 in the second peak at −0.03 V, which indicates that oxygen evolution in both peaks is due to the oxidation of peroxide. The slightly larger z-value of 2.4 e^-/O_2 in the second peak is probably due to some sort of side reaction. Recently, based on UV/vis and SERS studies, Yu and Ye have proposed that the second peak is due to the oxidation of LiO_2.[37] This reaction should come along with a z-value of only one. Based on the data presented in Figure 8B we have to reject this interpretation.

At even more positive potentials than −0.16 V oxygen evolution in Figure 6 continues in a shoulder (c.f. ionic current for mass 32). The z-values are probably distorted due to parallel electrochemical processes. That is why we cannot assign the evolved oxygen to any reduced oxygen species, or give any interpretation on its origin.

Figure 9 shows RRDE-results obtained at a gold-disk electrode and a glassy carbon (GC) ring electrode. The latter was set to a potential of 0.3 V, which is well inside the potential region of Li_2O_2-oxidation. In Figure 9B the current at the disc electrode and at low rotation speeds experiences a shoulder, much alike to the one observed in Figure 6, which indicates the change from the indirect to direct pathway of peroxide formation. The shoulder in the current at the disc is paralleled by a peak in the current at the ring. This is most probably due to the formation of superoxide at the disc electrode and its subsequent oxidation at the ring electrode, as has been discussed in literature several times[10,11] However, the transition from the direct to the indirect pathway of peroxide formation has not been observed in an RRDE-measurement before. This is due to the fact that in the current study the electrolyte was not saturated with oxygen, but purged with a mixture of only 10% O_2 and 90% Ar. Due to the low oxygen concentration in our experiment superoxide formation enters diffusion limitation at low rotation speeds before the mechanism of oxygen reduction shifts from the indirect to the direct pathway of peroxide formation. In oxygen saturated solution or with high rotation speeds (c.f. 2940 rpm in Figure 9) the transition from the indirect to the direct pathway of peroxide formation and electrode blocking, due to the precipitation of Li_2O_2, cannot be resolved.

Figure 9 shows that the transition from the indirect to the direct pathway of peroxide formation comes along with a second peak (low rotation speeds) or a shoulder (medium rotation speeds) in the current at the ring electrode. Since decomposition products are barely oxidized at the potential that was applied to the ring electrode (0.3 V, c.f. Figure 1 and Figure 6) the second shoulder is most probably due to the oxidation of reduced oxygen species. The likeliest reduced oxygen species that can react at the ring electrode is superoxide. Despite the fact that oxygen is predominantly reduced to Li_2O_2 at large overpotentials, it is still possible that a fraction of the oxygen is also reduced to superoxide. Indeed, in Figure 7A the z-value at potentials smaller −1.2 V remains somewhat below 2. This is also the case in other studies[7] which indicates that 10–20% of oxygen is reduced to superoxide in the potential range between −1.2 V and −1.35 V. The shoulder in the current at the ring is observed at even lower potentials and appears when the current at the gold (disc) electrode decreases significantly due to blocking by a film of Li_2O_2. We have proposed previously for oxygen reduction at platinum that Li_2O_2 exerts a geometric effect which increasingly inhibits the formation of peroxide. Li_2O_2 could influence the mechanism of oxygen reduction at gold electrodes in the same way. As a result the share of oxygen that is reduced

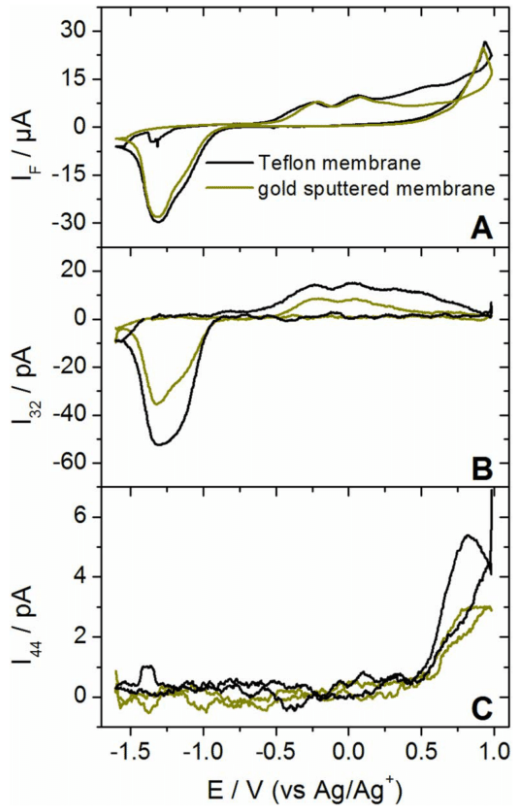

Figure 10. CV (A) and MSCV for mass 32 (B) and 44 (C) obtained in the dual thin layer cell with a smooth gold electrode in the upper compartment and a gold sputtered Teflon membrane (yellow curve; rough gold electrode) or a Teflon membrane (black curve) in the lower compartment. Electrolyte: 0.5 M $LiClO_4$ in DMSO; water content max 22 ppm; sweep rate: 10 mV/sec, flow rate: 5 µL/sec. The experiment was conducted under convective conditions.

to superoxide increases significantly as the electrode is deactivated. Hence, we observe a peak in the current at the ring electrode. This interpretation is also in good agreement with the results presented by Yu and Ye who have shown by means of UV/vis spectroscopy that parallel to peroxide also a significant amount of superoxide is formed and that the share increases as the electrode is deactivated.[37] RRDE-measurements in connection with potential step experiments also show that ring currents are observed irrespective to which potential the disc electrode is stepped, whereas the peak height of the ring current depends on the disc potential.[11]

It is the prevailing view in literature that the species that reacts at the ring electrode is superoxide.[6,8,10,11] However, it is also conceivable that hindered nucleation results in the formation of dissolved LiO_2^- which could react at the ring electrode. Since the value of z, which is below 2 suggestes the formation of superoxide, we deem this interpretation unlikely, but it cannot be ruled out based on the presented data.

RRDE-results obtained when smaller potentials were applied to the ring electrode can be found in the supporting information (Figures S3 to S6). Even at ring potentials lower than −0.7 V, the onset potential of oxygen evolution due to Li_2O_2-oxidation, a second peak in the current at the ring electrode is observed. This gives further support to the idea that superoxide reacts at the ring electrode.

When oxygen is reduced via the indirect pathway of peroxide formation, Li_2O_2 results from chemical disproportionation of superoxide. In order to investigate whether the presence of gold at open circuit can influence this reaction we performed the following experiment. We conducted oxygen reduction in our dual thin layer cell. In the first measurement (black curve in Figure 10) we used an unaltered Teflon membrane in the lower compartment as an interface between vacuum and electrolyte. In the second measurement this membrane was replaced by a gold sputtered Teflon membrane (yellow curve in Figure 10). Figure 10 shows the CVs and the MSCVs for masses 32 and 44 for both measurements.

In Figure 10 the CV remains largely unaffected, when the Teflon-membrane is changed to a gold sputtered Teflon-membrane. A shoulder due to superoxide formation appears in both cases, followed by a peak when the mechanism of oxygen reduction shifts to the direct pathway of peroxide formation.

The intensity of the ionic current for both mass 32 and 44 is reduced when the Teflon membrane is changed to a gold sputtered Teflon membrane. This might be due to changes in the exact geometry of the cell setup, when the membrane is changed (the geometry might be altered, when the spacers used are compressed). However, the changes in the MSCV for mass 32 go beyond a reduced sensitivity: The shape of the MSCV in the potential region of oxygen reduction now follows the shape of the CV and features a shoulder at low overpotentials. This means that in the potential region of superoxide formation less oxygen is consumed as compared to the potential region of peroxide formation. This is not the case when a Teflon membrane is used (black curve of Figure 10): Equal amounts of oxygen are reduced regardless whether superoxide or peroxide is formed electrochemically. Since the electrochemical process is not affected by the type of membrane in the lower compartment there is bound to be another process that yields oxygen and is indeed affected by the presence of gold. One possible reaction that would result in oxygen evolution is the disproportionation of superoxide to peroxide. This reaction is slow on the timescale of a DEMS experiment when a Teflon membrane is used (otherwise the transition from $z \approx 1$ e^-/O_2 to $z \approx 2$ e^-/O_2 would not be observable). However, the disproportionation of superoxide could be heterogeneously catalysed by gold at open circuit potential. Notwithstanding this, also any other gold catalysed reaction in which superoxide is oxidized could cause the changes in the MSCV for mass 32 in Figure 10B. We will follow up on this in another publication that will give further support to the notion that superoxide undergoes a heterogeneous reaction at gold at open circuit potential.

Discussion

Superoxide versus peroxide formation.—It is evident from Figure 7A that the z-value increases from approximately 1 e^-/O_2 at low overpotential to approximately 2 e^-/O_2 as the potential passes −1.2 V, which indicates that oxygen is reduced to superoxide at low overpotentials and at gold electrodes. At higher overpotentials oxygen is reduced to peroxide, which has also been proposed by others.[6,7,36,38]

Also the QCMB-results support the idea that the product distribution of oxygen reduction shifts from superoxide to peroxide: In Figure 4 there is a delay of about 250 mV between the potential at which oxygen reduction starts and at which the formation of a deposit is observed. A similar delay is present in Figure 6. Since superoxide is considered soluble its formation should not result in the formation of a deposit, whereas peroxide precipitates as Li_2O_2. The formation of the latter causes a frequency shift. The potential at which the formation of a deposit is observed corresponds well to the potential at which z increases from 1 e^-/O_2 to 2 e^-/O_2.

Decomposition of the electrolyte.—The evolution of CO_2 only occurs in the anodic sweep when oxygen was reduced in the previous cathodic sweep. The evolution of CO_2 indicates that electrolyte decomposition takes place (c.f. Figure 1 and Figure 6). The electrochemical oxidation of the electrolyte (which is the only carbon source in the system under investigation) should not depend on the reduction of oxygen in a previous cycle. Therefore, CO_2 evolution is the result of the electrochemical oxidation of decomposition products which form during oxygen reduction. The formation of decomposition products also shows up in the m.p.e.-values of the quiescent solution: Figure 5 shows that the m.p.e-values that are observed in the potential range of peroxide formation are much larger than expected for Li_2O_2 which indicates the additional deposition of decomposition products. However, it needs to be pointed out that in the absence of convection most of the reduced oxygen will precipitate as Li_2O_2,

eventually. Hence, in addition to oxygen that is reduced to Li_2O_2 via the direct pathway also superoxide will be reduced to Li_2O_2 via the transfer of 1 electron. The expected m.p.e value for the latter reaction is 46 g/mol $\cdot$ e$^-$. It can be expected that superoxide is present at potentials where the direct pathway of peroxide formation prevails because it was formed at low overpotential and remained at least partially in front of the electrode. A distortion to higher than expected m.p.e-values in the potential range of peroxide formation is, therefore, expected. However, when the overall mass change and the total charge in the potential region of oxygen reduction is considered, then the m.p.e-value amounts to 30 g/mol $\cdot$ e$^-$ which is still larger than the expected 23 g/mol $\cdot$ e$^-$ for Li_2O_2 formation.

On the other hand, an m.p.e.-value of 21.5 g/mol $\cdot$ e$^-$ and an m.p.O_2-value of 42 g/mol $\cdot$ O_2 is observed under convection conditions (c.f. Figure 7B). These values correspond well to those expected for Li_2O_2 formation. This appears to contradict the notion of an additional deposition of decomposition products which we derived from the larger than expected m.p.e-values obtained in quiescent solution. However, even at high overpotentials where peroxide formation dominates not all the electrochemically reduced oxygen species precipitate as Li_2O_2 on the surface of the electrode (c.f. RRDE measurements in Figure 9). When a portion of the reduced oxygen species is transported away under convection conditions then lower than expected m.p.e- and m.p.O_2-values would be observed because a portion of the current is not due to the formation of a solid deposit. Hence, the fact that the observed m.p.e.-values match well those expected for Li_2O_2 formation is just a coincidence that results from the additional deposition of decomposition products and an incomplete precipitation of reduced oxygen species.

Our results appear to be in contradiction to the results presented by Sharon et al. who found m.p.e.-values that fit well to the quantitative precipitation of pure Li_2O_2.[22] However, Sharon et al. used a cell that contained a fairly low volume of 3 ml electrolyte that was purged with oxygen throughout the experiment. Considering our results concerning superoxide formation and the influence of convection on the observed m.p.e.-values, the well fitting m.p.e.-values observed by Sharon et al. might be the result of convection caused by electrolyte purging.

Also the work of Torres et al. suggests that the exact experimental conditions have a significant effect on the observed m.p.e-value:[21,23] Due to a rough morphology of the Li_2O_2 deposit solvent molecules can be entrapped in the Li_2O_2 layer which results in very large m.p.e-values of 61 to 175 g/mol $\cdot$ e$^-$ during oxygen reduction in DMSO based electrolytes.[21] The formation of a rough film was confirmed by impedance analysis of the eQCMB. The experiment showed that the resistance in the BVD-equivalent circuit[32] increases, which shows up when the friction at the electrode electrolyte interface increases.[23] However, the experimental conditions in our study (cycling to large overpotentials) are different from those in the study of Torres et al. (step to moderate overpotentials)[23] and different morphologies of the deposit can be expected.[39] Notwithstanding this, it was also proposed that under the experimental conditions a reaction between Li_2O_2 and DMSO occurs that results in decomposition products.[21,40] The formation of the latter was confirmed via XPS.[40]

It is evident that interpretation of m.p.e-values is not straight forward as many effects can distort eQCMB results. If parts of the current result in the formation of soluble species parallel to the formation of a solid deposit, the m.p.e-values calculated according to Equation 3 are distorted to lower values. On the other hand electroless processes parallel to electrochemistry can also result in mass changes. The formation of decomposition products (this study) or voids in the deposit that entrap solvent molecules (Torres et al.[23]) are examples for the difficulties that arise if the oxygen reduction reaction in organic solvents is investigated.

Electrolyte decomposition takes place during oxygen reduction, but since two different reduced oxygen species are formed - superoxide and peroxide - the question arises which of these species (or intermediates that arise during its formation) initiates electrolyte decomposition. No mass deposition takes place in the potential range of superoxide formation, hence, no decomposition products precipitate on the electrode, whereas parallel to Li_2O_2-formation the deposition of decomposition products is observed. Therefore, peroxide or species that form during peroxide formation are the active species that initiates electrolyte decomposition - or at least causes the formation of those decomposition products that precipitate during oxygen reduction. The formation of a deposit would be expected at low overpotentials if superoxide was the active species that initiates electrolyte decomposition. Sawyer et al. have shown previously that a solution of superoxide is stable in DMSO over weeks.[41] This is supported by the fact that we have never observed formation of CO_2 after reduction of oxygen in an electrolyte of 0.1 M $TBAClO_4$ in DMSO (c.f. Figure S7). Since no mass deposition is observed above -1.2 V in our eQCMB measurements this is also true for Li^+-containing electrolytes, where the polarization of DMSO, by the large charge density of the Li^+-cation could facilitate any reaction between superoxide and DMSO. Electrolyte decomposition, therefore, takes place during peroxide formation. However, we cannot rule out that superoxide causes the formation of other decomposition products that remain in solution and are not detectable via eQCMB. Based on our results we cannot decide whether solid Li_2O_2 or any intermediate that occurs during peroxide formation initiates electrolyte decomposition.

It has been suggested before that decomposition of DMSO based electrolytes occurs during oxygen reduction.[17,22,40,42,43] However, our results might be perceived to contradict the results of others: Schroeder et al. have shown that DMSO exposed to Li_2O_2 does not undergo any decomposition.[44] Even though DMSO exposed to solid Li_2O_2 does not undergo any decomposition this does not mean that DMSO is stable when exposed to intermediates of electrochemical peroxide formation. Another report that appears to be in contradiction to our results is the work presented by Peng et al.[19] who conducted DEMS measurements on oxygen reduction and evolution from DMSO based electrolytes at gold electrodes. Peng et al. did not observe any CO_2 evolution at gold electrodes. However, the spectra presented exclude the potential range in which we observe CO_2 evolution. Furthermore, it is noteworthy that CO_2 evolution in our study takes place at the very same potential at which Peng et al. observe the evolution of CO_2 at carbon based electrodes (0.7 V vs $Ag/Ag^+ \approx 4.6$ V vs Li/Li^+). It is rather unlikely that the evolution of CO_2 observed by Peng et al. is due to carbon corrosion: The curves presented in Ref. 7 show that at glassy carbon similar amounts of CO_2 are evolved as at other electrode materials. By means of FTIR Peng et al. have shown that relatively small amounts of Li_2CO_3 and $LiHCO_3$ form when a Li-O_2 battery is discharged that employs a DMSO based electrolyte and an oxygen electrode manufactured from gold. The amount of Li_2CO_3 and $LiHCO_3$ formed upon discharge increases significantly when the oxygen electrode is manufactured from Super-P. Model batteries are discharged with low current densities and, therefore, at low overpotentials (different from the DEMS results shown by Peng et al. where the electrode was cycled into the potential window of direct peroxide formation). Under these conditions oxygen is reduced to superoxide at gold electrodes.[45] Li_2O_2 is formed afterwards via the chemical, lithium-induced disproportionation of superoxide where we do not observe electrolyte decomposition. However, at glassy carbon electrodes roughly 50% of oxygen is converted to peroxide via the direct, electrochemical transition of two electrons.[45] Since we have shown that electrolyte decomposition occurs during electrochemical peroxide formation the formation of decomposition products upon discharge of batteries with carbon based electrodes is expected. The effect of the electrode material on the formation of decomposition products upon discharge of lithium oxygen batteries which was observed by Peng et al. is understandable by the results presented here and in context with the results presented in Ref. 45.

The water content of 90 ppm in the DEMS measurement of Figure 1 is relatively high. It cannot be excluded that trace amounts of water have an effect on the evolution of CO_2. In fact, this is quite likely: From the supporting information of Ref. 7 it is clear that the evolved amounts of CO_2 tend to increase as the water content in the electrolyte increases. However, it is not clear whether there is a

primary or secondary effect of water. In the former case water would enhances electrolyte decomposition in the latter case water would facilitate oxidation of decomposition products and, hence, would make electrolyte decomposition more visible. Notwithstanding this, CO_2 evolution is also observed at a water content of only 20 ppm.[7]

Without spectroscopic evidence it is hard to comment on the exact nature of the decomposition products. The fact that CO_2-evolution proceeds without further consumption of oxygen gives a hint that CO_2-moiety is preformed in the decomposition product and can be released upon electrochemical oxidation (c.f. Supporting Information and Figure S8).

Our results suggest that it is beneficial to avoid the direct pathway of peroxide formation during battery discharge. Although Figure 2 suggests that the actual amounts of oxygen that are re-evolved as CO_2 are rather small, prolonged battery operation is not possible even when only small amounts of electrolyte are decomposed in each charge-discharge cycle. However, whether it is really beneficial to favor the indirect pathway of peroxide formation depends on the stability of the electrolyte under these operation conditions. We did not observe any electrolyte decomposition when oxygen was reduced to superoxide, however, intermediates that occur during disproportionation of superoxide might be able to induce electrolyte decomposition as well.

z-values at gold sputtered Teflon membranes.—In Ref. 18 we have shown that oxygen reduction at a gold sputtered Teflon membrane proceeds via the transfer of more than 1.5 electrons per oxygen over the whole potential region of oxygen reduction. This appears to contradict the results presented in Figure 7A and elsewhere[7] where we have shown that a transition from the direct to the indirect pathway of peroxide formation occurs as the overpotential increases. Yet, both results are reproducible: At smooth gold electrodes used in the dual thin layer cell we always observe a step in the z-value from close to 1 e^-/O_2 to nearly 2 e^-/O_2 (c.f. Ref. 7), while this step is far less pronounced when gold sputtered Teflon membranes are used as working electrode in the conventional cell (c.f. Figure 3 and Ref. 18). There is one obviouse difference between the experiments of Figures 1 and 6: The partial pressure of oxygen at the electrode.

In the conventional cell with the porous electrode electrochemistry takes place at the interface between electrolyte and vacuum. At the working electrode the concentration of oxygen is very low because oxygen readily passes over into the vacuum. In the dual thin layer cell electrochemistry does not take place at the interface between electrolyte and vacuum and the concentration in front of the electrode equals the concentration of oxygen in the bulk electrolyte (as long as no O_2 is reduced electrochemically). The Tafel-slope for the formation of superoxide is 120 mV/dec,[6] and, hence, a reduction of the concentration in oxygen by one decade will reduce the potential (i.e. increase the overpotential) at which a certain current due to superoxide formation is observed by 120 mV. At higher overpotentials the superoxide is reduced further to peroxide. The formation of lithium peroxide in the direct path is a surface limited (adsorption) process. At this point we do not know the reaction order with respect to O_2 or which reaction step is the rate limiting. However, it is not unreasonable to assume that the second electron transfer is slower than the first one, which corresponds to a Tafel slope of 40 mV. For a reaction order of one with respect to oxygen, this means that to maintain a given current at a lower O_2 concentration, the potential has to be decreased by only 40 mV per decade of concentration. In this case, the potential region of superoxide formation is much smaller in the conventional cell and is not well resolved form the potential region of peroxide formation. This might be one reason why we observe a z-value of 1.5 e^-/O_2 in the conventional cell and at low overpotentials, whereas z-value in the conventional cell in the same potential region is close to 1 e^-/O_2.

Another possible reason for a larger than expected z-value in the potential region of superoxide formation is the structure of the electrode: The thickness of the gold-layer is only 50 nm. Due to mechanical wear or due to shadowing during the sputter-process, it is likely that parts of the gold layer remain without electrical connection to the potentiostat and are, therefore, at open circuit potential. As already pointed out gold at open circuit potential causes oxygen evolution by catalysing disproportionation of superoxide to oxygen and peroxide or by some other reaction that results in the oxidation of superoxide (c.f. Figure 10). When parts of the gold electrode under potential control are close to those parts without, then diffusion to and reaction of superoxide at these sites is fast. This causes a lower ionic current for mass 32 whereas the faradaic current remains the same. Therefore, the calculated z-values are larger than expected. That is, oxygen is released in a reaction that requires no net charge transfer. This effect on the z-values is limited to measurements in the conventional cell because only there a rough gold electrode was used this. Both the onset potential for oxygen reduction (c.f. Figure 1 and Figure 6) and the transition potential from the indirect to the direct pathway of peroxide formation (c.f. Figure 3 and Figure 7) are shifted by 100 mV to lower potentials in the conventional cell. This is due to a Nernst shift because of the lower concentration of oxygen at the porous membrane. Therefore, it is more likely that the z-value of 1.5 e^-/O_2 at low overpotentials is due to the effect of gold particles at open circuit potential than due to the effect of kinetics.

True coulombic efficiency.—We have shown here and elsewhere[18] that there is a non-proportionality between the reduced and the evolved amounts of oxygen. We pointed out that a positive intercept with the x-axis (i.e. negative intercept with the y-axis) means that in each cycle a constant amount of the reduced oxygen is not available for oxygen evolution, while a slope smaller than one means that in addition also a certain portion of the reduced oxygen cannot be re-evolved.

In each cycle the potential passes through the region of indirect peroxide formation and, therefore, a constant amount of oxygen is reduced to superoxide. The superoxide produced in this potential region is either transported away from the electrode (due to convection, caused by purging of the electrolyte with oxygen) or undergoes a reaction under oxygen release at those parts of the gold electrode that are at open circuit. The z-value in the potential range of superoxide formation is then defined by the ratio of superoxide that undergoes a reaction to the superoxide that diffuses away (mind that also in the case of the gold sputtered Teflon membrane usually a minor step is observed). In either case oxygen that is reduced to superoxide cannot be evolved again in the anodic sweep. In each cycle the same amount of superoxide is formed which is not reoxidized to oxygen. Therefore, a positive intercept with the x-axis results.

As the potential region of direct, electrochemical peroxide formation is entered, electrolyte decomposition starts as well. For each carbon atom that is evolved as CO_2 in the anodic sweep at least one molecule of reduced oxygen is consumed irreversibly. This reduces the slope of the straight line in Figure 2A. CO_2 is only the end product of DMSO oxidation and it is, therefore, likely that the evolved amount of CO_2 does not represent the total amount of oxygen that is consumed due to electrolyte decomposition. In addition to electrolyte decomposition some of the reduced oxygen species will be transported away and may precipitate at locations without any electrical contact to the electrode. Both processes only consume a portion of the reduced oxygen, and reduce the slope of the straight line in Figure 2A.

It is also possible that water exerts an effect: It was shown by Andrieux et al.[46] that oxygen reduction in DMSO based electrolytes and in the presence of weak acids results in the formation of H_2O_2. The formation of soluble H_2O_2 in the presence of water upon discharge of Li-air batteries was also suggested by others.[30,47] The formation of soluble H_2O_2 in our study would reduce the slope in Figure 2 further. However, Andrieux et al. used acids with a much larger pka-value then water in DMSO.[48] Therefore, it is not clear whether the acidity of water is sufficient to provide protons. Furthermore, formation of H_2O_2 comes along with the formation of LiOH (as OH^- is bound to precipitate as LiOH). Accumulation of LiOH from cycle to cycle should show up with an increasing loss of activity, which we do not observe.

Characteristics of the deposit.—Both Torres et al. and Jie and Uosaki who investigated oxygen reduction in an electrolyte of 0.1 M $LiPF_6$ in DMSO by means of eQCMB did not consider the potential region of oxygen evolution.[20,21] Sharon et al. on the other hand only state that the same mass that was deposited during oxygen reduction was removed during the anodic run.[22] From that it was concluded that Li_2O_2 formation was reversible. However, closer examination of the curves shown by Sharon et al. reveals that the mass changes in the anodic run are observed at potentials positive of oxygen evolution. In a more recent study also Torres et al. have pointed out that the loss of mass in the potential region of oxygen evolution does not account for the masses that were deposited during oxygen reduction and that large overpotentials are required to return to the original state of the quartz.[23]

There are several phenomena in eQCMB measurements that can distort the observed mass changes significantly: The formation of a deposit on the electrode has a different interaction with the electrolyte. Therefore, a non-slip plane at the interface between electrolyte and electrode can turn into a slip plane or vice versa.[32] In addition, different double layer structures at the electrode and the deposit can distort mass changes significantly: When ions or molecules are specifically adsorbed at the electrode (or the deposit) they will be removed once the deposit forms (or once the deposit is removed).[49] In the case of thick coats solvent molecules and ions can be entrapped in the formed deposit.[23] However, those effects should not only affect the mass changes during oxygen evolution but also during oxygen reduction. These effects are, therefore, not fit to explain the missing mass changes during oxygen evolution.

In eQCMB studies connected to the oxidation of metal surfaces Schumacher et al. observed mass changes that were several times larger than expected from the transferred charge.[50,51] Schumacher et al. were able to assign the additional mass changes to a roughening of the metal surface. Cavities on the surface will cause electrolyte to be dragged along with the movement of the crystal which causes an additional mass load. It is important to note that the eQCMB does not measure the mass that rests on top of the quartz crystal (i.e. not the entire mass of the column of electrolyte that rests on top of the crystal) but the mass of the surrounding matter that follows the shear motion of the AT-cut quartz crystals. In a similar way also Torres et al. explain larger than expected mass changes during oxygen reduction.[23] We are going to elaborate in the following, why the cavity-effect described by Schumacher et al. is a reasonable explanation for the missing mass changes during oxygen evolution:

Figure 11 illustrates the mechanism we believe to be responsible for the missing mass changes in the potential region of oxygen evolution: Initially the electrode is free of any deposit (Figure 11A). As the potential region of direct, electrochemical peroxide formation is entered an inhomogeneous film of decomposition products (blue) and lithium peroxide precipitates on the electrode (Figure 11B), which results in a mass change. The deposition of decomposition products and Li_2O_2 goes on until the whole electrode is covered and oxygen reduction ceases (Figure 11C). Since the evolution of oxygen and CO_2 are two well separated processes Li_2O_2 is oxidized and removed from the electrode while a frame of decomposition products is left behind (Figure 11D). The remaining cavities in this frame are filled up with electrolyte, that is now forced to follow the oscillation movement of the crystal. Since the mass of Li_2O_2 is replaced by the mass of the electrolyte the expected mass changes are due the differences in the densities of the electrolyte and Li_2O_2, which are below the sensitivity limit. Only when the potential region of CO_2 evolution is entered (Figure 11E) a mass change is observed, because the mass of decomposition products is removed and the frame that forces the electrolyte in the cavities to follow the oscillation movement is destroyed.

In Figure 4C we have observed that initially the reduced quality factor decreases parallel to CO_2 evolution and returns to its original value once CO_2 evolution has stopped. This decrease indicates an increased friction at the interface between the electrode and the electrolyte parallel to CO_2 evolution. It is quite possible that the friction at the interface increases as the decomposition products lose contact to

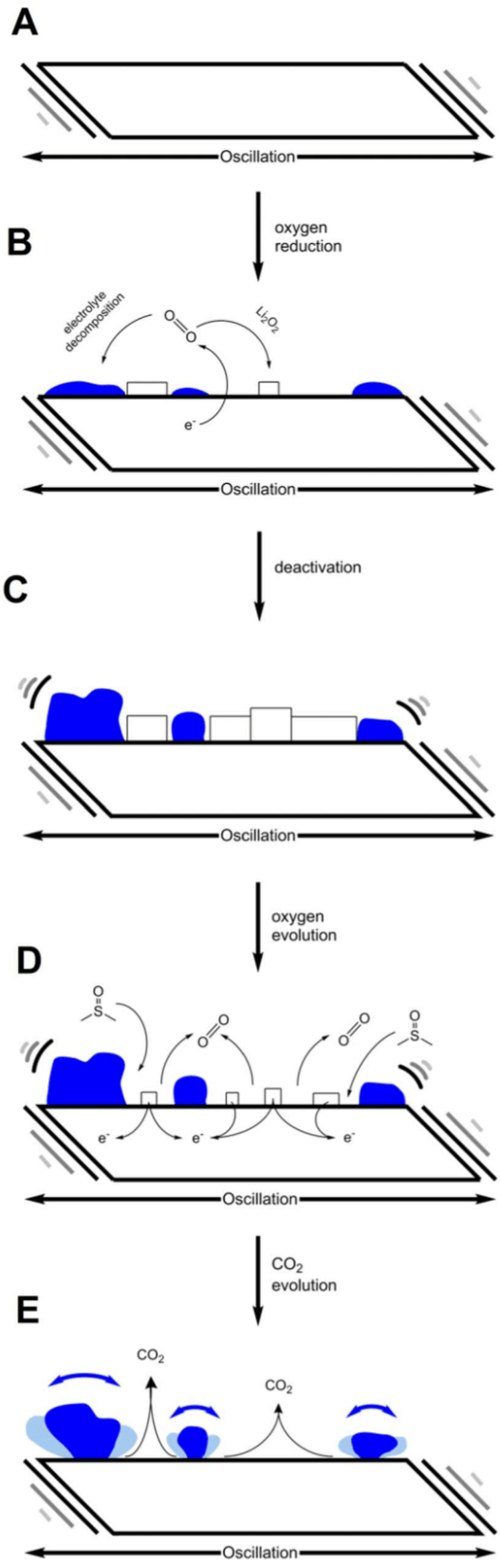

Figure 11. Illustration for the mechanism responsible for the missing mass change during oxygen evolution. During oxygen reduction an inhomogeneous deposit of Li_2O_2 and decomposition products forms on the electrode (B, C). In the potential region of oxygen evolution Li_2O_2 is oxidized and the remaining cavities are filled up by electrolyte (D). At even higher potentials decomposition products are oxidized to CO_2 (E). Although the above drawing might suggest otherwise we have recently shown that during oxygen reduction only 2 ML of Li_2O_2 are formed.[7]

the electrode. This situation is depicted in Figure 11E. Once CO_2 evolution has ceased also the reduced quality factor returns to its original value.

Conclusions

By means of DEMS it was shown that in addition to O_2 formation CO_2 evolution takes place in the anodic sweep, and that the evolved quantities of CO_2 linearly depend on the quantities of oxygen that were reduced in the previous cathodic sweep. Since DMSO is the only carbon source in the system under investigation, the evolution of CO_2 shows unambiguously that DMSO is decomposed during oxygen reduction. From the ratio of the faradaic current to the ionic current for mass 32 it was shown again that oxygen reduction at gold and in DMSO based electrolytes proceeds via the formation of superoxide at low overpotentials. Direct, electrochemical peroxide formation takes place only at high overpotentials. This transition is observed only to a limited degree when a gold sputtered Teflon-membrane is used as a working electrode. This fact has been assigned to the disproportionation of superoxide that is catalysed by gold at open circuit.

During oxygen reduction larger than expected m.p.e-values were observed, in quiescent solution. This has been assigned to the additional deposition of decomposition products, which are formed during oxygen reduction. When convection is applied m.p.e- and m.p.O_2-values fit very well to the expected formation of solid Li_2O_2. However, these values are just the result of incomplete precipitation of reduced oxygen species and additional deposition of decomposition products. No mass deposition in eQCMB measurements is observed when electrochemical oxygen reduction results in the formation of superoxide. From that we concluded that superoxide is not the active species that induces electrolyte decomposition. This finding has practical implications for lithium-air batteries: In order to avoid electrolyte decomposition it appears to be favorable to construct batteries in such a way that oxygen is reduced primarily to superoxide upon discharge. Superoxide undergoes lithium induced disproportionation in the aftermath. However, whether or not this discharge mode is really favorable depends on the stability of DMSO against intermediates that form during the disproportionation of superoxide.

In the anodic sweep no mass changes due to the oxidation of Li_2O_2 have been observed, although the evolution of oxygen under convection condition implies that Li_2O_2 must adhere to the electrode. This observation has been assigned to the structure of the deposit: The surface is covered by a heterogeneous film of Li_2O_2 and decomposition products. As Li_2O_2 is oxidized cavities remain in this film that are filled with electrolyte, hence offsetting the mass change due to removal of Li_2O_2.

It was shown that gold at open circuit catalyses a reaction that releases oxygen from superoxide either by disproportionation or oxidation of the latter. This reaction appears to be responsible for the differences observed in the z-values obtained at smooth and porous electrodes.

Acknowledgment

The authors gratefully acknowledge the Federal Ministry of Eduction and Research (FRG) for funding this work. This work is part of the “LuLi- Strom aus Luft und Li” project (FKZ:03X4624A).

References

1. G. Girishkumar, B. McCloskey, A. C. Luntz, S. Swanson, and W. Wilcke, *J. Phys. Chem. Lett.*, **1**, 2193 (2010).
2. M. W. Chase Jr., *Journal of Physical and Chemical Reference Data*, **Monograph 9**, 1 (1998).
3. J. D. Cox, D. D. Wagman, and V. A. Medvedev, *Hemisphere Publishing Corp.*, New York (1989).
4. D. Xu, Z.-l. Wang, J.-j. Xu, L.-l. Zhang, L.-m. Wang, and X.-b. Zhang, *Chemical Communications*, **48**, 11674 (2012).
5. W. Xu, J. Hu, M. H. Engelhard, S. A. Towne, J. S. Hardy, J. Xiao, J. Feng, M. Y. Hu, J. Zhang, F. Ding, M. E. Gross, and J.-G. Zhang, *Journal of Power Sources*, **215**, 240 (2012).
6. C. O. Laoire, S. Mukerjee, K. M. Abraham, E. J. Plichta, and M. A. Hendrickson, *J. Phys. Chem. C*, **114**, 9178 (2010).
7. C. Bondue, P. Reinsberg, A.-E.-A. A. Abd-El-Latif, and H. Baltruschat, *Physical Chemistry Chemical Physics*, 25593 (2015).
8. C. O. Laoire, S. Mukerjee, K. M. Abraham, E. J. Plichta, and M. A. Hendrickson, *J. Phys. Chem. C*, **113** 20127 (2009).
9. Y. Chen, S. A. Freunberger, Z. Peng, F. Barde, and P. G. Bruce, *Journal of the American Chemical Society*, **134**, 7952 (2012).
10. M. J. Trahan, S. Mukerjee, E. J. Plichta, M. A. Hendrickson, and K. M. Abraham, *J. Electrochem. Soc.*, **160**, A259 (2013).
11. W. Torres, N. Mozhzhukhina, A. Y. Tesio, and E. J. Calvo, *J. Electrochem. Soc.*, **161**, A2204 (2014).
12. R. Cao, E. D. Walter, W. Xu, E. N. Nasybulin, P. Bhattacharya, M. E. Bowden, M. H. Engelhard, and J.-G. Zhang, *ChemSusChem*, **7**, 2436 (2014).
13. E. J. Calvo and N. Mozhzhukhina, *Electrochemistry Communications*, **31**, 56 (2013).
14. V. Gutmann, *Coordination Chemistry Reviews*, **18**, 225 (1976).
15. M. Marinaro, P. Balasubramanian, E. Gucciardi, S. Theil, L. Jörissen, and M. Wohlfahrt-Mehrens, *ChemSusChem*, **8**, 3139 (2015).
16. M. Marinaro, U. Riek, S. K. Eswara Moorthy, J. Bernhard, U. Kaiser, M. Wohlfahrt-Mehrens, and L. Jörissen, *Electrochemistry Communications*, **37**, 53 (2013).
17. B. D. McCloskey, D. S. Bethune, R. M. Shelby, T. Mori, R. Scheffler, A. Speidel, M. Sherwood, and A. C. Luntz, *The Journal of Physical Chemistry Letters*, **3**, 3043 (2012).
18. C. J. Bondue, A. A. Abd-El-Latif, P. Hegemann, and H. Baltruschat, *J. Electrochem. Soc.*, **162**, A479 (2015).
19. Z. Peng, S. A. Freunberger, Y. Chen, and P. G. Bruce, *Science*, **337**, 563 (2012).
20. X. Jie and K. Uosaki, *J. Electroanal. Chem.*, **716**, 49 (2014).
21. W. R. Torres, A. Y. Tesio, and E. J. Calvo, *Electrochemistry Communications*, **49**, 38 (2014).
22. D. Sharon, M. Afri, M. Noked, A. Garsuch, A. A. Frimer, and D. Aurbach, *The Journal of Physical Chemistry Letters*, **4**, 3115 (2013).
23. W. R. Torres, L. Cantoni, A. Y. Tesio, M. del Pozo, and E. J. Calvo, *J. Electroanal. Chem.*, **765**, 45 (2016).
24. G. Gritzner, *Journal of Molecular Liquids*, **156**, 103 (2010).
25. H. Baltruschat, *Journal of the American Society for Mass Spectrometry*, **15**, 1693 (2004).
26. H. Baltruschat, in *Interfacial Electrochemistry*, A. Wieckowski Editor, p. 577 Marcel Dekker, Inc., New York, Basel (1999).
27. H. Baltruschat, R. Bussar, S. Ernst, and F. Hernandez-Ramirez, in *In-situ Spectroscopic Studies of Adsorption at the Electrode and Electrocatalysis*, S.-G. Sun, P. A. Christensen, and A. Wieckowski Editors, p. 471 Elsevier, Amsterdam (2007).
28. A. A. Abd-El-Latif and H. Baltruschat, in *Encyclopedia of Applied Electrochemistry*, G. Kreysa, K.-i. Ota, and R. Savinell Editors, p. 507 Springer New York Dordrecht Heidelberg London (2014).
29. A. A. Abd-El-Latif, C. J. Bondue, S. Ernst, M. Hegemann, J. K. Kaul, M. Khodayari, E. Mostafa, A. Stefanova, and H. Baltruschat, *Trends in Analytical Chemistry*, **70**, 4 (2015).
30. K. U. Schwenke, M. Metzger, T. Restle, M. Piana, and H. A. Gasteiger, *J. Electrochem. Soc.*, **162**, A573 (2015).
31. M. Safari, B. D. Adams, and L. F. Nazar, *The Journal of Physical Chemistry Letters*, **5**, 3486 (2014).
32. D. A. Buttry and M. D. Ward, *Chemical Reviews*, **92**, 1355 (1992).
33. G. Sauerbrey, *Zeitschrift für Physik*, **155**, 206 (1959).
34. J. Fuhrmann, A. Linke, H. Langmach, and H. Baltruschat, *Electrochimica Acta*, **55**, 430 (2009).
35. J. Fuhrmann, A. Linke, and H. Langmach, *Appl. Numer. Math.*, **61**, 530 (2011).
36. S. Schaltin, G. Vanhoutte, M. Wu, F. Barde, and J. Fransaer, *Physical Chemistry Chemical Physics*, **17**, 12575 (2015).
37. Q. Yu and S. Ye, *The Journal of Physical Chemistry C*, **119**, 12236 (2015).
38. L. Johnson, C. Li, Z. Liu, Y. Chen, S. A. Freunberger, P. C. Ashok, B. B. Praveen, K. Dholakia, J.-M. Tarascon, and P. G. Bruce, *Nat Chem*, **6**, 1091 (2014).
39. S. Lau and L. A. Archer, *Nano Letters*, **15**, 5995 (2015).
40. F. Marchini, S. Herrera, W. Torres, A. Y. Tesio, F. J. Williams, and E. J. Calvo, *Langmuir*, **31**, 9236 (2015).
41. D. T. Sawyer and J. S. Valentine, *Accounts of Chemical Research*, **14**, 393 (1981).
42. F. Marchini, S. E. Herrera, E. J. Calvo, and F. J. Williams, *Surface Science*, **646**, 154 (2016).
43. R. Younesi, P. Norby, and T. Vegge, *ECS Electrochemistry Letters*, **3**, A15 (2014).
44. M. A. Schroeder, N. Kumar, A. J. Pearse, C. Liu, S. B. Lee, G. W. Rubloff, K. Leung, and M. Noked, *ACS Applied Materials & Interfaces*, **7**, 11402 (2015).
45. C. J. Bondue, P. Reinsberg, A. A. Abd-El-Latif, and H. Baltruschat, *Physical Chemistry Chemical Physics*, **17**, 25593 (2015).
46. C. P. Andrieux, P. Hapiot, and J. M. Saveant, *Journal of the American Chemical Society*, **109**, 3768 (1987).
47. N. B. Aetukuri, B. D. McCloskey, J. M. García, L. E. Krupp, V. Viswanathan, and A. C. Luntz, *Nat Chem*, **7**, 50 (2014).
48. F. G. Bordwell, *Accounts of Chemical Research*, **21**, 456 (1988).
49. S. Bruckenstein and M. Shay, *Electrochimica Acta*, **30**, 1295 (1985).
50. R. Schumacher, G. Borges, and K. K. Kanazawa, *Surface Science*, **163**, L621 (1985).
51. R. Schumacher, J. G. Gordon, and O. Melroy, *Journal of Electroanalytical Chemistry and Interfacial Electrochemistry*, **216**, 127 (1987).

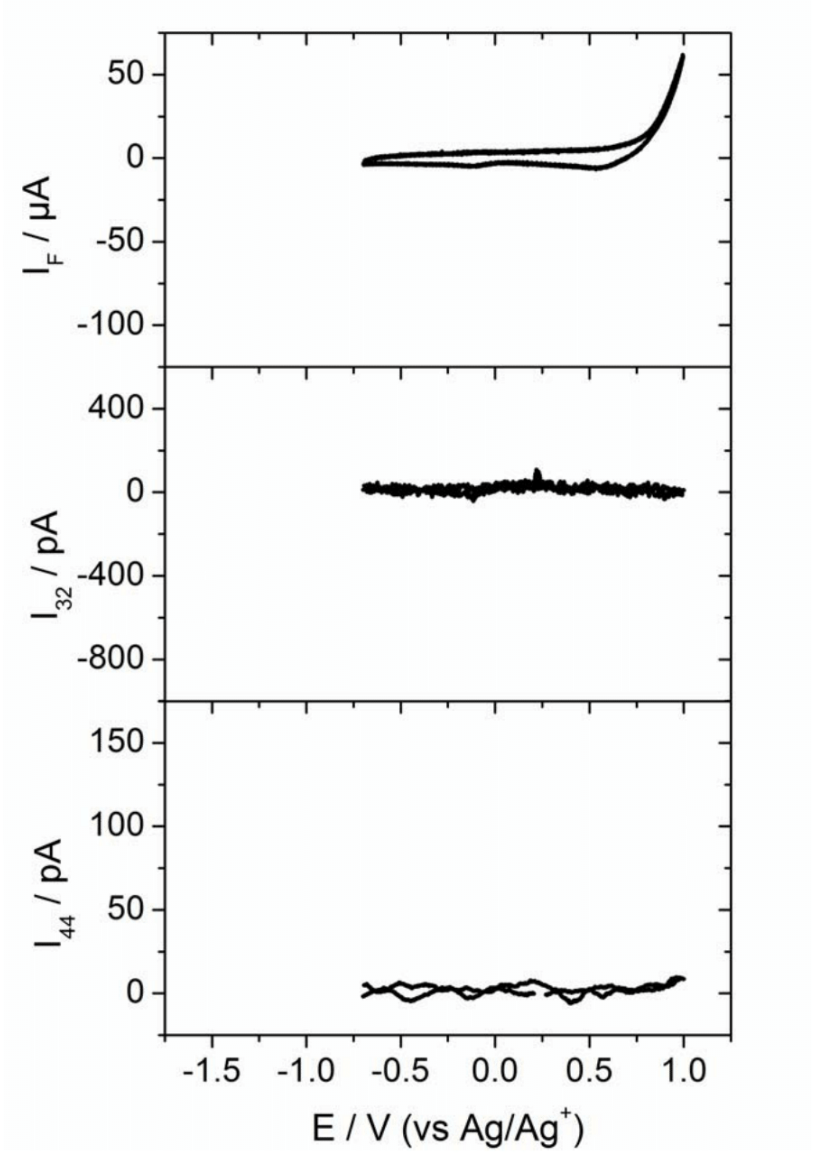

Figure S1: Potential scan in the conventional cell in the potential limits -0.75 V - 1.0V (excluding the potential region of oxygen reduction). Electrolyte 0.1 M $LiClO_4$ in DMSO. The electrolyte was purged with 100% oxygen.

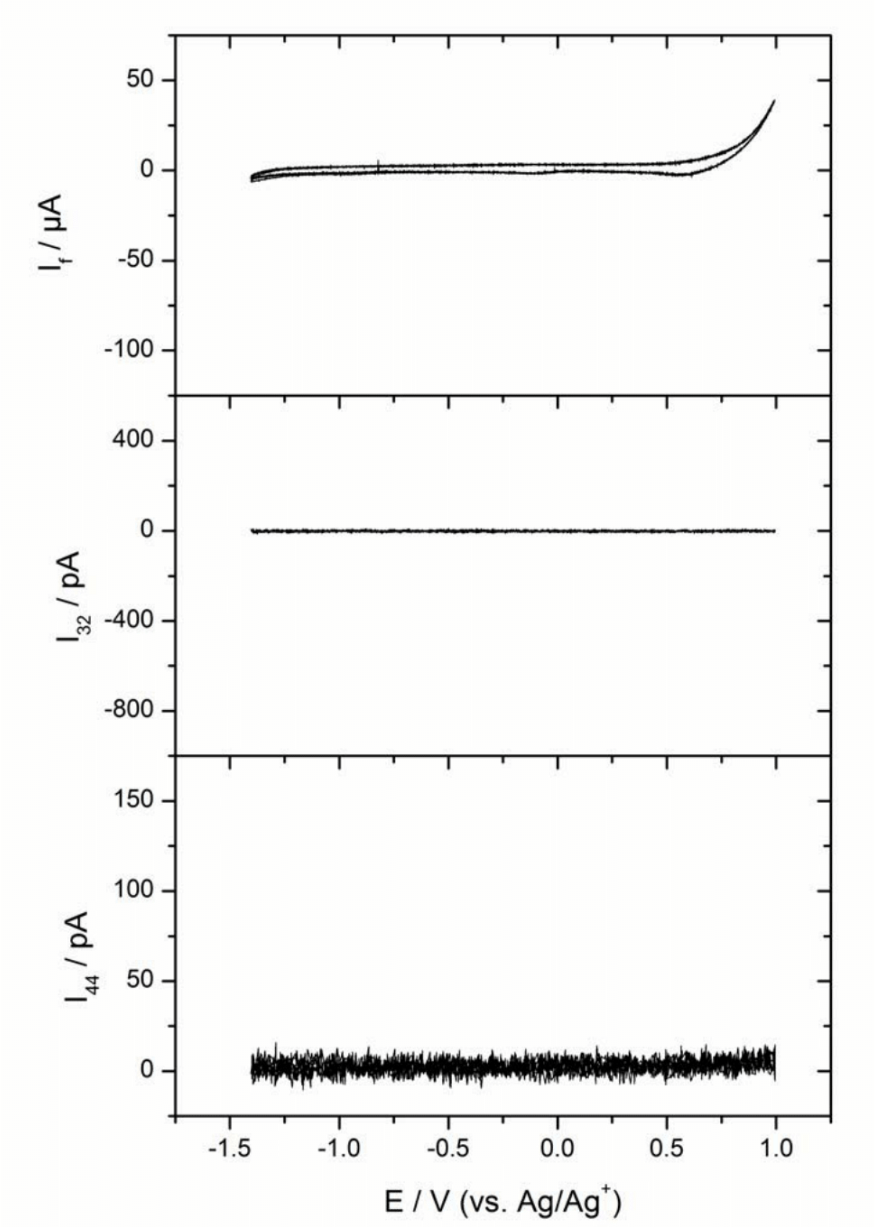

Figure S2: Potential scan in the conventional cell in the potential limits -1.4 V - 1.0V. Electrolyte 0.1 M $LiClO_4$ in DMSO. The electrolyte was purged with Argon.

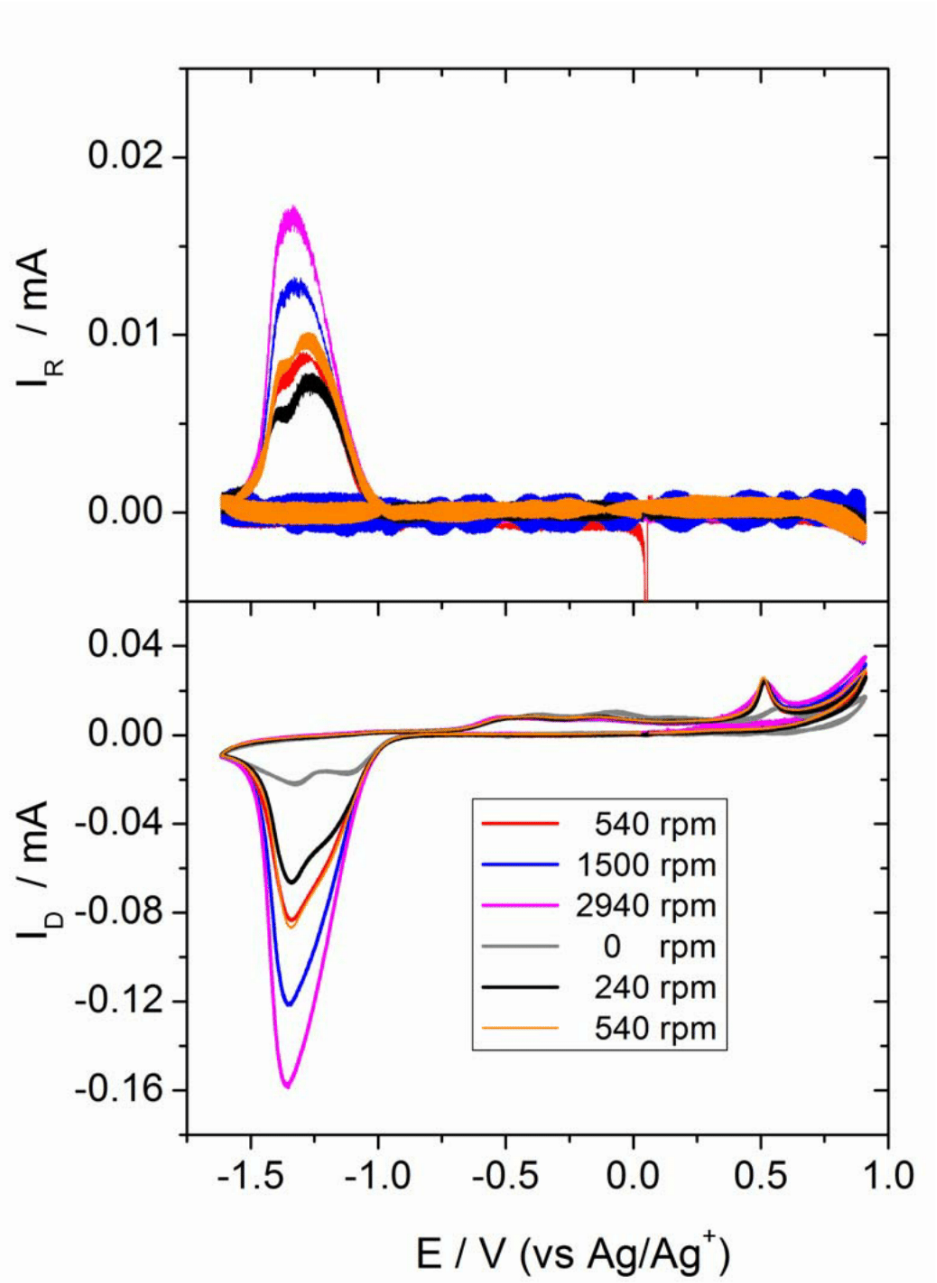

Figure S3: RRDE-measurement with various rotation speeds in an electrolyte of 0.1 M $LiClO_4$ in DMSO. The electrolyte was purge with a mixture of 10% oxygen and 90% argon. Disc: Gold; Ring: Glassy carbon (at -0.8 V). Water content: 400 ppm. Sequence in the legend follows the sequence of the experiments. The First experiment 540 rpm was repeated to check for superimposed time effects.

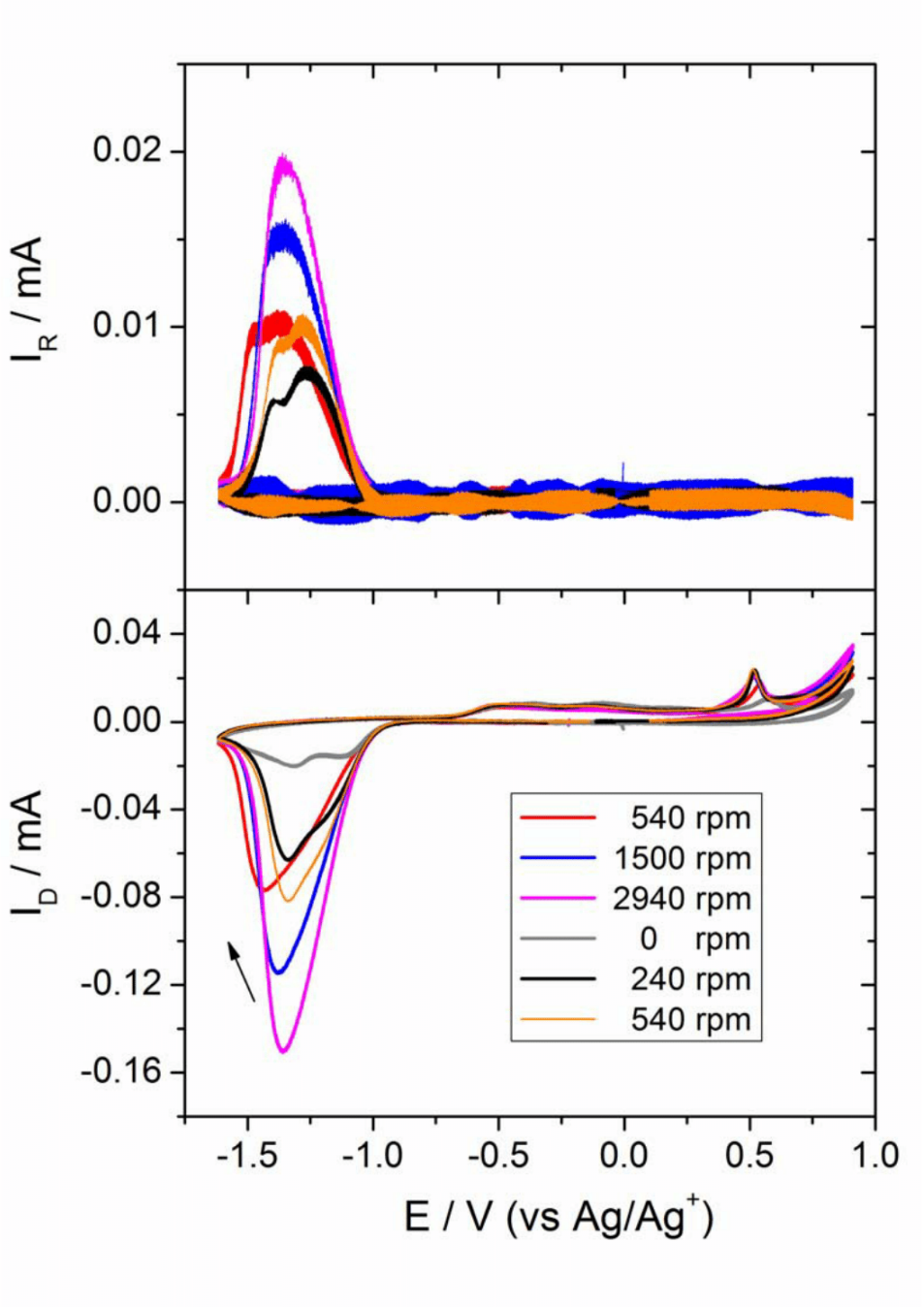

Figure S4: RRDE-measurement with various rotation speeds in an electrolyte of 0.1 M $LiClO_4$ in DMSO. The electrolyte was purge with a mixture of 10% oxygen and 90% argon. Disc: Gold; Ring: Glassy carbon (at -0.6 V). Water content: 400 ppm. Sequence in the legend follows the sequence of the experiments. The First experiment 540 rpm was repeated to check for superimposed time effects.

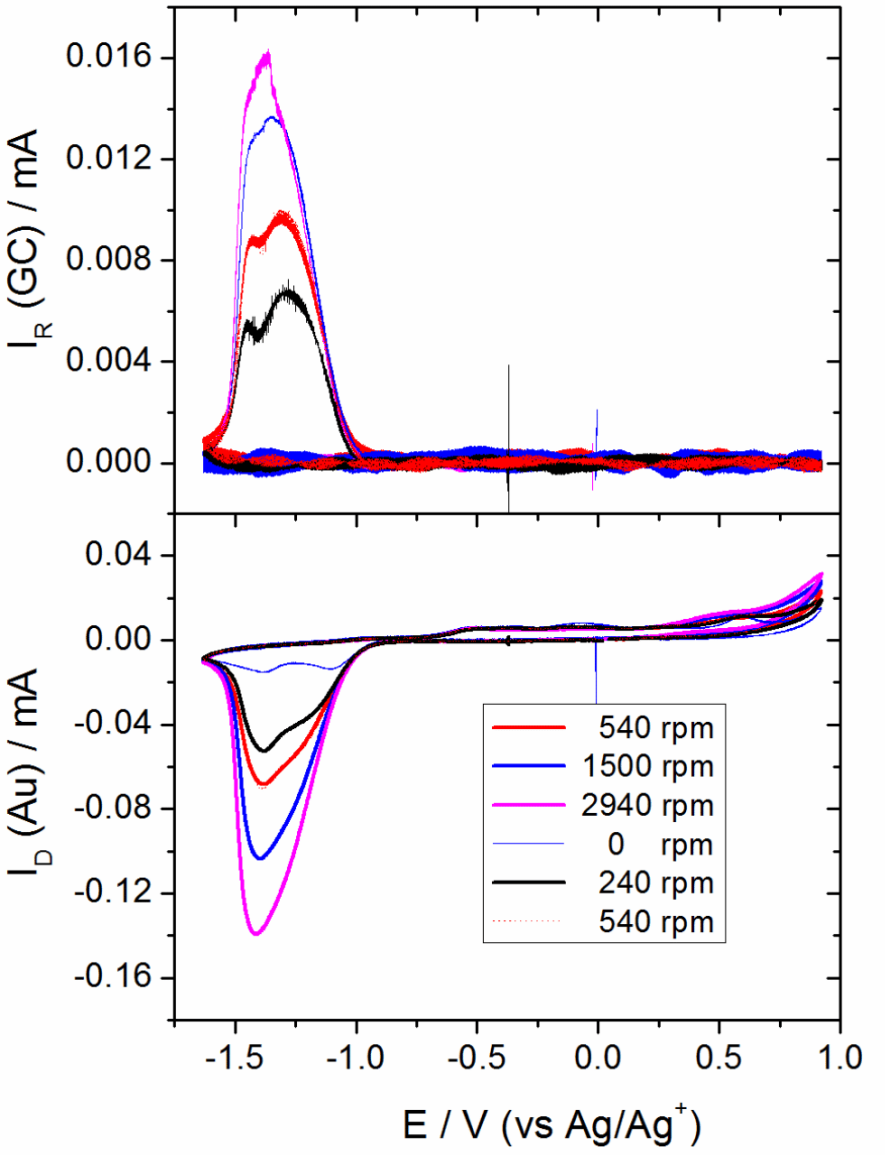

Figure S5: RRDE-measurement with various rotation speeds in an electrolyte of 0.1 M $LiClO_4$ in DMSO. The electrolyte was purge with a mixture of 10% oxygen and 90% argon. Disc: Gold; Ring: Glassy carbon (at -0.3 V). Water content: 400 ppm. Sequence in the legend follows the sequence of the experiments. The First experiment 540 rpm was repeated to check for superimposed time effects.

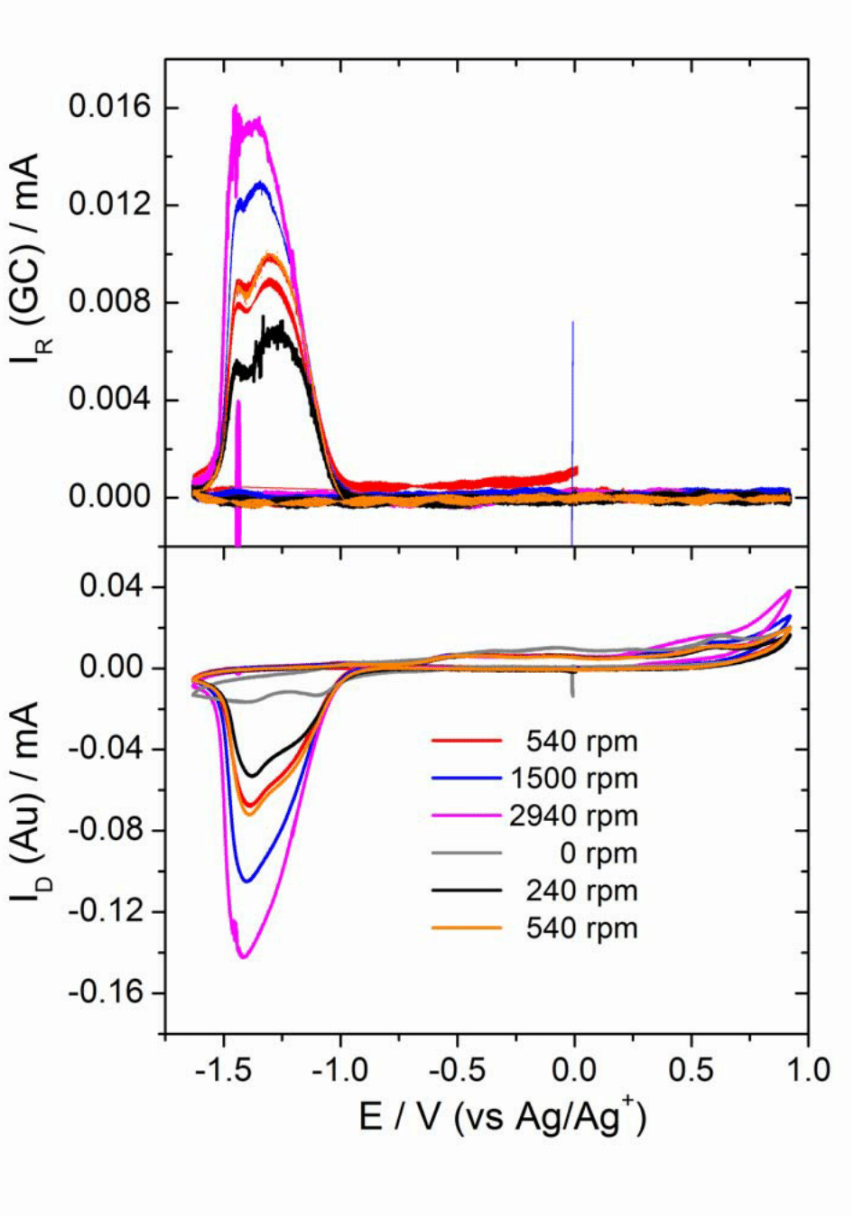

Figure S6: RRDE-measurement with various rotation speeds in an electrolyte of 0.1 M $LiClO_4$ in DMSO. The electrolyte was purge with a mixture of 10% oxygen and 90% argon. Disc: Gold; Ring: Glassy carbon (at 0.0 V). Water content: 400 ppm. Sequence in the legend follows the sequence of the experiments. The First experiment 540 rpm was repeated to check for superimposed time effects.

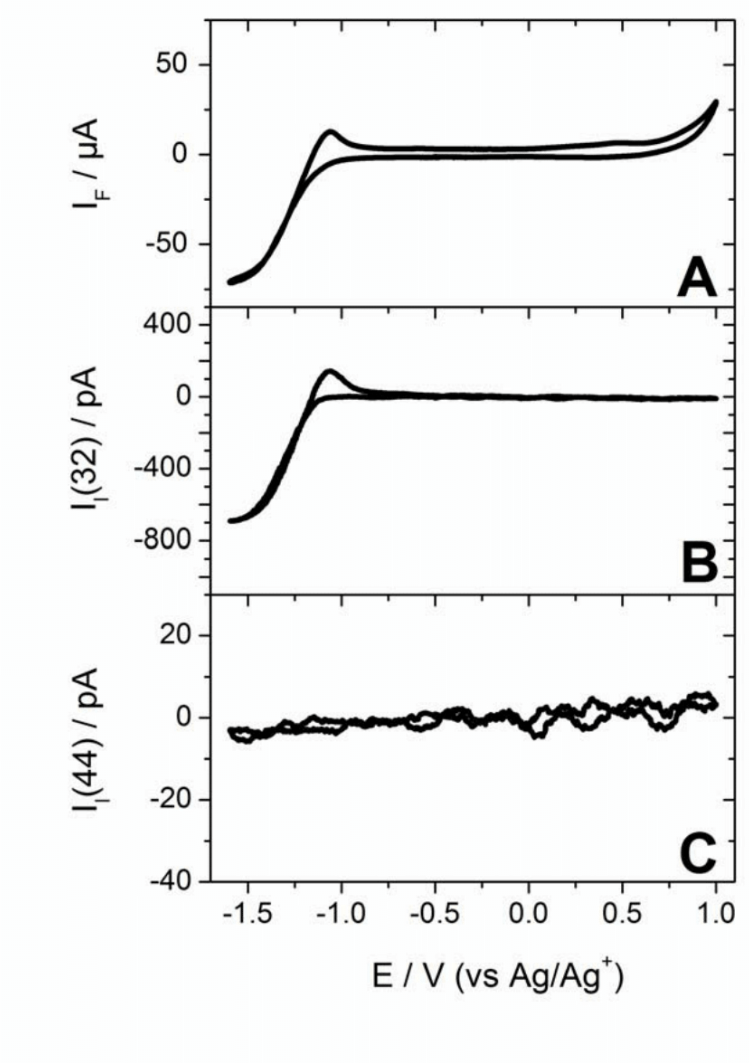

Figure S7: Oxygen reduction and evolution in a conventional cell in an electrolyte of 0.1 M $TBAClO_4$ in DMSO (oxygen saturated). Sweep rate: 20 mV/sec. A: Faradaic current; B: Ionic current for mass 32 (e.g. Oxygen); C: Ionic current for mass 44 (e.g. CO_2).

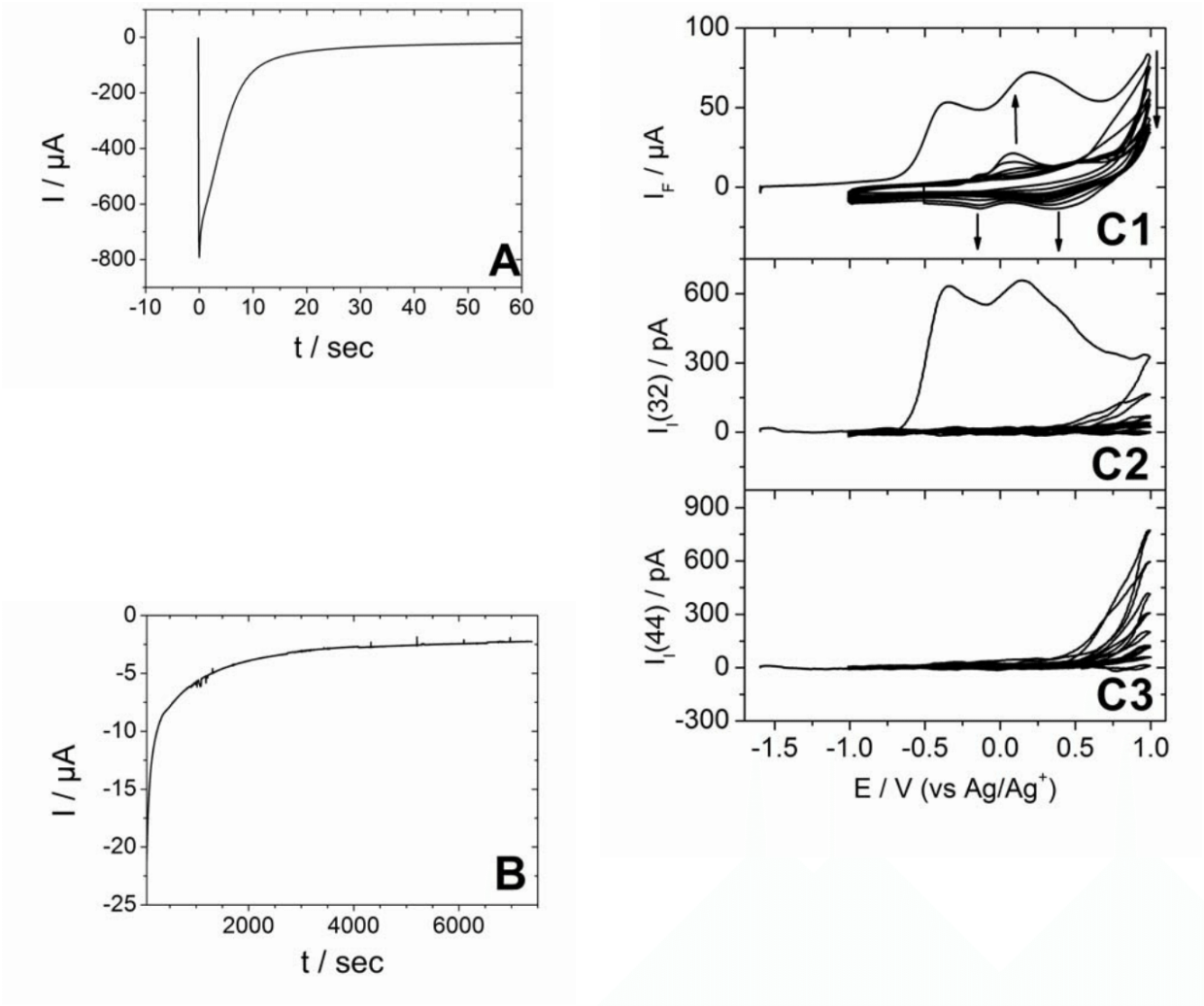

Figure S8: A and B: current time transient after a potential step to -1.6 V (A and B have different time scales). The experiment was done in a conventional cell. Oxygen is supplied to the electrolyte of 0.1 M $LiClO_4$ in DMSO from the gas side (200 mbar), while the electrolyte is purged with argon. C: CV and MSCV for mass 32 and mass 44 (nine cycles) obtained with a sweep rate of 20 mV/s. The space underneath the electrode is evacuated (no supply of oxygen) and the electrolyte is still purged with argon. C1: faradic current; C2: Ionic current for mass 32; C3: Ionic current for mass 44.

The experiment of Figure S8 was done in the conventional cell when the space underneath the working electrode was not connected to the vacuum of the mass spektrometer but filed with oxygen. Under these conditions the gold sputtered Teflon membrane operates as a gas diffusion electrode. We performed a potential step to -1.6 V and Figure S8A and S8B show

the current time transient. during oxygen reduction. After two hours the space underneath the working electrode was evacuated and the cell was connected to the mass spectrometer. We held the potential for 10 minutes at -1.6 V and purged the electrolyte with argon. Then we cycled in anodic direction and recorded 9 cycles in a potential window between -1.0 V and 1.0 V. Figure S8C shows the CV and the MSCV for mass 32 and mass 44.

Most of the oxygen is evolved in the first cycle. This is different in the case of CO_2 evolution where a signal in mass 44 is observed in 9 consecutive cycles. It is noteworthy that CO_2 evolution takes place in the absence of oxygen (the electrolyte was purged with argon after oxygen reduction was finished). Hence, CO_2 is evolved via oxidation of decomposition products without adding oxygen to the carbon atom. Hence, the decomposition products that evolve CO_2 already contain a CO_2-unit. In addition, CO_2 evolution is a potential dependent process that requires the transfer of charge. Therefore, CO_2 is not evolved from compounds like $LiHCO_3$ or Li_2CO_3 (although their presence cannot be ruled out). Carboxyl functions on the other hand would fit to the above description. Their oxidation releases CO_2 without further consumption of oxygen. However, we lack spectroscopic evidence to identify the exact nature of the decomposition products.

5. 3. Summary of Paper 3

In Paper 3 we have addressed the question why there is a negative intercept with the y-axis in the plot shown in Figure 7 of Paper 1 and in Figure 2A of Paper 3. In Paper 3 we propose that this is either due to the disproportionation of superoxide or due to some other reaction in the course of which superoxide is being oxidised. Either reaction takes place only at gold particles at open circuit potential. Because of the same reason we do not observe the transition from the direct to the indirect pathway of peroxide formation at gold sputtered electrodes: The reaction of superoxide becomes too fast to resolve this process from the electrochemical processes.

DEMS and eQCMB results presented in Paper 3 show that electrolyte decomposition is related to oxygen reduction. This supports the results presented by McCloskey *et al*. [35]. However, eQCMB results also show that superoxide is not the species that initiates electrolyte decomposition. It remains elusive which species initiates electrolyte decomposition and whether electrolyte decomposition can be avoided, when Li_2O_2 is formed by disproportionation of superoxide.

The eQCMB results presented in Paper 3 are rather curious: Missing mass changes during oxygen evolution, an effect of the convection on the observed m.p.e values during oxygen reduction and changes in the reduced quality factor parallel to CO_2 evolution. We were able to give a sound model that explains this behaviour, which was also based on RRDE measurements. Contradictions in literature concerning eQCMB results on oxygen reduction in lithium containing DMSO based electrolytes were (in part) resolved.

6. Paper 4 - A New 2-Compartment Flow Through Cell for the Simultaneous Detection of Electrochemical Reaction Products by a Detection Electrode and Mass Spectroscopy

6. 1. Introduction to Paper 4

In Paper 3 we have employed the RRDE technique to detect the formation of superoxide during electrochemical oxygen reduction in lithium containing electrolytes. Based on the DEMS results presented in Paper 2 and 3 as well as in Ref [39, 40, 70, 72] it was not unexpected to observe a current at the ring electrode when low overpotentials were applied to the disc electrode: Already Torres *et al*. [70] and Trahan *et al*. [72] observed in this potential region currents at the ring electrode when gold electrodes were employed as disc electrodes. This current was assigned to the oxidation of superoxide. This interpretation is in good agreement with a z-value of 1 e^-/O_2 at low overpotentials which was derived from DEMS data. However, it was unexpected to find a second peak or a shoulder in the ring current as the overpotential at the disc electrode increased. At large overpotentials oxygen is reduced to peroxide *via* the direct pathway at gold electrodes. Hence, a ring current due to oxidation of superoxide should not be observed. In Paper 2 we have suggested that a deposit of Li_2O_2 exerts a geometric effect and inhibits the direct pathway of peroxide formation. In paper 2 we have, therefore, suggested that a similar process takes place at the gold electrode: In the course of rapid deactivation the gold electrode loses its ability to catalyse the second electron transfer. Hence, an increasing share of oxygen is reduced to superoxide, resulting in an increased current at the ring electrode. However, we left the interpretation somewhat open in Paper 3 and mentioned that it is also possible that LiO_2^- reacts at the ring electrode. Based on the fact that we set the potential at the ring electrode to a value at which no CO_2 evolution in the DEMS-experiments is observed (0.3 V vs. Ag/Ag^+), we argue that the current at the ring electrode is not be due to the oxidation of decomposition products. This way of argumentation is not entirely flawless: As in the case with carbonate based electrolytes [22] a variety of decomposition products might arise upon oxygen reduction reaction in DMSO based electrolytes. It is possible that some of these decomposition products undergo an electrochemical reaction at lower potentials and that their oxidation does not result in CO_2 evolution. Figure 8 of Paper 3 underscores this argument: The z-value for oxygen evolution exceeds a value of 2 e^-/O_2 significantly. This might be due to the additional oxidation of decomposition products without concomitant CO_2 evolution.

When during an RRDE-experiment a ring current is observed this does not mean anything else but that the electrochemical reaction at the disk electrode results in a soluble species that can undergo an electrochemical reaction at the potential and the material of the

ring electrode. Identification of that species is of course possible when there is only one compound that can undergo an electrochemical reaction at the ring electrode. This is the case for instance when it is already known that the material of the ring electrode is selective towards one of a variety of possible reaction products formed at the disc electrode. However, this is certainly not the case for the oxygen reduction reaction in organic electrolytes where, aside from reduced oxygen species, there is the constant possibility of electrolyte decomposition *via* chemical or electrochemical means. It is, therefore, surprising that it is in general accepted that the observation of a current at the ring electrode can be assigned to the formation of superoxide at the disk electrode, when oxygen is reduced from organic electrolytes [39, 40, 70, 72].

Therefore, we have designed the 6-electrode cell which is presented in the following article. It allows RRDE-like applications in combination with DEMS. With this cell it is possible to investigate the reaction that takes place at the detection electrode *via* mass spectroscopy.

6. 2. A New 2-Compartment Flow Through Cell for the Simultaneous Detection of Electrochemical Reaction Products by a Detection Electrode and Mass Spectroscopy (as published in Electrochimica Acta)

The version of record of Paper 4 as published in the Elechtrochimica Acta is shown in the following. Publication in this Theses is possible due to kind permission of Elsevier (License Number: 3938390105653). Any use of the material of the article shown below is permissible only after proper citation:

C. J. Bondue, P. Königshoven and H. Baltruschat, *Elechrochica Acta*, **214**, 241-252 (2016).

Electrochimica Acta 214 (2016) 241–252

Contents lists available at ScienceDirect

Electrochimica Acta

journal homepage: www.elsevier.com/locate/electacta

A New 2-Compartment Flow Through Cell for the Simultaneous Detection of Electrochemical Reaction Products by a Detection Electrode and Mass Spectroscopy

C.J. Bondue, P. Königshoven, H. Baltruschat*

Institut für Physikalische und Theoretische Chemie, Universität Bonn, Römerstraße 164, D-53117 Bonn, Germany

ARTICLE INFO

Article history:
Received 6 June 2016
Received in revised form 1 August 2016
Accepted 2 August 2016
Available online 8 August 2016

Keywords:
DEMS
Flow Through Cell
RRDE
Oxygen Reduction
Organic Electrolytes

ABSTRACT

In this article we present a novel 2-compartment flow through cell (6-electrode cell). The 6-electrode cell allows the operation of two working electrodes independent from each other one of which serves as a detection electrode. A current at the detection electrode signifies the formation of soluble species at the generator electrode. This approach is reminiscent of an RRDE arrangement.

However, the 6-electrode cell allows combination of RRDE-analogue experiments with differential electrochemical mass spectroscopy (DEMS). Volatile products formed at the detection electrode, therefore, can be identified *via* mass spectroscopy, which is not possible with an RRDE-arrangements. At the same time it is possible to identify volatile products formed at the generator electrode.

We demonstrate the application of the 6-electrode cell for the oxygen reduction reaction in Li^+-containing DMSO based electrolyte. We will show that soluble products that react at the detection electrode are due to the oxidation of superoxide.

1. Introduction

The detection of electrochemical reaction products and intermediates is an ongoing challenge. A reasonable distribution of current and a continuous, well defined transport of reactants to the electrode as well as a short detection time, has to be ensured. To this end several cells have been designed to combine electrochemistry with mass spectroscopy [1–7].

Of these the dual thin layer cell has found ample applications in our group. It was introduced by Jusys *et al.* in 1999 [4] and was only slightly modified ever since. The cell was originally designed to combine electrochemical quartz crystal micro balance (eQCMB) measurements with differential electrochemical mass spectroscopy (DEMS) [4]. The dual thin layer cell is operated under continuous electrolyte flow, which causes a defined mass transport [8–12].

It is an interesting feature of the dual thin layer cell that the combination of eQCMB and DEMS allows both the detection of solid and volatile products of electrochemical reactions [4]. However, the most important benefit of the dual thin layer cell is that it allows to conduct DEMS measurements at smooth and even single crystalline electrodes under defined convection conditions. The dual thin layer cell made it possible to conduct DEMS studies on the electrochemical oxidation of fuels such as methanol [13–16] and ethanol [17–19]. Others investigated the effect of the oxidation of small molecules at BDD-electrodes [20–22]. Using the dual thin layer cell, the effect of the surface state of single crystal electrodes on the CO-oxidation [23] or hydrogen evolution were investigated [24]. Recently we have employed the dual thin layer cell to investigate oxygen reduction from organic electrolytes [25,26].

Extensive studies have been conducted to characterise the convection conditions in the dual thin layer [8–12]. This allowed us to use the cell in combination with mass spectroscopy to determine the solubility of gases and their diffusion coefficient in various electrolytes [12].

A modification of the original dual thin layer cell allows the combination of ATR-FTIR spectroscopy with DEMS [27]. This arrangement was used to investigate the CO-oxidation at platinum [27]. Another modification of the dual thin layer cell allows RRDE-like applications [28]. In those arrangements the steel holder (with the steel frit covered by the porous Teflon membrane) in the lower compartment is replaced by a second working electrode that is used to detect incoming electrochemical active products of the working electrode in the upper compartment [28]. This cell was

* Corresponding author.
E-mail address: baltruschat@uni-bonn.de (H. Baltruschat).

http://dx.doi.org/10.1016/j.electacta.2016.08.008
0013-4686/

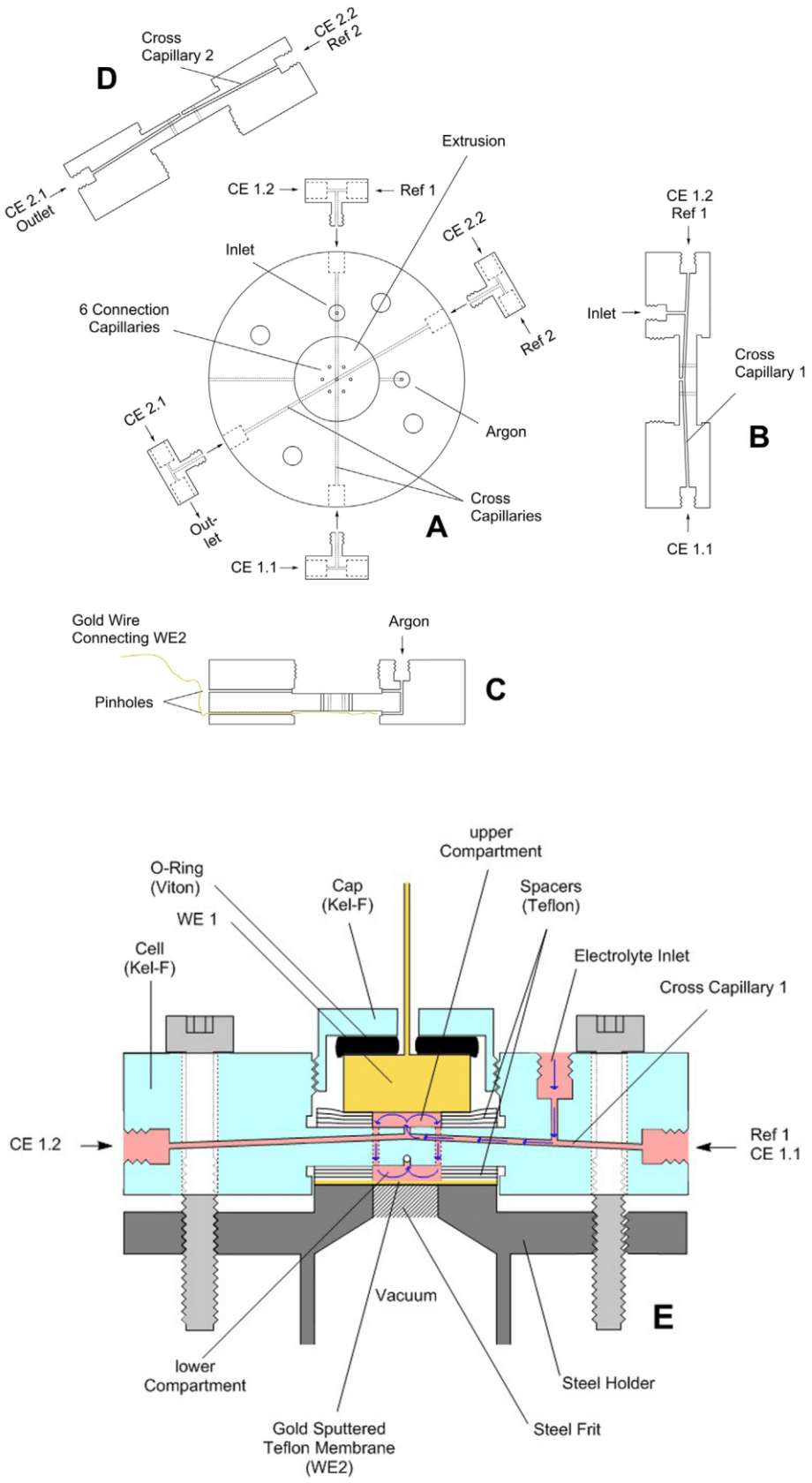

Fig. 1. Schematic drawing of the 6-electrode cell. A: Top view; B, C and D: cross section. E: cross section of the assembled cell.

used to study the oxygen reduction reaction at single crystal electrodes, which is hardly possible in an RRDE experiment [28]. However, the arrangement described by Jusys *et al.* cannot be combined with DEMS. Wang*et al.* have introduced a double-band-electrode channel flow differential electrochemical mass spectrometry cell that allows RRDE-like applications in combination

with DEMS [7]. In that arrangement the electrolyte flows past a generating electrode, a porous PTFE membrane and afterwards past a detection electrode. Volatile products formed at the generating electrode evaporate at the PTFE membrane into the vacuum and electrochemical active products undergo a reaction at the detection electrode [7].

Arrangements as those described by Wang *et al.* [7] and Jusys *et al.* [28] for RRDE-like applications are possible, when the employed electrolyte has sufficient conductivity. With acidic or alkaline electrolytes of high enough concentration this is usually the case. However, the low conductivity of organic electrolytes prohibits such an RRDE-analogous use of the dual thin layer cell. Therefore, the conductivity of the electrolyte must be high in order to avoid a severe *iR*-drop.

Here we present a 6-electrode cell which is a modification of the dual thin layer cell that allows RRDE-like DEMS-experiments when electrolytes of low conductivity are employed or when a large *iR*-drop is expected. In the present study we demonstrate how the 6-electrode cell can be used to identify which intermediate of oxygen reduction in DMSO based electrolytes reacts at the detection electrode. Identification of this intermediate is possible due the quantitative detection of volatile reaction products formed at the second working electrode.

The 6-electrode cell is also of interest for studies of other reactions where selectivity of the ring electrode in an conventional RRDE-arrangement cannot be taken for granted. This is for instance the case for CO_2 reduction [29] or oxidation of NH_3 [30]. Large current densities due to concomitant hydrogen during CO_2 reduction and the *iR*-drop associated therewith render an RRDE-like application of the dual thin layer cell even in aqueous electrolytes impossible. However, the 6-electrode cell is of general interest for the investigation of any electrochemical reaction in organic electrolytes that involve gashouse species (*e.g.* hydrogen evolution, CO_2-reduction) because these electrolytes are usually low conducting and there is a persistent danger that electrolyte decomposition occurs. Hence, it is necessary to ensure that the species reacting at the detection electrode is not a product of electrolyte decomposition.

RRDE-like applications in the 6-electrode cell despite low conductivity of the electrolyte are possible due to the use of a second reference electrode that probes the potential of the working electrode in the lower compartment separately.

2. Experimental

2.1. Chemicals

Tetrabutylammonium perchlorate (electrochemical grade) and lithium perchlorate (battery grade) were purchased from Sigma Aldrich. Dimethyl sulfoxide (extra dry over molecular sieve) was purchased from across organics. The electrolyte purged with a custom made mixture of argon and oxygen (Ar: O_2 = 80: 20) that was obtained from AirLiquide. Argon which was used to purge the same cell was of 99.999 purity and was obtained from the same company.

2.2. DEMS Setup

Experiments were performed at a differentially pumped DEMS-system. The first pumping stage was pumped with a turbo molecular pump with a suction power of 200 L/s and the second stage was pumped with a turbo molecular pump with a suction power of 50 L/s. The ionic current was recorded with a quadrupole mass spectrometer (QMA 430, Pfeiffer Vacuum).

The data of the electrochemical experiments were acquired with an A/D converter card (NI6021, National Instruments) in conjunction with an connection box (BNC-Connector block 2110, National Instruments).

2.3. Cell design

The described cell is manufactured from Kel-F® and is a modification of our dual-thin-layer-cell [4]. Fig. 1 shows a schematic drawing of this cell in an on top view (Fig. 1A) and in three different side views (Fig. 1B–D). The exact geometries of the cell can be found in the Fig. S1 in the supporting information. The cell is circular and an extrusion is placed in the centre of the cell both on the top side as well as on the bottom side. The extrusions are necessary to hold the working electrode (upper side) and the steel holder (bottom side) which is shown in Fig. 1E. The side view in Fig. 1E shows that the steel holder and working electrode are placed on PTFE spacers. The space that is left between cell body and working electrode is called upper compartment and the space between cell body and steel holder is called lower compartment. Six capillaries arranged in a hexagon (Fig. 1A) connect the upper compartment with the lower compartment (Fig. 1B–E). In the centre of the cell a drilling connects the upper compartment *via* cross capillary 1 to the electrolyte inlet, to the counter electrodes CE1.1 and CE1.2 as well as to the reference electrode Ref1 (Fig. 1B and E). Cross capillary 2 is rotated by 30° to cross capillary 1 and connects the lower compartment to the electrolyte outlet, to the counter electrodes CE2.1 and CE2.2 as well as to the reference electrode Ref2 (Fig. 1D). Except for the six connection capillaries there is no direct connection between cross capillaries 1 and cross capillary 2. A screw joint at both ends of the cross capillaries allows to mount T-pieces to the cell. The reference and the counter electrodes are inserted into the T-piece *via* Luer locks. Also the electrolyte inlet is connected *via* a Luer lock to a glass storage vessel.

Fig. 1E shows a schematic cross section of the cell during an experiment. The working electrode is pressed on the PTFE spacers *via* a Kel-F® cap that can be screwed into the cell body. In order to achieve a good distribution of the applied force, an O-ring is placed between cap and working electrode. (This approach is problematic, though, if single crystals are to be used because the crystal might grind on the Teflon spacers. When working with the dual thin layer cell we usually use a clamp to apply a strong enough force to avoid electrolyte leakage at the interface between spacers and electrode. In order to enable experiments with single crystals it would be possible to use a clamp with this cell as well. However, given that so many items are attached to the periphery of the cell already, a screw-in cap is the much more comfortable solution.)

Oxygen reduction from air at the backside of the electrode is a parasitic process. In addition, oxygen that diffuses through the Teflon spacers and enters the mass spectrometer causes an unsteady baseline. Therefore, the cell is purged with argon throughout the experiment. This is achieved *via* the argon inlet. A Luer lock allows the connection to a PTFE tube. Argon is inserted to the upper and lower compartment *via* two capillaries. There it is led *via* countersinks around the working electrode and the steel holder, respectively, and leaves the cell through two pinholes afterwards (Fig. 1C).

During an experiment the electrolyte is placed in a storage vessel which is connected to the electrolyte inlet *via* a Luer lock. Due to hydrostatic pressure the electrolyte flows through the cell on its own. A peristaltic pump placed at the outlet slows the electrolyte flow down to the favoured level. The electrolyte enters the cell through the electrolyte inlet and flows through cross capillary 1 to the upper compartment. From there it enters the lower compartment through six connection capillaries. The electrolyte leaves the lower compartment through cross capillary 2. The blue arrows in Fig. 1E show the pathway of the electrolyte.

In order to prevent liquid electrolyte from entering the vacuum of the mass spectrometer, a PTFE membrane with an average pore diameter of 20 nm is placed on top of the steel holder. A steel frit provides mechanical support for the membrane. In order to allow the use of the membrane as a working electrode a metal film of 50 nm thickness is sputter deposited. A 0.05 mm gold wire pressed between membrane and spacers connects the membrane to a potentiostat. The gold wire is placed in the capillary that leads argon from the lower compartment to the outside (*c.f.* Fig. 1C).

2.4. Instrumental Arrangements

We modified the dual thin layer cell in the presented form in order to be able to introduce a second reference electrode that allows us to probe the potential of a working electrode in the lower compartment. Because of the large electrolyte resistance in the small capillaries the usual 4-electrode arrangement (as for RRDE studies) is not possible. In the 6-electrode cell the current of WE1 does not flow through the 6 connection capillaries to the counter electrode placed at the outlet (as in the duel thin layer cell) but through cross capillary 1 to CE1.2. Therefore, no *iR*-drop occurs when the potential of the working electrode in the lower compartment is probed by reference electrode 2 *via* cross capillary 2. However, this arrangement requires two potentiostats, each of which is connected to a working electrode, to a reference electrode and a set of two counter electrodes. The counter electrodes CE1.1 and CE1.2 are the set of counter electrodes that belong to working electrode WE1 and correspondingly CE2.1 and CE2.2 belong to working electrode WE2. CE1.2 and CE2.2 are connected *via* a 1 MΩ resistance to the respective potentiostat, whereas CE1.1 and CE2.1 are connected *via* a 1 Ω resistance. This arrangement was found to be necessary to achieve an optimal distribution of current. To avoid any current flow between the counter electrodes connected to the two different potentiostats, which would lead to an additional *iR* drop within the cell, the two potentiostats have to be electronically decoupled.

Therefore, only one potentiostat can be employed as a grounded source, whereas the other potentiostat is used as a floating source. We chose to employ potentiostat 1 which is connected to WE1 as a grounded source. Potentiostat 2 which is connected to WE2 along with the function generator is decoupled from ground *via* an isolation transformer. Special care must be taken to avoid grounding by other means (*e.g.* dangling cables).

The data of both potentiostat were acquired with the same computer with an inbuilt A/D converter (differential input). The connection box of the A/D converter card allows to decouple the signal source from ground *via* a 100 MΩ resistance.

3. Calibration

Baltruschat [8] has discussed in detail that calibration of the dual thin layer cell is necessary to correlate faradaic current and ionic current in a (semi)quantitative way. This can only be done by performing an electrochemical reaction of known stoichiometry under similar conditions as the actual experiment [8].

In the case of the 6-electrode cell two calibration measurements are necessary because four quantities have to be correlated to each other. These quantities are the faradaic current at WE1 (I_F^{WE1}), the faradaic current at WE2 (I_F^{WE2}), the ionic current for mass 32 due to the reaction at WE1 ($I_{I,32}^{WE1}$) and the ionic current for mass 32 due to the reaction at WE2 ($I_{I,32}^{WE2}$).

We will derive in Appendix A.1 the theory that underlies the application of the 6-electrode cell. In the following paragraphs, however, we will restrict ourselves to the most relevant equations in a simplified form.

3.1. Calibration Reaction of the 6-Electrode Cell

As in the case with the dual thin layer cell [31,32] also in the present study calibration was achieved by reduction of oxygen from an electrolyte of 0.5 M $TBAClO_4$ in DMSO. Fig. 2 shows the resulting curves of the calibration measurement. Both in the red and in the black curve of Fig. 2A WE1 is cycled in the potential range between 0.0 V and -1.6 V. As the potential at WE1 becomes more negative than -1.0 V oxygen is reduced quantitatively to superoxide (*i.e.* all the reduced oxygen forms superoxide, not all oxygen in the electrolyte is reduced). At potentials lower than -1.2 V the reaction becomes diffusion limited. Once oxygen reduction starts at WE1 the ionic current for mass 32 decreases below zero (Fig. 2C). (The negative ionic current is due to the subtractions of the background current caused by the continues, diffusion limited evaporation of dissolved O_2 into the vacuum.)

The difference between the red and the black curve in Fig. 2C is quite severe. This is due to the experimental arrangement: A platinum sputtered Teflon membrane is used in the lower compartment, which was kept at a potential of 0.0 V. This potential is sufficient to evolve oxygen from superoxide that is generated at WE1. Hence, the evolution of oxygen at WE2 offsets the consumption of oxygen at WE1. The current due to the oxidation of superoxide at WE2 is shown in Fig. 2B (we will discuss in the Appendix A.1 Eq. (A1.14) why a small faradaic current at WE2 can offset the ionic current due to the reaction at WE1).

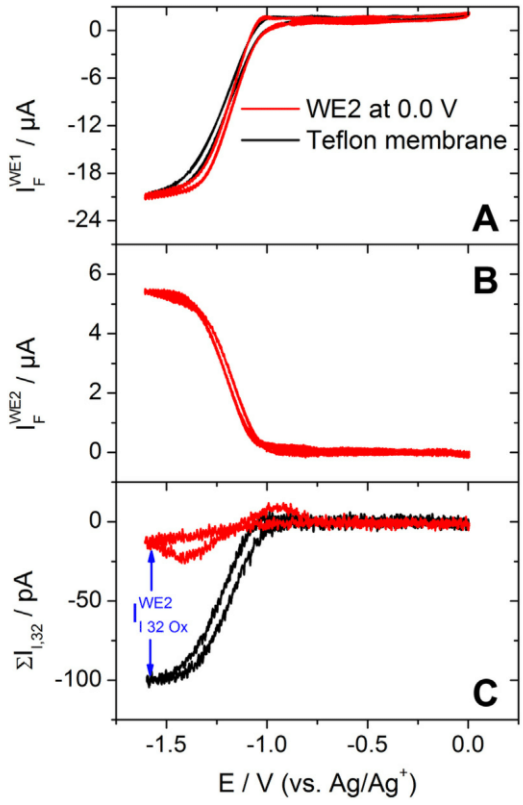

Fig. 2. A: CV at WE1 and B: corresponding current at WE2 (if present) obtained in an electrolyte of 0.5 M $TBAClO_4$ in DMSO which was purged with a mixture of argon and oxygen (Ar: O_2 = 80: 20). C: MSCV for mass 32. The red curves were obtain when a potential of 0.0 V was applied to a platinum sputtered Teflon membrane and the black curves were obtained when a ordinary Teflon membrane was placed in the lower compartment. Sweep rate: 10 mV/sec; Flow rate 5 µL/sec. (For interpretation of the references to color in this figure legend, the reader is referred to the web version of this article.)

In Fig. 2C the measured ionic current is called $\sum I_{I,32}$, because the ionic currents $I_{I,32}^{WE1}$ and $I_{I,32}^{WE2}$ are superimposed. In the black curve a Teflon sputtered membrane is placed in the lower compartment. Therefore, no electrochemical reaction can take place in the lower compartment. Hence, the ionic current $\sum I_{I,32}$reflects only the consumption of oxygen at WE1 and no other signal is superimposed.

3.2. Introduction and Determination of the faradaic transfer efficiency $N_{F,Su}$

In the calibration experiment of Fig. 2 superoxide that is transported from the upper compartment to the lower compartment can be re-oxidised to oxygen at WE2. However, only a fraction of the superoxide will actually undergo a reaction at WE2 (the majority of superoxide will leave the cell along with the electrolyte through the outlet). This share is the faradaic transfer efficiency $N_{F,Su}$ (the index "Su" indicates superoxide), which is the analogue of the collection efficiency N of an RRDE arrangement. According to Eq. (1) $N_{F,Su}$ can be determined from the ratio of the faradaic current at WE1 and WE2 (*c.f.* Appendix A.1)

$$N_{F,Su} = \frac{I_F^{WE2}}{I_F^{WE1}} \tag{1}$$

From the red curves in Fig. 1A and B we obtained a faradaic current of -20.97 μA at WE1 and a faradaic current of 5.41 μA at WE2. Hence, the faradaic transfer efficiency of superoxide is

$$N_{F,Su} = 0.26$$

3.3. Introduction and Determination of the Calibration Constants $K_{1,32}^*$ and $K_{2,32}^*$

DEMS is a (semi)quantitative method and, therefore, the ionic current is proportional to the faradaic current. The relationship is given by Eq. (2) (*c.f.* Appendix A.1),

$$z \cdot I_I = K^* \cdot I_F \tag{2}$$

in whichz is the number of transferred electrons, I_I is the ionic current, I_F is the faradaic current and the proportionality constant K^* is called the calibration constant. K^* contains the sensitivity of the mass spectrometer but also the probability that the product of an electrochemical reaction passes into the vacuum of the mass spectrometer. The latter depends on the cell geometry and will be far larger for WE2 than for WE1 because WE2 is placed immediately at the interface between vacuum and electrolyte. Hence, two calibration constants are required: One to correlate I_F^{WE1} and $I_{I,32}^{WE1}$ (which is K_1^*) the other to correlate I_F^{WE2} and $I_{I,32}^{WE2}$ (which is K_2^*). In K^* also the fragmentation pattern of oxygen enters: We measure the ionic current for mass 32 rather than the much smaller ionic current for mass 16. Hence, we add the index "32" to K^*. For the present study where we want to correlate the ionic current for mass 32 with the faradaic current due to oxygen reduction we require $K_{1,32}^*$ and $K_{2,32}^*$.

It is straight forward to determine $K_{1,32}^*$ from the black curves in Fig. 1A and C. The faradaic current at WE1 is $I_F^{WE1} = -20.84\mu A$. In the black curve of Fig. 1C $\sum I_{I,32}$ equals $I_{I,32}^{WE1}$ because no reaction takes place at WE2 and $I_{I,32}^{WE2}$ is zero. Hence, with a ionic current $I_{I,32}^{WE1} = -99.87pA$ and a z-value of one (superoxide) we obtain

$$K_{1,32}^* = 4.79 \cdot 10^{-6}$$

via Eq. (2).

In principle it is possible to obtain $K_{2,32}^*$ by the reduction of oxygen at WE2, while WE1 is disconnected. However, we chose a different approach: the calibration constant $K_{2,32}^*$ is obtained from the red and the black curves in Fig. 1. From the black curve in Fig. 1 we obtain $I_{I,32}^{WE1}$. However, we can only determine $\sum I_{I,32}$ not $I_{I,32}^{WE2}$ from the red curve ($\sum I_{I,32} = -12.54\,pA$) and $I_{I,32}^{WE2}$ remains inaccessible through direct measurement. Notwithstanding this, we can determine $I_{I,32}^{WE2}$ when $I_{I,32}^{WE1}$ is subtracted from $\sum I_{I,32}$. By this procedure we obtain $I_{I,32}^{WE2} = 87.3pA$ and from the faradaic current at WE2 which is $I_F^{WE2} = 5.41\mu A$, we obtain *via* Eq. (2)

$$K_{2,32}^* = 16.14 \cdot 10^{-6}$$

In the calibration measurement that led to the black curve in Fig. 1 we did not simply disconnect WE2 but we removed it all together and replaced it with a Teflon membrane. This procedure causes a change of the geometry of the cell, which affects the transfer efficiency.

Therefore, we conduct our experiments in the following sequence: First we calibrate the cell *via* the reduction of oxygen from an electrolyte of 0.5 M $TBAClO_4$ in DMSO at WE1 and re-oxidation of the formed superoxide at WE2 (red curve in Fig. 1). Then we change to an electrolyte of 0.5 M $LiClO_4$ in DMSO. From this electrolyte we reduce oxygen at the electrode in the upper compartment and re-oxidise soluble species that are transported from the upper compartment to the lower compartment at WE2 which is placed at 0.0 V (red curve in Fig. 2).

For the second set of measurements we remove the 6-electrode cell from the steel holder and replace both the Teflon spacers and the membrane. After we have reassembled the 6-electrode cell we reduce oxygen in the first measurement from the lithium containing electrolyte (black curve in Fig. 2) and then (after extensive washing of the cell and of the storage vessel with dried DMSO) we reduce oxygen from the TBA^+ containing electrolyte in the second measurement (black curve in Fig. 1).

Any changes of the geometry factor will affect both the calibration measurements and the measurements in Li-containing electrolyte in the same way. These changes enter the calibration constant $K_{2,32}^*$ which corrects the effects of an altered geometry factor during evaluation.

4. Results and Discussion

In the present study we want to demonstrate the use of the 6-electrode cell by investigation of oxygen reduction in lithium containing DMSO based electrolytes at a polycrystalline gold electrode. In the past we have used the dual thin layer cell to the same end [31,32].

Fig. 2 shows two sets of curves which were obtained in the same way as those in Fig. 1 when a Li-containing electrolyte is used: The red curves were obtained when a platinum sputtered Teflon membrane was used as a working electrode (E_{WE2} = 0.0 V) in the lower compartment and the black curves were obtained when the platinum electrode was changed to an ordinary Teflon membrane. The CVs resemble those curves we have obtained in previous studies at gold electrodes [31,32]. This is also true for the MSCV for mass 32 that was obtained when no second working electrode was employed. In the potential region of oxygen reduction, the CV has a shoulder at low overpotentials. This shoulder is due to the reduction of oxygen to superoxide. At larger over potentials lithium peroxide is formed electrochemically *via* the direct transfer of two electrons [25]. Since Li_2O_2 is deposited on the working electrode, the working electrode is deactivated and a peak is observed both in the CV and in the MSCV for mass 32.

From the black curves in Fig. 2 we obtain I_F^{WE1} and $I_{I,32}^{WE1}$ (because there is no WE2 and $\sum I_{I,32}$ equals $I_{I,32}^{WE1}$). Therefore, we can calculate from Eq. (2) the number of electrons that are transferred at WE1 per reduced molecule of oxygen (z^{WE1}). The z-value is shown in Fig. 3 as a function of the applied potential. The curve resembles those shown in previous studies [25].

z^{WE1} is only an average value because oxygen can be reduced to several products (superoxide, peroxide, oxide) and z^{WE1} is a function of product distribution. Therefore, it is possible to calculate the share of oxygen $\chi(Su)$ that is reduced to superoxide from z^{WE1} according to Eq. (3) (*c.f.* Appendix A.2)

$$\chi(Su) = 2 - z^{WE1} \tag{3}$$

In Fig. 2 the CV remains unaffected when a potential is applied to the second working electrode (red curve) in the lower compartment. This is not surprising since there is a spatial separation between WE1 and WE2. Therefore, the electrochemistry at WE2 should not affect the electrochemistry at WE1 in any way. Notwithstanding this, the MSCV for mass 32 changes significantly. The potential of 0.0 V at WE2 is sufficient to oxidise all the incoming superoxide and to re-evolve oxygen. Hence, in total less oxygen is consumed and the ionic current for mass 32 decreases less. The shape of the MSCV for mass 32 now somewhat resembles the shape of the CV. At low overpotentials there is a shoulder and as the potential decreases a peak appears.

In a previous study we have shown an RRDE measurement on the reduction of oxygen from a Li-containing DMSO based electrolyte [31]. The shape of the ring current observed in that study resembles the shape of the current observed at WE2 in Fig. 2.

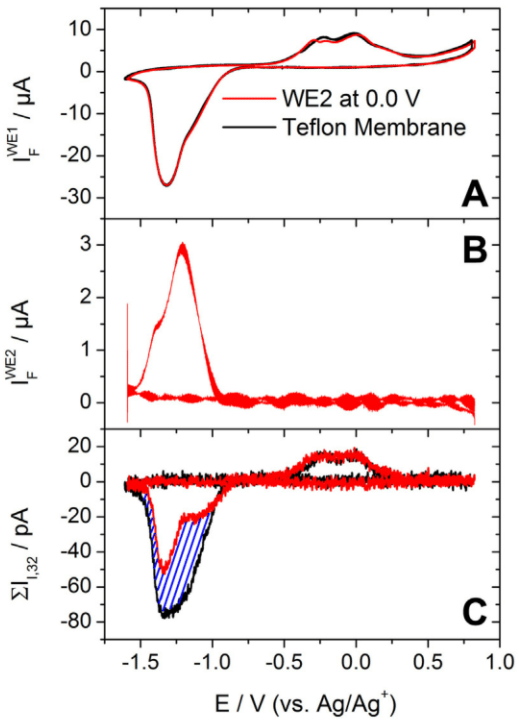

Fig. 3. A: CV at WE1 and B: corresponding current at WE2 (if present) obtained in an electrolyte of 0.5 M $LiClO_4$ in DMSO which was purged with a mixture of argon and oxygen (Ar: O_2 = 80: 20). C: MSCV for mass 32. The red curves were obtain when a potential of 0.0 V was applied to a platinum sputtered Teflon membrane and the black curves were obtained when a ordinary Teflon membrane was placed in the lower compartment. Sweep rate: 10 mV/sec; Flow rate 5 µL/sec. (For interpretation of the references to color in this figure legend, the reader is referred to the web version of this article.)

The current at WE2 increases as WE1 enters the potential of oxygen reduction. Once the overpotential at WE1 becomes large enough, that oxygen is reduced electrochemically to peroxide the current at WE2 decreases, but does not drop to zero. At those potentials at which the activity of WE1 sharply decreases and the current drops to zero, a shoulder appears in the current at WE2. In a previous study we wondered whether this shoulder is due to the formation of superoxide formed parallel to peroxide or whether other intermediates of electrochemical peroxide formation (*e.g.* LiO_2^-) are transported away [31]. We are now able to address this question with the help of the 6-electrode cell.

The cross-hatched area in Fig. 2 corresponds to $I_{I,32}^{WE2}$. $I_{I,32}^{WE2}$ was calculated from $\sum I_{I,32}$ (red curve in Fig. 2) and $I_{I,32}^{WE1}$ (black curve in Fig. 2) and is plotted along with I_F^{WE2} as a function of the potential at WE1 in Fig. 4. $I_{I,32}^{WE2}$ follows the general shape of I_F^{WE2}. Initially $I_{I,32}^{WE2}$ increases as the overpotential increases, passes through a maximum and at even larger overpotentials a shoulder appears. From I_F^{WE2} and $I_{I,32}^{WE2}$ we can determine *via* Eq. (2) the number of electrons z^{WE2} that are required to re-evolve one molecule of oxygen. z^{WE2} remains close to 1 e^-/O_2 irrespective of the potential at WE1 in Fig. 5, we can show that only superoxide reacts at WE2. It is a very interesting feature that we cannot only detect the formation of intermediates, but that we can also identify the intermediate in question. In that respect the 6-electrode cell is superior to a conventional RRDE-arrangement.

Aside from Eq. (3) it is also possible to determine $\chi(Su)$ in two other ways. In Eq. (4) $\chi(Su)$ is determined from the faradaic currents at WE1 and WE2 (*c.f.* Appendix A.3). This approach is the same that is usually used in RRDE measurements. Similar to Eq. (4) the share of oxygen that is reduced to superoxide can also be calculated from the ionic currents $I_{I,32}^{WE1}$ and $I_{I,32}^{WE2}$ *via* Eq. (5) (*c.f.* Appendix A.4). In Eq. (5) N_r is the transfer ratio, which is defined in Appendix A.1.

$$\chi(Su) = \frac{2 \cdot I_F^{WE2}}{N_F \cdot I_F^{WE1} + I_F^{WE2}} \tag{4}$$

$$\chi(Su) = \frac{I_I^{WE2}}{N_r \cdot I_I^{WE1}} \tag{5}$$

It is noteworthy that we can determine the ionic current independent from the faradaic current. Therefore, the values determined for $\chi(Su)$ by Eqs. (4) and (5) are independent from each

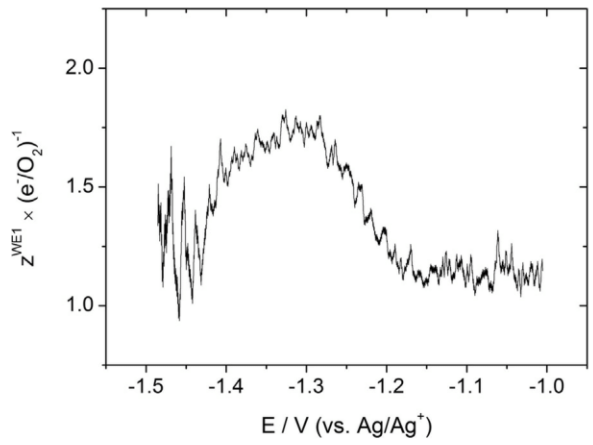

Fig. 4. z^{WE1}-value plotted as a function of the potential. The values on display were calculated according to Eq. (2) from the data presented in Fig. 3.

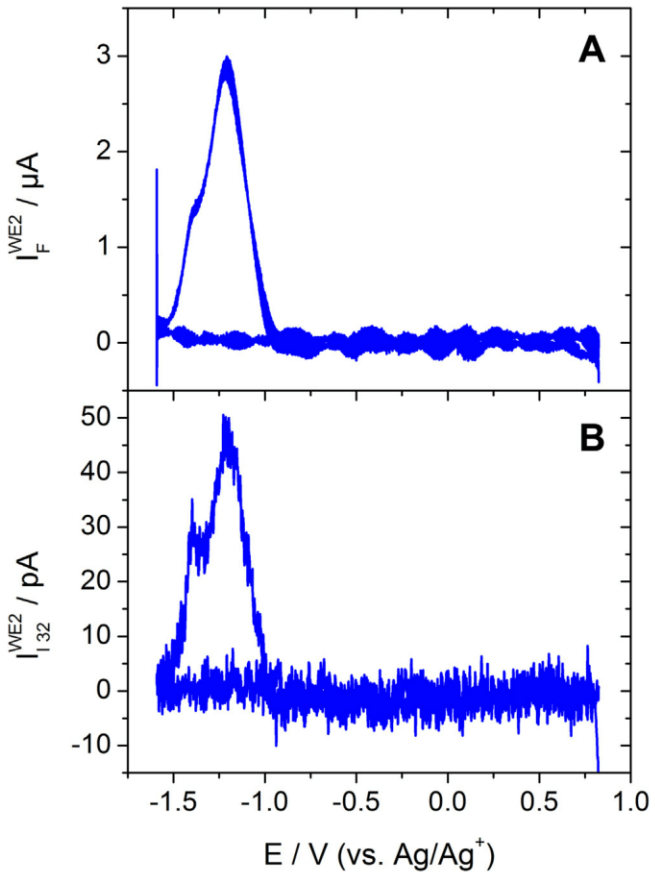

Fig. 5. I_F^{WE2} (A) and $I_{I,32}^{WE2}$(B) as a function of the potential applied to WE1. $I_{I,32}^{WE2}$ was calculated by subtraction of $I_{I,32}^{WE1}$ from $\sum I_{I,32}$ (obtained from the data presented in Fig. 3). $I_F^{WE2}$was already shown in Fig. 3.

other. However, the values determined from Equation 3 are not linearly independent from those determined by Equation 4 and 5.

In Fig. 6 we show the share of oxygen that is reduced to superoxide as a function of potential. We obtained the displayed values from Eqs. (3)–(5). At low overpotentials oxygen is largely reduced to superoxide. As the overpotential increases the share of oxygen that is reduced to superoxide drops to 20 to 40%. However, in the course of rapid deactivation of WE1 oxygen is reduced to superoxide again. This finding is in good agreement to the spectroscopic studies performed by Yu *et al.* in the same electrolyte system at gold electrodes [33]. The finding that we obtain the same results by Eqs. (3)–(5), which are in good agreement with the results of others [33], emphasise the reliability and quality of the data gathered with the 6-electrode cell.

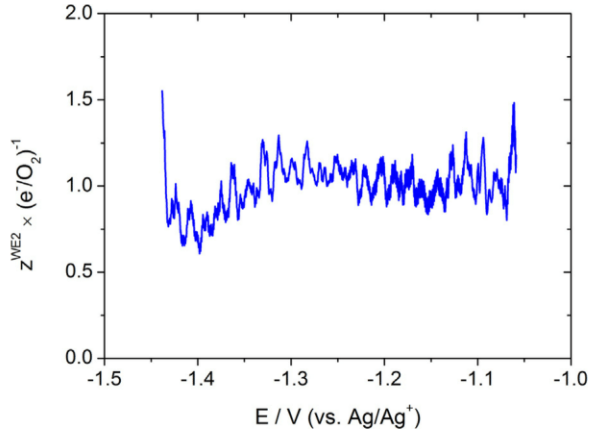

Fig. 6. Average z^{WE2}-value plotted as a function of the potential. The values on display were calculated according to Eq. (2) from the data presented in Fig. 5.

As pointed out above it is not possible to simply leave the metal sputtered working electrode at open circuit because superoxide undergoes a heterogeneous reaction at the second working electrode that results in oxygen evolution. We have shown in a previous study that a gold sputtered electrode in the lower compartment at open circuit changes the MSCV for mass 32 significantly [31]. In that study we wondered whether gold at open circuit catalyses the disproportionation of superoxide or whether gold catalyses a reaction between superoxide and components in the electrolyte, which results in the evolution of oxygen. With the 6-electrode cell we are able to address that question at least qualitatively. Fig. 7 shows the CV and MSCV for mass 32 when oxygen is reduced from an electrolyte of 0.5 M $LiClO_4$ in DMSO at WE1 and when WE2 is kept at open circuit potential (green curve). In Fig. 7 for comparison also the MSCVs for mass 32 are added when a potential is applied to WE2 (red curve) and when WE2 is replaced by a Teflon membrane (black curve). Both curves were already shown in Fig. 2.

In Fig. 8 there is no difference between the MSCV for mass 32 that was obtained when WE2 was left at open circuit and the MSCV for mass 32 that was obtained when a potential of 0.0 V was applied to WE2. When a potential of 0.0 V is applied to the WE2, every incoming superoxide is oxidised electrochemically to oxygen. If platinum at open circuit catalysed the lithium induced disproportionation of superoxide, only every second superoxide would release oxygen while the other half would be precipitated as Li_2O_2. Hence, it would be expected that the green curve in Fig. 7 is located between the red and the black curve if superoxide disproportionated. This is evidently not the case and a strong indication that superoxide undergoes some other reaction at the surface of the platinum electrode. Currently we do not know what compound in the electrolyte acts as a oxidising agent. There are several possibilities: Cl^{VII} in perchlorate has a large capacity to accept electrons, but due to the high activation barrier for the reduction of perchlorate especially in the absence of protons this seems unlikely. Superoxide reacts with DMSO to $DMSO_2$

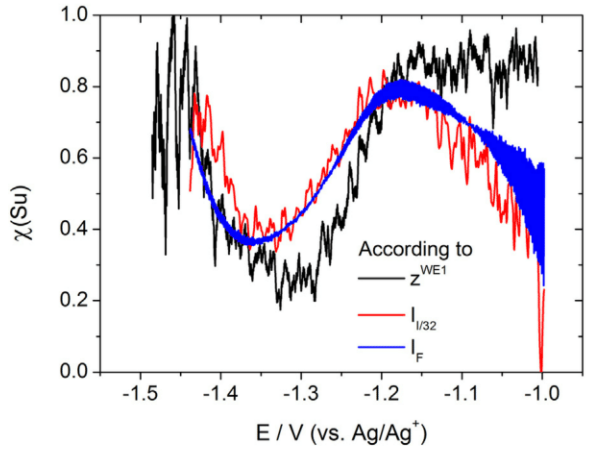

Fig. 7. Share of oxygen that is reduced to superoxide at WE1 plotted as a function of potential. Black: calculated according to Eq. (3) from the average z^{WE1} values presented in Fig. 4; red: Calculated according to Eq. (5); blue: Calculated according to Eq. (4) from the data presented in Fig. 3. (For interpretation of the references to color in this figure legend, the reader is referred to the web version of this article.)

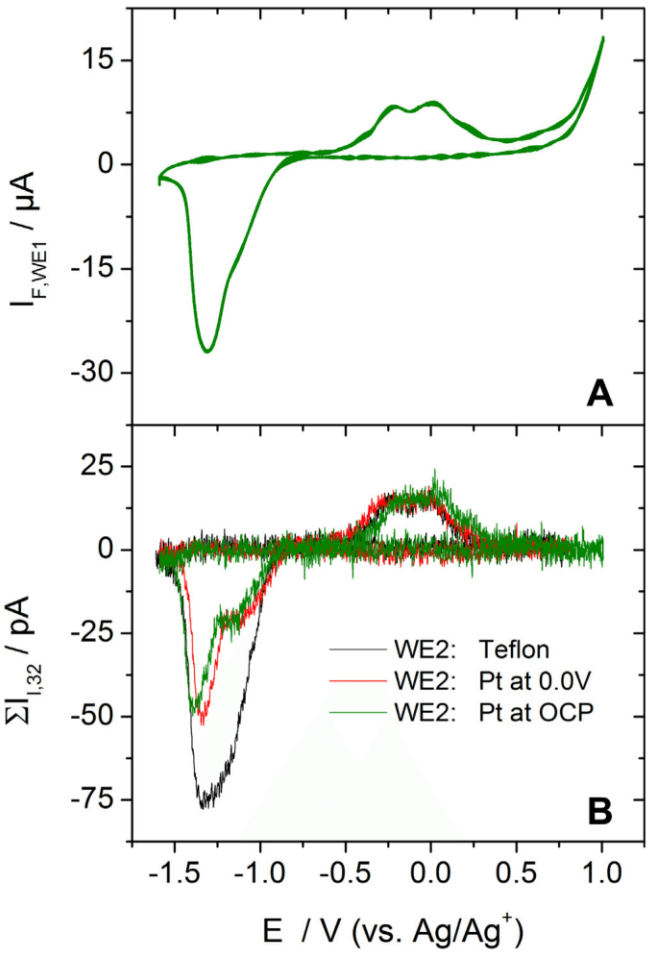

Fig. 8. CV (A) and MSCV for mass 32 (B) when oxygen is reduced at gold from an electrolyte of 0.5 M $LiClO_4$ in DMSO and when no potential is applied to WE2 (green). For comparison the MSCVs for mass 32 are added that were obtained when a potential of 0.0 V was applied to a platinum sputtered Teflon membrane (red) and when an ordinary Teflon membrane was place in the lower compartment (black). (For interpretation of the references to color in this figure legend, the reader is referred to the web version of this article.)

(dimethylsulfone) rather then to DMS (dimethylsulfide) [34]. This renders DMSO an unlikely oxidizing agent as well. There are rather large oxidation currents at WE1 when the potential surpasses 0.8 V. It is likely that oxidation products formed at WE1 adsorb at WE2 and stick to the surface until they are reduced by superoxide. However, DMSO is oxidised electrochemically to $DMSO_2$, [35] which should not be reduced by superoxide.

It is not improbable to assume that in gas diffusion electrodes of Li-O_2 batteries a number of particles are not in contacted and are at open circuit potential. The reaction between compounds in the electrolyte and superoxide at metal electrodes at open circuit could also occur at these sites in a Li-O_2 battery. If true, this would have wider implications for the design of gas diffusion electrodes for Li-O_2 batteries. However, whether the reaction between compounds in the electrolyte and superoxide has any implication for current Li-O_2 battery research depends on the exact nature of the reaction which is still elusive.

5. Conclusion

In here we have presented a 6-electrode cell which is a modification of the dual thin layer cell introduced by Jusys *et al.* [4]. The 6-electrode cell and the experimental procedure described in this work allow to combine RRDE-like experiments with DEMS. This is even possible when electrolytes with low conductivity are employed

We have demonstrated the use of the cell for oxygen reduction from Li-containing DMSO based electrolytes at gold electrodes. This allowed us to identify the exact nature of electrochemical active compounds that were generated at WE1 and detected at WE2. In addition, we were able to rule out that the disproportionation of superoxide at metal electrodes is responsible for the electroless evolution of oxygen. We were unable to answer these questions beyond doubt in a previous study [31].

Acknowledgements

The authors gratefully acknowledge the Federal Ministry of Eduction and Research (FRG) for funding this work. This work is part of the "LuLi- Strom aus Luft und Li" project (FKZ:03×4624A).

Appendix A. A.1 Introduction to the Theory of the 6-Electrode Cell

(A1.1) A.1 Introduction to the Theory of the 6-Electrode Cell

In the following section we will introduce a large number of quantities which often only differ in a super- or subscript. We have listed all quantities in Table 1 to assist the reader.

In this theory section we will consider the following scenario: During the experiment the potential at the working electrode in the upper compartment (WE1) is cycled in a potential range that is chosen in accordance with the redox system in solution. An electrochemical reaction at WE1 produces species x which, due to forced convection, is transported into the lower compartment. There, species x can evaporate into the mass spectrometer which causes a positive contribution to the ionic current for species x. At the same time a fixed potential is applied to the second working electrode. The potential is chosen such that species x undergoes a diffusion limited electrochemical reaction in the lower compartment (or a potential is chosen such that no reaction occurs at WE2). Due to the electrochemical reaction at WE2 the amount of species x entering the mass spectrometer will be reduced. Hence, the contribution of WE2 to the ionic current for species x will be negative. There is also the case that volatile species x reacts to non-volatile species y at WE1 which reacts back to species x at WE2. Transfer of the equations that are derived in the following to that case is straight forward and will not be discussed in detail.

Derivation of the faradaic transfer efficiency: The current at the second working electrode (I_F^{WE2}) is proportional to the amount $\dot{n}_{F,x}^{WE2}$ of species x that undergoes an electrochemical reaction per unit of time and is given by Eq. (A1.1)

$$I_F^{WE2} = \dot{n}_{F,x}^{WE2} \cdot z_x^{WE2} \cdot F \tag{A1.1}$$

In principle Eq. (A1.1) is the first derivative of Faraday's law with respect to time where z_x^{WE2} is the number of electrons that are transferred when one molecule of species x undergoes a reaction at WE2. F in Eq. (A1.1) is Faraday's constant. Eq. (A1.1) is only valid when all the current at WE2 is due to the reaction of species x to the same product. If also other substances then species x undergo a reaction at WE2, we have to consider the current efficiency $\alpha_{eff,x}^{WE2}$. The current efficiency is the fraction of the overall current at WE2 (I_F^{WE2}) that is due to the reaction of species x ($I_{F,x}^{WE2}$). In that case Eq. (A1.2) instead of Eq. (A1.1) has to be used.

$$\alpha_{eff,x}^{WE2} \cdot I_F^{WE2} = I_{F,x}^{WE2} = \dot{n}_{F,x}^{WE2} \cdot z_x^{WE2} \cdot F \tag{A1.2}$$

Table 1
List of quantities that will be introduced in the following section.

I_F^{WE1}	Faradaic current measured at WE1
I_F^{WE2}	Faradaic current measured at WE2
$I_{F,x}$	Amount of the faradaic current due to the generation/consumption of species x, without any regard where the faradaic current was measured.
$I_{F,x}^{WE1}$	Amount of the faradaic current at WE1 due to the generation/consumption of species x
$I_{F,x}^{WE2}$	Amount of the faradaic current at WE2 that is due to the electrochemical reaction of species x
$I_{I,m,x}^{WE1}$	Ionic current for mass m due to species x that was generated/consumed at WE1 and that (does not) enter(s) the vacuum.
$I_{I,m,x}^{WE2}$	Ionic current for mass m due to species x that was generated/consumed at WE2 and that (does not) enter(s) the vacuum.
$\sum I_{I,m,x}$	Ionic current for mass m due to species x that (does not) enter(s) the vacuum, without any regard at which working electrode species x was formed/consumed.
$\sum I_{I,m,x}$	Overall ionic current for mass m due to species x entering the vacuum.
$I_{F,Su}^{WE1}$	Amount of the current at WE1due to the generation of superoxide; subscript *Su* is used when species x is superoxide
$I_{F,Ox}^{WE1}$	Amount of the current at WE1due to the reduction of oxygen; subscript *Ox* is used when species x is oxygen
$\alpha_{eff,x}^{WE1}$	Current efficiency; the share of the faradaic current at WE1 that is due to the generation/consumption of species x
$\alpha_{eff,x}^{WE2}$	Current efficiency; the share of the faradaic current at WE2 that is due to an electrochemical reaction of species x
z_x^{WE1}	number of electrons that are transferred during generation/consumption of one molecule of species x at WE1
z_x^{WE2}	number of electrons that are transferred per molecule of species x that undergoes electrochemical reaction at WE2
F	Faraday's constant
$\dot{n}_{F,x}^{WE1}$	Amount of species x that is generated/consumed per unit of time at WE1
$\dot{n}_{F,x}^{WE2}$	Amount of species x that undergoes an electrochemical reaction at WE2 per unit of time
$\dot{n}_{I,x}^{WE1}$	Amount of species x that is generated/consumed per unit of time at WE1 and that (does not) enter(s) the vacuum
$\dot{n}_{I,x}^{WE2}$	Amount of species x that is generated/consumed per unit of time at WE2 and that (does not) enter(s) the vacuum
$\dot{n}_{I,x}$	Amount of species x that that (does not) enter(s) the vacuum per unit of time, without any regard at which working electrode species x was formed/consumed.
N	Collection efficiency of an RRDE arrangement
$N_{F,x}$	Faradaic transfer efficiency; share of the species x that is generated at WE1 and undergoes reaction at WE2
$N_{I,x}^{WE1}$	Ionic transfer efficiency; share of species x generated/consumed at WE1 that (does not) enter(s) the vacuum.
$N_{I,x}^{WE2}$	Ionic transfer efficiency; share of species x generated/consumed at WE2 that (does not) enter(s) the vacuum.
$K_{m,x}^{\circ}$	Calibration constant of the mass spectrometer; it contains the probabilities that species x is ionized, that species x forms a fragment with mass m and that the fragment with mass m is detected.
$K_{1,m,x}^{*}$	Calibration constant that allows correlation of $I_{F,x}^{WE1}$ with $I_{I,m,x}^{WE1}$ when species x has a fragment with mass m
$K_{2,m,x}^{*}$	Calibration constant that allows correlation of $I_{F,x}^{WE2}$ with $I_{I,m,x}^{WE2}$ when species x has a fragment with mass m
$K_{m,x}^{*}$	Calibration constant that allows correlation of $I_{F,x}$ with $I_{I,m,x}$ when species x has a fragment with mass m, without any regard to the working electrode.

We will not consider here the more general case that species x can react to various products with various values for z_x^{WE2}.

Similar to Eq. (A1.1) the faradaic current at WE1 (I_F^{WE1}) is given by Eq. (A1.3).

$$I_F^{WE1} = \dot{n}_{F,x}^{WE1} \cdot z_x^{WE1} \cdot F \tag{A1.3}$$

in which $\dot{n}_{F,x}^{WE1}$ is the amount of species x that is generated at WE1 per unit of time and $z_x^{WE1}$is the number of electrons that are transferred, when one molecule of species x is formed at WE1.

Eq. (A1.3) only holds when all the faradaic current that is following at WE1 results in the generation of species x. Otherwise the current efficiency $\alpha_{eff,x}^{WE1}$ has to be introduced into Eq. (A1.3). The current efficiency is the fraction of the overall current that is used to generate a particular species. In that case Eq. (A1.4) instead of Equation A1.3 needs to be used

$$\alpha_{eff,x}^{WE1} \cdot I_F^{WE1} = I_{F,x}^{WE1} = \dot{n}_{F,x}^{WE1} \cdot z_x^{WE1} \cdot F \tag{A1.4}$$

Only those molecules of species x that are generated at WE1 can react at WE2. Therefore, $\dot{n}_{F,x}^{WE2}$ is proportional (but not equal) to $\dot{n}_{F,x}^{WE1}$. According to Eq. (A1.5) the proportionality constant between $\dot{n}_{F,x}^{WE2}$ and $\dot{n}_{F,x}^{WE1}$ is the faradaic transfer efficiency $N_{F,x}$

$$\dot{n}_{F,x}^{WE2} = N_{F,x} \cdot \dot{n}_{F,x}^{WE1} \tag{A1.5}$$

Inserting Eqs. (A1.1) and (A1.3) into Eq. (A1.4) and rearrangement yields Eq. (A1.6)

$$N_{F,x} = \frac{\alpha_{eff,x}^{WE2} \cdot z_x^{WE1} \cdot I_F^{WE2}}{\alpha_{eff,x}^{WE1} \cdot z_x^{WE2} \cdot I_F^{WE1}} \tag{A1.6}$$

Are z_x^{WE1}, z_x^{WE2}, $\alpha_{eff,x}^{WE1}$and $\alpha_{eff,x}^{WE2}$ known, then the faradaic transfer efficiency $N_{F,x}$ can be determined. Eq. (A1.6) becomes Eq. (1) when z_x^{WE1}, z_x^{WE2}, $\alpha_{eff,x}^{WE1}$and $\alpha_{eff,x}^{WE2}$ are considered one. Since, oxygen is reduced quantitatively to superoxide in an electrolyte of 0.5 M $TBAClO_4$ in DMSO this assumption is valid.

At this point it is worthwhile to emphasise that there is a difference between the collection efficiency and the transfer efficiency of the dual thin layer cell. No discussion on the difference will be given here and the interested reader is referred to Reference [8] for further information. Unfortunately the faradaic transfer efficiency $N_{F,x}$ of the 6-electrode cell is the analogue of the collection efficiency N of an RRDE-arrangement. For obvious

reasons we will stick to the terminology introduced for the flow through thin layer cell and for the dual thin layer cell [8].

RRDE arrangements are often used to determine the share of intermediates or side products formed during electrochemical reactions. In order to be able to do so at least the collection efficiency N needs to be known. The 6-electrode cell can be used to the same end if the faradaic transfer efficiency $N_{F,x}$ is known. However, different from N it is not possible to calculate $N_{F,x}$ purely from the geometry of the cell, because the geometry is much more complex (as well as the geometry factor [8,11,12]) and changes with every setup of the 6-electrode cell. This is due to the compressibility of the Teflon spacers. In addition, it was shown for the dual thin layer cell that the transfer efficiency is a function of the flow rate [8]. This is different for an RRDE-arrangement where, as long as conditions are chosen under which laminar flow prevails, N is independent of the rotation speed. The dependence of N_F and the performance of the 6-electrode cell was tested in an aqueous chloride containing electrolyte by the reduction of Cu^{2+} to Cu^{+} at WE1 and subsequent oxidation of Cu^{+} at WE2 (*c.f.* Supplemental Information).

Derivation of the calibration constants $K^*_{1,m,x}$ and $K^*_{2,m,x}$: According to Eq. $\dot{n}_{I,x}$(A1.7) the ionic current $I_{I,m,x}$ for a fragment with the mass m equals the overall influx $\dot{n}_{I,x}$ of a species x into the mass spectrometer that has a fragment with this mass m times $K^{\circ}_{m,x}$ [8].

$$I_{I,m,x} = K^{\circ}_{m,x} \cdot \dot{n}_{I,x} \tag{A1.7}$$

$K^{\circ}_{m,x}$ in Eq. (A1.7) is the calibration constant of the mass spectrometer that contains all parameters and settings which influence the signal intensity *via* the probabilities of ionization and detection as well as the fragmentation pattern [8]. $\dot{n}_{I,x}$ in Eq. (A1.7) is proportional (but not equal) to $\dot{n}_{F,x}$ which is the amount of species x that is formed at the working electrode. The relationship between $\dot{n}_{I,x}$ and $\dot{n}_{F,x}$ is given in Eq. (A1.8)

$$\dot{n}_{I,x} = N_{I,x} \cdot \dot{n}_{F,x} \tag{A1.8}$$

where$N_{I,x}$ is the ionic transfer efficiency. Insertion of Eq. (A1.8) into Eq. (A1.7) and considering Faraday's law yields Eq. (A1.9)

$$I_{I,m,x} = K^{\circ}_{m,x} \cdot N_{I,x} \cdot \frac{\alpha_{eff,x} \cdot I_F}{z_x \cdot F} \tag{A1.9}$$

Eq. (A1.9) is valid irrespective of the working electrode. However, considering different parameters at WE1 and WE2 we obtain Eqs. (A1.10a) and (A1.10b).

$$I^{WE1}_{I,m,x} = K^{\circ}_{m,x} \cdot N^{WE1}_{I,x} \cdot \frac{\alpha^{WE1}_{eff,x} \cdot I^{WE1}_F}{z^{WE1}_x \cdot F} \tag{A1.10a}$$

$$I^{WE2}_{I,m,x} = K^{\circ}_{m,x} \cdot N^{WE2}_{I,x} \cdot \frac{\alpha^{WE2}_{eff,x} \cdot I^{WE2}_F}{z^{WE2}_x \cdot F} \tag{A1.10b}$$

$I^{WE1}_{I,m,x}$ is the contribution of WE1 and $I^{WE2}_{I,m,x}$ is the contribution of WE2 to the overall ionic current $\sum I_{I,m,x}$ for mass m. The latter is given by Eq. (A1.11)

$$\sum I_{I,m,x} = I^{WE1}_{I,m,x} + I^{WE2}_{I,m,x} \tag{A1.11}$$

It is noteworthy that the ionic transfer efficiencies $N^{WE1}_{I,x}$ and $N^{WE2}_{I,x}$for WE1 and WE2, respectively, differ significantly from each other. WE2 is a metal sputtered Teflon membrane placed at the interface between electrolyte and vacuum. Naturally the ionic transfer efficiency is high as volatile species formed at or very close to the interface can easily pass into the gas phase and have little chance to diffuse into the bulk of solution. For such electrodes and in the absence of convection Tegtemeyer *et al.* found a transfer efficiency of 0.95 for the oxidation of pre-adsorbed CO [3]. The ionic transfer efficiency $N^{WE1}_{I,x}$ of WE1 is much smaller because it is necessary to transport species x from WE1 in the upper compartment to the lower compartment, where it can pass into the gas phase. In the course of this transport process species x can diffuse into the bulk of the electrolyte. Therefore, the value of $N^{WE1}_{I,x}$ deviates significantly from 1. The ionic transfer efficiency of both WE1 and WE2 depend on the exact convection conditions [3,8]. One might assume that the ionic transfer efficiency $N^{WE1}_{I,x}$ and the faradaic transfer efficiency $N_{F,x}$ of species x are equal. That is, the same transport process is responsible for the detection of $\dot{n}^{WE1}_{F,x}$ either *via* $\dot{n}^{WE2}_{F,x}$ or *via* $\dot{n}^{WE1}_{I,x}$. Indeed, this is true if the transfer to the gas phase and the electrochemical reaction at WE2 itself are very fast,*i.e.* in the limiting case of diffusion limitation. However, if due to a lower volatility transfer of the species into the vacuum is slower, $N^{WE1}_{I,x}$ will be much smaller. *E.g.* the faradaic transfer efficiency of superoxide is 0.26 while the ionic transfer efficiency of superoxide $N^{WE1}_{I,Su}$ is zero, as superoxide is not volatile enough to pass into the gas phase.

The calibration constant $K^{\circ}_{m,x}$ and the ionic transfer efficiency of species x $N_{I,x}$ can be combined to a single calibration constant $K^*_{m,x} = K^{\circ}_{m,x} \cdot N_{I,x}/F$. Substitution in Eqs. (A1.10a) and (A1.10b) yields Eqs. (A1.12a) and (A1.12b).

$$I^{WE1}_{I,m,x} = K^*_{1,m,x} \cdot \frac{\alpha^{WE1}_{eff,x} \cdot I^{WE1}_F}{z^{WE1}_x} \tag{A1.12a}$$

$$I^{WE2}_{I,m,x} = K^*_{2,m,x} \cdot \frac{\alpha^{WE2}_{eff,x} \cdot I^{WE2}_F}{z^{WE2}_x} \tag{A1.12b}$$

In order to correlate the ionic current to the faradaic current quantitatively $K^*_{m,x}$ must be known. Therefore, calibration with an electrochemical reaction of known stoichiometry (*i.e.* known $\alpha^{WE1}_{eff,x}$, $\alpha^{WE2}_{eff,x}$, z^{WE1}_x and z^{WE2}_x) is necessary. In that case $K^*_{1,m,x}$ can be calculated *via* Eq. (A1.12a) from $I^{WE1}_{I,m,x}$ and I^{WE1}_F. Accordingly, $K^*_{2,m,x}$ can be calculated from $I^{WE2}_{I,m,x}$ and I^{WE2}_F *via* Eq. (A1.12b). Eq. (2) is a simplification of Eqs. (A1.12a) and (A1.12b).

$\sum I_{I,m,x}$ as a function of I^{WE1}_F: I^{WE2}_F is proportional to I^{WE1}_F, if all the current at WE2 is due to the reaction of species that were formed at WE1. In that case it is possible to express the ionic current at WE2 $I^{WE2}_{I,m,x}$ as a function of the faradaic current at WE1 I^{WE1}_F. We obtain Eq. (A1.13) when we rearrange Eq. (A1.6) and insert it in Eq. (A1.12b).

$$I^{WE2}_{I,m,x} = K^*_{2,m,x} \cdot \frac{N_{F,x} \cdot \alpha^{WE1}_{eff,x} \cdot I^{WE1}_F}{z^{WE1}_x} \tag{A1.13}$$

The overall ionic current $\sum I_{I,m,x}$ can then be expressed as Eq. (A1.14), which we obtain when we insert Eqs. (A1.12a) and (A1.13) in Eq. (A1.11).

$$\sum I_{I,m,x} = \frac{K^{\circ}_{m,x} \cdot \alpha^{WE1}_{eff,x} \cdot I^{WE1}_F}{z^{WE1}_x} \left(N^{WE1}_{I,x} \cdot N^{WE2}_{I,x} - N_{F,x} \right) \tag{A1.14}$$

As pointed out before the ionic transfer efficiency $N^{WE2}_{I,x}$ is close to one. In addition, the ionic transfer efficiency $N^{WE1}_{I,x}$ and the faradaic transfer efficiency $N_{F,x}$ are of similar magnitude. Therefore, the expression in the parenthesis is close to zero. That is the reason

why $\sum I_{I,m,x}$ is close to zero when in the calibration measurement of Fig. 1 oxygen is reduced at WE1 and evolved at WE2.

We can also define a transfer ratio of species x $N_{r,x}$. This transfer ratio can be derived by division of Eq. (A1.12a) through Eq. (A1.13) which yields:

$$\frac{I_{I,y}^{WE1}}{I_{I,y}^{WE2}} = \frac{N_{I,x}^{WE1}}{N_{I,x}^{WE2} \cdot N_{F,x}} = N_{r,x} \tag{A1.15}$$

(A2.1) A.2 Derivation of Eq. (3)

When z_{Ox}^{WE1} is determined from Eq. (2) or, more accurately, from Eq. (A1.12a) we only obtain an average value of z_{Ox}^{WE1}, which is given by Eq. (A2.1)

$$z_{Ox}^{WE1} = \frac{\dot{n}_{F,Su}^{WE1}}{\dot{n}_{F,Ox}^{WE1}} + 2 \cdot \frac{\dot{n}_{F,Pe}^{WE1}}{\dot{n}_{F,Ox}^{WE1}} + 4 \cdot \frac{\dot{n}_{F,O}^{WE1}}{\dot{n}_{F,Ox}^{WE1}} \tag{A2.1}$$

In Eq. (A2.1) $\frac{\dot{n}_{F,Su}^{WE1}}{\dot{n}_{F,Ox}^{WE1}}$ is the share of oxygen that is reduced to superoxide, $\frac{\dot{n}_{F,Pe}^{WE1}}{\dot{n}_{F,Ox}^{WE1}}$ is the share that is reduced to peroxide and $\frac{\dot{n}_{F,O}^{WE1}}{\dot{n}_{F,Ox}^{WE1}}$ is the share that is reduced to oxide. z_{Ox}^{WE1} in Fig. 3 is always smaller 2 e^-/O_2. Therefore, we can assume that the share of oxygen that is reduced to oxide is negligible. Hence, we can simplify Eq. (A2.1) to Eq. (A2.2).

$$z_{Ox}^{WE1} = \frac{\dot{n}_{F,Su}^{WE1}}{\dot{n}_{F,Ox}^{WE1}} + 2 \cdot \left(1 - \frac{\dot{n}_{F,Su}^{WE1}}{\dot{n}_{F,Ox}^{WE1}}\right) \tag{A2.2}$$

Rearranging Eq. (A2.2) yields Eq. (3)

$$\chi(Su) = \frac{\dot{n}_{F,Su}^{WE1}}{\dot{n}_{F,Ox}^{WE1}} = 2 - z_{Ox}^{WE1} \tag{3}$$

(A1.6) A.3 Derivation of Eq. (4)

The faradaic transfer efficiency $N_{F,x}$ for species x is defined by Eq. (A1.6).

$$N_{F,x} = \frac{\alpha_{eff,x}^{WE2} \cdot z_x^{WE1} \cdot I_F^{WE2}}{\alpha_{eff,x}^{WE1} \cdot z_x^{WE2} \cdot I_F^{WE1}} \tag{A1.6}$$

Usually both $\alpha_{eff,x}^{WE1}$ and $\alpha_{eff,x}^{WE2}$ is unknown. Therefore, it is not possible to determine from Eq. (A1.6) the share of species x with respect to other species formed at WE1, without additional information.

However, for the reduction of oxygen in lithium-containing DMSO based electrolyte we know that $\alpha_{eff,x}^{WE2}$ is one. We arrived at that conclusion because we found that the average value of z_{Ox}^{WE2} in Fig. 5 is one which is a strong indication that oxygen evolution at WE2 is due to the oxidation of superoxide. For the formation of superoxide at WE1 in lithium containing DMSO based electrolyte Eq. (A1.6) simplifies to Eq. (A3.1).

$$N_{F,Su} = \frac{I_F^{WE2}}{\alpha_{eff,Su}^{WE1} \cdot I_F^{WE1}} \tag{A3.1}$$

The current efficiency of superoxide is given by Eq. (A3.2)

$$\alpha_{eff,Su}^{WE1} = \frac{I_{F,Su}^{WE1}}{I_{F,Su}^{WE1} + I_{F,Pe}^{WE1} + I_{F,O}^{WE1}} = \frac{\dot{n}_{F,Su}^{WE1}}{\dot{n}_{F,Su}^{WE1} + 2 \cdot \dot{n}_{F,Pe}^{WE1} + 4 \cdot \dot{n}_{F,O}^{WE1}} \tag{A3.2}$$

In Fig. 3 the average value of z_{Ox}^{WE1} never exceeds 2 e^-/O_2. Therefore, we can assume that the formed amount of oxide is negligible and Eq. (A3.2) simplifies to Eq. (A3.3).

$$\alpha_{eff,Su}^{WE1} = \frac{\dot{n}_{F,Su}^{WE1}}{\dot{n}_{F,Su}^{WE1} + 2 \cdot \dot{n}_{F,Pe}^{WE1}} \tag{A3.3}$$

Insertion of Eq. (A3.3) into Eq. (A3.1) yields Eq. (A3.4)

$$N_{F,Su} = \frac{I_F^{WE2}}{\frac{\dot{n}_{F,Su}^{WE1}}{\dot{n}_{F,Su}^{WE1} + 2 \cdot \dot{n}_{F,Pe}^{WE1}} \cdot I_F^{WE1}} \tag{A3.4}$$

rearanging leads to

$$\frac{\dot{n}_{F,Su}^{WE1}}{\dot{n}_{F,Su}^{WE1} + 2 \cdot \dot{n}_{F,Pe}^{WE1}} = \frac{I_F^{WE2}}{N_{F,Su} \cdot I_F^{WE1}} \quad |\cdot 2/_{()^{-1}}$$

$$\dot{n}_{F,Su}^{WE1} + 2 \cdot \frac{\dot{n}_{F,Pe}^{WE1}}{2 \cdot \dot{n}_{F,Su}^{WE1}} = \frac{N_{F,Su} \cdot I_F^{WE1}}{2 \cdot I_F^{WE2}} \quad | - \frac{\dot{n}_{F,Pe}^{WE1}}{2 \cdot \dot{n}_{F,Su}^{WE1}}$$

$$\frac{\dot{n}_{F,Su}^{WE1} + \dot{n}_{F,Pe}^{WE1}}{2 \cdot \dot{n}_{F,Su}^{WE1}} = \frac{N_{F,Su} \cdot I_F^{WE1}}{2 \cdot I_F^{WE2}} - \frac{\dot{n}_{F,Pe}^{WE1}}{2 \cdot \dot{n}_{F,Su}^{WE1}}$$

With $\dot{n}_{F,Ox}^{WE1} = \dot{n}_{F,Su}^{WE1} + \dot{n}_{F,Pe}^{WE1}$, $\dot{n}_{F,Pe}^{WE1} = \frac{I_{F,Pe}^{WE1}}{2F}$ and $\dot{n}_{F,Su}^{WE1} = \frac{I_{F,Su}^{WE1}}{F}$ we obtain

$$\frac{\dot{n}_{F,Ox}^{WE1}}{2 \cdot \dot{n}_{F,Su}^{WE1}} = \frac{N_{F,Su} \cdot I_F^{WE1}}{2 \cdot I_F^{WE2}} - {}^{1}\Big/_{2 \cdot \frac{I_{F,Pe}^{WE1}}{I_{F,Su}^{WE1}}}$$

with $I_{F,Su}^{WE1} = \frac{I_{F,Su}^{WE2}}{N_{F,Su}} = \frac{I_F^{WE2}}{N_{F,Su}}$ and $I_F^{WE1} - I_{F,Su}^{WE1} = I_{F,Pe}^{WE1}$ $I_F^{WE1} - I_{F,Su}^{WE1} = I_{F,Pe}^{WE1}$ we obtain

$$\frac{\dot{n}_{F,Ox}^{WE1}}{2 \cdot \dot{n}_{F,Su}^{WE1}} = N_{F,Su} \cdot I_F^{WE1} - {}^{1}\Big/_{\frac{2N_{F,Su}\left(I_F^{WE1} - I_{F,Su}^{WE1}\right)}{2 \cdot I_F^{WE2}}}$$

$$\frac{\dot{n}_{F,Ox}^{WE1}}{2 \cdot \dot{n}_{F,Su}^{WE1}} = {}^{1}/_{2}N_{F,Su} \cdot I_F^{WE1} + I_F^{WE2} \quad |^{()^{-1}}\Big/_{\frac{1}{2}}$$

We finally arrive at Eq. (4) from which we can determine the share $\chi(Su)$ of oxygen that is reduced to superoxide

$$\chi(Su) = \frac{\dot{n}_{F,Su}^{WE1}}{\dot{n}_{F,Ox}^{WE1}} = \frac{2 \cdot I_F^{WE2}}{N_{F,Su} \cdot I_F^{WE1} + I_F^{WE2}} \tag{4}$$

(A4.1) A.4 Derivation of Eq. (5)

We can also determine the amount of oxygen that is reduced to superoxide from the ionic currents $I_{I,32,Ox}^{WE1}$ and $I_{I,32,Ox}^{WE2}$. Combining Eqs. (A1.5) and (A1.8) yields Eq. (A4.1)

$$\dot{n}_{F,x}^{WE1} = \frac{\dot{n}_{I,x}^{WE1}}{N_{I,Ox}^{WE2} \cdot N_{F,x}} \tag{A4.1}$$

Considering Eq. (A4.1) we can write the share of oxygen that is reduced at WE1 to superoxide as in Eq. (A4.1)

$$\frac{\dot{n}_{F,Su}^{WE1}}{\dot{n}_{F,Ox}^{WE1}} = \frac{\frac{\dot{n}_{I,Ox}^{WE2}}{N_{I,Ox}^{WE2} \cdot N_{F,Su}}}{\frac{\dot{n}_{I,Ox}^{WE1}}{N_{I,Ox}^{WE1}}} \tag{A4.2}$$

Inserting Eq. (A1.8) in Eq. (A4.2) and considering the transfer ratio $N_{r,Ox/Su}$ we obtain Eq. 5a

$$\chi(Su) = \frac{\dot{n}_{F,Su}^{WE1}}{\dot{n}_{F,Ox}^{WE1}} = \frac{I_{l,Ox}^{WE2}}{N_{r,Ox/Su} \cdot I_{l,Ox}^{WE1}} \quad (5)$$

Appendix B. Supplementary data

Supplementary data associated with this article can be found, in the online version, at http://dx.doi.org/10.1016/j.electacta.2016.08.008.

References

[1] S. Bruckenstein, R.R. Gadde, Use of a porous electrode for in situ mass spectrometric determination of volatile electrode reaction products, Journal of the American Chemical Society 93 (1971) 793–794.

[2] O. Wolter, J. Heitbaum, Differential Electrochemical Mass Spectroscopy (DEMS) – a new method for the study of electrode processes, Ber. Bunsenges. Phys. Chem. 88 (1984) 2–6.

[3] D. Tegtmeyer, A. Heindrichs, J. Heitbaum, Electrochemical on line mass spectrometry on a rotating electrode inlet system, Ber. Bunsenges. Phys. Chem. 93 (1989) 201–206.

[4] Z. Jusys, H. Massong, H. Baltruschat, A New Approach for Simultaneous DEMS and EQCM: Electro-oxidation of Adsorbed CO on Pt and Pt-Ru, J. Electrochem. Soc 146 (1999) 1093.

[5] T. Hartung, H. Baltruschat, Differential Electrochemical Mass Spectrometry using smooth electrodes: Adsorption and H/D-exchange reactions of benzene on Pt, Langmuir 6 (1990) 953–957.

[6] P. Bogdanoff, P. Friebe, P. Alonso-Vante, A new inlet system for differential electrochemical mass spectrometry applied to the photocorrosion of p-InP (111) single crystals, J. Electrochem. Soc. 145 (1998) 576–582.

[7] H. Wang, E. Rus, H.D. Abruña, New Double-Band-Electrode Channel Flow Differential Electrochemical Mass Spectrometry Cell: Application for Detecting Product Formation during Methanol Electrooxidation, Analytical Chemistry 82 (2010) 4319–4324.

[8] H. Baltruschat, Differential electrochemical mass spectrometry, Journal of the American Society for Mass Spectrometry 15 (2004) 1693–1706.

[9] T. Löffler, Charakterisierung und Anwendung einer neuen Dünnschichtzelle für die elektrochemische Massenspektrometrie, Institut für Physikalische und Theoretische Chemie, Universität Bonn, Bonn, 1997, pp. 93.

[10] J. Fuhrmann, A. Linke, H. Langmach, A numerical method for mass conservative coupling between fluid flow and solute transport, Appl. Numer. Math. 61 (2011) 530–553.

[11] J. Fuhrmann, A. Linke, H. Langmach, H. Baltruschat, Numerical calculation of the limiting current for a cylindrical thin layer flow cell, Electrochimica Acta 55 (2009) 430–438.

[12] M. Khodayari, P. Reinsberg, A.-E.-A.A. Abd-El-Latif, C. Merdon, J. Fuhrmann, H. Baltruschat, Determining Solubility and Diffusivity by Using a Flow Cell Coupled to a Mass Spectrometer, ChemPhysChem (2016), doi:http://dx.doi.org/10.1002/cphc.201600005.

[13] Z. Jusys, J. Kaiser, R.J. Behm, Composition and activity of high surface area PtRu catalysts towards adsorbed CO and methanol electrooxidation: A DEMS study, Electrochimica Acta 47 (2002) 3693–3706.

[14] Z. Jusys, J. Kaiser, R.J. Behm, Methanol Electrooxidation over Pt/C Fuel Cell Catalysts: Dependence of Product Yields on Catalyst Loading, Langmuir 19 (2003) 6759–6769.

[15] H. Wang, T. Löffler, H. Baltruschat, Formation of intermediates during methanol oxidation: A quantitative DEMS study, J. Appl. Electrochem. 31 (2001) 759–765.

[16] A. Cuesta, M. Escudero, B. Lanova, H. Baltruschat, Cyclic Voltammetry, FTIRS, and DEMS Study of the Electrooxidation of Carbon Monoxide Formic Acid, and Methanol on Cyanide-Modified Pt(111) Electrodes, Langmuir 25 (2009) 6500–6507.

[17] A.A. Abd-El-Latif, E. Mostafa, S. Huxter, G. Attard, H. Baltruschat, Electrooxidation of ethanol at polycrystalline and platinum stepped single crystals: A study by differential electrochemical mass spectrometry, Electrochimica Acta 55 (2010) 7951–7960.

[18] H. Wang, Z. Jusys, R.J. Behm, Ethanol electro-oxidation on carbon-supported Pt, PtRu and Pt3Sn catalysts: A quantitative DEMS study, Journal of Power Sources 154 (2006) 351–359.

[19] E. Mostafa, A.-E.-A.A. Abd-El-Latif, R. Ilsley, G. Attard, H. Baltruschat, Quantitative DEMS study of ethanol oxidation: effect of surface structure and Sn surface modification, Physical Chemistry Chemical Physics 14 (2012) 16115–16129.

[20] I. Kisacik, A. Stefanova, S. Ernst, H. Baltruschat, Oxidation of carbon monoxide, hydrogen peroxide and water at a boron doped diamond electrode: the competition for hydroxyl radicals, Physical Chemistry Chemical Physics 15 (2013) 4616–4624.

[21] N.-L. Michels, A. Kapałka, A.A. Abd-El-Latif, H. Baltruschat, C. Comninellis, Enhanced ammonia oxidation on BDD induced by inhibition of oxygen evolution reaction, Electrochemistry Communications 12 (2010) 1199–1202.

[22] A. Kapałka, B. Lanova, H. Baltruschat, G. Fóti, C. Comninellis, Electrochemically induced mineralization of organics by molecular oxygen on boron-doped diamond electrode, Electrochemistry Communications 10 (2008) 1215–1218.

[23] G. Samjeské, H. Xiao, Baltruschat, Ru Decoration of Stepped Pt Single Crystals and the Role of the Terrace Width on the Electrocatalytic CO Oxidation, Langmuir 18 (2002) 4659–4666.

[24] S.p. Fierro, T. Nagel, H. Baltruschat, C. Comninellis, Investigation of the oxygen evolution reaction on Ti/IrO2 electrodes using isotope labelling and on-line mass spectrometry, Electrochemistry Communications 9 (2007) 1969–1974.

[25] C.J. Bondue, P. Reinsberg, A.A. Abd-El-Latif, H. Baltruschat, Oxygen reduction and oxygen evolution in DMSO based electrolytes: the role of the electrocatalyst, Physical Chemistry Chemical Physics 17 (2015) 25593–25606.

[26] P. Reinsberg, C. Bondue, H. Baltruschat, Mechanistic investigation of the oxygen reduction in magnesium ion-containing dimethyl sulfoxide, Electrochimica Acta 200 (2016) 214–221.

[27] M. Heinen, Y.X. Chen, Z. Jusys, R.J. Behm, In situ ATR-FTIRS coupled with on-line DEMS under controlled mass transport conditions: A novel tool for electrocatalytic reaction studies, Electrochimica Acta 52 (2007) 5634–5643.

[28] Z. Jusys, J. Kaiser, R.J. Behm, A novel dual thin-layer flow cell double-disk electrode design for kinetic studies on supported catalysts under controlled mass-transport conditions, Electrochimica Acta 49 (2004) 1297–1305.

[29] J. Zhang, W.J. Pietro, A.B.P. Lever, Rotating ring-disk electrode analysis of CO2 reduction electrocatalyzed by a cobalt tetramethylpyridoporphyrazine on the disk and detected as CO on a platinum ring, J. Electroanal. Chem. 403 (1996) 93–100.

[30] K. Endo, Y. Katayama, T. Miura, A rotating disk electrode study on the ammonia oxidation, Electrochimica Acta 50 (2005) 2181–2185.

[31] C.J. Bondue, M. Hegemann, C. Molls, T.E.H. Baltruschat, A Comprehensive Study on Oxygen Reduction and Evolution in DMSO, J. Electrochem. Soc. (2016) submitted.

[32] C. Bondue, P. Reinsberg, A.-E.-A.A. Abd-El-Latif, H. Baltruschat, Oxygen Reduction and Oxygen Evolution in DMSO Based Electrolytes: Role of the Electrocatalyst, Physical Chemistry Chemical Physics (2015) 25593–25606.

[33] Q. Yu, S. Ye, In Situ Study of Oxygen Reduction in Dimethyl Sulfoxide (DMSO) Solution: A Fundamental Study for Development of the Lithium-Oxygen Battery, The Journal of Physical Chemistry C 119 (2015) 12236–12250.

[34] D.T. Sawyer, J.S. Valentine, How super is superoxide? Accounts of Chemical Research 14 (1981) 393–400.

[35] N. Mozhzhukhina, L.P.M. éndez De Leo, E.J. Calvo, Infrared Spectroscopy Studies on Stability of Dimethyl Sulfoxide for Application in a Li-Air Battery, The Journal of Physical Chemistry C 117 (2013) 18375–18380.

Supplementary

Cell Geometry

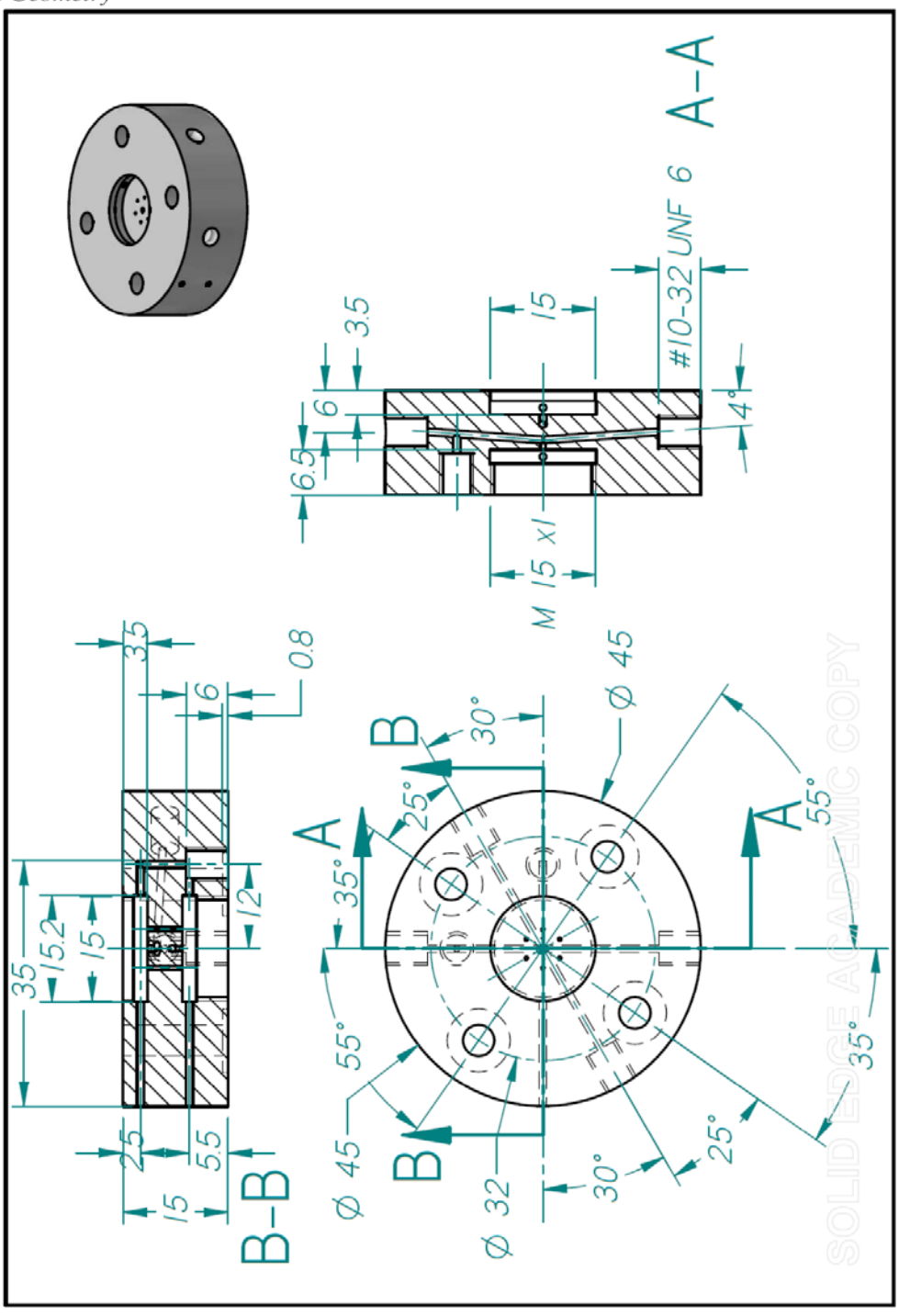

Figure S1: Technical drawing of the 6-electrode cell

Figure S1 shows the exact measures of the 6-electrode cell introduced in the present paper.
S1/5
Pfad: S:\Bondü\Paper 4\Supporting Info

Characterisation of the 6-Electrode Cell

Following the procedure described by Hamann and Vielstich [1] the 6-electrode cell was characterised in an aqueous electrolyte of 0.5 M KCl that contained 1 mM $CuCl_2$. The working electrode WE1 in the upper compartment was a polycrystalline platinum electrode and the working electrode WE2 was a platinum sputtered Teflon membrane. All counter and reference electrodes were cupper wires. Different from the case in an organic electrolyte CE1.2 and CE2.2 are connected via a 100 kΩ and CE1.1 and CE2.1 are connected via a 100 Ω resistance. During the experiment WE1 was cycled in a potential window between -400 mV and 900 mV, and WE2 was held at 550 mV throughout the experiment.

Figure S2 shows the cathodic sweeps of the CVs that are obtained for four different flow rates. As the potential at WE1 decreases below 350 mV Cu^{II} is reduced to Cu^{I}. As WE2 is set to 550 mV the reverse reaction takes place and I_F^{WE2} becomes positive. As soon as the potential becomes more negative then -220 mV at WE1 the bulk deposition of copper takes place. Hence, the amount of I_F^{WE1} increases twofold. In parallel I_F^{WE2} drops to zero, because the supply with Cu^{I} ceases.

In Figure S3 I_F^{WE1} t -180 mV (diffusion limited) is plotted versus $u^{1/3}$ whereas u is the flow rate of the electrolyte. Figure S3 shows that a linear relationship exists between I_F^{WE1} and $u^{2/3}$. For the dual thin layer cell and for flow rates larger ~5µL/s the relationship in Equation S1 was found which evidently also holds for the 6-electrode cell [2].

$$I_{Diff} = g \cdot z \cdot F \cdot c \cdot D^{2/3} \cdot u^{x} \qquad \text{eq. S1}$$

In Equation S1 g is a geometry factor that varies in each cell setup, D is the diffusion coefficient of the reactant, c is the concentration of the reactant and x is either 1 (at low flow rates) or 1/3 (at large flow rates).

In Figure S4 N_f is plotted as a function of the flow rate. N_f was calculated from $I_{f,WE1}$ and $I_{f,WE2}$ according to Equation 1. As already shown for the dual thin layer cell N_f decreases significantly as the flow rate increases [3].

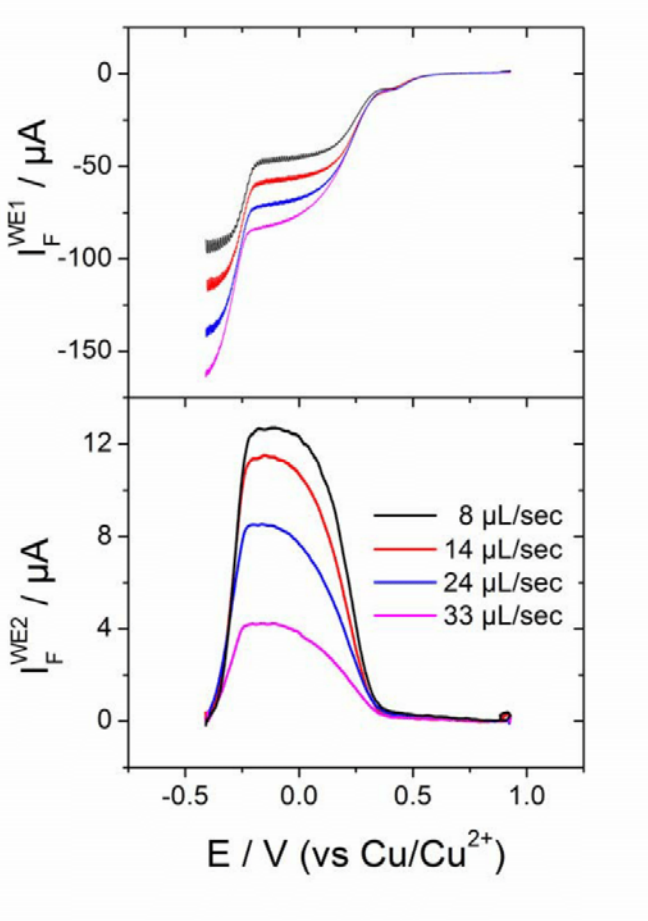

Figure S2: I_F^{WE1} and I_F^{WE2} as a function of the potential applied to WE1 in an aqueouse electrolyte of 0.5 M KCl containing 1 mM $CuCl_2$.

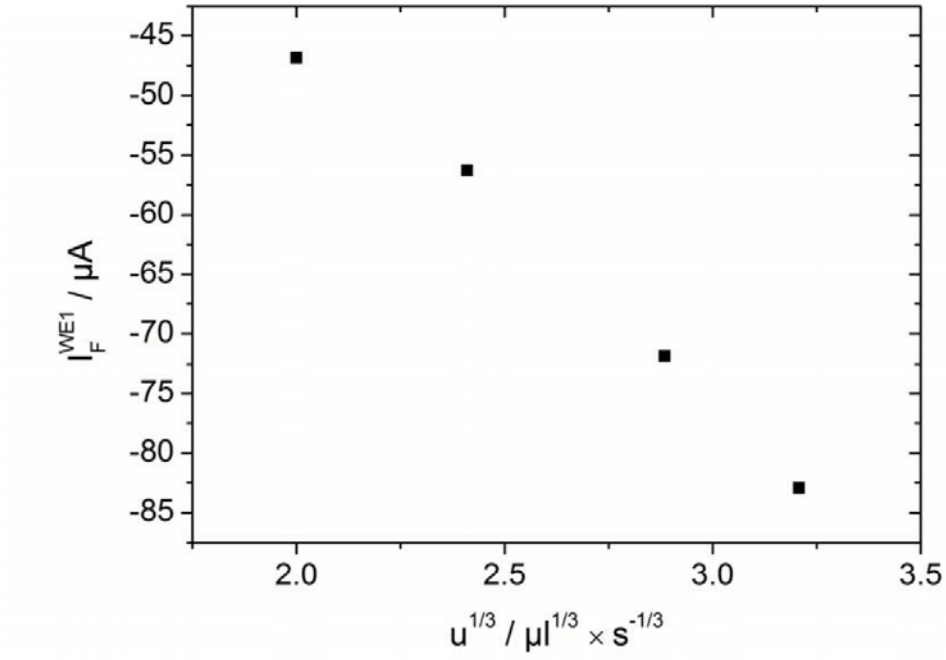

Figure S3: I_F^{WE1} obtained at -180 mV as a function of the flow rate to the power of 1/3.

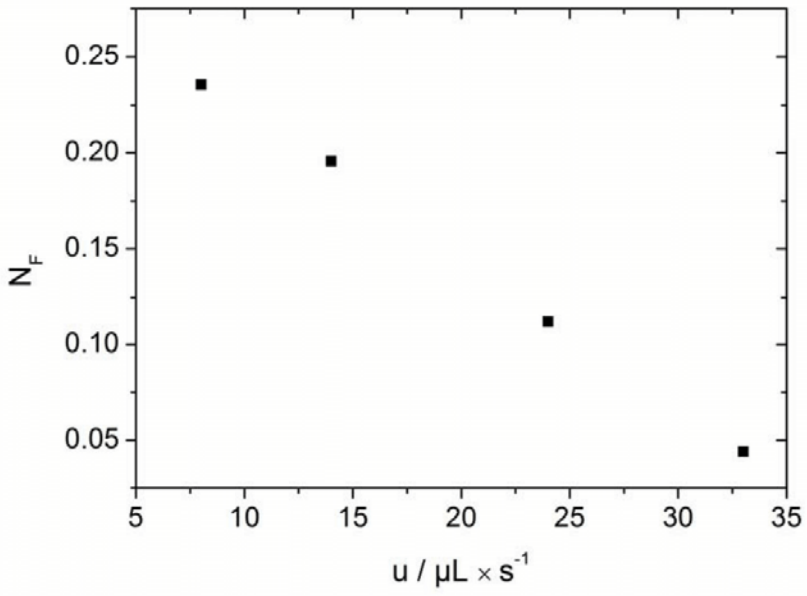

Figure S4: N_F calculated according to Equation 6 from the data presented in Figure S2 as a function of the flow rate.

[1] C.H. Hamann, W. Vielstich, ElEktrochemie, 3 ed., Wiley-VCH1998.

[2] M. Khodayari, P. Reinsberg, A.-E.-A.A. Abd-El-Latif, C. Merdon, J. Fuhrmann, H. Baltruschat, Determining Solubility and Diffusivity by Using a Flow Cell Coupled to a Mass Spectrometer, ChemPhysChem, 10.1002/cphc.201600005 (2016).

[3] H. Baltruschat, Differential electrochemical mass spectrometry, Journal of the American Society for Mass Spectrometry, 15 (2004) 1693-1706.

6. 3. Summary of Paper 4

In Paper 4 we have introduced the 6-electrode cell. We demonstrate the use of the cell for the oxygen reduction reaction in DMSO based electrolytes and developed an experimental procedure on how to conduct the experiment. Based on the theories developed for the dual thin layer cell we derived important equations, that allowed us to correlate 4 different quantities with each other: I_F^{WE1} (the faradic current at WE1), I_F^{WE2} (the faradic current at WE2), $I_{I,32}^{WE1}$ (the ionic current for mass 32 due to the reaction at WE1) and $I_{I,32}^{WE2}$ (the ionic current for mass 32 due to the reaction at WE2). Hence, we were able to determine the number of electrons transferred per oxygen both at WE1 and WE2. Furthermore, we could determine the share of oxygen that is reduced to superoxide intermediate by three different means.

The finding that at the detection electrode indeed 1 electron per evolved molecule of oxygen is transferred shows that that the intermediates that react at the ring electrode during RRED-experiments on the oxygen reduction in DMSO based electrolytes are indeed superoxide as proposed previously [39, 40, 70, 72]. This is not only true for low overpotentials where we came to the same conclusion based on DEMS-experiments conducted in the dual thin layer cell (Paper 2, Paper 3) but also for large overpotentials where the direct pathway of peroxide formation should dominate. In Paper 3 we mentioned the possibility that the shoulder in the current observed at the ring electrode when the potential at the disc electrode passes -1.2 V could be due to the oxidation of LiO_2^- that failed to nucleate at the disc electrode. This possibility is now refuted.

Furthermore, we can show that at a certain point an increasing share of oxygen is again reduced to superoxide as the electrode is covered with lithiumperoxide. We have discussed in Paper 2 that Li_2O_2 exerts a geometric effect on the platinum electrode that inhibits the second electron transfer. The gold electrode appears to be effected in the same way by the Li_2O_2-deposit.

In Paper 3 we have found that the MSCV for mass 32 changes when a metal sputtered Teflon membrane is place in the lower compartment of the dual thin layer cell. At open circuit potential the metal electrode appears to have the capacity to evolve oxygen from the incoming superoxide intermediates. We can show in Paper 4 that the reaction that takes place at the metal sputtered Teflon membrane is not the dismutation of superoxide but a heterogeneous catalysed oxidation of superoxide. This reaction is only possible when other compounds are reduced at the same time. It is still unknown which compound is reduced by superoxide but the electrolyte is the most probable source of electrons. If true, this has larger implications for current battery research: Superoxide induced electrolyte decomposition catalysed by construction parts of the electrode must be avoided under any circumstances.

7. Summary of the Presented Results and Discussion in Light of Literature Results

In the presented studies, we have investigated the oxygen reduction reaction in organic electrolytes, particularly in DMSO based electrolytes. We have shown in Paper 1 that in the presence of TBA^+, electrochemical reduction of oxygen results in the quantitative formation of superoxide. Although Laoire *et al*. have proposed that in organic electrolytes and in the absence of hard *lewis* acids oxygen is reduced to superoxide, it was not shown that this reaction is quantitative [39, 40]. In our first study, we were able to establish the quantitative nature of this reaction. This finding allowed us to calibrate the dual thin layer cell and is, therefore, the fundament for the studies that followed.

Based on kinetic considerations, Laoire *et al*. have suggested that the presence of hard *lewis* acids, such as Li^+ and Na^+ cause the formation of peroxides, whereas soft *lewis* acids favour the formation of superoxide [39, 40]. Indeed, the thermodynamic instability of lithium superoxide [43, 44] suggests that in the presence of Li^+, oxygen reduction will eventually lead to the formation of Li_2O_2. But thermodynamics do not give any information on how Li_2O_2 is formed: Laoire *et al*. proposed that at low overpotentials and in Li^+-containing DMSO based electrolytes, oxygen is reduced to superoxide, whereas electrochemical oxygen reduction results in peroxide at high overpotentials [40]. RRDE- [70, 72] and EPR-measurements [73] in DMSO based electrolytes, also suggest that superoxide forms at low overpotentials. This findings support the mechanism presented by Laoire *et al*. [40].

The results which we have presented in Paper 2 and in Paper 3 show that a transition from the indirect to the direct pathway of peroxide formation takes place, indeed. However, this is only true for the gold electrode. Laoire *et al*. have based their mechanism on experiments that were performed with a glassy carbon electrode [40], whereas we have shown that the indirect and the direct pathway of peroxide formation proceed in parallel at this electrode material, irrespective of the applied potential. Also the EPR-studies performed by Cao *et al*. [73] and the RRDE-measurements presented by Trahan *et al*. used carbon electrodes. This raises the question whether it is just a coincidence that the mechanism presented by Laiore *et al*. turned out to hold only for gold electrodes in our experiments or whether the history of the carbon electrode exerts an influence on the actual mechanism of oxygen reduction (*e.g*. through functional groups that form on the carbon electrode in previous experiments).

However, hard *lewis* acids do not necessarily cause the formation of peroxides: Upon discharge of sodium-air batteries, the formation of both, NaO_2 [74, 75] and Na_2O_2 [76-78] has been observed. In these batteries, tetraglyme based electrolytes were employed. Therefore, comparison to the results presented in Paper 2 is difficult, because in these

experiments, DMSO based electrolytes were employed. However, similar to battery studies we have found that under some conditions NaO_2 is formed and under other conditions Na_2O_2 is formed. In our case, the electrode material is the defining factor. It was shown that the differences in the above mentioned Na-air battery studies are not due to the electrode material [75]. Instead, these differences apparently are due to the presence of trace amounts of water [79].

Thus, the *lewis* acidity of the cation is only one factor among others that defines the product of electrochemical oxygen reduction. In the absence of hard *lewis* acids, the formation of peroxide appears to be impossible, but it depends on the kinetics of the electrode process, whether peroxide or superoxide is formed in the presence of hard *lewis* acids (although the instability of superoxide in the presence of Li^+ means that oxygen reduction leads to Li_2O_2 eventually if Li^+ is available). Figure 10 in Paper 2 shows that the charge density of the cation exerts an influence on the kinetics of oxygen reduction. We were the first to quantify this effect in the form presented in Paper 2, where it was shown that a direct relationship between the charge density of the cation and the half-wave potential of peroxide formation exists. But aside from the cation, there is a range of parameters that also influence the kinetics of the oxygen reduction reaction in organic media, such as the solvent of the electrolyte. Laoire *et al*. proposed that a large donor number of the solvent will favour the indirect pathway of peroxide formation [39, 40]. This view has been supported by various groups [61, 71, 72]. However, recently others have suggested that instead of the donor number, the acceptor number of the solvent is the decisive parameter [80].

In Paper 2, we were able to show that the presence of water favours the indirect pathway of peroxide formation when a gold electrode is used. This finding is in line with the observation that trace amounts of water lead to the formation of toroid shaped particles upon discharge of lithium-air batteries operating with various solvents [81, 82]. It was suggested that large Li_2O_2 particles form because oxygen is first reduced to superoxide which will then be deposited as Li_2O_2, preferentially at certain sites of the electrode. In addition, Xia *et al*. have recently shown that very low amounts of water in tetraglyme based electrolytes of sodium-air batteries tilt the distribution of discharge products away from Na_2O_2 towards NaO_2 [79].

Given that water has a lower donor number than DMSO (75 kJ/mol compared to 125 kJ/mol), it is unlikely that the effect of water is due to the donor number. On the other hand water has a larger acceptor number than DMSO (54.8 compared to 19.3). Therefore, the effect of water which we have described in Paper 2 might support the theory by Khetan *et al*., who suggested that a large acceptor number favours the indirect pathway of peroxide formation because a better solvation of superoxide can be achieved.

This actually does not contradict the idea of an additional effect of the donor number of the solvent on the peroxide/superoxide formation: In Paper 2 we have pointed out that the effect of the cation might result from its need to coordinate to superoxide in order to enable the second electron transfer that leads to the formation of peroxide. It is conceivable that a solvent with a large donor number will mask the cation which is therefore not available to coordinate to superoxide. However, too little is known about the double layer region to decide whether this is a likely scenario. Xia *et al*. have pointed out that the water concentration in their experiments is too low to assure a proper solvation of the superoxide [79], which contradicts the effect of the acceptor number proposed by Khetan *et al*. [80]. Instead, Xia *et al*. suggested that water acts as a phase transfer catalyst. We have suggested in Paper 2 that water interferes somehow with the electrode kinetics, by participating in the double layer region. But also here it must be pointed out that because of lack of knowledge on the nature of the double layer structure this is speculative.

A further influencing factor on the mechanism of oxygen reduction is the electrode material. We have shown in Paper 2 that at gold electrodes a transition from the direct to the indirect pathway of peroxide formation takes place. At rhodium the electrochemical oxygen reduction always results in the formation of peroxide, that is, even at low overpotentials. This is also true for platinum, although the formation of a Li_2O_2 deposit appears to exert a geometric effect that increasingly tilts product distribution towards superoxide formation. We also found that at carbon and ruthenium both the indirect and the direct pathway of peroxide formation take place in parallel, irrespective of the applied potential. Finally, the most important finding from a fundamental point of view is that no oxygen reduction takes place at the diamond surface of the BDD-electrode. This shows unambiguously that oxygen reduction is an innersphere reaction: Even the first electron transfer that leads to the formation of superoxide can only take place when oxygen is specifically adsorbed at the surface of the electrode. Hence, oxygen reduction is a heterogeneous, electrocatalytic reaction. Although Lu *et al*. have previously reported that the achievable current density at a given potential during oxygen reduction depends on the electrode material [36], we were the first to show that the electrode material influences the pathway by which oxygen is reduced or whether oxygen reduction can take place at all. But it remains elusive, which characteristic of the electrode material influences the reaction pathway: Theoretical calculations for the oxygen reduction reaction in aqueous electrolytes where either hydrogenperoxide or water is formed, suggest that the difference between the free adsorption enthalpy of OH and OOH at the electrode material defines whether the $2e^-$- or the $4e^-$-process dominates [41]. In analogy to the oxygen reduction reaction in aqueous electrolytes it is conceivable that the free adsorption enthalpy of O_2^- determines whether the indirect or the direct pathway of peroxide formation takes place in non-aqueous electrolytes. In that line of thought, O_2^- (or O_2Li)

remains adsorbed and a second electron transfer is possible when the free adsorption enthalpy is large, whereas O_2^- desorbs otherwise. However, more data are required to decide whether this is a plausible scenario.

In addition to the electrode material, the structure of the electrode has an impact on the oxygen reduction reaction in lithium containing DMSO based electrolytes as well. In Paper 2 we have inferred from a step in the z-value that at gold electrodes the mechanism of oxygen reduction changes from the indirect to the direct pathway of peroxide formation at gold electrodes when the overpotential is increased. As was shown in Paper 1 and Paper 3, such a step is less pronounced (if present at all) when a gold sputtered electrode is used. In paper 3, we have attributed this difference either to the disproportionation of superoxide or due to another (unspecefied) reaction during which superoxide is oxidised which is catalysed by gold at open circuit potential. Portions of the porous electrode might be at open circuit, because they have lost their connection to the electrode. Indeed, we were able to show that at metal electrodes at open circuit potential an unknow reaction takes place. Our experiments with a novel two compartment cell revealed that this reaction consumes superoxide and evolves oxygen. Such a reaction has not been discribed before and it is not clear which compound in the electrolyte has the capacity to oxidise superoxide.

It is not straightforward to relate the above mentioned results to current battery research, that is based on the construction and cycling of model lithium-air batteries: Because model batteries are closed systems, it is hardly possible to investigate which processes take place during operation and, therefore, it is not possible to infer beyond doubt why certain observations appear. As pointed out previously, *post mortem* analysis of discharge batteries revealed the formation of toroid shaped particles of Li_2O_2 in some cases [81-85] and films of Li_2O_2 in others [83-85]. Film formation is observed in the absence of water [85] and at large current densities [83-85], whereas particles form in the presence of water [81, 82, 85] and at a low current densities [83-85]. Apparently the formation of toroid shaped Li_2O_2 particles allows for a deeper discharge of the battery [81, 82], most probably because no insulating film of Li_2O_2 is formed which deactivates the electrode. It has also been observed that a deeper discharge is possible when the oxygen electrode is made from gold instead of carbon black [32, 34, 86]. Hence, conditions under which a favourable discharge behaviour was observed (presence of trace amounts of water, use of gold electrodes, high overpotentials) are the same conditions under which oxygen reduction proceeds *via* the indirect pathway of peroxide formation. Indeed, some authors in the above mentioned battery studies have proposed the involvement of superoxide. Our studies substantiate these assumptions and therefore make a significant contribution to the lithium-air battery research.

But it has to be emphasised that severe problems on the route to practical lithium-air batteries remain: Although parameters have been identified that lead to a favourable discharge behaviour, charging of these batteries remains problematic: Already in the initial stage of charge rather high potentials are required. But at a certain point during charging the potential starts to increases to levels that stop short of DMSO oxidation (during charge of model batteries the experimentalist defines a certain charging current and the potential is adjusted to sustain this current) [32, 86]. Such an increase of the charging potential of model lithium-air batteries operating with ether and carbonate based electrolytes was previously related to a change from a desired to in undesired charging reaction. McCloskey *et al*. showed that the increase of the potential from one plateau to another takes place when oxygen evolution stops and CO_2-evolution starts [87]. The observed increase of the potential is probably due to the depletion of reduced oxygen species in the electrode in the course of oxygen evolution (charging). As no reduced oxygen species are available for oxidation at a given potential, the potential has to increase to allow other reactions in order to sustain the preset charging current. As carbonate based electrolytes undergo a reaction with reduced oxygen species during discharge, only a very small fraction of the reduced oxygen is deposited as Li_2O_2 in the electrode [21-28]. During charging of the battery most of the Li_2O_2 is oxidised after a short period of time. After this periode charging (defined as the same amount of charge passed as during discharge) of the battery is not yet complet. Hence, the potential increases to levels where decomposition products of the electrolyte are oxidised to CO_2. A similar behaviour of the charging potential in model batteries employing DMSO based electrolytes [34, 88] can indicate that the evolution of oxygen does not produce sufficient charge to complete the charging cycle of the battery. However, this is no proof that the true coulombic efficiency is lower one. An increase of the charging potential can also take place when due to a thermodynamic stabilisation a fraction of the Li_2O_2 is more difficult to oxidise.

We have shown in Paper 2 that not only the reduction of oxygen but also the oxidation of Li_2O_2 is an electrocatalytic reaction. The oxidation of Li_2O_2 proceeds faster at platinum electrodes than at gold electrodes. In addition, the oxidation of Li_2O_2 takes place in two distinguishable waves at gold electrodes. We have ascribed this behaviour to the formation of two monolayers of Li_2O_2 on gold whereas one monolayer interacts more strongly with the gold surface than the other. This interpretation was supported by measurements at gold Au(111) single crystals.

Even if the increasing charging potential comes along with a true coulombic efficiency lower one, this does not necessarily indicated the consumption of reduced oxygen species *via* parasitic reactions such as electrolyte decomposition. In model batteries Li_2O_2 might have been deposited at sites in the electrode without electric contact. Li_2O_2 deposited on

these sites cannot be re-oxidised and the potential needs to increase in order to sustain other reactions. It is therefore of interest whether all the reduced oxygen eventually forms Li_2O_2. By means of redox titration Schwenke *et al*. have shown that only 65% of the reduced oxygen form Li_2O_2 in tetraglyme based electrolytes [82] and Aetukuri *et al*. found a Li_2O_2-yield between 75 - 82% in DMSO based electrolytes [81]. Similarly we have shown in Paper 1 and in Paper 3 that only 2/3 of the reduced oxygen can be re-evolved as oxygen in the following anodic sweep. However, as in a model battery there are two possible reasons for a true coulombic efficiency much smaller one: (1) Electrolyte decomposition during oxygen reduction and (2) incomplete oxidation of reduced oxygen species.

However, it is clear that at least a fraction of the reduced oxygen species that are unavailable for oxygen evolution, participate in electrolyte decomposition during oxygen reduction. We observe CO_2 (Paper 2 and Paper 3) evolution in the anodic sweep only when oxygen was reduced in the previous cathodic sweep and, since DMSO is the only source of carbon, CO_2 evolution indicates unambiguously electrolyte decomposition. Indeed, the relationship between evolved amounts of CO_2 and reduced amounts of O_2 (Paper 3) are a strong indication that electrolyte decomposition takes place during oxygen reduction. In addition, larger than expected m.p.e-values indicate the deposition of decomposition products during oxygen reduction. This is in agreement with literature results where XPS- [89, 90], eQCMB- [91] and DEMS- [35] measurements show that electrolyte decomposition occurs in DMSO based electrolytes during oxygen reduction. Electrolyte decomposition reduces the true coulombic efficiency because reduced oxygen species undergo an irreversible chemical reaction. Electrolyte decomposition during discharge, therefore, is a possible explanation for the bad charging behaviour of model lithium-air batteries that employ DMSO based electrolytes. However, a bad charging behaviour is also observed in batteries that favour the indirect pathway of peroxide formation. So far we can ascribe electrolyte decomposition only to the direct pathway of peroxide formation. But the absence of any proof for electrolyte decomposition during the indirect pathway of peroxide does not mean that it does not take place. In our view it is not yet clear whether DMSO is stable under operation conditions of lithium-air batteries. At any rate it has to be taken into account that superoxide can undergo a reaction at metals at open circuit potential as shown in Paper 4. This reaction depletes the electrolyte of reduced oxygen species which cannot be reoxidiesed. Whether this reaction occurs in model lithium-air batteries is unknown, but it might take place at construction parts of the battery. If so other reactions have to take place during battery charging in order to complete a full charging cycle.

It needs mentioning that other authors, in contradiction to our view, consider DMSO based electrolytes stable and fit for operation in lithium-air batteries [34, 92]. In Paper 3 we gave a discussion on why the data presented in Ref. [92] and [34] do not provide sufficient

evidence to support that statement. Notwithstanding this, there is no conclusion on the stability of DMSO that is generally accepted. This is best exemplified by the group of Calvo where in one publication the authors provide spectroscopic evidence for the stability of DMSO during oxygen reduction [93] and in another publication spectroscopic evidence for the instability of DMSO (neither author provided a discussion on the contradiction) [90].

Sharon *et al*. provided eQCMB results which were considered to show that oxygen reduction in lithium containing DMSO based electrolytes leads to the quantitative formation of Li_2O_2 which is then oxidised again quantitatively in the anodic sweep [94]. However, Sharon *et al*. did not consider the partial formation of superoxide during oxygen reduction which is not deposited quantitatively as Li_2O_2 when the m.p.e-values were determined (the m.p.e-values therefore only appear to fit well to the quantitative formation of Li_2O_2). In addition, Sharon *et al*. assigned mass changes to the oxygen evolution although the potential region does not fit to this interpretation. In our eQCMB studies we found no mass changes during oxygen evolution. We have ascribed this finding to the formation of an inhomogeneous film during oxygen reduction that consists of both, Li_2O_2 and decomposition products. In the anodic sweep, Li_2O_2 is oxidised first, leaving behind cavities on the surface that are filled with electrolyte. The additional mass of the electrolytes offsets the mass loss due to Li_2O_2 oxidation. Larger mass changes occur when the decomposition products are oxidised.

We have shown in Paper 3 that superoxide is not the active species that initiates electrolyte decomposition (at least not the kind of electrolyte decomposition that leads to solid decomposition products detectable by eQCMB). This suggests that it is possible to avoid electrolyte decomposition during discharge of lithium-air batteries by favouring the indirect pathway of peroxide formation. But as pointed out above this is not necessarily true, because electrolyte decomposition might also occur during disproportionation of superoxide. Further research is required to investigate whether electrolyte decomposition is only due to the electrochemical formation of peroxide or also occurs during disproportionation of superoxide. Previous studies that aimed to show that electrolyte decomposition occurs were done under conditions where it is to be expected that oxygen reduction proceeds at least partially *via* the direct pathway of peroxide formation (Indeed, this might be the reason for contradicting results on CO_2 evolution concerning model battery studies performed by McClosky *et al*. [35] and Peng *et al*. [34].) It is a significant question whether electrolyte decomposition can be avoided if proper discharge conditions are chosen that favour the indirect pathway of peroxide formation. So far ensuring electrolyte stability has been a challenge.

If it turns out that DMSO is stable under conditions where the indirect pathway of peroxide formation is favoured, then two of the above mentioned reasons would explain the unsatisfying charging behaviour: Firstly, larger Li_2O_2 particles might lose mechanical and

electronic contact to the electrode when Li_2O_2 layers that adhere to the electrode are oxidised. Secondly, Li_2O_2 might be preferentially deposited on sites in the electrode that do not have any electric contact in the first place. (It is conceivable that carbon, of which most gas diffusion electrodes at present are manufactured, does not catalyse the heterogeneous oxidation of superoxide by an unknown compound in the electrolyte) In either case, oxygen evolution would cease at an early stage of charge and the true columbic efficiency would remain far below 1. In both cases only redox mediators would help to achieve a full recharge [95]. However, redox mediators are likely to introduce new problems: They are usually organic molecules that feature conjugated π-electron systems and are, therefore, prone to a chemical attack of reduced oxygen species.

8. Outlook

As outlined in detail in the previous section, our work relates well to the current lithium-air battery research. Our results are significant as they provide approaches to the understanding of observations made in studies on lithium-air batteries. I consider this significant, because I find it hard to belief that practical lithium-air batteries can ever be realised without a profound understanding of the oxygen reduction reaction in organic electrolytes. Our work has contributed to deepen the understanding of the oxygen reduction reaction, but truth be told we are only scratching at the surface. The discussion of our results in Section 6 has revealed *that* we know that there are a number of parameters that influence the mechanism of oxygen reduction reaction, but we do not know *why* and *how*.

However, in my opinion the most pressing and interesting question is whether the effects of cation, electrolyte, additives, and electrode materials work independently from each other or whether they interact. For instance: Does gold always favour the indirect pathway of peroxide formation at low overpotentials or do combinations with other parameters exist which cause gold to favour the direct pathway of peroxide formation, whereas platinum favours the indirect pathway under the same conditions? To address this question it is necessary to create a larger data stock and to systematically investigate the impact of a variety of combinations of different electrolytes, additives, cations, and electrode materials on the mechanism of oxygen reduction. In such a study it would be relatively irrelevant whether the electrolyte undergoes a chemical reaction with reduced oxygen species (as long as it is possible to discriminate between the direct and the indirect pathway of peroxide formation). Such a vast scale study would still only address the question "*what is?*", but it could be flanked with efforts to address the question "*why is?*".

Adsorption Isotherm of Superoxide

In Section 6 I mentioned the theory that similar to the situation in aqueous electrolytes, the free adsorption enthalpy of O_2^- on the respective surface might be the factor that decides whether the electrode favours the direct or the indirect pathway of peroxide formation. To test this theory, it is necessary to determine the free adsorption enthalpy of O_2^-. Anson *et al*. [96] and Christie *et al*. [97] have demonstrated that double potential-step chronocoulometry can be used to determine the surface concentration of an adsorbate at a given potential. These measurements can be used to determine the adsorption isotherm of O_2^- from a solution of superoxide at various temperatures. A plot of the logarithm of the surface concentration at a given potential versus the reciprocal temperature should yield the

free adsorption enthalpy. It would be interesting to see whether the potential at which the transition from the indirect to the direct pathway of peroxide formation takes place correlates to the potential where the free adsorption enthalpy of superoxide exceeds a certain threshold value (this threshold value is likely to depend on the cation, but the determination of the adsorption isotherm must be done in the absence of hard *lewis* acids, so that superoxide cannot be reduced further). To provide theoreticians who could derive a causation from such a correlation with an adequate data base, these measurements should be conducted at single crystal surfaces (Au(111) and Pt(111) are experimentally best accessible).

Reaction Order of Oxygen and Lithium

Also because of other reasons the knowledge of the adsorption isotherm would be quite interesting: Our group has recently found that the reaction order of oxygen for the oxygen reduction reaction in Mg^{2+}-containing DMSO based electrolytes at platinum electrodes is close to zero [98]. This indicates that the surface is saturated either with oxygen or superoxide in the investigated potential range. Knowledge of the adsorption isotherm would allow us to decide whether the surface is saturated with oxygen or superoxide. Indeed, it would be interesting to conduct the measurements done by Reinsberg also in Li^+ containing solutions and at gold electrodes, where a transition from the indirect to the direct pathway of peroxide formation is observed. Is the reaction order in oxygen and in Li^+ also zero (Reinsberg also found a reaction order of zero in Mg^{2+}) in the potential range where oxygen is reduced electrochemical only to superoxide? Does the reaction order in oxygen increase with the temperature (which would be expected as the surface should not be saturated with adsorbates at high temperatures) and does the temperature influence the potential at which the transition from the indirect to the direct pathway of peroxide formation takes place?

Properties of the Solvent: Donor Number, Acceptor Number or Something Else?

In Section 6 I have pointed out that it is still not well understood how the electrolyte influences the mechanism of oxygen reduction reaction, or indeed, which property of the electrolyte is of importance: The acceptor or the donor number? To answer this questions, it is necessary to examine whether the potential at which the transition from the indirect to the direct mechanism takes place depends on the acceptor, the donor number, or on other parameters of the solvent. DEMS measurements in the dual thin layer cell should be conducted for a variety of solvents with different donor and acceptor numbers at least at gold and platinum electrodes.

If the free adsorption enthalpy of superoxide must exceed a certain threshold value, it is likely that the acceptor number exerts an effect: A larger acceptor number will cause a better solvation of superoxide (*i.e.*, a more negative free solvation enthalpy). Hence, the

adsorption enthalpy of superoxide will become less negative in a solvent with a large acceptor number. This is likely to have an influence on the potential at which the transition from the indirect to the direct mechanism takes place. A small adsorption enthalpy means that the residence time of superoxide at the surface is smaller than the time required to transfer the second electron. Therefore, the second electron transfer is only possible when its rate constant exceeds that of the desorption of superoxide. An increase of the former requires a higher overpotential. An alternative view is that a higher overpotential is required to keep superoxide adsorbed. Given that superoxide is an anion that should desorb as the potential becomes more negative this appears to be a rather unlikely scenario. However, as pointed out in Paper 2 the transfer of the second electron requires probably the coordination of a cation to superoxide, which would result in a neutrally charge particle. In addition, superoxide as a weak *lewis* base should be very well polarizable, so that confined between a positive charged cation and a negative electrode superoxide forms a dipole. It is, therefore, conceivable that superoxide will adsorb more strongly with its positive charge end to the electrode as the potential becomes more negative.

It seems to be clear from literature results that a large donor number in the solvent is required to observe the formation of superoxide during oxygen reduction [40, 61, 71]. But does this also mean that superoxide can only be generated in solvents with a large donor number? Indeed, it is conceivable that a large donor number causes a very good solvation of Li^+ and, therefore, introduces an activation barrier for the Li^+-induced disproportionation of superoxide. In this case, the donor number would only slow down the disproportionation of superoxide and, hence, would only affect our ability to detect superoxide. That is, the indirect pathway of peroxide formation could also take place in acetonitrile where superoxide formation has never been observed *via* the RRDE-technique [70, 72]. In this line of though the donor number of acetonitril would be too small to stabilise superoxide long enough to detect it during an RRDE-experiment. The RRDE-technique allows the detection of intermediates only if its half-life is larger than 10^{-3} seconds [99].

Effect of Additives: Another Way to Investigate the Effect of Solvent Properties

Additives like water can work in the same way as already discussed for the solvents. Hence, additives might just add a large donor or acceptor numbers to the solvent or they could undergo a strong interaction with the electrode material, which might reduce the ability of the electrode material to transfer the second electron. The above suggested experiments (DEMS-measurements, double potential step chronocoulometry) could also be done to investigate the influence of additives. Aside from water, other additives could be investigated: NH_3, $NH_{(3-x)}R_x$, R_2O, R_2S, urea, and organic compounds of boron (although here both stability of the compound and safety might be an issue). The first of the aforementioned

compounds feature a free electron pair and could, therefore, act as electron donors, whereas boron compounds have an electron deficiency and might, therefore, act as electron acceptor. The influence of the acceptor number of the additive should be studied in a solvent with a low acceptor number and a solvent with a low donor number should be used to study the influence of the donor number of the additive.

Geometric Effect: Potential Step Experiments and Adsorption Mode

On the other hand it is also likely that a specific interaction between solvent and electrode influences the mechanism of oxygen reduction. This is possible, for instance, when the adsorbed solvent exerts a geometric effect which prohibits the adsorption of superoxide or oxygen in a certain mode. This, however, is a prerequisite for the reduction to peroxide. In this case, there would be no correlation between the acceptor / donor number and the potential at which the transition from the indirect to the direct pathway of peroxide formation takes place. However, it is not clear beyond doubt whether a certain adsorption mode of superoxide or oxygen is required to form peroxide. Based on what we think is a geometric effect of electro-deposited Li_2O_2 on the oxygen reduction reaction, we have proposed that oxygen must adsorb in a bridge position at platinum to form peroxide. To strengthen the case for a geometric effect, it would be advisable to conduct potential step experiments in the dual thin layer cell and to check whether the z-value really depends on the amount of deposited Li_2O_2. Such an experiment would eliminate any effect of the potential that may overlie the respective measurements described in Paper 2 (indeed those experiments should not be limited to platinum, but all electrode materials should be subject to potential step experiments). But it will be difficult to determine the adsorption mode of oxygen or superoxide at the polarised electrode. In the case of superoxide, SERS or ATR-FTIR (attenuated total reflection fourier transformed infrared) spectroscopy may be employable to that end.

Another way to check whether it is possible to exert a geometric effect on the oxygen reduction reaction is to block certain adsorption sites (threefold hollow site, bridge position) with adsorbates. If peroxide formation or oxygen reduction is strongly inhibited on these surfaces, this would be a strong indication that a geometric effect exists. However, it will be difficult to find surfaces where adsorbates block certain sites, but do not alter the electronic properties of the surface *via* a ligand effect.

Spectroscopic Investigations on the Effect of the Cation

In Section 6 I have considered the possibility that solvents with a large donor number mask the cation, which we think must coordinate to adsorbed superoxide in order to facilitate the second electron transfer. It will be difficult to test whether the solvent can inhibit the

cation to coordinate to superoxide. Again, SERS or ATR-FTIR spectroscopy might show whether M-O stretching modes (M = Li^+, Na^+, K^+ etc.) appear at potentials close to the transition from the indirect to the direct pathway of peroxide formation. Furthermore, it would be interesting to see whether complexing agents like crown ethers might able to inhibit the appearance of M-O stretching modes under similar conditions.

Electrolyte Stability

Aside from these fundamental questions for the oxygen reduction reaction in organic electrolytes, some questions with more direct consequences for the lithium-air battery research remain. The most important question is whether electrolyte decomposition also occurs during disproportionation of superoxide. Oxygen should be reduced to superoxide for a prolonged period of time from the gas phase in the conventional cell in quiescent solution. The formation of superoxide should take place although we observe a z-value of 1.5 e^-/O_2 even at low overpotentials and in this kind of cell. The larger than expected z-value was assigned to a chemical reaction of superoxid at gold particles at open circuit potential that releases oxygen (e.g. disroportionation of superoxide). However, superoxid that does not undergo a reaction at those particles will be deposited sooner or later as Li_2O_2 on those parts of the gold electrode which are under potential control. An additional faradic charge that does not corresponds to the evolved amounts of oxygen in the following anodic sweep would occur if electrolyte decomposition takes place during disproportionation of superoxid and if the resulting decomposition products are electrochemical active.

The Effect of CO_2

In the lithium-air battery literature, the effect of CO_2 on the oxygen reduction reaction has largely been neglected. However, Gowda *et al*. [100] and Lim *et al*. [101] have conducted practical and theoretical studies on the matter. They have concluded that the irreversible formation of Li_2CO_3 during oxygen reduction in the presence of CO_2 is inevitable. Lim *et al*. found experimentally that Li_2CO_3 is the sole discharge product in DMSO based electrolytes, whereas both, Li_2O_2 and Li_2CO_3 are formed in DME (Dimethoxyethane) based electrolytes. Therefore, it should be tested whether the Li_2CO_3 formation is really inevitable. Based on DFT calculations, Lim *et al*. suggested that the dielectric constant of the solvent decides whether superoxide will form a complex with Li^+ (LiO_2) that will ultimately lead to Li_2O_2 or whether it forms a complex with CO_2 (CO_4^-) that will ultimately lead to Li_2CO_3. According to Lim *et al*., the activation barrier for the formation of LiO_2 results from the need of Li^+ to leave its solvation sphere. Hence, if the solvation of Li^+ is reduced, the activation barrier for the Li^+-induced disproportionation of superoxide is lower and the formation of Li_2O_2 is favoured. However, this would also mean that the lifetime of superoxide is reduced.

Since a long lifetime of superoxide appears to be desirable to allow the formation of large Li_2O_2 particles upon discharge of lithium-air batteries, such an approach seems disadvantageous. Thus, a relatively high activation barrier for the lithium induced disproportionation of superoxide and an even higher activation barrier for the formation of CO_4^- are required. A better solvation of superoxide should increase the activation barrier for the formation of both, LiO_2 and CO_4^-. Maybe it is possible to maintain a large enough activation barrier for the formation of LiO_2 when the acceptor number of the solvent is increased. That way, the formation of Li_2O_2 particles may still be possible when the donor number is decreased at the same time. The formation of Li_2CO_3 could be inhibited when the activation barrier for the formation of LiO_2 is sufficiently decreased below the activation barrier for the formation of CO_4^-. The easiest approach to test whether Li_2CO_3 formation can be avoided by choosing the proper solvent (or additive) is to conduct DEMS measurements on the oxygen reduction reaction in a variety of solvents and in the presence of CO_2. The formation of Li_2CO_3 should show up in a z-value of 4 e^-/O_2, whereas Li_2O_2 formation comes along with a z-value of 2 e^-/O_2. Indeed, the observation of a z-value of 1 e^-/O_2 would be desired, because this would mean that superoxide does not undergo reaction with CO_2 or Li^+ on the investigated time scale.

However, even if a z-value of 1 e^-/O_2 is observed it is still not clear whether superoxide will eventually form Li_2O_2, Li_2CO_3, or both. UV/vis experiments could be conducted to determine the rate constant of Li^+-induced disproportionation of superoxide. If the time constant for the decline of the adsorption band due to superoxide does not depend on the presence or absence of CO_2, then Li_2O_2 formation takes place. Finally, these measurements should be conducted in a temperature range that is expected during operation of a practical lithium-air battery.

The above mentioned finding that oxygen reduction in the presence of CO_2 leads to Li_2CO_3 is quite curious. The formation of Li_2CO_3 requires the cleavage of the O,O-bond. This should raise the question how CO_2 brings about the cleavage of the O,O-bond as it is hard to understand at this point why the activation barrier for this step is acceptable in the presence of CO_2 but not in its absence. Although I cannot suggest any concrete experiments to conduct, I belief it is worthwhile to investigate the mechanism of the oxygen reduction reaction in the presence of CO_2 further. The evolution of oxygen from Li_2CO_3 takes place at ~900 mV more positive than from Li_2O_2 [6, 7]. In principal this is in the potential range where DMSO is still stable. There are probably large activation barriers for this reaction (in particular since an O,O-bond has to be formed) but if conditions could be found that make this reaction possible this would be highly interesting for applications in lithium-air batteries.

Both, Gowda *et al*. [100] and Lim *et al*. [101], have suggested that the dielectric constant of the solvent determines the share of reduced oxygen species that eventually form

Li_2O_2 (in competition to Li_2CO_3). The mechanism on how the dielectric constant affects the final product of oxygen reduction is similar to the effect I proposed for the effect of the donor number on the indirect pathway of peroxide formation. Indeed, I do not belief that it can be ruled out that other properties than the donor or the acceptor number define the mechanism of oxygen reduction reaction. In fact I belief that the scientific community in the field has fixated on the donor number as the defining parameter, prematurely. However, farther above I have suggested to use additives to alter the properties of electrolytes and to check by these means how the donor and acceptor number affect the oxygen reduction reaction. If the finding of these experiments is that there is no correlation between the effect of the additive on the mechanism of the oxygen reduction reaction and its donor or acceptor number, it would be easy to check whether there is another property of the additive (dielectric constant, pka-value, polarity, etc.) that correlates with the observed effects.

9. Appendix

A1 Sulfolane

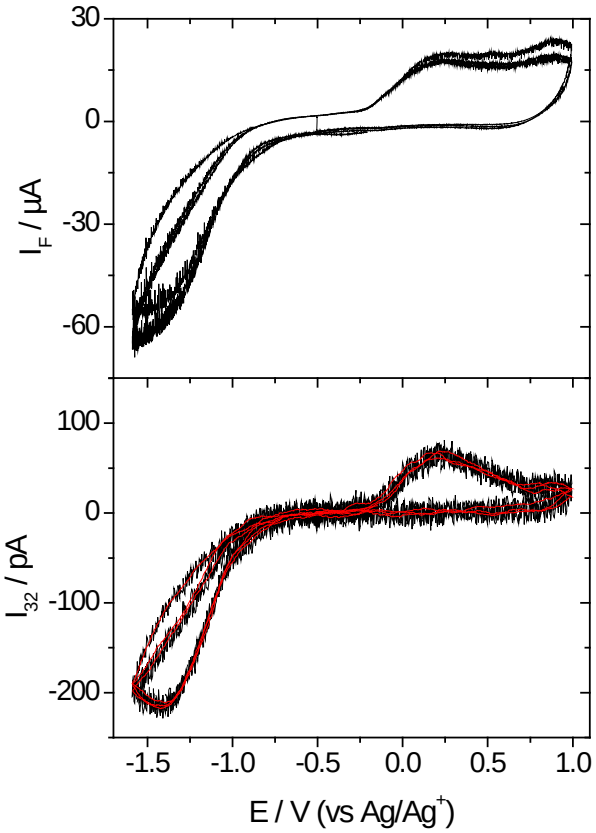

Figure A1.1: CV and MSCV for mass 32 an oxygen saturated electrolyte of 1 M LiClO4 in sulfolane. The experiment was done in the classical cell and a gold sputtered Teflon membrane was used as a working electrode.

Both the reductive current in the CV and the consumption of oxygen in the MSCV in Figure A1.1, indicate that oxygen reduction begins at -0.75 V in an electrolyte of 1 M $LiClO_4$ in sulfolane. In the anodic sweep oxygen evolution starts at -0.2 V. The true columbic efficiency in Figure A1.1 is about 30%. That is not much but comparable to DMSO based electrolytes.

A2 Benzonitrile

Figure A2.1 shows the CV and MSCVs obtained in an argon saturated electrolyte of 0.2 M $LiClO_4$ in Benzonitrile. For this DEMS measurement the classical cell with a working electrode of gold sputtered Teflon was employed. Severe electrolyte decomposition takes place at potentials smaller -1.3 V which is evident from the large reductive current in the CV and the evolution of H_2.

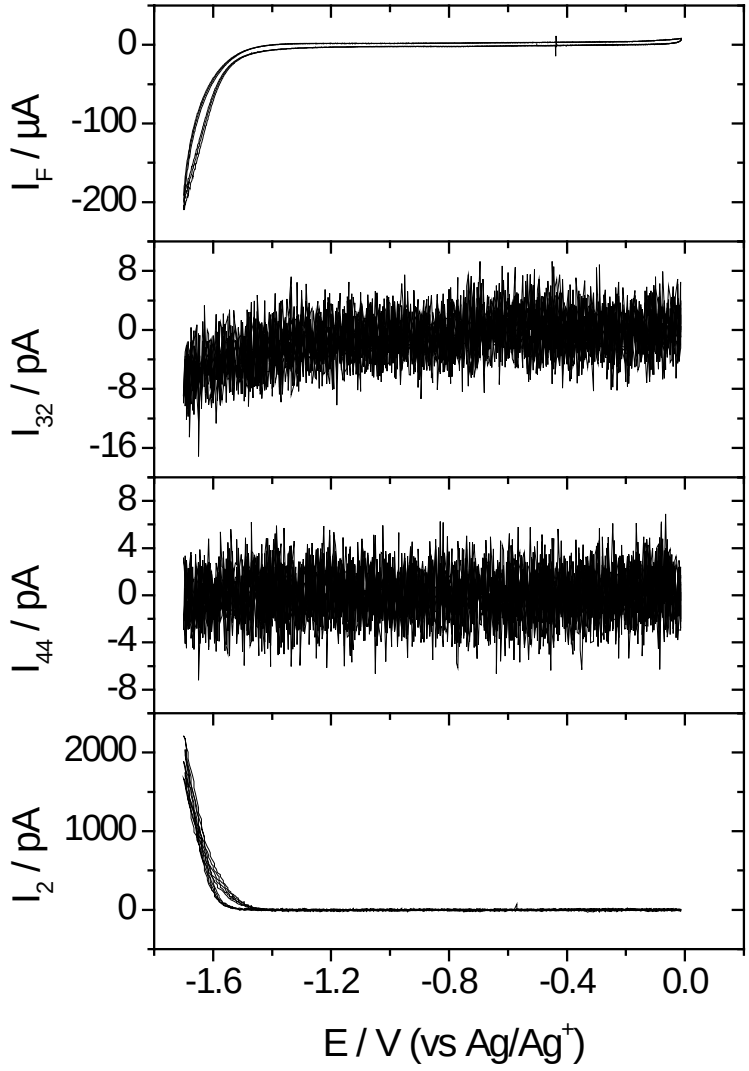

Figure A2.1: CV and MSCV for mass 32, 44 and 2 obtained in the classical cell at a gold sputtered Teflon membrane. Electrolyte 0.2 M $LiClO_4$ in Benzonitrile. The electrolyte was purged with argon.

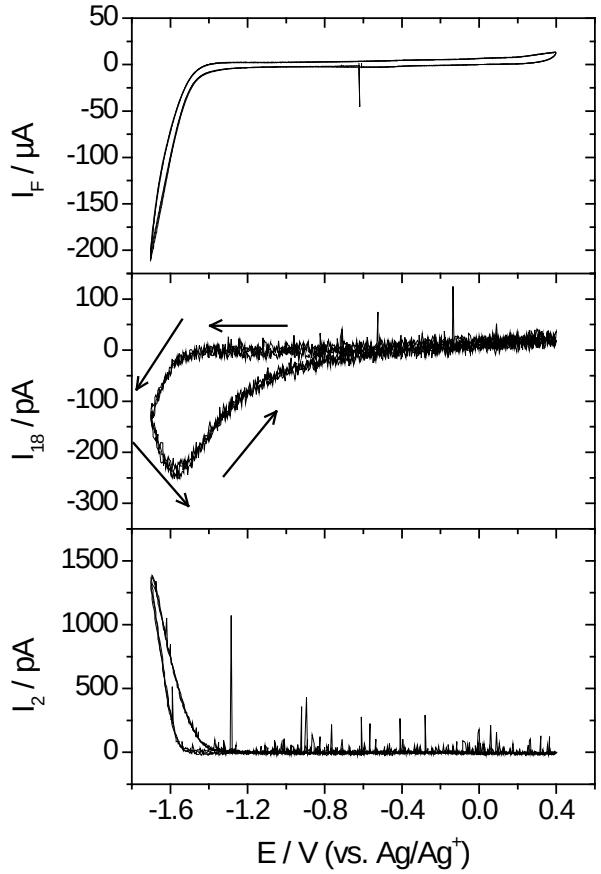

Figure A2.2: CV and MSCV for mass 18 and 2 obtained in the classical cell at a gold sputtered Teflon membrane. Electrolyte 0.2 M $LiClO_4$ in Benzonitrile. The electrolyte was purged with argon.

The consumption of H_2O (signified by a negative ion current for mass 18) parallel to the evolution of a signal an mass 2 in Figure A2.2 suggests that water is the source of hydrogen. Benzonitrile is immiscible with water, but trace amounts of water still dissolve in Benzonitrile. The water content is unknown and the solvent was used as received.

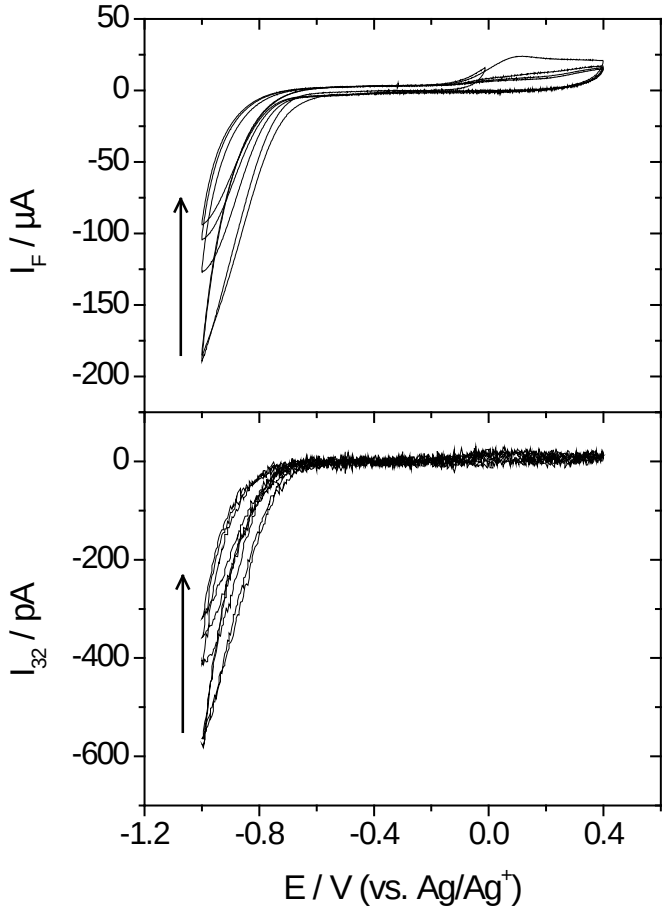

Figure A2.3: CV and MSCV for mass 32 obtained in the classical cell at a gold sputtered Teflon membrane. Electrolyte 0.2 M $LiClO_4$ in Benzonitrile. The electrolyte was purged with oxygen.

Figure A2.3 shows the CV and MSCV for mass 32 in an O_2 satturatedelectrolyte of 0.2 M $LiClO_4$ in Benzonitrile. Both the reduction current in the CV and the consumption of oxygen in the MSCV indicate that oxygen reduction begins at -0.65 V in this electrolyte. However, oxygen reduction in the cathodic run is not followed by oxygen evolution in the subsequent anodic run. Furthermore the current in the potential region of oxygen reduction drops from cycle to cycle. No reactivation is achieved in the potential range between -1.1 V and 0.4 V.

A3 Tetraglyme

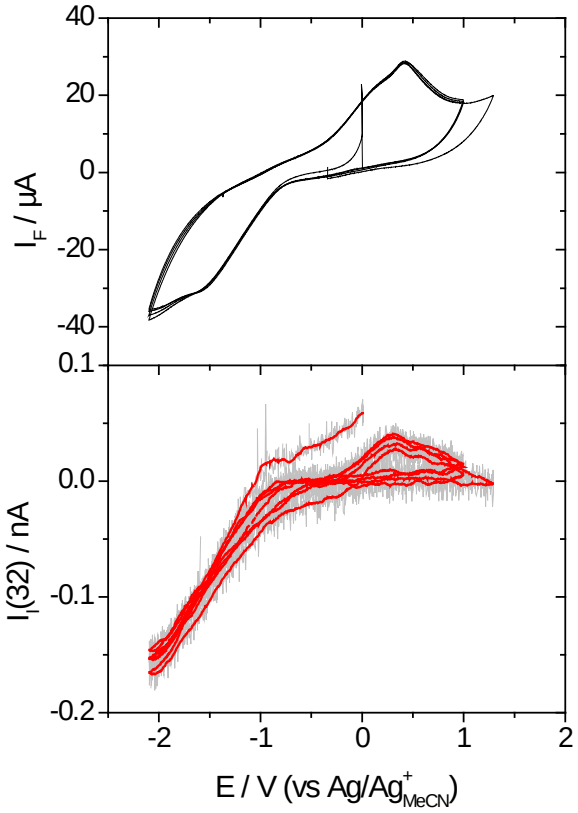

Figure A3.1: CV and MSCV for mass 32 an oxygen saturated electrolyte of 0.1 M LiClO4 in tetraglyme. The experiment was done in the classical cell and a gold sputtered Teflon membrane was used as a working electrode.

Both the reductive current in the CV and the consumption of oxygen in the MSCV in Figure A3.1, indicate that oxygen reduction begins at -0.75 V in an electrolyte of 0.1 M $LiClO_4$ in tetraglyme. In the anodic sweep oxygen evolution starts at -0.2 V. The true columbic efficiency in Figure A3.1 is about 10%.

A4 Memory effect of the DEMS

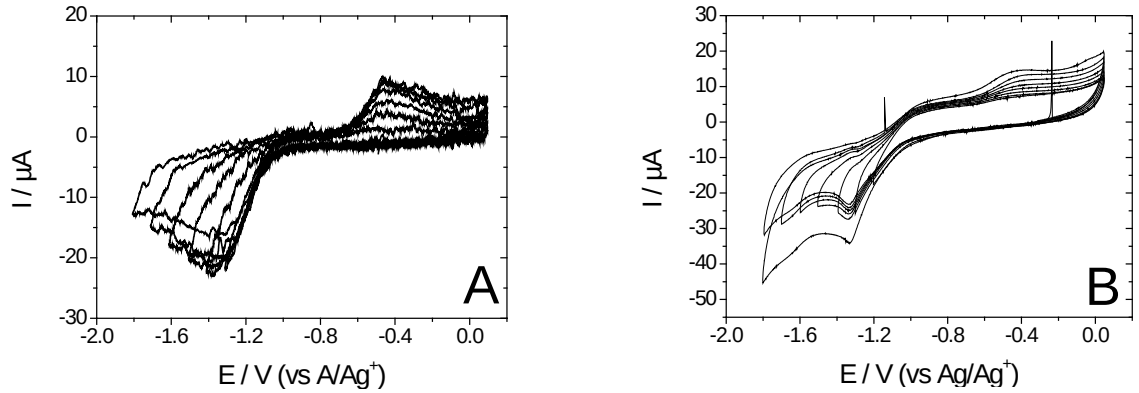

Figure A4.1: CVs obtained in a classical cell with a gold sputtered Teflon membrane as working electrode. The used electrolyte was 0.1 M $LiClO_4$ in DMSO purged with oxygen. A: CV in a classical cell, that was connected to a rotary pump that was not in contact with NMP prior to the experiment. B: CV in the very same cell and with the very same electrolyte as in A, after transfer of the cell to a DEMS at which NMP was used in prior experiments.

Figure 4.1 shows how the CV obtained in 0.1 M $LiClO_4$ in DMSO changes when it is recorded in a classical cell that is connected to a rotary pump (Figure 4.1A) and when this very cell is transferred to a DEMS system where NMP was used prior to the experiment. In order to rule out any effect due to contaminations, glassware and tubes were cleaned in chromic acid and dried at 100°C prior to the experiment. CVs as those in Figure 4.1B were observed several times, but only when a classical cell was attached to a DEMS system at which previously NMP was used. We call the impact of old measurements on the electrochemistry "memory effect of the DEMS".

The CV in Figure 4.1B cannot be generated, when NMP is added to a DMSO based electrolyte. Therefore, NMP it self is not responsible for the changes in the CV. However, NMP-vapour might damage construction parts of the DEMS made from plastics which causes them to release semi-volatile reaction products. Given that transport through the porous Teflon membrane is highly effective, even low vapour pressures of reaction products might affect the electrochemistry.

We were not able to determine the exact cause of the observed contamination, but CVs like those observed in Figure 4.1B were never observed again, once work with NMP was stopped in the group. Whether cross contaminations as those observed between NMP and DMSO also exist with other electrolyte systems is not known.

A5 Porous Teflon membranes as gas diffusion electrodes

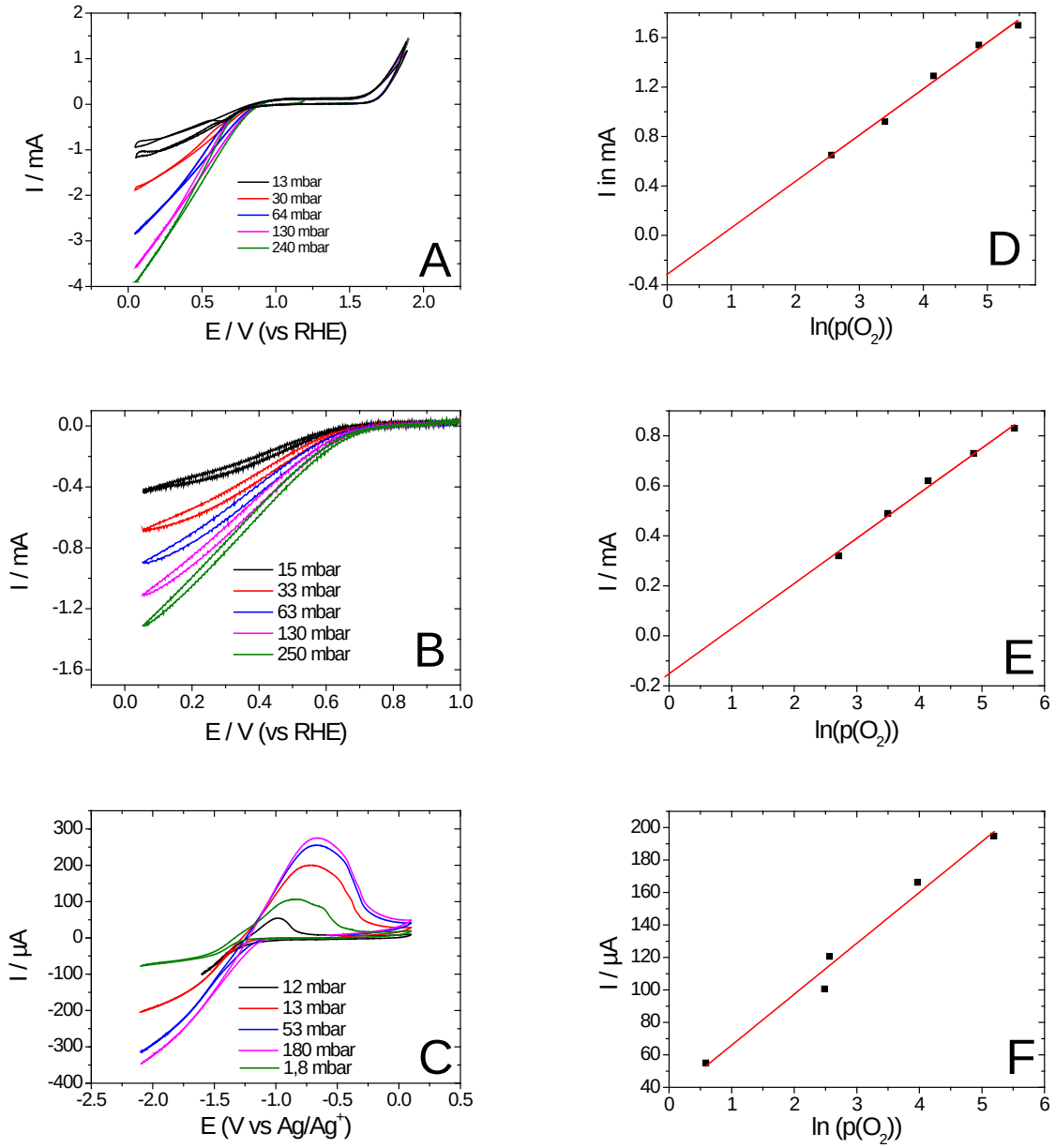

Figure 5.1: CVs obtained in the classical cell (A-C), when the space below the metal sputtered Teflon membrane the indicated oxygen pressures were applied. A: Pt-electrode in 0.5 M H_2SO_4; B: Ag-electrode in 0.1 M KOH; C: Au-electrode in 0.1 M $TBAClO_4$ in DMSO. In the layers D-F the current at a given potential is plotted as a function of the logarithm of the oxygen partial pressure. D: At 0.5 V at platinum; E: At 0.3 V at silver; F: At -1.6 V at gold.

In DEMS volatile compounds in the electrolyte evaporate at the interface between vacuum and electrolyte and diffuse through the Teflon membrane to the mass spectrometer. The opposite is also possible: Gaseous compounds can diffuse through the Teflon membrane into the electrolyte. In an arrangement where underneath the Teflon membrane not vacuum but a certain partial pressure of an electrochemical active gas is applied the membrane works as a gas diffusion electrode. The transport of gases through the gas phase is highly effective compared to the transport of dissolved gases through the liquid phase of the

electrolyte. Therefore, the amount of current in an electrochemical experiment is not limited by mass transport through the electrolyte, but by the kinetics of the electrochemical reaction. This is of course of importance when in an electrochemical process involving gaseous reactance, such as the discharge of a lithium-air battery, high conversion rates are aimed for. Figure 5.1 shows how the current during oxygen reduction from the gas phase at metal sputtered Teflon membranes in aqueous and non-aqueous electrolytes depends on the partial pressure of oxygen. Surprisingly, there is no linear relationship between partial pressure and current but a logarithmic relationship. We do not know yet, why this is. A possible explanation could be the exposed surface area when the pressure is alter. In that view the electrolyte would penetrate deeper into the pores when the pressure underneath the membrane is low and a larger share of the sputtered deposited metal would be in contact with the electrolyte. This theory could be checked in experiments in which the overall pressure underneath the membrane is kept constant. This could be achieved by using mixtures argon-oxygen mixtures with different concentrations of oxygen. Under these conditions the exposed surface area should not change.

10. References

[1] A. Puigarnau, Europa 2020 Eine Strategie für intelligentes, nachhaltiges und integratives Wachstum, 2010.
[2] Energiekonzept - für eine umweltschonende, zuverlässige und bezahlbare Energieversorgung, 2010.
[3] Nationaler Entwicklungsplan Elektromobilität der Bundesregierung, 2009.
[4] F. Cheng, J. Chen, Metal-air batteries: from oxygen reduction electrochemistry to cathode catalysts, *Chemical Society Reviews*, **41**, 2172-2192 (2012).
[5] K.M. Abraham, Z. Jiang, A polymer electrolyte-based rechargeable lithium/oxygen battery, *J. Electrochem. Soc.*, **143**, 1-5 (1996).
[6] M.W. Chase, Jr., NIST-JANAF Themochemical Tables, Fourth Edition, Journal of Physical and Chemical Reference Data, Monograph 9 (1998) 1-1951.
[7] J.D. Cox, D.D. Wagman, V.A. Medvedev, CODATA Key Values for Thermodynamics, Hemisphere Publishing Corp., New York, (1989).
[8] V.A. Agubra, J.W. Fergus, The formation and stability of the solid electrolyte interface on the graphite anode, *Journal of Power Sources*, **268**, 153-162 (2014).
[9] T. Ogasawara, A. Débart, M. Holzapfel, P. Novák, P.G. Bruce, Rechargeable Li2O2 Electrode for Lithium Batteries, *Journal of the American Chemical Society*, **128**, 1390-1393 (2006).
[10] A.K. Thapa, Y. Hidaka, H. Hagiwara, S. Ida, T. Ishihara, Mesoporous b-MnO_2 Air Electrode Modified with Pd for Rechargeability in Lithium-Air Battery, *J. Electrochem. Soc*., **158**, A1483-A1489 (2011).
[11] A.K. Thapa, K. Saimen, T. Ishihara, Pd/MnO_2 Air Electrode Catalyst for Rechargeable Lithium/Air Battery, *Electrochem. Solid State Lett.*, **13**, A165-A167 (2010).
[12] A. Débart, A.J. Paterson, J. Bao, P.G. Bruce, α-MnO_2 Nanowires: A Catalyst for the O_2 Electrode in Rechargeable Lithium Batteries, *Angewandte Chemie*, **120**, 4597-4600 (2008).
[13] A. Débart, J. Bao, G. Armstrong, P.G. Bruce, An O-2 cathode for rechargeable lithium batteries: The effect of a catalyst, *Journal of Power Sources*, **174**, 1177-1182 (2007).
[14] Y.-C. Lu, Z. Xu, H.A. Gasteiger, S. Chen, K. Hamad-Schifferli, Y. Shao-Horn, Platinum−Gold Nanoparticles: A Highly Active Bifunctional Electrocatalyst for Rechargeable Lithium−Air Batteries, *Journal of the American Chemical Society*, **132**, 12170-12171 (2010).
[15] X. Ren, S.S. Zhang, D.T. Tran, J. Read, Oxygen reduction reaction catalyst on lithium/air battery discharge performance, *Journal of Materials Chemistry*, **21**, 10118-10125 (2011).
[16] D. Zhang, Z.H. Fu, Z. Wei, T. Huang, A.S. Yu, Polarization of Oxygen Electrode in Rechargeable Lithium Oxygen Batteries, *J. Electrochem. Soc.*, **157**, A362-A365 (2010).
[17] A.K. Thapa, T. Ishihara, Mesoporous α-MnO_2/Pd catalyst air electrode for rechargeable lithium–air battery, *Journal of Power Sources*, **196**, 7016-7020 (2011).
[18] H. Cheng, K. Scott, Carbon-supported manganese oxide nanocatalysts for rechargeable lithium–air batteries, *Journal of Power Sources*, **195**, 1370-1374 (2010).
[19] M. Mirzaeian, P.J. Hall, Preparation of controlled porosity carbon aerogels for energy storage in rechargeable lithium oxygen batteries, *Electrochimica Acta*, **54**, 7444-7451 (2009).
[20] S.R. Younesi, S. Urbonaite, F. Björefors, K. Edström, Influence of the cathode porosity on the discharge performance of the lithium-oxygen battery, *Journal of Power Sources*, **196**, 9835-9838 (2011).
[21] B.D. McCloskey, D.S. Bethune, R.M. Shelby, G. Girishkumar, A.C. Luntz, Solvents' Critical Role in Nonaqueous Lithium-Oxygen Battery Electrochemistry, *J. Phys. Chem. Lett.*, **2**, 1161-1166 (2011).
[22] S.A. Freunberger, Y. Chen, Z. Peng, J.M. Griffin, L.J. Hardwick, F. Barde, P. Novak, P.G. Bruce, Reactions in the Rechargeable Lithium-O_2 Battery with Alkyl Carbonate Electrolytes, *Journal of the American Chemical Society*, **133**, 8040-8047 (2011).
[23] V.S. Bryantsev, M. Blanco, Computational Study of the Mechanisms of Superoxide-Induced Decomposition of Organic Carbonate-Based Electrolytes, The Journal of Physical *Chemistry Letters*, **2**, 379-383 (2011).
[24] V.S. Bryantsev, V. Giordani, W. Walker, M. Blanco, S. Zecevic, K. Sasaki, J. Uddin, D. Addison, G.V. Chase, Predicting Solvent Stability in Aprotic Electrolyte Li-Air Batteries:

Nucleophilic Substitution by the Superoxide Anion Radical ($O_2^{\bullet-}$), *J. Phys. Chem. A*, **115**, 12399-12409 (2011).
[25] G.M. Veith, N.J. Dudney, J. Howe, J. Nanda, Spectroscopic Characterization of Solid Discharge Products in Li-Air Cells with Aprotic Carbonate Electrolytes, *J. Phys. Chem. C*, **115**, 14325-14333 (2011).
[26] J. Xiao, J. Hu, D. Wang, D. Hu, W. Xu, G.L. Graff, Z. Nie, J. Liu, J.-G. Zhang, Investigation of the rechargeability of Li-O(2) batteries in non-aqueous electrolyte, *Journal of Power Sources*, **196**, 5674-5678 (2011).
[27] W. Xu, V.V. Viswanathan, D. Wang, S.A. Towne, J. Xiao, Z. Nie, D. Hu, J.-G. Zhang, Investigation on the charging process of Li_2O_2-based air electrodes in Li-O_2 batteries with organic carbonate electrolytes, *Journal of Power Sources*, **196**, 3894-3899 (2011).
[28] W. Xu, K. Xu, V.V. Viswanathan, S.A. Towne, J.S. Hardy, J. Xiao, D. Hu, D. Wang, J.-G. Zhang, Reaction mechanisms for the limited reversibility of Li-O_2 chemistry in organic carbonate electrolytes, *Journal of Power Sources*, **196**, 9631-9639 (2011).
[29] C.O. Laoire, S. Mukerjee, E.J. Plichta, M.A. Hendrickson, K.M. Abraham, Rechargeable Lithium/TEGDME-LiPF6/O-2 Battery, *J. Electrochem. Soc.*, **158**, A302-A308 (2011).
[30] L. Cecchetto, M. Salomon, B. Scrosati, F. Croce, Study of a Li-air battery having an electrolyte solution formed by a mixture of an ether-based aprotic solvent and an ionic liquid, *Journal of Power Sources*, **213**, 233-238 (2012).
[31] M. Marinaro, S. Theil, L. Jörissen, M. Wohlfahrt-Mehrens, New insights about the stability of lithium bis(trifluoromethane)sulfonimide-tetraglyme as electrolyte for Li–O_2 batteries, *Electrochimica Acta*, **108**, 795-800 (2013).
[32] M. Marinaro, U. Riek, S.K. Eswara Moorthy, J. Bernhard, U. Kaiser, M. Wohlfahrt-Mehrens, L. Jörissen, Au-coated carbon cathodes for improved oxygen reduction and evolution kinetics in aprotic Li–O_2 batteries, *Electrochemistry Communications*, **37**, 53-56 (2013).
[33] H. Wang, K. Xie, L. Wang, Y. Han, N-methyl-2-pyrrolidone as a solvent for the non-aqueous electrolyte of rechargeable Li-air batteries, *Journal of Power Sources*, **219**, 263-271 (2012).
[34] Z. Peng, S.A. Freunberger, Y. Chen, P.G. Bruce, A Reversible and Higher-Rate Li-O_2 Battery, *Science*, **337**, 563-566 (2012).
[35] B.D. McCloskey, D.S. Bethune, R.M. Shelby, T. Mori, R. Scheffler, A. Speidel, M. Sherwood, A.C. Luntz, Limitations in Rechargeability of Li-O_2 Batteries and Possible Origins, *The Journal of Physical Chemistry Letters*, **3**, 3043-3047 (2012).
[36] Y.-C. Lu, H.A. Gasteiger, Y. Shao-Horn, Catalytic Activity Trends of Oxygen Reduction Reaction for Nonaqueous Li-Air Batteries, *Journal of the American Chemical Society*, **133**, 19048-19051 (2011).
[37] M.E. Peover, B.S. White, The formation of the superoxide ion by electrolysis of oxygen in aprotic solvents, *Chemical Communications* (London), 183-184 (1965).
[38] D.T. Sawyer, J.L. Roberts Jr, Electrochemistry of oxygen and superoxide ion in dimethylsulfoxide at platinum, gold and mercury electrodes, *Journal of Electroanalytical Chemistry (1959)*, **12**, 90-101(1966).
[39] C.O. Laoire, S. Mukerjee, K.M. Abraham, E.J. Plichta, M.A. Hendrickson, Elucidating the Mechanism of Oxygen Reduction for Lithium-Air Battery Applications, *J. Phys. Chem. C*, **113**, 20127-20134 (2009).
[40] C.O. Laoire, S. Mukerjee, K.M. Abraham, E.J. Plichta, M.A. Hendrickson, Influence of Nonaqueous Solvents on the Electrochemistry of Oxygen in the Rechargeable Lithium-Air Battery, *J. Phys. Chem. C*, **114**, 9178-9186 (2010).
[41] V. Viswanathan, H.A. Hansen, J. Rossmeisl, J.K. Nørskov Unifying the $2e^-$ and $4e^-$ Reduction of Oxygen on Metal Surfaces, *The Journal of Physical Chemistry Letters*, **3**, 2948-2951 (2012).
[42] A.J. Appleby, J.O.M. Bockris, E.B. Budevski, B.E. Coneway, A.R. Despic, R.R. Dogonadze, M. Enyo, D. Inman, S.U.M. Khan, L.I. Krishtalik, A.M. Kuznetsov, D.G. Lovering, R. Memming, E.J. Judd, A. Sadkowski, M.R. Tarasevich, E. Yeager, Kinetics and Mechanism of Electrode Processes, Plenum Press, New York, 1983.

[43] L. Andrews, Infrared Spectrum, Structure, Vibrational Potential Function, and Bonding in the Lithium Superoxide Molecule LiO_2, *The Journal of Chemical Physics*, **50**, 4288-4299 (1969).
[44] W. Hesse, M. Jansen, W. Schnick, Recent results in solid state chemistry of ionic ozonides, hyperoxides, and peroxides, *Progress in Solid State Chemistry*, **19**, 47-110 (1989).
[45] A.J. Bard, L.R. Faulkner, Electrochemical Methods: Fundamentals and Applications, 2nd ed., John Wiley & Sons Inc., New York, Weinheim, 2001.
[46] H. Baltruschat, Differential electrochemical mass spectrometry, *Journal of the American Society for Mass Spectrometry*, **15**, 1693-1706 (2004).
[47] S. Bruckenstein, R.R. Gadde, Use of a porous electrode for in situ mass spectrometric determination of volatile electrode reaction products, *Journal of the American Chemical Society*, **93**, 793-794 (1971).
[48] M. Petek, S. Bruckenstein, An isotopic labeling investigation of the mechanism of the electrooxidation of hydrazine at platinum: An electrochemical mass spectrometric study, *Journal of Electroanalytical Chemistry and Interfacial Electrochemistry*, **47**, 329-333 (1973).
[49] M. Petek, S. Bruckenstein, B. Feinberg, R.N. Adams, Anodic oxidation of substituted methoxyphenols. Mass spectrometric identification of methanol formed, *Journal of Electroanalytical Chemistry and Interfacial Electrochemistry*, **42**, 397-401 (1973).
[50] R.R. Gadde, S. Bruckenstein, The electroduction of nitrite in 0.1 M $HClO_4$ at platinum, *Journal of Electroanalytical Chemistry and Interfacial Electrochemistry*, **50**, 163-174 (1974).
[51] L. Grambow, S. Bruckenstein, Mass spectrometric investigation of the electrochemical behavior of adsorbed carbon monoxide at platinum in 0.2 M sulphuric acid, *Electrochimica Acta*, **22**, 377-383 (1977).
[52] O. Wolter, J. Heitbaum, Differential Electrochemical Mass Spectroscopy (DEMS) - a new method for the study of electrode processes, *Ber. Bunsenges. Phys. Chem.*, **88**, 2-6 (1984).
[53] B. Bittins-Cattaneo, E. Cattaneo, P. Königshoven, W. Vielstich, New developments in Electrochemical Mass Spectroscopy, in: A.J. Bard (Ed.) Electroanalytical Chemistry, A series of advances, 1991, pp. 181-220.
[54] T. Löffler, Charakterisierung und Anwendung einer neuen Dünnschichtzelle für die elektrochemische Massenspektrometrie, Institut für Physikalische und Theoretische Chemie, Universität Bonn, Bonn, 1997, pp. 93.
[55] G. Eggert, J. Heitbaum, Electrochemical Reactions of Propylenecarbonate and Electrolyes Solved Therein - a DEMS Study, *Electrochimica Acta*, **31**, 1443-1448 (1986).
[56] D. Tegtmeyer, A. Heindrichs, J. Heitbaum, Electrochemical on line mass spectrometry on a rotating electrode inlet system, *Ber. Bunsenges. Phys. Chem.*, **93**, 201-206 (1989).
[57] Z. Jusys, H. Massong, H. Baltruschat, A New Approach for Simultaneous DEMS and EQCM: Electro-oxidation of Adsorbed CO on Pt and Pt-Ru, *J. Electrochem. Soc.*, **146**, 1093 (1999).
[58] R.G. Compton, C.R. Greaves, A.M. Waller, A general computational method for mass-transport problems involving wall-jet electrodes and its application to simple electron-transfer, ECE and DISP1 reactions, *J. Appl. Electrochem.*, **20**, 575-585 (1990).
[59] J. Yamada, H. Matsuda, Limiting diffusion currents in hydrodynamic voltammetry: III. Wall jet electrodes, *Journal of Electroanalytical Chemistry and Interfacial Electrochemistry*, **44**, 189-198 (1973).
[60] M. Khodayari, P. Reinsberg, A.-E.-A.A. Abd-El-Latif, C. Merdon, J. Fuhrmann, H. Baltruschat, Determining Solubility and Diffusivity by Using a Flow Cell Coupled to a Mass Spectrometer, *ChemPhysChem*, 1647-1655 (2016).
[61] L. Johnson, C. Li, Z. Liu, Y. Chen, S.A. Freunberger, P.C. Ashok, B.B. Praveen, K. Dholakia, J.-M. Tarascon, P.G. Bruce, The role of LiO2 solubility in O2 reduction in aprotic solvents and its consequences for Li-O_2 batteries, *Nat Chem*, **6**, 1091-1099 (2014).
[62] D.A. Buttry, M.D. Ward, Measurement of interfacial processes at electrode surfaces with the electrochemical quartz crystal microbalance, *Chemical Reviews*, **92**, 1355-1379 (1992).
[63] G. Sauerbrey, Verwendung von Schwingquarzen zur Wägung dünner Schichten und zur Mikrowägung, *Zeitschrift für Physik*, **155**, 206-222 (1959).
[64] S.J. Martin, V.E. Granstaff, G.C. Frye, Characterization of a quartz crystal microbalance with simultaneous mass and liquid loading, *Analytical Chemistry*, **63**, 2272-2281 (1991).

[65] S. Bruckenstein, M. Shay, Experimental aspects of use of the quartz crystal microbalance in solution, *Electrochimica Acta*, **30**, 1295-1300 (1985).
[66] K.K. Kanazawa, J.G. Gordon, Frequency of a quartz microbalance in contact with liquid, *Analytical Chemistry*, **57**, 1770-1771 (1985).
[67] K. Keiji Kanazawa, J.G. Gordon, The oscillation frequency of a quartz resonator in contact with liquid, *Analytica Chimica Acta*, **175**, 99-105 (1985).
[68] F. Wudy, C. Stock, H.J. GHores, Measurment Methodes: Electrochemical: Quartz Microbalance, in: J. Garche (Ed.) Encylopedia of Electrochemical Power Sources, Elsevier, Amsterdam, 2009, pp. 660 - 672.
[69] J. Kestin, M. Sokolov, W.A. Wakeham, Viscosity of liquid water in the range -8°C to 150°C, *Journal of Physical and Chemical Reference Data*, **7**, 941-948 (1978).
[70] W. Torres, N. Mozhzhukhina, A.Y. Tesio, E.J. Calvo, A Rotating Ring Disk Electrode Study of the Oxygen Reduction Reaction in Lithium Containing Dimethyl Sulfoxide Electrolyte: Role of Superoxide, *J. Electrochem. Soc.*, **161**, A2204-A2209 (2014).
[71] E.J. Calvo, N. Mozhzhukhina, A rotating ring disk electrode study of the oxygen reduction reaction in lithium containing non aqueous electrolyte, *Electrochemistry Communications*, **31**, 56-58 (2013).
[72] M.J. Trahan, S. Mukerjee, E.J. Plichta, M.A. Hendrickson, K.M. Abraham, Studies of Li-Air Cells Utilizing Dimethyl Sulfoxide-Based Electrolyte, *J. Electrochem. Soc.*, **160**, A259-A267 (2013).
[73] R. Cao, E.D. Walter, W. Xu, E.N. Nasybulin, P. Bhattacharya, M.E. Bowden, M.H. Engelhard, J.-G. Zhang, The Mechanisms of Oxygen Reduction and Evolution Reactions in Nonaqueous Lithium–Oxygen Batteries, *ChemSusChem*, **7**, 2436-2440 (2014).
[74] P. Hartmann, C.L. Bender, M. Vračar, A.K. Dürr, A. Garsuch, J. Janek, P. Adelhelm, A rechargeable room-temperature sodium superoxide (NaO_2) battery, *Nat Mater*, **12**, 228-232 (2013).
[75] C.L. Bender, P. Hartmann, M. Vračar, P. Adelhelm, J. Janek, On the Thermodynamics, the Role of the Carbon Cathode, and the Cycle Life of the Sodium Superoxide (NaO_2) Battery, *Advanced Energy Materials*, **4**, 1301863 (2014).
[76] W. Liu, Q. Sun, Y. Yang, J.-Y. Xie, Z.-W. Fu, An enhanced electrochemical performance of a sodium-air battery with graphene nanosheets as air electrode catalysts, *Chemical Communications*, **49**, 1951-1953 (2013).
[77] Q. Sun, Y. Yang, Z.-W. Fu, Electrochemical properties of room temperature sodium–air batteries with non-aqueous electrolyte, *Electrochemistry Communications*, **16**, 22-25 (2012).
[78] J. Kim, H.-D. Lim, H. Gwon, K. Kang, Sodium-oxygen batteries with alkyl-carbonate and ether based electrolytes, *Physical Chemistry Chemical Physics*, **15**, 3623-3629 (2013).
[79] C. Xia, R. Black, R. Fernandes, B. Adams, L.F. Nazar, The critical role of phase-transfer catalysis in aprotic sodium oxygen batteries, *Nat Chem*, **7**, 496-501 (2015).
[80] A. Khetan, A. Luntz, V. Viswanathan, Trade-Offs in Capacity and Rechargeability in Nonaqueous Li-O2 Batteries: Solution-Driven Growth versus Nucleophilic Stability, *The Journal of Physical Chemistry Letters*, **6**, 1254-1259 (2015).
[81] N.B. Aetukuri, B.D. McCloskey, J.M. García, L.E. Krupp, V. Viswanathan, A.C. Luntz, Solvating additives drive solution-mediated electrochemistry and enhance toroid growth in non-aqueous Li-O_2 batteries, *Nat Chem*, **7**, 50-56 (2014).
[82] K.U. Schwenke, M. Metzger, T. Restle, M. Piana, H.A. Gasteiger, The Influence of Water and Protons on Li_2O_2 Crystal Growth in Aprotic Li-O_2 Cells, *J. Electrochem. Soc.*, **162**, A573-A584 (2015).
[83] B.D. Adams, C. Radtke, R. Black, M.L. Trudeau, K. Zaghib, L.F. Nazar, Current density dependence of peroxide formation in the Li-O_2 battery and its effect on charge, *Energy & Environmental Science*, **6**, 1772-1778 (2013).
[84] R.R. Mitchell, B.M. Gallant, Y. Shao-Horn, C.V. Thompson, Mechanisms of Morphological Evolution of Li_2O_2 Particles during Electrochemical Growth, *The Journal of Physical Chemistry Letters*, **4**, 1060-1064 (2013).
[85] A.C. Luntz, B.D. McCloskey, Nonaqueous Li-Air Batteries: A Status Report, *Chemical Reviews*, **114**, 11721-11750 (2014).

[86] M. Marinaro, P. Balasubramanian, E. Gucciardi, S. Theil, L. Jörissen, M. Wohlfahrt-Mehrens, Importance of Reaction Kinetics and Oxygen Crossover in aprotic Li–O_2 Batteries Based on a Dimethyl Sulfoxide Electrolyte, *ChemSusChem*, **8**, 3139-3145 (2015).
[87] B.D. McCloskey, R. Scheffler, A. Speidel, D.S. Bethune, R.M. Shelby, A.C. Luntz, On the Efficacy of Electrocatalysis in Nonaqueous Li-O_2 Batteries, *Journal of the American Chemical Society*, **133**, 18038-18041 (2011).
[88] M. Marinaro, P. Balasubramanian, E. Gucciardi, S. Theil, L. Jörissen, M. Wohlfahrt-Mehrens, The importance of reaction reaction kinetics and oxygen crossover in aprotic Li-O_2 batteries based on a dymethyl sulfoxide electrolyte, *ChemSusChem*, accepted (2015).
[89] Y. Shao, S. Park, J. Xiao, J.-G. Zhang, Y. Wang, J. Liu, Electrocatalysts for Nonaqueous Lithium–Air Batteries: Status, Challenges, and Perspective, *ACS Catalysis*, **2**, 844-857 (2012).
[90] F. Marchini, S. Herrera, W. Torres, A.Y. Tesio, F.J. Williams, E.J. Calvo, Surface Study of Lithium-Air Battery Oxygen Cathodes in Different Solvent-Electrolyte pairs, *Langmuir*, **31**, 9236-9245 (2015).
[91] W.R. Torres, A.Y. Tesio, E.J. Calvo, Solvent co-deposition during oxygen reduction on Au in DMSO LiPF6, *Electrochemistry Communications*, **49**, 38-41 (2014).
[92] M.A. Schroeder, N. Kumar, A.J. Pearse, C. Liu, S.B. Lee, G.W. Rubloff, K. Leung, M. Noked, DMSO-Li2O2 Interface in the Rechargeable Li-O_2 Battery Cathode: Theoretical and Experimental Perspectives on Stability, *ACS Applied Materials & Interfaces*, **7**, 11402-11411 (2015).
[93] N. Mozhzhukhina, L.P. Méndez De Leo, E.J. Calvo, Infrared Spectroscopy Studies on Stability of Dimethyl Sulfoxide for Application in a Li-Air Battery, *The Journal of Physical Chemistry C*, **117**, 18375-18380 (2013).
[94] D. Sharon, M. Afri, M. Noked, A. Garsuch, A.A. Frimer, D. Aurbach, Oxidation of Dimethyl Sulfoxide Solutions by Electrochemical Reduction of Oxygen, *The Journal of Physical Chemistry Letters*, **4**, 3115-3119 (2013).
[95] Y. Chen, S.A. Freunberger, Z. Peng, O. Fontaine, P.G. Bruce, Charging a Li-O_2 battery using a redox mediator, *Nat Chem*, **5**, 489-494 (2013).
[96] F.C. Anson, J.H. Christie, R.A. Osteryoung, A study of the adsorption of cadmium(II) on mercury from thiocyanate solutions by double potential-step chronocoulometry, *Journal of Electroanalytical Chemistry and Interfacial Electrochemistry*, **13**, 343-353 (1967).
[97] J.H. Christie, R.A. Osteryoung, F.C. Amson, Application of double potential-step chronocoulometry to the study of reactant adsorption. theory, *Journal of Electroanalytical Chemistry and Interfacial Electrochemistry*, **13**, 236-244 (1967).
[98] P. Reinsberg, Sauerstoffreduktion in Dimethylsulfoxid unter Verwendung von $Mg(ClO_4)_2$ als Leitsalz, Institut für Physikalische und Theoretische Chemie, Rheinische Friedrich-Wilhelms-Universität Bonn, Bonn, 2015.
[99] W.J. Albery, S. Bruckenstein, Ring-disc electrodes. Part 5.-First-order kinetic collection effciencies at the ring electrode, *Transactions of the Faraday Society*, **62**, 1946-1954 (1966).
[100] S.R. Gowda, A. Brunet, G.M. Wallraff, B.D. McCloskey, Implications of CO_2 Contamination in Rechargeable Nonaqueous Li-O2 Batteries, *The Journal of Physical Chemistry Letters*, **4**, 276-279 (2013).
[101] H.-K. Lim, H.-D. Lim, K.-Y. Park, D.-H. Seo, H. Gwon, J. Hong, W.A. Goddard, H. Kim, K. Kang, Toward a Lithium–"Air" Battery: The Effect of CO_2 on the Chemistry of a Lithium–Oxygen Cell, *Journal of the American Chemical Society*, **135**, 9733-9742 (2013).